MOLECULAR DESIGN AND SYNTHESIS OF NEW CYANOPYRIDONE-BASED SMALL MOLECULES FOR OLED APPLICATIONS

Thesis

Submitted in partial fulfillment of the requirements for the degree

of DOCTOR OF PHILOSOPHY

by

VISHRUTHA K S

DEPARTMENT OF CHEMISTRY

NATIONAL INSTITUTE OF TECHNOLOGY KARNATAKA

SURATHKAL, MANGALORE - 575 025

JANUARY 2024

DECLARATION

By the Ph.D. Research Scholar

I hereby declare that the Research Thesis entitled "**Molecular design and synthesis of new cyanopyridone-based small molecules for OLED applications**" which is being submitted to the **National Institute of Technology Karnataka, Surathkal** in partial fulfillment of the requirements for the award of the Degree of Doctor **of Philosophy** in **Chemistry** is a *bonafide report of the research work carried out by me*. The material contained in this Research Thesis has not been submitted to any University or Institution for the award of any degree.

Vishruthkss

Vishruth K S
Reg. No. 187032,187CY007
Department of Chemistry

Place: NITK, Surathkal
Date: 01/04/2024

CERTIFICATE

This is to certify that the Research Thesis entitled "**Molecular design and synthesis of new cyanopyridone-based small molecules for OLED applications**" submitted by **Ms. Vishrutha K S** (Register Number: 187032,187CY007) as the record of the research work carried out by her is *accepted as the Research Thesis submission* in partial fulfillment of the requirements for the award of degree of Doctor of Philosophy.

01.04.2024

Prof. B. Ramachandra Bhat
Research Supervisor

Prof. A. Vasudeva Adhikari
Research Supervisor

02/04/2024

Chairman- DRPC

विभागाध्यक्ष / H.O.D.
रसायन शास्त्र विभाग/ Chemistry Dept.
राष्ट्रीय प्रौद्योगिकी संस्थान कर्नाटक, सुरत्कल
NITK SURATHKAL
मंगलूरु-५७५ ०२५, कर्नाटक
MANGALURU-575 025, KARNATAKA

DEDICATED TO MY BELOVED PARENTS

ACKNOWLEDGEMENTS

It has been a great and memorable time in my life to pursue my Ph.D. studies at the National Institute of Technology, Karnataka. First and foremost, I thank the almighty **GOD** for instilling a curious spirit in me and giving me the wisdom, patience, and strength to successfully complete my thesis. My research would not have been possible without the support and contributions of many people who kindly helped me to make this dissertation possible.

I would like to express my profound sense of gratitude to my research supervisor **Dr. Airody Vasudeva Adhikari**, a Retired Professor, at the Department of Chemistry, NITK for his invaluable guidance, and tremendous academic support throughout the course of this investigation. He constantly encouraged and inspired me with his intensive research capability at every stage of my research. The directions he gave and the knowledge he shared in each and every single step of this work made it all possible. It has been a great honor and pleasure to conduct my Ph.D. journey under his supervision. I am extremely thankful to him for all his support during my research work.

Besides my advisor, I would like to express my sincere gratitude to my co-guide **Prof. Ramachandra Bhat**, Department of Chemistry, NITK for all the academic as well as administrative support, and encouragement to complete this endeavor successfully.

I sincerely thank **Prof. Bhallamudi Ravi**, Director, NITK, for providing the necessary facilities to carry out this research work. I express my earnest thanks to the RPAC members, Dr. Vijayendra S. Shetti. Department of Chemistry, and Prof. M. N. Sathyanarayan, Department of Physics, NITK for insightful comments and constructive criticism towards the improvement of research quality.

My special thanks to **Dr. Hidayath Ulla,** NCFIexE, IIT Kanpur for providing the fabrication facility for OLED devices.

I am also thankful to Prof. A. N. Shetty, Prof. A. C. Hegde, Prof. D. K. Bhat, Prof. A. M. Isloor, Prof. Udaya Kumar D, Prof. D. R. Trivedi, Dr. S. S. Mal, Dr. S. Dutta, Dr. D. Chakraborty, and Dr. L. Vellanki, Department of Chemistry for their constant support and encouragement. I also wish to extend my gratitude to all non-teaching staff in the Department of Chemistry.

I thank the University of Mysore, Manipal Institute of Technology (MIT), Manipal and Mangalore University for providing NMR and Mass Spectral facilities.

I also thank my group members Dr. Vinayakumara, Dr. Rajalakshmi K., Mr. Madhukara Acharya, Ms. Sruthi H., and Mr. S. S. Sudhanva Prasad for their constant support, encouragement, and company.

I am grateful to my dear friends Mrs. Anjana. Ms. Shreleeka K M, Mrs. Lavanya, Mrs. Feyona, Mr. Shreeganesha, Mr. Anees Muhammed, and Mr. Dinesha P, for their support and help during my research work. I extend my sincere thanks to all the research scholars in the Department, for their constant help and support.

My special thanks to Dr. Bratin Das, Department of Chemical Engineering IIT, Madras for helping me to do theoretical studies.

Mere words are not enough to express my gratitude to my family, father Mr. Saganappa, and mother Mrs. Rathnamma, for instilling in me the virtues of perseverance, commitment, love, and prayers. I also thank my brother Mr. Yashwant, Mr Sudhanva, my aunty Mrs. Hema, and my husband Mr. Divakar for their constant support, and relentless encouragement to strive for excellence. Finally, I thank all my family members and friends for their love and constant support.

VISHRUTHA K S

ABSTRACT

In recent years, due to their widespread use in electronic devices like organic light-emitting diodes (OLEDs), organic field-effect transistors (OFETs), organic light-emitting transistors (OLETs), organic solid-state lasers, organic solar cells (OSCs) and biomedical devices, the development of efficient organic π-conjugated small molecules has been a vital part in the field of electronics. Essentially, these materials mainly stand out because of their well-organized molecular structures, simple synthetic methods, straightforward purification procedures, amenability to solution and vacuum deposition processing while fabrication, and the ability to fine-tune functional properties through relatively straightforward structural engineering.

Over the past decade, due to their potential applications in the next-generation solid-state lighting sources and flat panel displays, OLEDs have garnered a lot of attention. Several efforts have been devoted to the development of new emissive materials to satisfy market requirements such as high luminescence quantum yield in the solid state, good amorphous film-forming properties, high thermal stability, and color purity.Based on the detailed literature survey, forty-two new conjugated small molecules, *viz.* **$C_{1\text{-}42}$** (**Series 1-7**) were designed as potential emitters for OLED applications. All of them were successfully synthesized and well characterized. Further, they were subjected to in-depth optical, electrochemical, thermal, theoretical, and electroluminescence studies. The solvatochromic study clearly indicated the nonpolar nature of the ground state and the presence of ICT behavior in the molecules. New OLEDs were fabricated employing selected twenty-eight newly synthesized compounds (**Series 1-4**) as emitters. From these studies, it is clear that the synthesized molecules possess all the prerequisites to act as an emissive layer in an OLED device. DFT calculations revealed their FMO, HOMO-LUMO energy levels, and spatial charge distribution in the molecules. Interestingly, fabricated devices containing **C_3**, **C_{11}**, **C_{19}** and **C_{26}** showed an EQE of 5.32, 5.91, 4.18 and 4.18 %, respectively. In the OLED devices, **C_3** gives yellow emission, **C_{11}** shows green light emission **C_{19}** exhibits cyan light and C_{26} shows bluish-green light.

****

CONTENTS

LIST OF FIGURES

LIST OF TABLES

LIST OF ABBREVATIONS

TFT	Thin film transistors
OLED	Organic light-emitting diodes
OFET	Organic-field-effect transistors
HOMO	Highest occupied orbitals
LUMO	Lowest unoccupied orbitals
D-A	Donor-Acceptor
Φ_{PL}	Quantum yield
LEDs	Light-emitting diodes
NLO	Non-linear optics
PVs	Photovoltaics
TFTs	Thin-film transistors
GaAs	Gallium arsenide
SM-OLED	Molecule organic light-emitting diode
PLED	Polymer light-emitting diode
Tg	Glass transition temperature
HTL	Hole transporting layer
EML	Emissive layer
ETL	Electron transporting layer
LE	Luminescent efficiency
ITO	Indium tin oxide
IQE	Internal quantum efficiency
EQE	External quantum efficiency
OSCs	Organic solid-state lasers

CT	Charge transfer
LE	Local excited
PLQY	Photoluminescent quantum yield
AIE	Aggregation-induced emission
TADF	Thermally Active Delayed Fluorescence
ΔE_{ST}	Distance between Singlet and triplet state
RGB	Red, green, and blue
FTIR	Fourier transform infrared spectroscopy
NMR	Nuclear magnetic resonance
ICT	Intramolecular charge transfer
T_d	Decomposition Temperature
DFT	Density Functional Theory
F_4TCNQ	2,3,5,6-tetrafluoro-7,7,8,8-tetracyanoquinodimethane,
α-NPD	4,4’-bis[*N*-(1-naphthyl)-N-phenyl-L-amino]-biphenyl,
TPBi	2,2',2"-(1,3,5-benzinetriyl)-*tris*(1-phenyl-1-*H*-benzimidazole),
LiF	Lithium fluoride
Al	Aluminium
J-V-L	Current density-voltage-luminance
EODs	Electron-only devices
HODs	Hole-only devices
J-V	Current density versus voltage
EL	Electroluminescence spectra
CIE	Commission Internationale de L'Eclairage

INTRODUCTION

Abstract

Chapter 1 *deals with a brief introduction to organic semiconductors, classifications of organic semiconductors, optical properties of small molecules, and application of organic semiconductors in optoelectronics. Further, it includes the introduction to LEDs, classification of LEDs, light emitting mechanism of LEDs, device structures of OLEDs, different methods for fabrication of OLEDs, and finally characterization of the OLEDs.*

1.1 A BRIEF INTRODUCTION TO ORGANIC ELECTRONIC MATERIALS

Organic electronic materials are the breakthroughs in the field of Optoelectronics, which is not only a center of attraction for research but has also expanded its realm from the corner of the research laboratories to the day-to-day life of the common man. Over the last two decades, organic devices' design and performance have undergone ground-breaking changes. In 1987, C.W.Tang pioneered cutting-edge advancements in designing organic optoelectronic devices. Since then, it has found numerous applications in various fields. Thin film transistors (TFT), organic light-emitting diodes (OLED), solar cells, sensors, and photorefractive devices are some of the major fields where organic compound-based devices are employed. The extensive application of these organic devices has made them a promising material to meet the demands and requirements of the modern world technologically[10].

Semiconductors, being the constructing monomeric units of the modern electronic devices, are crucial in deciding the overall performance of an electronic device. These are the materials that do not conduct electricity at room temperature and their resistivity lies between that of an insulator and a conducting material. Either by using a dopant or employing a specific temperature, these materials gain the property of conducting electricity[23]. The outstanding contributions made by Hideki Shirakawa, Alan Heeger, and Alan MacDiarmid to organic semiconductors are remarkable, so they obtained the Nobel Prize in the year 2000; thereupon semiconductors have

gained considerable attention among researchers. The high usage and requirement of the consumer give stimulation for searching efficient materials for making electronic components, used for portable and electronic devices. Organic materials exhibit remarkable features in terms of their photo and electrical conductivity, electroluminescence, and their ability to be finely tuned[11]. The distinctive features inherent in organic molecular substances have firmly established their crucial role in advancing the field of cutting-edge electronic devices.

Semiconductors can be mainly classified into two subgroups, *viz*. Organic semiconductors and Inorganic semiconductors. Organic semiconductors have attractive properties such as higher electrical conductivity, ion mobility, low band gap, absorption, and emission of light in the visible spectral range and are made of carbon-based materials. These materials hold promise for lightweight, inexpensive, flexible substrates that can be used and processed in solution at low temperatures. Therefore, organic semiconductors find their applications in electronic devices such as organic light-emitting diodes, organic photovoltaics, and organic-field-effect transistors (OFET). Nonetheless, organic semiconductors have some drawbacks in electronic performance as compared to inorganic counterpart. The drive to produce organic electronics comes from the advantages afforded by organic materials over traditional silicon-based inorganic semiconductors. The synthesis of organic materials is easy and less expensive as compared to inorganic semiconductors, and the device fabrication method is less expensive.

Generally, organic materials have good solubility in one or more organic solvents; this nature helps in solution processing, low-cost, and effective large-area device fabrication techniques such as spin coating, inject printing, and roll screen printing. To obtain high-performing devices, inorganic semiconductors require the annealing step, which is done normally at a high temperature whereas the organic semiconductors have very low annealing temperatures, adding an extra advantage to organic semiconductors over inorganic semiconductors[12]. Another dominant characteristic of organic semiconductors is that their properties can be customized for a particular application by altering the structure with the different functional groups.

Organic semiconductors are classified into two major groups, based on the structure of the organic molecules employed in making the semiconductor. They are (i) Conjugated small molecules, and (ii) Conjugated polymers.

***Conjugated small molecules**:*

Conjugated small molecules can be either a single molecule or an oligomer. These molecules show several advantages over conjugated polymers. Conjugated polymers have poor reproducibility, difficult purification steps, and inconsistent control of molecular weight. The small molecule possesses many important properties such as straightforward synthesis, facile purification, and definite molecular weight; all these factors give good reproducibility in the device performances. Rarely, some of the conjugated materials are having highly crystalline nature, which is not soluble in the solvent, in such cases thermally evaporated deposition techniques are employed to fabricate the electronic device with these molecules.

Optical properties of small molecules:

The band gap between the highest occupied orbitals (HOMO) and lowest unoccupied orbitals (LUMO) in the organic conjugated molecules is attributed to the overlap of the π bonding and π^* antibonding molecular orbitals which gives the electron density along the molecules. These HOMO and LUMO of the organic molecules are equivalent to the conduction and valence bands in the inorganic semiconductors. The supply of energy to these molecules makes electrons to excite from π to π^* states which reflects in the absorption spectra of the molecule. Similarly, when the electrons return from π^* to π gives the emission spectra. Meanwhile, various photophysical phenomena occur during the absorption and emission processes such as fluorescence, phosphorescence, and radiation-less decay. The process of fluorescence occurs when the singlet state electron comes to the ground state; but, in case, this excited singlet state electron undergoes intersystem crossing generating the triplet state, triplet state electrons come to the ground state resulting in the phosphorescence. In some cases, the excited state electron does not emit light, which in turn undergoes a nonradioactive transition from excited state to ground state, and this energy is utilized for vibration and rotational motion of the molecules[33]. The wavelength of the emitted light depends upon the conjugation in the molecules and it can be controlled by the

alteration of the chemical structure of the conjugation in the molecule. The chemical structure can be altered by the introduction of the functional group, or by making the molecules with non-π-conjugated sequences, which break the π orbital overlap. By tuning the HOMO-LUMO energy levels of the molecule, light emission is possible over the entire visible region of the spectrum. The tuneable emissive nature is particularly attractive for lighting and display applications. The emission capacity of a molecule can be measured in terms of quantum yield (Φ_{PL}), which is defined as the ratio of the number of photons emitted to the number of photons absorbed. It is expressed as given in Eq.**1.1**.

$$\Phi_{PL} = Photons_{EM}/Photons_{ABS} \ldots\ldots\ldots\ldots\ldots \textbf{(1.1)}$$

Theoretically, the maximum quantum yield must be 1. The quantum yield of the luminescence can be measured by two methods, *viz.* primary and secondary methods. The secondary method involves two techniques, *i.e.* the relative and absolute methods. From an absolute method, we can determine the quantum yield at a solid state. However, in the relative method, the quantum yield of the sample can be determined in the solution state with respect to a standard sample of known quantum yield by using equation Eq. **1.2**.

$$\Phi_S = \Phi_r(A_r I_s/A_s I_r)\ldots\ldots\ldots\ldots\ldots\ldots\ldots\ldots\ldots\ldots \textbf{(1.2)}$$

In Eq. **1.2,** Φs represents the quantum yield of the sample, A represents the excitation wavelength and I represent the relative integrated fluorescence intensity. The subscript s represents the unknown sample and r represents a known standard sample. The known standard samples used for the quantum yield measurements are 9, 10-diphenyl anthracene in cyclohexane (Φ_{PL}=0.90), quinine sulfate in 1N H_2SO_4 (Φ_{PL}=0.546), and rhodamine 101 in ethanol (Φ_{PL}=1).

1.2 CONJUGATED SMALL MOLECULES

There are two types of conjugated small molecules, *i e.* (i) Simple conjugated, and (ii) Donor-Acceptor (D-A) type conjugated small molecules.

Simple conjugated molecules:

Simple conjugated systems consist of the same kind of molecules. They have either hole-transporting properties or electron-transporting properties and possess less

conductive properties in undoped states. Hence, it is important to add the dopant to increase the charge transporting properties[17].

The simple conjugated molecules show some drawbacks, such as less stability in ambient temperature, undergoing a reduction in the presence of moisture and the difficulty in final removal of the dopant, in turn, may damage the fabricated devices. Further, these simple materials require either *p*-type or *n*-type characteristic to conduct electricity during the fabrication of the electronic device.

Donor-Acceptor (D-A) type conjugated molecules:

D-A type conjugated small molecules possess both the donor and acceptor groups in the molecule and own localized redox sites. They may contain alternate D and A moieties. D-A type molecules show less electron transport from the redox site and hence show less conductivity. The less band gap provides good charge transporting properties to these molecules. The presence of the alternative donor and acceptor group leads to a narrow band gap[15].

Further, the interaction between the donor and the acceptor groups result in the mixing of the high-lying HOMO energy level of the donor and the low-lying LUMO energy level of the acceptor which gives the small energy band gap in a semiconductor with a novel electronic structure as well as bipolar charge transporting properties. **Figure 1.1.** Shows the schematic representation of the band gap in the case of the D-A type conjugated molecules.

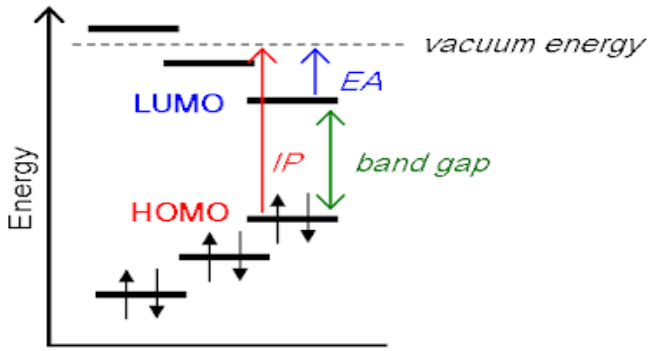

Figure 1.1. Schematic representation of band gap in case of D-A type conjugated molecule

The alternate donor and acceptor groups in the molecules give novel physical properties. So, it can be employed in making a device that requires high charge storage capabilities such as batteries and supercapacitors. In the case of the donor-acceptor type molecules, doping is not necessary to enhance their charge-carrying properties.

Applications of conjugated small molecules:

In general, conjugated molecules have two main group applications. The first group application is to utilize conductivity as the main property and the second group application utilizes electro-activity as the main property. The first group application involves the printed circuit board, artificial nerves, antistatic clothing, conducting adhesives, *etc*. on the other hand, electro-activity based application includes light-emitting diodes (LEDs), non-linear optics (NLO), photovoltaics (PVs), thin-film transistors (TFTs), *etc*.

1.3 LIGHT-EMITTING DIODES (LEDs)

Light-emitting diode is a unique type of semiconducting device, which shows electroluminescence properties when it is electrically biased in the forward direction, it emits an incoherent narrow spectrum of light. In 1955, Rubin Braunstein reported the emission of infrared rays from gallium arsenide (GaAs) and other semiconductor alloys for the first time. Interestingly, in 1961 Bob Biard and Gary Pittman showed the emission of infrared rays when an electric current passed through GaAs. Further, they received a patent for the infrared LED. Based on this principle, Nick Holonyak Jr. developed the first visible-spectrum LED in 1962.

It consists of a chip of semiconducting materials impregnated, with an impurity to create a *p*-*n* junction. When the voltage is applied, current flows easily from the anode or *p*-side to the cathode or *n*-side, but not in the reverse direction. This hole and electron meet each other forming excitons that liberate energy in the form of light. The color and wavelength of the emitted light depend on the band gap of the materials forming the *p*-*n* junction. In the case of silicon or germanium diode, due to the indirect band gap, electrons and holes meet by a non-radioactive transition which does not produce any optical emission[44].

Advantages of LEDs:

LEDs show some important advantages over incandescent or gas-discharge lighting such as

a. LEDs can be switched on and off quickly without causing any harm.
b. LEDs enable smaller device designs and increased efficiency, ultimately extending the life of battery-powered devices.
c. LEDs can be dimmed without affecting the quality or color of the emitting light.
d. LEDs are highly resistant to damage from vibrations and shocks.
e. LEDs have a long operational lifespan, far surpassing traditional lighting technologies.
f. LEDs can withstand variations in pressure conditions.
g. LEDs offer the option to choose specific emission spectra, allowing for tailored lighting solutions.

Nowadays, LEDs are considerably used in lamps, flashlights, free space optics, communications, movement sensors, touch sensors, printers, *etc.* At present, inorganic materials like GaAs, aluminum gallium arsenide, gallium arsenide phosphide, indium gallium nitride, and zinc selenide are the most commonly used semiconductors in LEDs. Nevertheless, inorganic semiconductors have some disadvantages, such as they are more expensive, thermally less stable, more sensitive to environmental changes, and causing difficulty in fabrication. The emissive materials used for OLED applications should have a high quantum yield in the solid state which in turn implies the good efficiency and overall performance of the device.

Generally, there are two types of organic electroluminescent diodes, *viz.* small-molecule organic light-emitting diode (SM-OLED) and polymer light-emitting diode (PLED). The electroluminescent behaviour is almost the same in both the classes of diodes and the important difference lies in the fabrication method for the formation of thin organic film. SM-OLED is gaining more interest as it could make use of vacuum-deposited multilayer stacks, which is the dominant factor for display lifetime and efficiency.

1.3.1 Polymer materials-based LEDs (PLEDs)

PLEDs are normally fabricated using a polymer that can approach large display sizes and full color at a lower cost *via* solution-based deposition techniques. The thermal evaporation deposition method enables complicated multilayer device architecture and renders excellent devices with high efficiencies. In contrast, solution-based deposition limits the fabrication of the composite device structure as the solvent used for one layer can re-dissolve or otherwise damage the previous layers.

Poly (*p*-phenylene vinylene) (PPV) is the first well-known example of the conjugated polymer studied by Burroughes et al. (2005). Polymer materials due to their high molecular weight have the ability to form a thin film for full-spectrum color display. They require a small amount of power for the light production in the device. The literature provides numerous reports on OLEDs based on conjugated polymers.

However, these polymeric materials have some drawbacks. Their large molecular weight compels a more difficult path for their production. After synthesis, it demands a highly complicated means of purification. Further, their structural demerits would bring about a degradation in their performance. Because of these disadvantages, small molecules can be used as alternative emitters in LEDs.

1.3.2 Small molecule materials-based OLEDs

The electroluminescence was first observed in a device containing a single crystal of anthracene and its application perspective was limited until 1987. OLED based on multilayer small molecules was fabricated for the first time by vacuum deposition technique using Alq_3 (Tris(8-hydroxyquinoline) aluminum (III)) which exhibited high luminous efficiency with low driving voltage. Thereafter, organic compounds were used as organic semiconductors for fabricating the efficient multi-layered structure of OLEDs by subsequent evaporation under high vacuum techniques. Generally, the conjugated small molecule has well-defined molecular structures, an easy purification method by well-known techniques, and specific structure-property correlations. A thin film of this material can be made by evaporating the powder material in a vacuum chamber at a high temperature and

deposition on the substrate. By this method, a film with good thickness, uniformity, and high purity can be obtained.

The required criteria for small molecular materials to be used in the devices are as follows:

a. The material should exhibit exceptional thermal stability to withstand the high temperature during thermal evaporation (typically within the range of 150 to 400 ^{o}C) without undergoing structural degradation. This enables the material to readily evaporate and condense onto a cool substrate within a vacuum chamber.
b. It is imperative that the deposited film exhibits outstanding quality and purity. Typically, these films should fall within a thickness range of 5 to 200 nm
c. To prevent undesired crystallization during the condensation process, the material should possess a notably high glass transition temperature (Tg). This characteristic ensures that the material maintains an amorphous or non-crystalline state under the given conditions.

In the small molecular device, the emissive layer separates the electron-transporting and hole-transporting materials resulting in the formation of the junction, sandwiched between anode and cathode electrodes. Small molecular OLEDs must have efficient quantum yield, higher mobility, and charge carriers. Electron and charge recombination occurs at the interface of the HTL and ETL layers.

1.3.3 OLED light-generating mechanism

The schematic diagram of typical LED with its EL mechanism is shown in **Figure 1.2.** When a voltage is applied across the device, the electron moves from the cathode to the LUMO of the organic molecule and the hole moves from the anode to the HOMO of the molecule. The electrostatic force of attraction makes an electron and hole move towards each other. Further, holes and electrons recombine to form the excitons, which are in a bound state of the hole and electron. The decay of the excited state results in the relaxation of the energy levels of the electrons accompanied by the emission of radiation. The excitons formed during this process

may be a singlet or a triplet state depending on how the spin of an electron and hole have been combined. There are three triplet states generated for each singlet state. Singlet-state electron decay gives fluorescence whereas triplet-state electron decay gives phosphorescence.

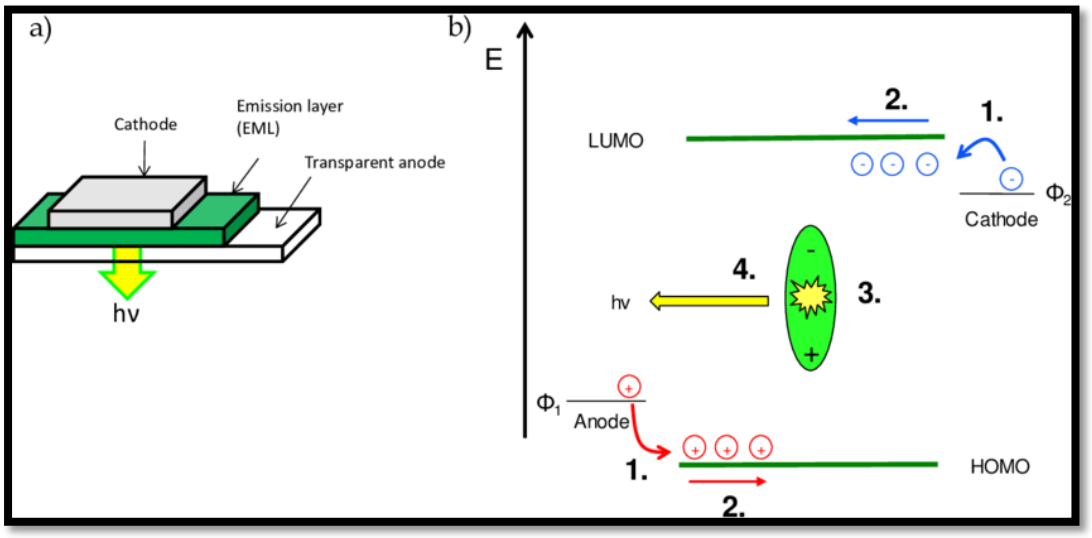

Figure 1.2. Schematic diagram of a typical LED device

Many characteristics of organic molecules are fundamentally determined by their molecular bonding, which is the sum of attractive and repulsive interactions between neighbouring molecules.

The luminescent efficiency (LE) for most of the OLEDs is only 25%. The rest will be consumed in the phosphorescence. In order to significantly increase the efficiency of OLED devices, it is important to balance the charge-carrying capacity of the emitting molecules used in the devices. It has been noted that in most of the reported conjugated molecules, the barrier between the LUMO of the molecule and the work function of the cathode is much larger than the barrier between the HOMO of the molecule and the work function of the anode. This results in the imbalance of the injection between electrons and holes, thus giving the reduced efficiency of the OLED devices. There are two methods to improve the efficiency of OLEDs. The first method is to utilize the low-work function metals such as Ca, and Li as a cathode, but the high reactivity of these metals reduces the durability of the device. The second method is the insertion of the electron-transporting layer between the emitter and

cathode and a hole-transporting layer between the anode and an emitter. The main difficulty of this method is the fabrication of the double-layer OLEDs.

Double-layered OLED and its energy levels of different layers are schematically represented in **Figure 1.3.** Multilayered OLEDs consist of a transparent electrode made up of indium tin oxide (ITO) coated as a thin layer on a transparent substrate followed by a hole transporting layer (HTL), an emissive layer (EML), electron transporting layer (ETL), and a cathode, respectively as shown in **Figure 1.3.**

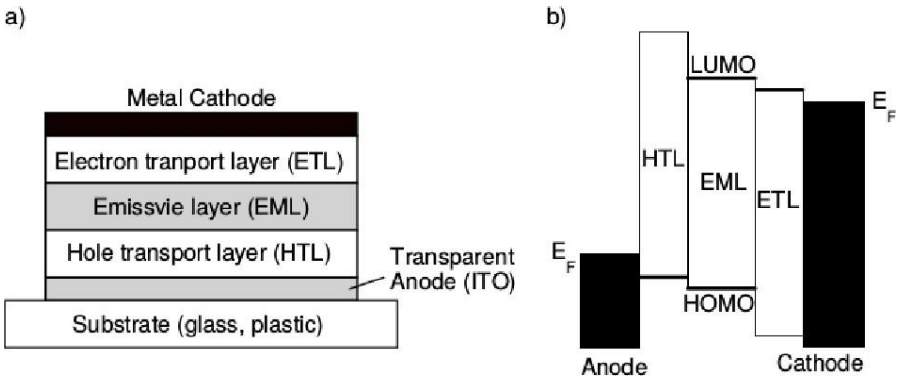

Figure 1.3. (a) Schematic representation of a double-layer OLED; (b) Energy levels of different layers

1.3.4 Device structure

OLEDs consist of an anode, a cathode, an electron-transporting layer, a hole-transporting layer, and an emitting layer. The properties of each layer are discussed below.

Anode materials:

The anode material is generally formed on the substrate and must have some typical requirements, as follows:

- Anode materials should exhibit excellent electrical conductivity to minimize contact resistance within the device.
- An important characteristic is a high work function, which facilitates the efficient injection of holes into the organic layers of the device.
- The chosen materials must be capable of forming uniform and adherent films, ensuring proper coverage of the substrate. Additionally, they should exhibit good wettability to enhance the even spreading of organic layers.

- Anodes should possess remarkable thermal and chemical stability to withstand the operating conditions and prevent degradation over time.
- Optimal transparency is vital to enable emitted light to exit the device efficiently, ensuring that the organic electronic device functions effectively.

Indium tin oxide (ITO) is the most commonly used anode. It has a high work function varying between 4.5 to 4.8 eV. Because of its large band gap and transparency in the visible region, it is selected as an anodic material.

Cathode materials:

The selection of the cathode materials depends upon the extent of reducing the energy barrier between the electrode and the adjacent organic layer. In most cases, metal alloys or pure metals are used as cathode materials. The cathode materials should have the basic properties that are listed below:

- Cathode materials need to exhibit strong electrical conductivity.
- It is essential for these materials to possess a low work function to facilitate the efficient injection of electrons into adjacent organic layers.
- The ability to form uniform films and ensure good contact with neighboring organic layers is crucial.
- Cathode materials should maintain their structural and chemical integrity even under the challenging conditions of heat and exposure to chemicals.

Metals such as calcium, magnesium, aluminium, and their alloys are used as a cathode. The problem with low-work function metals is that they are very susceptible to air and moisture, which leads to air oxidation. In most cases, cathode materials normally degrade by the formation and enlargement of non-emissive dark spots. In order to get rid of this unwanted issue, a very thin layer of LiF or CsF can be added.

Hole transport materials (HTM):

The hole-transporting materials serve a vital function in multi-layered small organic OLED devices by aiding the movement of positively charged carriers (holes) from the anode into the emissive layer, essentially acting as a pathway for hole conduction. In the context of polymer-based OLEDs, HTMs are unnecessary because

the polymers themselves possess the ability to transport holes through a process known as charge hopping.

HTMs should possess the following specific characteristics to effectively serve their role:

- They should possess a lower ionization potential.
- They should exhibit a lower electron affinity.
- Materials must readily undergo oxidation.
- They maintain stability in a one-electron oxidized state.
- Their highest occupied molecular orbital (HOMO) level should be comparatively low.
- Materials are capable of functioning as an electron-blocking layer to prevent electrons from reaching the anode.

The electron-rich triarylamine is the most commonly used hole-transporting material. Other interesting HTM includes: *N,N'*-bis(3-methylphenyl)-*N,N'*-diphenyl-[1,1-diphenyl]-4,4'-dimine(TPD), *N*,*N*-di[(1-naphthyl)-*N,N'*-diphenyl]-1,1-biphenyl)-4,4-diamine(NPD) and 4,4,4-tris(*N*-3-methylphenyl-*N*-phenylamino)triphenylamine.

Electron transporting materials (ETM):

Electron-transporting materials play a vital role in constructing the OLEDs. The electron-transporting layer behaves as conducting material and helps electrons move from the cathode to organic layers. Metal chelates and certain heterocyclic compounds based on triazole and oxadiazole are being used effectively as ETMs.

ETM must meet the following requirements:

- Matching the work function of the cathode and decreasing the potential between the cathode and emitter.
- Possessing a high electron affinity.
- Demonstrating exceptional electron transport mobility.
- Maintaining stability in the one-electron reduced state.
- Exhibiting excellent thermal stability, often associated with a high glass transition temperature T_g.

- Demonstrating strong film-forming characteristics and good wettability to minimize the occurrence of pin-hole defects.
- Serving as an effective hole-blocking layer to prevent the passage of holes toward the cathode, thereby preserving the integrity of the emitting layer.

1.3.5 Device designing

Electroluminescent devices have undergone significant advancements in fabrication techniques since their inception. These techniques primarily fall into two categories; (i) dry technology and (ii) wet technology. The dry coating method involves thermal evaporation under a high vacuum. Polymer-based molecules can be deposited by solution procedures and low molecular weight small organic molecular substances can be deposited under a high vacuum by thermal evaporation. Whereas the wet technique makes use of spin coating or inkjet printing.

Dry coating method:

The thermal evaporation deposition method is a versatile approach for depositing a wide range of materials, including inorganic compounds and metals. It is particularly valuable for creating small organic molecules-based OLED devices. This technology involves depositing materials within a high-vacuum chamber that is isolated within an argon-nitrogen-filled glove box. The process utilizes a boat-shaped container typically constructed from materials like tungsten. This container serves a dual purpose: it acts as a vessel for holding the sample and functions as a resistive heating element to raise the temperature of the organic material.

Wet coating system:

Wet coating systems encompass a range of techniques, including dip coating, spray coating, ink-jet printing, and spin coating. Among these methods, spin coating stands out as the most commonly employed due to its simplicity and versatility. Unlike dry coating methods, spin coating does not require a high vacuum environment, which significantly reduces coating expenses. The crucial criterion for the success of a spin coating system is the solubility of the coating material in an organic solvent. This solubility ensures that they can be dissolved and evenly spread over the substrate during the spinning process. The solution-based approach in spin

coating is known for its ease of use and cost-effectiveness. However, it does come with a significant drawback: the potential for re-dissolving previously deposited layers if not handled carefully.

One advantage aspect of spin coating is the ability to control film thickness by adjusting the solvent concentration in the solution. This level of control allows for precise tuning of the coating thickness to meet specific requirements or performance criteria.

1.3.6 Device characterization

The OLED devices are associated with the emission of visible light; therefore, a number of photometric characterizations must be performed to study the quality of the designed device. It includes quantum efficiency, power efficiency, and luminous efficiency. These properties are discussed below.

The quantum efficiency of OLEDs:

Quantum efficiency plays a crucial role in the design of OLEDs, serving as a vital parameter that significantly influences their overall performance. OLED performance primarily depends on the ability to convert electrons into photons, which can be quantified through several parameters, including quantum efficiency, power efficiency, and luminous efficiency, depending on specific objectives. Quantum efficiency, in particular, is a fundamental measure, as it directly assesses an OLED's capacity to emit light.

Quantum efficiency can be further divided into two key components; internal quantum efficiency (IQE) and external quantum efficiency (EQE). These components help to dissect and understand the efficiency of electron-photon conversion within the device and its effectiveness in producing external light emission.

Internal quantum efficiency (IQE):

IQE is a numerical measure that relates the total number of photons generated within a device to the number of injected electron-hole pairs. It can be formulated as Eq **1.3**.

$$\mu_{int} = N_{int}/N_c \ldots\ldots\ldots\ldots\ldots\ldots\ldots\ldots \textbf{(1.3)}$$

where N_{int} is the total number of photons generated within the device, N_c is the total number of injection charge carrier pairs, μ_{int} is the IQE. In a fluorescent OLED device, for instance, it can also be represented as given in Eq **1.4**.

$$IQE = \Phi_f \eta_s \gamma \ldots\ldots\ldots\ldots\ldots\ldots\ldots\ldots \quad (\mathbf{1.4})$$

where γ is the charge balance factor, η_S denotes the singlet fraction in all excitons, Φ_f indicates the quantum efficiency of the photoluminescence.

External quantum efficiency (EQE):

EQE is a key metric used to evaluate the performance of optoelectronic devices such as solar cells, photodetectors, and light-emitting diodes (LEDs). EQE quantifies the ratio of photons that are actually emitted by the device to the total number of injected electron-hole pairs. Mathematically, it is expressed as mentioned in Eq **1.5.**

$$\mu_{ext} = N_{ext}/N_c \ldots\ldots\ldots\ldots\ldots\ldots\ldots\ldots\ldots\ldots \quad (\mathbf{1.5})$$

where N_{ext} represents the total number of the photons emitted from the device, Nc signifies the total number of injected electron-hole pairs, and μ_{ext} shows EQE.

It is important to note that the EQE value may be lower than the internal quantum efficiency (IQE) due to various factors like partial photon absorption during their transmission through the device's surface or reflection at the interface between the device and its surrounding medium, often caused by the difference in refractive indices. As a result, EQE is a more reliable indicator of the device's true emitting material performance because it considers only the photons that are effectively emitted by the device.

EQE, which directly characterizes the device's efficiency, can be determined using Eq **1.6.**

$$EQE = \eta_{op} \Phi_{fl} \eta_r \gamma \ldots\ldots\ldots\ldots\ldots\ldots\ldots\ldots \quad (\mathbf{1.6})$$

where η_{op} represents the light out-coupling factor, η_r denotes the ratio of the singlet or triplet excitons, Φ_{fl} stands for the photoluminescence quantum yield, and γ represents charge carrier balance factors.

1.4 MOTIVATIONS FOR THE CURRENT RESEARCH WORK

Organic light-emitting diodes are among the category of organic-based devices, and they contributed to the flourishing of the industry of smartphones, colored light sources, and curved TV screens. OLED technology is attractive due to its significant superiority, such as full color and large-area display, board viewing angle, transparency relatively low power consumption, and high luminescence efficiency. Presently, organic electronics is known not only as a promising academic field but also as a prominent industry gaining in market-rate every year. Now, OLED technologies can be additionally enhanced by investigation into some problematic areas such as the low stability of colored light emission, high cost, and the short lifetime of the devices. To overcome these issues**,** the organic chemists can contribute a lot. They can design and synthesize pure organic compounds with required properties for the successful application in devices. But still, efforts are continuing to achieve high performance of the devices. Keeping the above-mentioned points in view, there is a need for the design and development of suitable small-molecule based organic materials that have excellent emitting properties. In addition, there is plenty of scope for designing TADF emitters for highly efficient luminescence devices. Interestingly, most of the reported materials were of D-A type, which effectively gives high performance OLEDs.

1.5 BROAD OBJECTIVES OF THE PRESENT WORK

Over the last two decades, tremendous research has progressed in the field of organic semiconductors due to their stimulating electronic and optoelectronic properties which enable the development of new exciting electronic devices. Several different classes of organic materials were found to exhibit semiconducting properties including conjugated oligomers, polymers, and columnar liquid crystal molecules. They found extensive applications in field-effect transistors (OFTETs), organic light-emitting diodes (OLEDs), organic photovoltaic cells (OPVs), and sensors. Recently, organic small molecules emerged as one such kind of semiconducting material. Hence, small molecules can successfully be employed in all the above-mentioned devices to improve the device's performance.

In this context, a large number of research groups all around the world are enormously working on the design and development of new small molecules with functional properties. As the literature suggests, integrating the properly substituted heterocyclic system at the core as well as incorporating the donor-accepter conduit is the best way to achieve the luminescence property.

The overall aim of the present work is to design new small organic conjugated molecules showing good emitting properties. For this, we have contemplated choosing strong and bulky donor as well as acceptor groups like aromatic/heteroaromatic scaffolds for the new design. New synthetic schemes have been planned for their synthesis. It has been thought of characterizing all the newly synthesized compounds with regard to thermal, optoelectronic, and electroluminescence properties. Further, on the basis of their properties, fabrications of new OLEDs have been planned to study device parameters like EL quantum efficiency, maximum luminance, and turn-on voltage in detail. In-depth study of their structure-property relationship has been also contemplated.

A detailed literature survey on push-pull type small conjugated molecules based on different aromatic/heteroaromatic systems has been discussed in the next chapter. It also follows the specific objectives of the proposed research work.

1.6 THESIS STRUCTURE

The whole thesis is systematically divided into six chapters. **Chapter 1** outlines a brief introduction to organic semiconductors, the classification of organic semiconductors, and the application of organic semiconductors. It also explains the light emission mechanism of OLED and different methods for the fabrication of the OLED device. **Chapter 2** highlights the review of the literature survey on the design and development of various heterocycle-based small molecules. In addition to this, it includes the scope and objectives of the present research work, arrived at based on the literature review. The experimental protocols for the synthesis of forty-two new heterocyclic derivatives and their complete structural characterization has been elaborated in **Chapter 3**. The next chapter, *i.e.* **Chapter 4** discusses a detailed account of the investigation of the optical and electrochemical properties of the synthesized small molecules. It also includes their theoretical investigations. Detailed

OLED device fabrication as well as their performance studies has been discussed in **Chapter 5**. Finally, **Chapter 6** includes a summary and outcomes of the entire research work.

LITERATURE REVIEW, SCOPE, AND OBJECTIVES OF THE PRESENT WORK

Abstract

This chapter covers an introductory account of D-A type small molecules and a review of reported literature on the design, synthesis, and material characterizations of various heterocycle-based D-A type organic materials. In addition, it comprises the scope and objectives of the present research work, arrived at on the basis of a detailed literature survey.

2.1 INTRODUCTION

In recent years, due to their widespread use in devices like organic light-emitting diodes (OLEDs), organic field-effect transistors (OFETs), organic light-emitting transistors (OLETs), organic solid-state lasers, organic solar cells (OSCs) and biomedical devices, the development of efficient organic π-conjugated small molecules has been a vital part in the field of electronics. Essentially, these molecules mainly stand out because of their well-organized molecular structures, simple synthetic methods, straightforward purification procedures, amenability to solution and vacuum deposition processing, and the ability to fine-tune functional properties through relatively straightforward structural engineering. Over the past decade, due to their potential applications in the next-generation solid-state lighting sources and flat panel displays, OLEDs have garnered a lot of attention. Several efforts have been made by academia, industry, and research groups to develop high-efficiency and long-life span OLEDs based on organic small molecules

In our proposed work, it has been contemplated to concentrate on the design of small conjugated molecules carrying interesting electron-rich species and electron-deficient units linked through certain conjugated spacers. In the following section, a detailed literature survey on reported D-A, D-A-D, D-π-A, only D types of small molecules-based emitters, for OLED application, has been elaborated. These compounds possess different donor systems such as carbazole, pyrene, phenothiazine, diphenylamine, and triphenylamine. Also, they contain different acceptor units like

diphenyl sulphoxide, triazine, barbituric acid, cyano, and carbonyl functional groups. Some of them possess conjugate π-linkers in between donor and acceptor units.

2.1.1 Cyanopyridone - an overview

3-Cyanopyridine-2-one (**S-2.1**) is a basic *N*-heterocyclic compound, which has a conjugated system of six π electron that are delocalized over the ring. The molecule is planar and thus, follows the Huckel criteria for aromatic system. In contrast to benzene, the electron density is not evenly distributed over the ring, reflecting the negative inductive effect to the nitrogen atom. For this reason, the ring has a diploe moment and a weaker resonant stabilization. The nitrogen is involved in the π-bonding aromatic system using its unhybridized *p* orbital. The lone pair is in a sp^2 orbital, projecting outward from the ring in the same plane. As a result, the lone pair does not contribute to the aromatic system but importantly influences the chemical properties, as it easily supports bond formation *vi*a an electrophilic attack. It is a highly electron deficient *N*-heterocycle, belonging to *n*-type.

The presence of pyridine in any conjugated system provides an excellent electron-transporting ability and good optical properties including outstanding chemical and thermal stabilities. These properties can be further enhanced by incorporating a cyano group at the third position of this core.

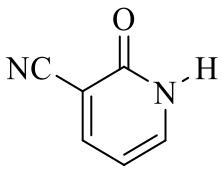

S-2.1

2.1.2 D-A type small molecules containing carbazole unit as a donor

Carbazole is a tricyclic heteroaromaic compound comprising a pyrrole ring fused in between two benzene moieties as depicted in **S-2.2.** As an important class of heterocyclic moieties, carbazole and its derivatives have been widely investigated in optoelectronic applications owing to their excellent charge-transporting properties apart from interesting photoconductive, photo-refractive, and light-emitting behaviour. Carbazole derivatives possess many advantages as optoelectronic materials

mainly due to their predictable HOMO-LUMO energy levels, which can be easily tuned through chemical substitution, and high thermal stability, rendering them suitable candidates for thermal evaporation. In addition, carbazole, being a cheap raw material can easily be substituted through simple routes to yield derivatives of high photochemical stability and also it has the ability to quickly form relatively stable radical cations.

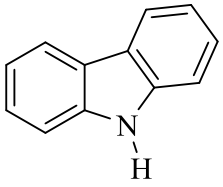

S-2.2

Che et al. in 2011 reported a new carbazole-based donor type simple blue-light emitting material **S-2.3.** This newly synthesized molecule had a band gap of 3.2 eV. When fabricated through a vacuum deposition process, the OLED device showed a high current efficiency of 11.5 cd/A, the brightness of 1800 cd/m^2 at 8.5V and its EQE was found to be 1.7%.

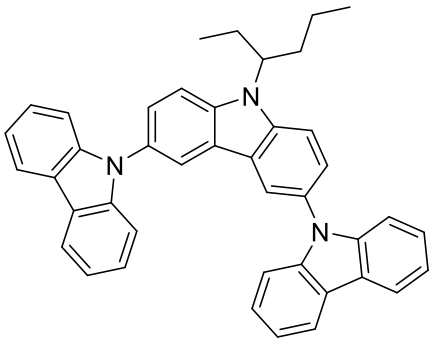

S-2.3

Adachi et al. in 2012 designed a series of highly efficient D-A type emitters based on carbazolydicyanobenzene. It comprises carbazole as an electron donor and dicyanobenzene as an electron acceptor (**S-2.4, S-2.5**). By varying the substituent numbers and the relative position of the dicyanobenzene and carbonyl groups, high photoluminescence efficiency, as well as various emission colors was achieved. **S-2.4** showed green emission, while **S-2.5** displayed orange emission. Their external quantum efficiency was found to be 11.2% and 8%, respectively.

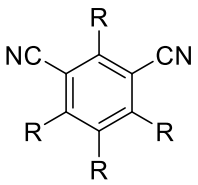

S-2.4

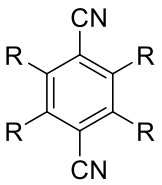

S-2.5

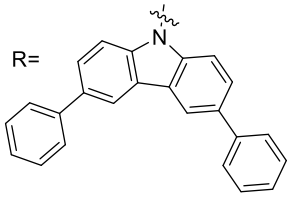

In 2013, the same group reported an interesting D-A type carbazole-based derivative carrying 1,3,5-triazine as an acceptor unit, **S-2.6**. Here, the triazine ring has three potential modification sites, and hence it is a suitable building block for the construction of organic semiconductor molecules. The molecule was shown to exhibit EQE of 15%.

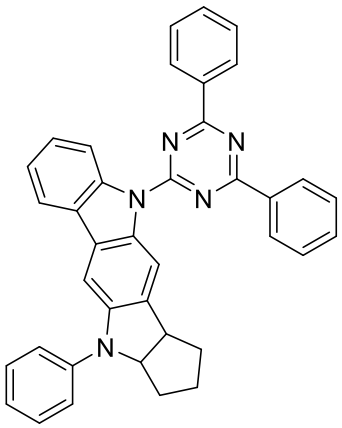

S-2.6

Zhang et al. (2013) adopted a D-π-A structural strategy with phenyl-substituted carbazole as a donor and diphenyl sulphoxide as an acceptor to construct two intra-molecular charge-transferring emitters **S-2.7** and **S-2.8** for OLED fabrication. Benefited from the weak CT state as determined by carbazole or sulfone unit, these emitters failed to show the red-shift phenomenon and achieved deep blue emission in a solid-film state. Interestingly, the device using **S-2.7** as an emitter achieved a current efficiency of 1.89 cd/A and an EQE of 4.21%.

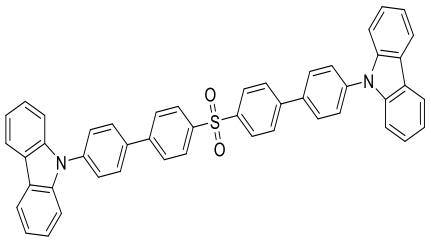

S-2.7

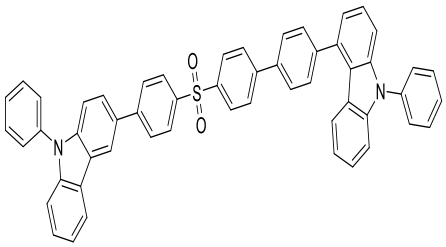

S-2.8

Li and his co-workers (2015) synthesized a series of new D-π-A type carbazole-based spiro[fluorine-9,9-thioxanthene] derivatives (**S-2.9** to **S-2.12**) in search of blue emitters. Here, the spiral structure was expected to mitigate the common aggregation-caused quenching problem. The spiro compounds **S-2.9**, and **S-2.10** are of local excited (LE) type, whereas **S-2.11**, and **S-2.12** are charge transfer (CT) emitters. The LE state emitters realized deep blue and sky-blue emissions. The authors reported that **S-2.10** displayed a high EQE efficiency of 2.03%.

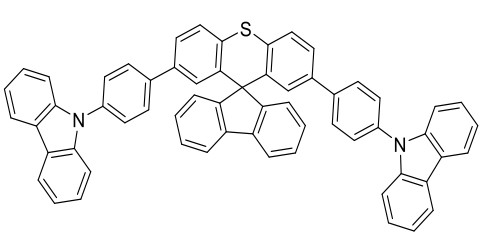

S-2.9

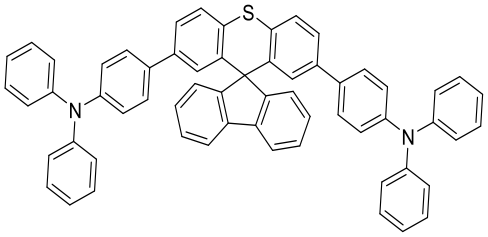

S-2.10

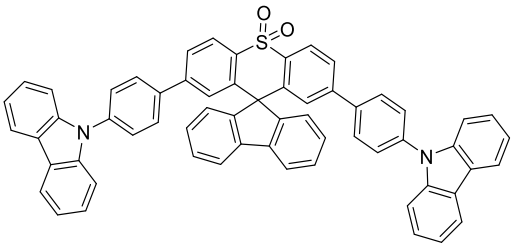

S-2.11

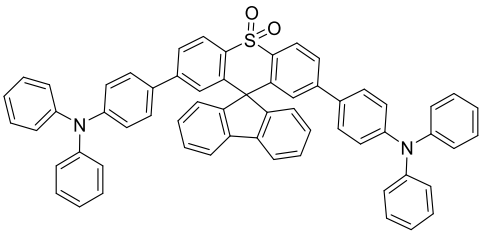

S-2.12

In 2015, Chin and his associates prepared three simple carbazole-based donor type materials **S-2.13, S-2.14,** and **S-2.15** for OLED application. They fabricated the devices by using *N*,*N*-bis(naphthalene-1-yl)-*N*,*N*-bis(phenyl)benzidine as hole-transporting materials, and $Ir(Piq)_3$ as a dopant. They reported that the emitters **S-**

2.13, S-2.14, and **S-2.15** displayed luminescence efficiency of 5.2, 6.3, and 7.0 cd/A, respectively, and EQE values 6.9, 7.1, and 8.4%, respectively.

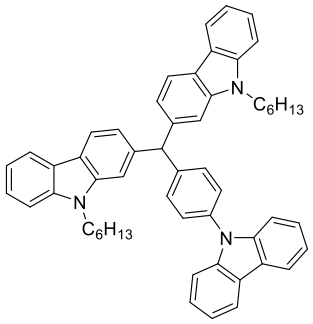

S-2.13

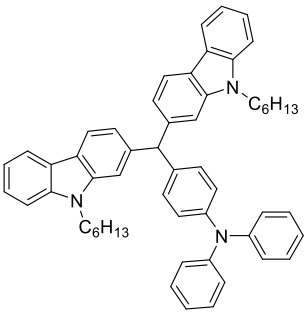

S-2.14

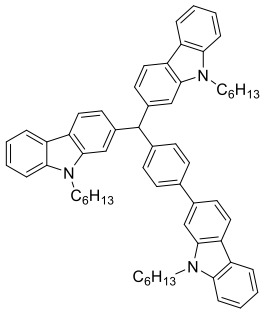

S-2.15

Lee and his co-workers (2015) introduced benzoflurocarbazole and benzothionocarbazole as electron-donating units to an electron acceptor unit, *viz*. dicyanobenzene. These compounds, **S-2.16**, and **S-2.17** are of D-A-D type and showed blue emission. Further, they found that **S-2.16,** and **S-2.17** displayed good OLED performance. The EQE of these two compounds were found to be 12.1 and 11.8%, respectively.

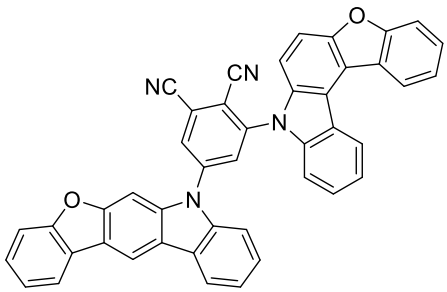

S-2.16

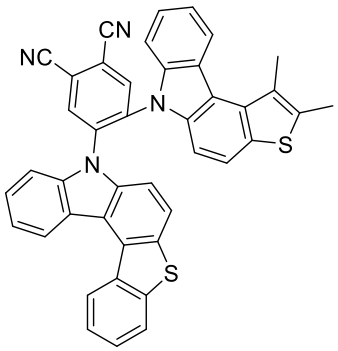

S-2.17

Recently, Gov et al. (2017) designed three star-shaped D-π-A-π-D type molecules (**S-2.18, S-2.19** and **S-2.20**) carrying carbazole as a donor and 1,3,5-triazine as an acceptor. The authors studied their fluorescence and AIE properties. These newly synthesized molecules displayed high optical properties in excited states compared to their ground states, and showed a large extent of emission in polar solvents, in a range of 432-549 nm with a high quantum yield. The results indicated

that carbazole and triazine moieties have the full potential to be used as donor and acceptor units, respectively while designing new emitters.

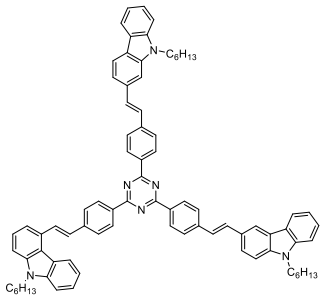

S-2.18

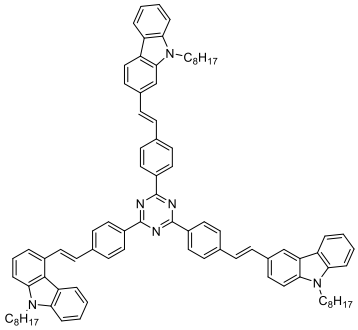

S-2.19

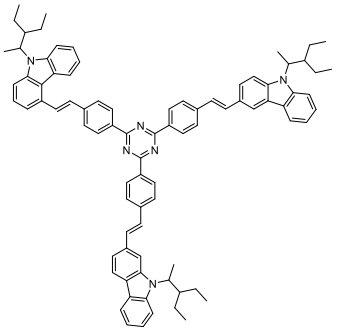

S-2.20

The group led by Cheng-Ying et al. (2022) reported a triphenylethene-carbazole based bipolar D-A type molecules having cyano and sulfonyldibene as acceptor moieties, **S-2.21**, and **S-2.22**. The group investigated the photophysical, thermal, and electrochemical characteristics of the designed molecules. Among them, the compound **S-2.22** exhibited a sky-blue emission in the OLED device with an external quantum efficiency of 5.6% and high luminescence of 2921 cd/m^2.

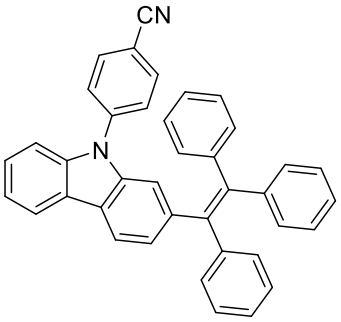

S-2.21

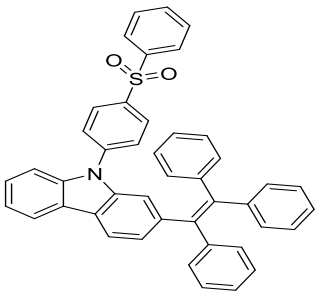

S-2.22

Dong Chen et al. (2023) synthesized bipolar carbazoe-based (D-A type) emissive materials, **S-2.23**, and **S-2.24**. They introduced an electron-withdrawing pyridine group to promote electron-injecting ability for **S-2.23**. Among these two molecules, **S-2.23** showed an EQE of 24.6%.

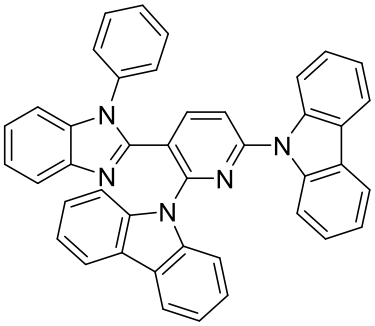

S-2.23

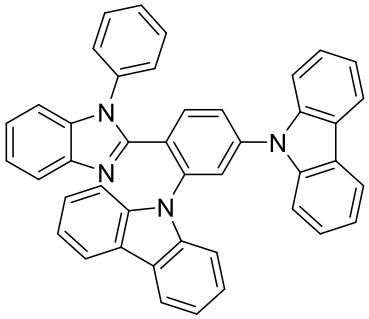

S-2.24

2.1.3 D-A type small molecules containing pyrene scaffold as a donor

Pyrene is a polycyclic aromatic compound. Its structure is shown in **S-2.25**. It received much attention among the various polycyclic aromatic hydrocarbons, because they allow effective control of absorption and emission properties *via* regioselective functional group substitution of its active sites at 3rd, 6th, and 8th positions. Its derivatives act as good donors. Therefore, pyrene-based D-A type compounds are used as efficient light-emitting materials. They show high emission quantum yield in solution and solid states, and their color-tunable emission characteristics are due to intramolecular charge transfer (ICT) behaviour, caused by donor or acceptor units. Pyrene system has the planar nature, which leads to intermolecular π-π interactions and induces aggregation, fluorescence quenching, red-shift characteristics, and broad emission bands. Its substitution leads to nonplanrity of the system. These properties have been utilized by many studies seeking to develop fluorescent sensors.

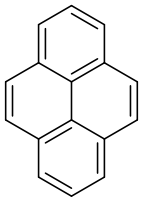

S-2.25

Deb et al. (2015) synthesized three pyrene-vinyl-tetraphenylethylene (TPE) based donor type conjugated materials **S-2.26, S-2.27**, and **S-2.28** through conventional Heck coupling reaction. The planar structure of pyrene and the rotor

nature of tetraphenylethylene could be beneficial for improving the fluorescence quantum efficiency in both solid and solution states, and the quantum yields for these compounds were found to be 17, 48, and 98%, respectively. Among the three compounds, **S-2.26** showed a low quantum yield in the THF solution. This is because it contains one TPE unit and one pyrene unit. Here, the rooter nature of TPE controls the quantum yield over the planar nature of pyrene.

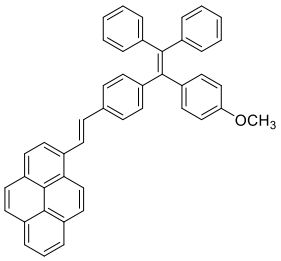

S-2.26

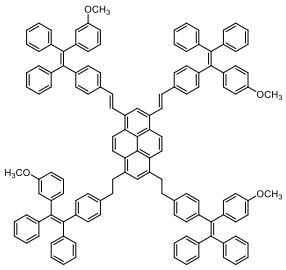

S-2.27

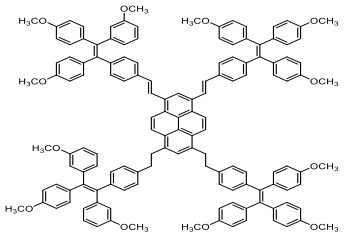

S-2.28

In 2016, Kim et al. synthesized two pyrene-based donor type molecules, *i.e.* **S-2.29** and **S-2.30**, wherein the two pyrene systems are connected through different aryl cores, *viz*. 1-naphthyl fluorine and the binaphthyl groups. These groups would induce the non-planar structural features for the compound and thus enhancing their photoluminescence properties by preventing self-aggregation. In solution states, **S-2.29** exhibited the external quantum efficiency, absorption maximum and emission maximum of 2.48%, 345 nm and 426 nm, respectively, while in the thin film state, it showed the emission maximum and band gap of 446 nm and 3.29 nm, respectively.

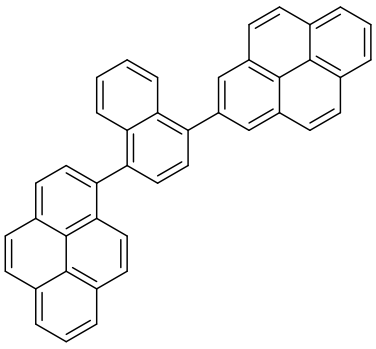

S-2.29

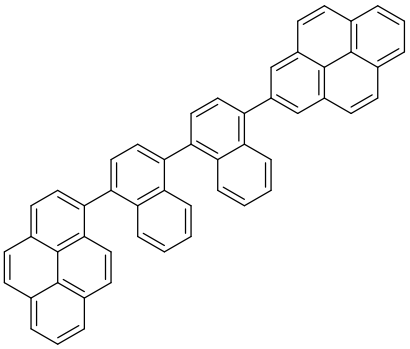

S-2.30

In 2017, Tang and his group developed a potential donor type molecule**, S-2.31** by introducing a pyrene ring at the C_2 position of the imidazole core as a blue

emitter. It was shown to possess an absorption maximum at 329 nm and emission maximum at 446 nm, with a band gap of 3.81 eV. The compound was used in the OLED device and was found to be a stable pure blue emitter with EQE of 4.57% at a luminance of 1000 cd/m^2.

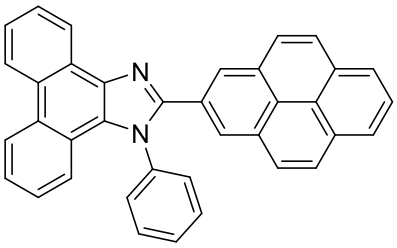

S-2.31

In 2018, Mina et al. synthesized a series of simple pyrene derivatives, **S-2.32, S-2.33** and **S-2.34** and studied their photophysical and electroluminescence properties. Here, pyrene was selected as a core system mainly due to certain advantages such as high quantum efficiency, thermal and chemical stability. The photoluminescent quantum yields (PLQY) of these synthesized molecules were found to be 43, 55, and 69%, respectively. Among them, **S-2.34** showed the highest value due to its highly twist structure. When these synthesized materials were applied to non-doped OLEDs as an emitter, they showed an EQE 1.59, 3.47 and 7.1%, respectively.

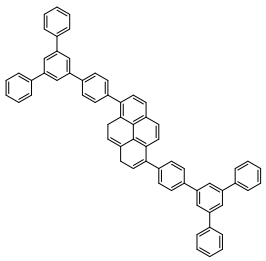

S-2.32

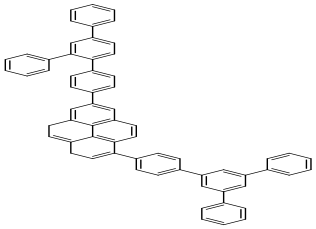

S-2.33

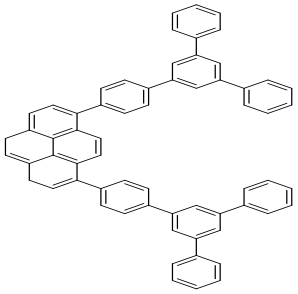

S-2.34

Recently, a research group led by Xing designed a series of donor and D-A type Y-shaped pyrene-based, solid-state blue emitters (**S-2.35 to S-2.39**) and synthesized them using Suzuki cross-coupling reaction starting from 1,3-dibromo-7-*tert*-butyl pyrene. The substitution of the benzene ring of the Y-shaped molecule can alter the crystal structure and hence crystal packing array. Depending on the electron-donating or electron-accepting nature of the substituent, the molecules exhibited good

thermal and photophysical properties. The presence of electron-accepting groups, *i.e.* cyano (**S-2.39**) and aldehyde (**S-2.40**) facilitates the extension of its π-conjugation length, and hence leads to delocalization of electron density causing blue emission.

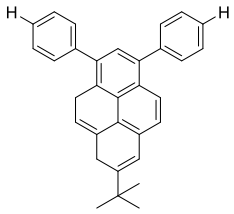

S-2.35

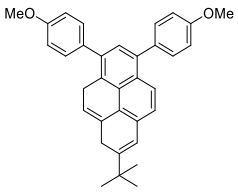

S-2.37

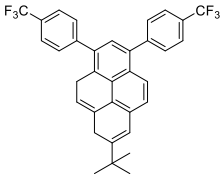

S-2.38

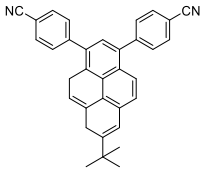

S-2.39

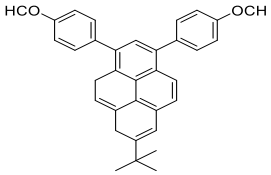

S-2.40

2.1.4 D-A type small molecules carrying diphenylamine as a donor.

Diphenylamine is a derivative of aniline with the formula $(C_6H_5)_2N$**:** consisting of an amine bound to phenyl groups. The bulky phenyl groups in diphenylamine are electron rich scaffolds, this electron-richness makes it a strong donor system. Therefore, their derivatives act as good emitting materials. **S-2.41** indicates its structure.

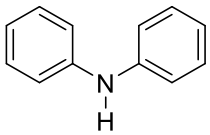

S-2.41

In 2010, Ket et al. designed a novel bipolar donor type bifluorence, **S-2.42** containing diphenylamine and fluorene units as donors. Its band gap was found to be 2.9 eV. Its EQE is 2.1 % and current efficiency is 6.5 cd/A.

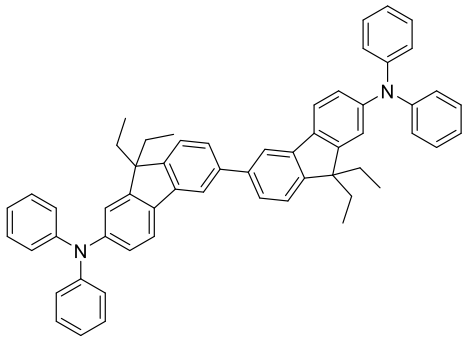

S-2.42

Adachi and his group in 2012 prepared two interesting D-A-D type compounds, **S-2.43** and **S-2.44** carrying diphenylamine as a donor and diphenylsulfoxide as an acceptor. Here, diphenylsulfoxide scaffold was selected to contract molecules with TADF properties, because the oxygen of the sulfonyl group has significant electronegativity, which makes the sulfonyl group a powerful electron-withdrawing moiety. In addition, the sulfonyl group of diphenylsulfoxide exhibits a tetrahedral geometry, which limits the conjugation in the structure. Therefore, the ΔE_{ST} values of these molecules were found to be 0.54, and 0.32 eV, respectively. Their EQE values are 2.9, and 9.9%, respectively.

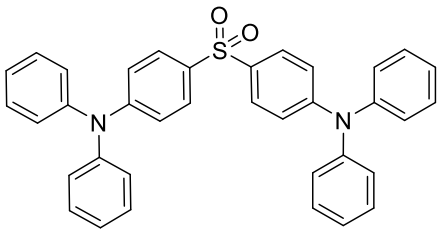

S-2.43

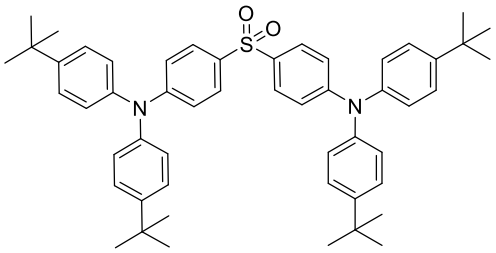

S-2.44

In 2017, Mah et al. synthesized three new A-D-A type small molecules, *i.e.* **S-2.45, S-2.46**, and **S-2.47**, by connecting the electron donating diphenylamine moiety with electron withdrawing cyano-pyridyl ring through Knovenangel condensation protocol. These donor and acceptor units were linked directly through cyano-vinylene linkage. The presence of this linkage increases the flexibility, energy levels, the planarity of the π-conjugated system, and optoelectronic properties. The observed λ_{max} values of these compounds are 440 and 447 nm and λ_{em} values are 498, and 499 nm, respectively.

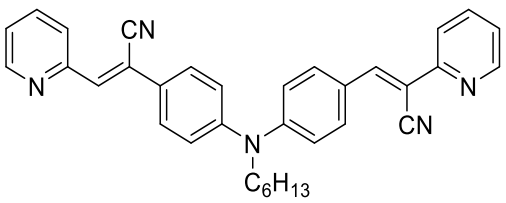

S-2.45

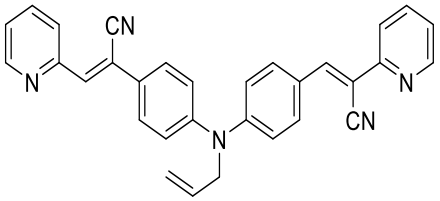

S-2.46

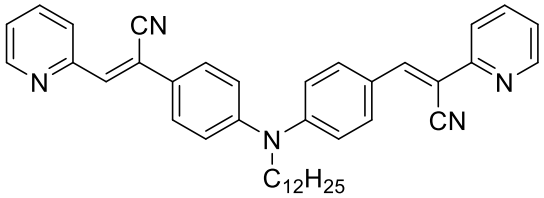

S-2.47

In 2017, Sun et al, synthesized two new diphenylamine-based D-A-D type compounds, **S-2.48** and **S-2.49** with good TADF properties; their energy difference between singlet and triplet was found to be 0.114 and 0.098 eV, respectively. These two molecules showed a delayed fluorescence and have similar values of lifetimes (about 10 micro second) because of almost similar ΔE_{ST}. Among them, **S-2.48** displayed an enhanced efficiency in the device because of increased internal quantum efficiency through up-converted triplet excitons to singlet state due to small overlap between energy levels of electron donating and electron withdrawing units as well as small ΔE_{ST}.

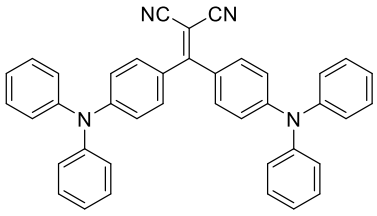

S-2.48

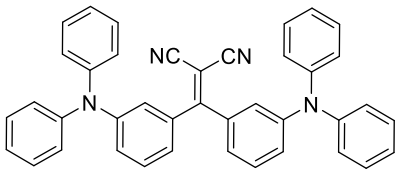

S-2.49

In 2019, Rui and his team prepared the D-D-π-A configured compounds **S-2.50, S-2.51**, and **S-2.52**, having diphenylaminophenyl as a donor, and different acceptor units. These newly synthesized molecules have λ_{max} at 485, 456, 516 nm and with quantum yields of 26, 31, and 80%, respectively. Further, the authors estimated the energy difference between singlet and triplet of these molecules. The estimated

values are 0.55, 0.55 and 0.80 eV, respectively. Based on the above-mentioned results, these newly synthesized molecules have good potential to be used as emitters.

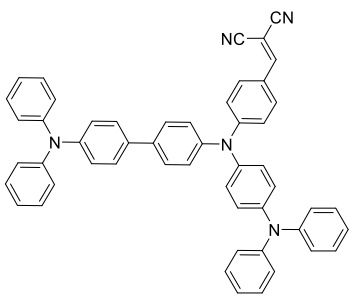

S-2.50

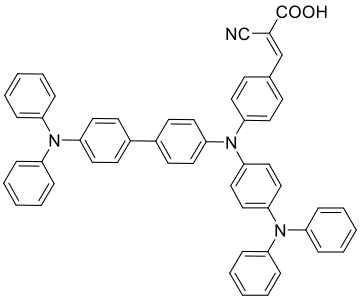

S-2.51

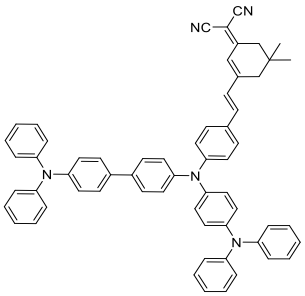

S-2.52

2.1.5 D-A type small molecules carrying triphenylamine as a donor

The structure of triphenylamine (**S-2.53**) contains three phenyl groups attached to N atom. It is having a very strong electron-donating nature. Because of this property, its presence imparts good TADF as well as hole-transporting behavior for its derivatives and hence they possess good optical properties. In addition, TPA derivatives are capable of undergoing oxidation to form cationic radicals accompanying a noticeable change of coloration.

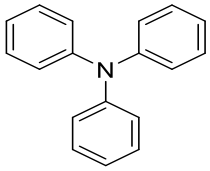

S-2.53

In 2012, Jia et al. synthesized two new D-A-D type compounds **S-2.54**, and **S-2.55**, having triphenylamine as a donor and 1,3,5 triazine as an acceptor unit. Since triphenylamine moiety has an ability to prevent orderly molecular packing, its presence improves the glass-transition temperature and brings about high hole-transporting properties. Using these molecules as an emissive layer, the authors fabricated the OLED devices, which exhibited a good performance with low turn-on voltage of 3 V and maximum luminance efficiency of 4.9 cd/A for **S-2.54** and 4.0 cd/A for **S-2.55**.

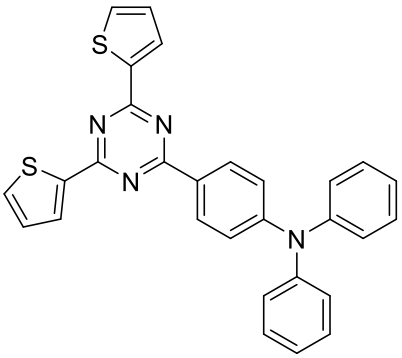

S-2.54

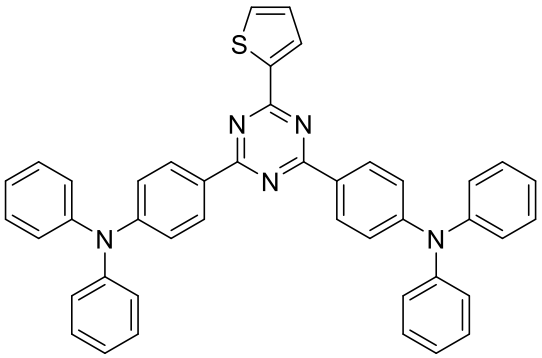

S-2.55

Keeping in view of the fact that the triphenylamine unit exhibits an excellent electron donating ability, Ma et al. (2012) reported a twist D-A configured triphenylamine-phenantro[9,10-d]imidazole **S-2.56**. In the fabricated OLED device, the molecule achieved a maximum current efficiency of 5.66 cd/A and a maximum external quantum efficiency of 5.02%.

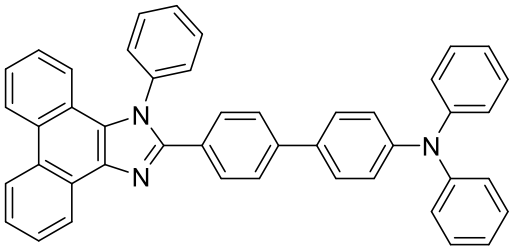

S-2.56

In 2014, Xin et al. reported a series of three D-π-A type of organic materials **S-2.57, S-2.58**, and **S-2.59** as potential emitters. These synthesized molecules showed λ_{max} at 398, 439, 406 nm and λ_{em} at 506, 624 and 596 nm, respectively. Their calculated quantum yields were found to be high and they were considered to be potential candidates for OLED application as emitters.

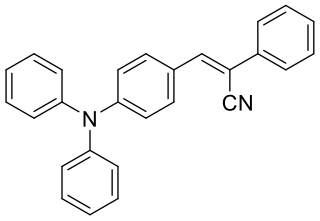

S-2.57

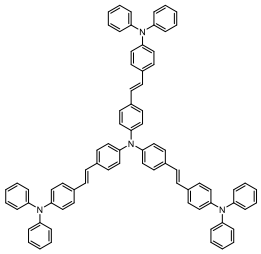

S-2.58

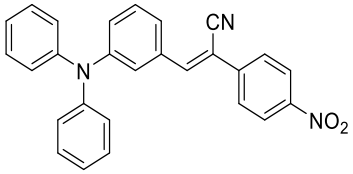

S-2.59

Su et al. (2015) developed two novel naphtholimidalozyl derivatives of triphenylamine, *i.e.* **S-2.60**, and **S-2.61** as effective emitters. They studied their photopysical and electrochemical properties in detail. These newly synthesized molecules were shown to possess good optoelectronic properties. The estimated EQE values of new molecules were found to be 6.60 and 5.95, % respectively.

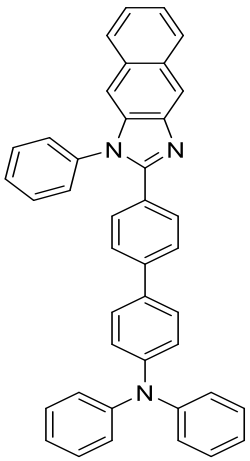

S-2.60

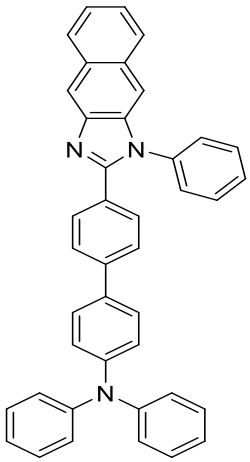

S-2.61

Liu and his associates, in 2016 reported a V-shaped molecule **S-2.62** having triphenylamine as a donor and phenanthroimidazole as an acceptor. The newly synthesized molecule was found to possess good optoelectronic properties. Further, a non-doped organic light-emitting diode fabricated using **S-2.62** emits deep blue light with a quantum yield of 4.92%.

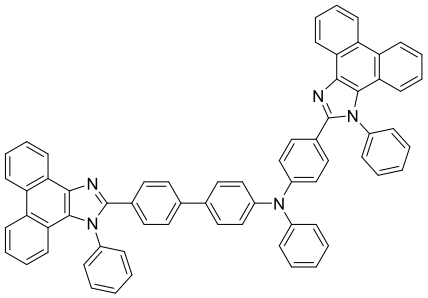

S-2.62

Recently, Jar et al. (2017) synthesized two new star-shaped elecrtolumiscent D-π-A type molecules **S-2.63** and **S-2.64** with triphenylamine as an electron releasing group phenanthroimidazole as electron accepting unit. These materials showed a good thermal stability as well as high glass transition temperature. Their electrochemical analysis reveals that both the materials have distinct oxidation and reduction behaviours. OLED device with **S-2.63** as a green emitter displayed high external quantum efficiency of 4.14% with lower turn-on voltage of 2.95 V than that of **S-2.64**.

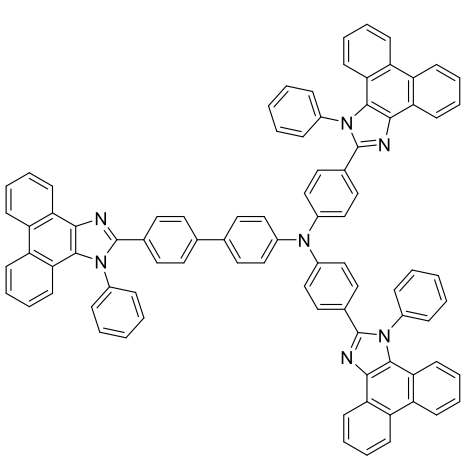

S-2.63

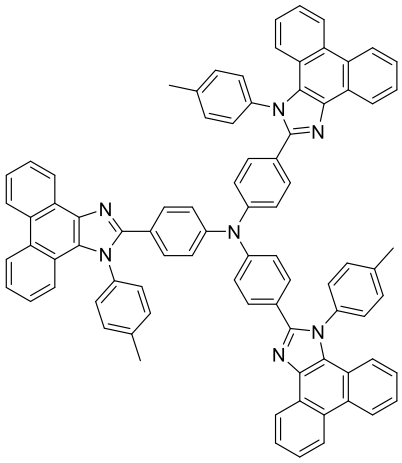

S-2.64

2.1.6 D-A type small molecules possessing phenothiazine moiety as a donor

Phenothiazine is a hetero-tricyclic scaffold having butterfly shaped system as shown in **S-2.65**. It contains both N and S heteroatoms in the ring. It has drawn the attention of many researchers from various disciplines due to their special properties. It possesses a large π conjugated electroactive rigid molecular backbone, high molar absorption coefficients, intense luminescence, *etc*. The presence of sulphur and nitrogen makes phenothiazine an excellent electron donor molecule. It has been

demonstrated that the crystallinity, hole mobility, thermal stability, optical, electrochemical and aggregation properties, *etc*. of phenothiazine can be modulated by judicious functionalization of the backbone.

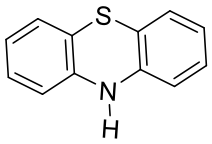

S-2.65

Bryce and co-workers (2016) designed two phenothiazine-based D-A-D type emitters **S-2.66**, and **S-2.67**. They synthesized these compounds starting from simple phenothiazine. The target compounds contain phenothiazine as a donor group and dibenzothiophene-*S,S*-dioxide as an acceptor core. Among these two compounds, unsubstituted **S-2.66** showed a good EQE of 18.8% compared to the substituted **S-2.62**.

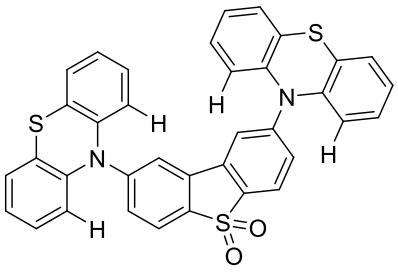

S-2.66

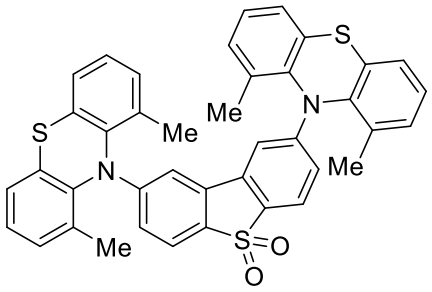

S-2.67

Qiu et al. (2017) synthesized two phenothiazine based D-A type blue light emitters, *i.e.* **S-2.68,** and **S-2.69**, carrying phenothiazine as a donor group and 1,4,5-triphenyl-1*H*-imidazole (**S-2.68**) and phenanthro[9,10-*d*]imidazole (**S-2.69**) as acceptor moieties. The OLED device with **S-2.69** showed a showed better EQE of 3.41%, a maximum current efficiency of 7.20 cd/A and power efficiency of 4.00 lm/W compared to **S-2.68** based device.

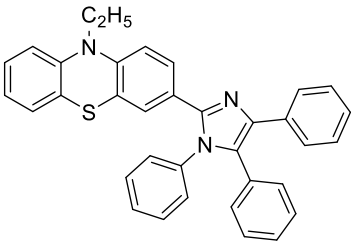

S-2.68

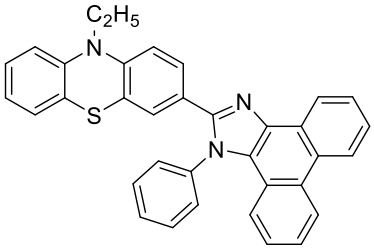

S-2.69

Suh et al. (2018) synthesized D-A-D type TADF material, **S-2.70** containing phenothiazine as a donor group and benzonitrile as an acceptor unit. They proposed that deviation of the central axis of donor moiety away from orthogonality with acceptor effects the reverse intersystem crossing mechanism. Fabricated device of **S-2.70** showed a maximum current and maximum power efficiency of 17.2 cd/A, and 12.0 lm/W, respectively.

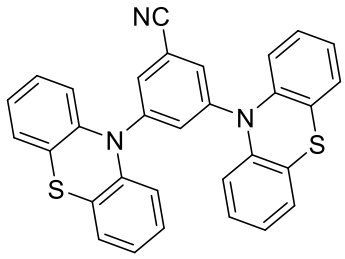

S-2.70

Adachi and co-workers (2018) reported a phenothiazine based emitter containing three phenothiazine moieties as donor units and 2,4,6-triphenyl-1,3,5-triazine as an acceptor moiety. The fabricated OLED based on **S-2.71** showed yellowish-green with turn-on voltage of 4.20 V, a maximum current efficiency of 58.60 cd/A, power efficiency of 17.40 lm/W, and EQE of 17.40%.

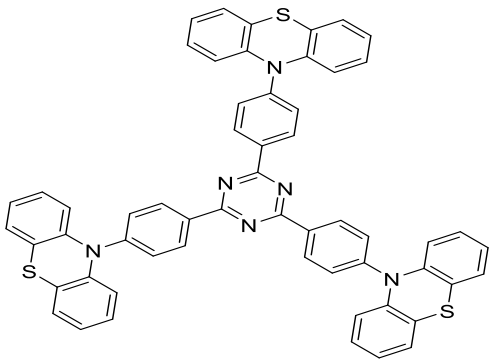

S-2.71

2.2 SALIENT FEATURES OF THE LITERATUR REVIEW

Based on the detailed literature review, the following observations can be drawn.

- The push-pull (D-A) architecture is a widely used strategy to design efficient organic emitters.
- The organic molecules should possess good light absorption and emission properties in the solid state.
- Materials should have high quantum yield in solid states.
- The HOMO-LUMO energy levels of the small molecules should match with the HOMO-LUMO energy levels of the hole transporting layer and electron transporting layer used in the device respectively.
- The separation between HOMO and LUMO of the molecules helps to reduce the singlet-triplet distance, which directly affects the efficiency of the OLED device.
- Carbazole and triphenylamine derivatives are considered to be most promising donor systems in OLEDs.
- With the slight variation in D-A interactions in the basic structure, it is possible to tune the emission color.
- No reports are available on D-A type small molecules involving cyanopyridone as an acceptor unit.
- Overall, there is an extensive scope for proper designing the new molecular structures to achieve the desired optical and electrochemical properties.

2.3 SCOPE AND OBJECTIVES OF PRESENT WORK

Till date, several organic emitters with different structural configurations have been explored as effective emissive materials for OLED applications. Indeed, there are still challenges to designing and synthesizing small molecules for OLED

and identifying the parameters limiting the performance of OLED. By modifying the design strategy of the molecule, one can easily alter the optical as well as electrochemical properties, which affect majorly on light emissive ability and different charge-transfer processes in the device. The development of highly efficient emissive materials is still one of the most thrilling researches in the OLED field. So, there is much scope for developing suitable low-cost and eco-friendly organic emissive materials for OLED applications.

Keeping in view of the fact that cyanopyridone-based D-A type molecules have been little explored as effective emitters, the present work has been focused on this interesting core.

Based on the above-mentioned facts, as well as the literature review, the following objectives have been intended in the present research studies.

1. To design and synthesize seven new series of D-A-D type cyanopyridone-based organic small molecules carrying different donors such as triphenylamine **(Series-1),** pyrene (**Series-2**), carbazole (**Series-3**), phenothiazine (**Series-4**), *N*,*N*-diphenylamine (**Series-5**), and *N*,*N*-diphenylaniline (**Series-6** and **-7**) and varied auxiliary donors such as thienyl, tolyl, 4-hydroxy phenyl, anisolyl, phenyl, biphenyl, *etc*.

2. To characterize newly synthesized molecules by FTIR,^{1}H NMR,^{13}C NMR, and Mass spectroscopy techniques

3. To perform the photophysical, electrochemical, thermal, theoretical, and EL studies and to assess their structure-property relationship

4. To fabricate OLEDs and evaluate the device parameters such as EL quantum efficiency, maximum luminance, and turn-on voltage of the new device.

MOLECULAR DESIGN, SYNTHESIS, AND STRUCTURAL CHARACTERIZATION OF NEW CYANOPYRIDONE-BASED ORGANIC SMALL MOLECULES

Abstract

This chapter covers the structural design of seven series of cyanopyridone-based D-A-D type small molecules. Further, it comprises detailed synthetic pathways and purification techniques used for newly designed compounds. Furthermore, it involves structural characterization of targeted molecules, using FTIR, ^{1}*H NMR,* ^{13}*C NMR, and Mass spectral studies. In addition, a detailed discussion on structural elucidation has been included in it.*

3.1 INTRODUCTION

After conducting a detailed review of existing literature, it is evident that various design strategies have been employed to create emitters for OLED applications. These strategies include D-A, D-π-A, D-A-D, D-π-A-π-D, D-D-π-A, and A-D-A designs. The literature also highlights the use of diverse donor and acceptor groups in these entities. Among the different interesting donor units discussed, carbazole, triphenylamine, pyrene, phenothiazine, and diphenylamine have been emerged as promising options, exhibiting desirable thermal, electrochemical, and electroluminescent properties. Keeping in view of their several advantages with these donor units, our current research aims to develop novel organic small molecules bearing triphenylamine, pyrene, carbazole, phenothiazine, and diphenylamine as a donor component with varying secondary auxiliary donor groups like benzene, toluene, biphenyl, aniline, anisole, phenol and thiophene. In all the molecules cyanopyridones has been selected as a fixed electron accepting unit.

In general, the emissive layer of the OLED must possess an energy level that matches the charge carrier injection and acceptance of both holes and electrons. In order to gain the bipolar nature, an emissive layer must be capable of forming a stable cation and anion radicals which is the ensuing consequence of electron transporting and hole transporting phenomena. Usually, while designing a bipolar material, hole and electron transporting properties play an essential role, for which appropriate

electron-donating and electron-withdrawing moieties are to be chosen. This is because the donor group has the hole-transporting ability while the acceptor unit has the electron-carrying property.

3.2 MOLECULAR DESIGN OF NEW CYANOPYRIDONE DERIVATIVES

In the following section, design of seven new series of D-A-D type cyanopyridone-based organic small molecules carrying different donors has been described. The new design includes triphenylamine (**Series-1**), pyrene (**Series-2**), carbazole (**Series-3**), phenothiazine (**Series-4**), *N*,*N*-diphenylamine (**Series-5**), and *N*,*N*-diphenylaniline (**Series-6** and **-7**) as primary donors and varied auxiliary donors such as thienyl, tolyl, 4-hydroxy phenyl, anisolyl, phenyl, biphenyl, *etc*. Their properties have been fine-tuned through the incorporation of suitable donors. Further, varieties of synthetic strategies were employed to yield these compounds through multi-step sequences. **Schemes 3.1-3.7** encapsulates the synthetic pathway for the newly designed molecules, adhering to the standardized synthesis route across all the series.

In the present work we are chosimg the cyanopyridone as a fixed acceptor , It has been well-established that pyridine-2-one is an interesting n-type highly electron-deficient nitrogen heterocyclic entity; its presence in any conjugated system provides an excellent electron-transporting ability, good optical properties including outstanding chemical and thermal stabilities, which can be further enhanced by incorporating a cyano group at the third position of this core .pyridine and cyanide group shows the TADF properties. This cyanopyridone is less explore in the OLED field. Keeping this in view, 3-cyanopyridine-2-one has been carefully chosen as an excellent electron acceptor core unit in the present design. This cyanopyridone cores finds their application in solar cells also. It has properties to exhibits the liquid crystal nature [52,53,54,55].

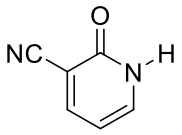

3.2.1 Design of triphenylamine substituted cyanopyridones (Series-1, C_{1-7})

In **series-1,** seven new D-A-D configured small heterocyclic molecules have been designed. These compounds carrying a triphenylamine system as a fixed donor, and 3-cyanopyridine-2-one as a fixed acceptor with varying aromatic/heteroaromatic donors such as simple benzene (**C_1**), toluene (**C_2**), biphenyl (**C_3**), aniline (**C_4**), anisole (**C_5**), phenol (**C_6**), and thiophene (**C_7**). It has been well-established that pyridine-2-one is an interesting *n*-type highly electron-deficient nitrogen heterocyclic entity; its presence in any conjugated system provides an excellent electron-transporting ability, good optical properties including outstanding chemical and thermal stabilities, which can be further enhanced by incorporating a cyano group at the third position of this core. In view of this, 3-cyanopyridine-2-one has been carefully chosen as an excellent electron acceptor core unit in the present design. Further, the triphenylamine moiety was selected as a fixed donor because of its strong electron-donating nature and ability to decrease the aggregation-induced fluorescence quenching of the planar conjugated core, excellent thermal, photochemical, and morphological stabilities and good hole-transporting capacity *via* the radical cation species. Additionally, they possess high values of the highest occupied molecular orbital (HOMO) energy levels allowing efficient hole injection. In the present design, triphenylamine has been attached to the 4^{th} position, and different aromatic donors have been linked to the 6^{th} position of the cyanopyridone core to constitute the D-A-D configuration, thereby attaining desired electrochemical and optical properties due to their structural facilitation. **Figure 3.1** summarizes the designed triphenylamine based compounds.

Red, green, and blue (RGB) are the primary colours that are mandatory for a full-colour display. In addition to the three primary colours, yellow emission is an essential chromaticity component for many applications as diverse as RGBY-TV and lithography labs to traffic and signal lights. It helps boost the colour rendering indexes (CRI) of white OLEDs for use in high-quality solid-state lighting while posing minimal risk to the eye's retina. Consequently, yellow light has found widespread application in settings such as signal systems, factories producing light-sensitive materials, and research laboratories. In effect, due to its relatively low suppression effect per lumen on melatonin secretion, it effectively acts as a backbone emission for

night-time lighting sources with a very low color temperature that are physiologically friendly. Consequently, there is a persistent requirement for research and development into yellow light-emitting layers, which typically offer lower drive voltages and, thus use less power, without sacrificing luminance efficiency, lifetime, or color purity in the devices. However, there is a dearth of efficient materials with pure yellow emission for device applications. Keeping this in mind, the present series has been designed with the hope that they emit yellow light. In the new design, triphenylamine was attached to the 4th position, and different aromatic donors have been linked to the 6th position of the cyanopyridone core to constitute the D-A-D configuration, thereby attaining desired electrochemical and optical properties due to their structural facilitation. **Figure 3.1**. Shows the designed triphenylamine substituted cyanopyridones.

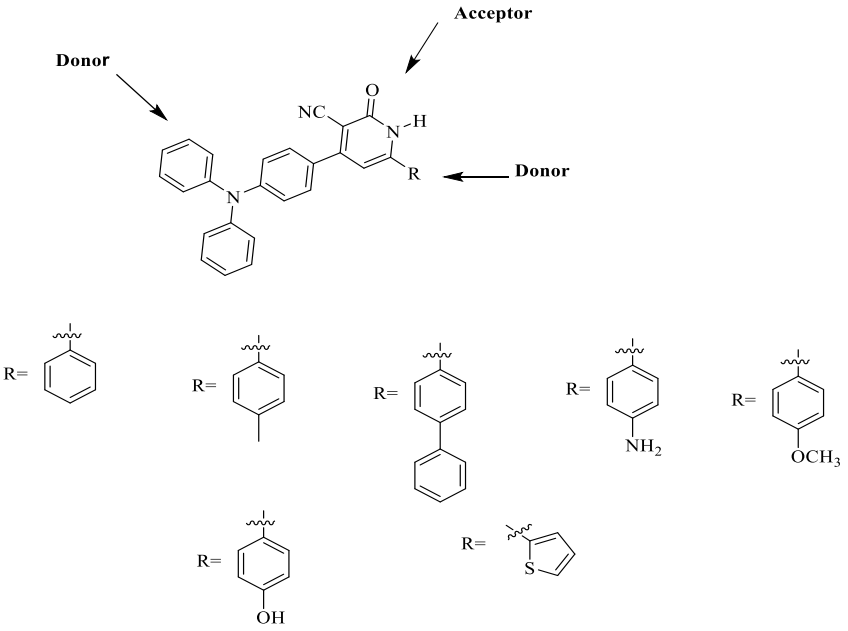

Figure 3.1. Design of triphenylamine substituted cyanopyridones **C_{1-7}** (**Series-1**)

3.2.2 Design of pyrene appended cyanopyridones (Series-2, C_{8-14})

Pyrene, a polycyclic aromatic system, is an excellent electron-donating scaffold exhibiting a good charge-carrying ability and high fluorescence emission. Further, the increased tendency towards the π-π* stacking of its four fused benzene rings leads to a strong intermolecular interaction in the solid state, thereby resulting in a significant red-shift of the fluorescence emission and good fluorescence quantum

yield of pyrene derivatives. Thus, pyrene derivatives are good luminogens due to a number of favourable characteristics like resistance to photo and thermal-degradation owing to their high chemical stability, high fluorescence quantum efficiency, good charge transport properties, ease of synthesis/modification, and low cost. Hence, they are excellent green emitters, which can find applications as an emissive layer in OLEDs. Pyridine-2-one and its cyano derivatives have shown to be effective acceptor molecules in designing push-pull type emitters owing to their very high electron-withdrawing power, electron transporting ability, and low-lying LUMO energy levels. Moreover, they are highly stable due to strong intermolecular interactions[61].

More profoundly, searching for reliable and highly efficient primary colour RGB (red, green, and blue) emitters is vital for developing effective devices. In this mission, achieving the ultrapure green fluorescence is challenging, as it demands a strictly well-defined peak emission wavelength and narrower spectrum half-width compared to the other colours. In addition, the recommendation ITU-*R* BT-2020 for the colour reproduction area of the display has also become an impediment for the green emitters because BT.2020 standard insists the monochromatic RGB primaries with an extremely narrow bandwidth which is indeed a difficult job to accomplish. All these factors have fetched substantial importance to the green emitters in the colour reproduction area of the display. So, there is a great need to develop high-efficiency deep green organic emitters with a narrow emission line width that can be suitably used to produce high-performance OLEDs.

Keeping all these points in view, seven new D-A-D type compounds have been designed choosing 3-cyanopyridine-2-one as a fixed electron acceptor core, pyrene as a fixed electron donor, and varying secondary donor groups, such as phenyl (**C_8**), tolyl (**C_9**), biphenyl (**C_{10}**), 4-aminophenyl (**C_{11}**), 4-methoxyphenyl (**C_{12}**), 4-hydroxyphenyl (**C_{13}**), and 2-thienyl (**C_{14}**) as possible green emitting materials. **Figure 3.2**. summarizes the design strategy involved in **Series-2**.

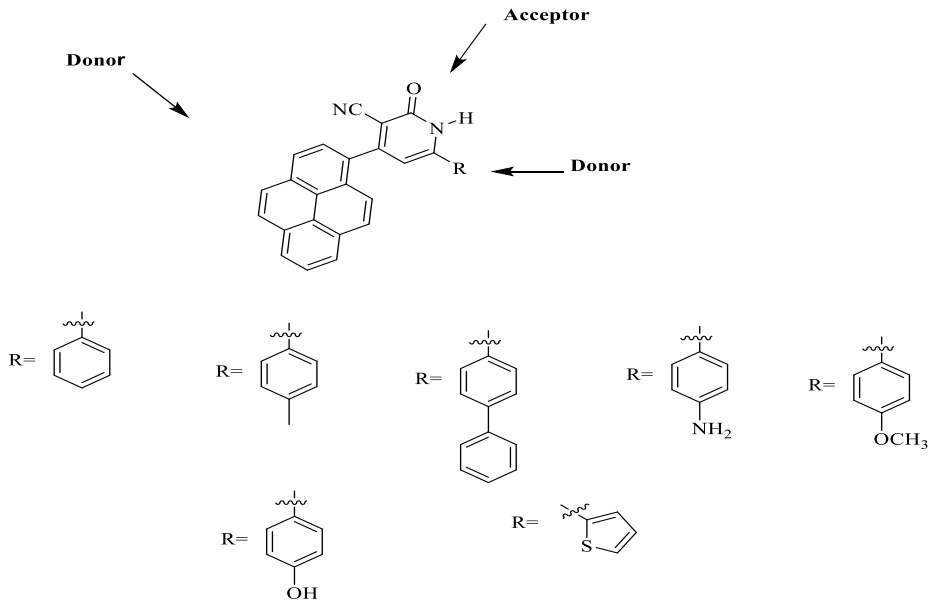

Figure 3.2. Design of pyrene appended cyanopyridones $\mathbf{C_{8\text{-}14}}$ (**Series-2**)

3.2.3 Design of carbazole-cyanopyridone conjugates (Series-3, $\mathbf{C_{15\text{-}21}}$)

A novel series, $\mathbf{C_{15\text{-}21}}$, consisting of seven D-A-D configured carbazole-cyanopyridones bearing varied secondary donor units has been designed. In the new design, *N*-alkylated carbazole acts as the fixed donor and cyanopyridone serves as the fixed acceptor to obtain bipolar transport characteristics in the luminophores. The varied auxiliary donors like phenyl ($\mathbf{C_{15}}$), tolyl ($\mathbf{C_{16}}$), biphenyl ($\mathbf{C_{17}}$), 4-aminophenyl ($\mathbf{C_{18}}$), 4-methoxyphenyl ($\mathbf{C_{19}}$), 4-hydroxyphenyl ($\mathbf{C_{20}}$), and 2-thienyl ($\mathbf{C_{21}}$) moieties have been incorporated in order to fine-tune their properties. The carbazole unit has been chosen as the fixed donor because of its derivatives find applications in many optoelectronic devices, for instance, organic thin film transistors (OTFTs), organic solar cells, and OLEDs due to their high thermal stability, emission efficiency, easy chemical functionalization, good film-forming ability, and their potential hole-transporting mobility associated with the electron-donating ability of the *N*-heterocyclic core ring. Additionally, carbazole, being an aromatic and inexpensive starting material with multiple linkage positions on the ring, is capable of bringing about a high quantum yield as well as good thermal, photochemical, and morphological stability for its derivatives.

Over the past few years, considerable progress has been made in developing highly efficient red and green emitters, and many red and green OLEDs with excellent performance have been reported. However, the quest for an efficient blue emitter remains challenging compared to its counterparts. The main obstacle to achieving efficient blue emission lies in material's inherent characteristics, particularly large optical band gaps. A wide band gap restricts charge delocalization, leading to difficulties in electron injection. A high voltage is required to operate such an emitter in the device. The higher the voltage, the more heat is generated, so the blue emitter possesses low efficiency and a short device lifetime. Consequently, developing blue materials with good EL characteristics and a long lifetime is highly desirable for achieving commercial requirements. **Figure 3.3**. displays the designed approach used for the D-A-D type carbazole-based cyanopyridones[35].

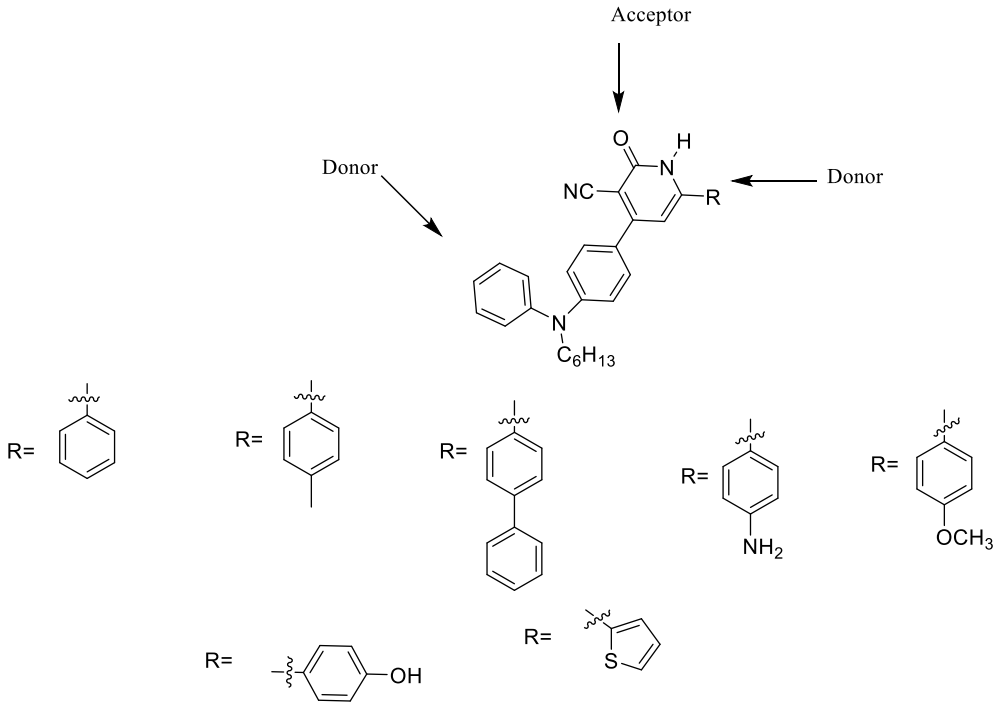

Figure 3.3. Design of carbazole-cyanopyridone conjugates **$C_{15\text{-}21}$** (**Series-3**)

3.2.4 Design of phenothiazine-cyanopyridone hybrid derivatives (Series-4, $C_{22\text{-}28}$)

The structural design of seven new D-A-D configured phenothiazine-based molecules is shown in **Figure 3.4**. In the new design, phenothiazine was used as a fixed donor group, cyanopyridone was used as a fixed acceptor core, with a varying

secondary donor groups such as phenyl (**C_{22}**), tolyl (**C_{23}**), biphenyl (**C_{24}**), 4-aminophenyl (**C_{25}**), 4-methoxyphenyl (**C_{26}**), 4-hydroxyphenyl (**C_{27}**), and 2-thienyl (**C_{28}**). Among the family of heterocyclic donors, phenothiazine is a well-known building block with distinct features of (i) strong electron-donating character, (ii) a nonplanar butterfly type conformation, (iii) tuneable redox properties, (iv) availability of multiple modifiable sites and ease of functionalization, and (iv) cheap and commercial availability. Finally the presence of electron-rich sulphur and nitrogen hetero-atoms and the ionization potential of 6.73 eV are well suited for contracting the D-A type materials[32].

From the last few years lots of progress has been done in developing the primary RGB emitters, and many red and green OLEDs with excellent performance have been obtained. However, the journey towards efficient blue emitters has been met with formidable hurdles. The main problem of achieving the blue emission is large band gap of the materials. These wider gaps pose issues for electron movement, necessitating higher operational voltages. However, the consequence is heightened heat generation, leading to deceased efficiency and a shortened device lifespan for the blue emitter. As a result, there exists a lot of scopes for developing new blue light emitting materials.

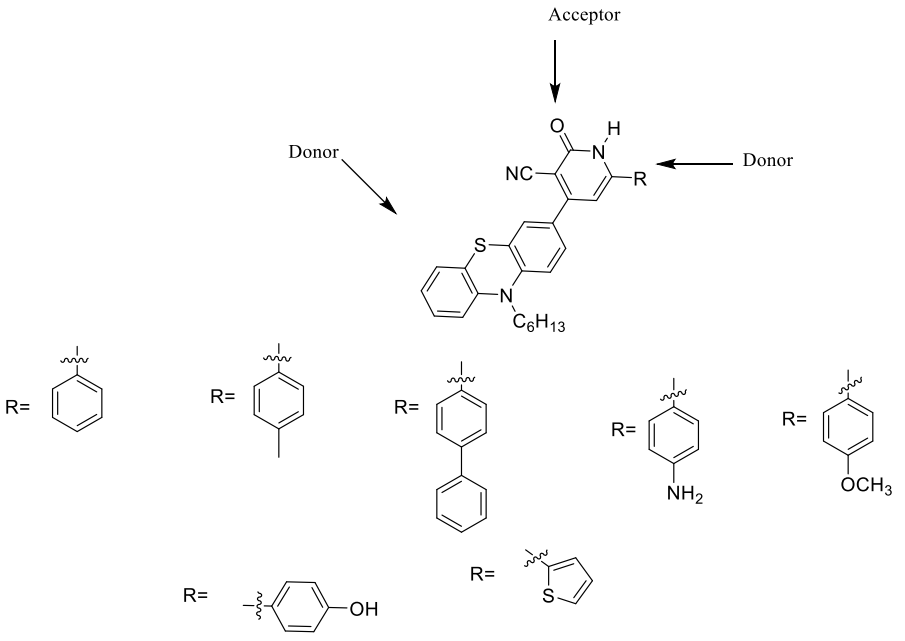

Figure 3.4. Design of phenothiazine-cyanopyridone hybrid derivatives **$C_{22\text{-}28}$** (**Series-**

4)

3.2.5 Design of diphenylamine-based cyanopyridone derivatives (Series-5, C_{29-34})

In **Series-5**, six new D-A-D type molecules consisting of diphenylamine as a fixed donor and cyanopyridone as a fixed acceptor scaffold, with a varying secondary donor groups such as phenyl (**C_{29}**), tolyl (**C_{30}**), biphenyl (**C_{31}**), 4-methoxyphenyl (**C_{32}**), 4-hydroxyphenyl (**C_{33}**), and 2-thienyl (**C_{34}**) have been designed. In all the compounds, DPA was chosen as a fixed donor because of its high electron donating ability. DPA has a pyramidal geometry in the ground state and planar geometry in the first excited state. It changes from this pyramidal geometry around the N-atom with unequal torsional angles of the phenyl groups to the planar geometry. The two major features play an important role in the intra-molecular dynamics and in the chemical behavior of the molecules. The features include (i) the equilibrium orientation of the phenyl rings of the phenyl group around the C-N groups relative to the C-N-C plane, and (ii) the frequencies of the corresponding torsional motions. These interesting properties of diphenylamine make it a preferred candidate for using as a donor group in the emitter. The design of series-5 compounds are shown in **Figure 3.5**.

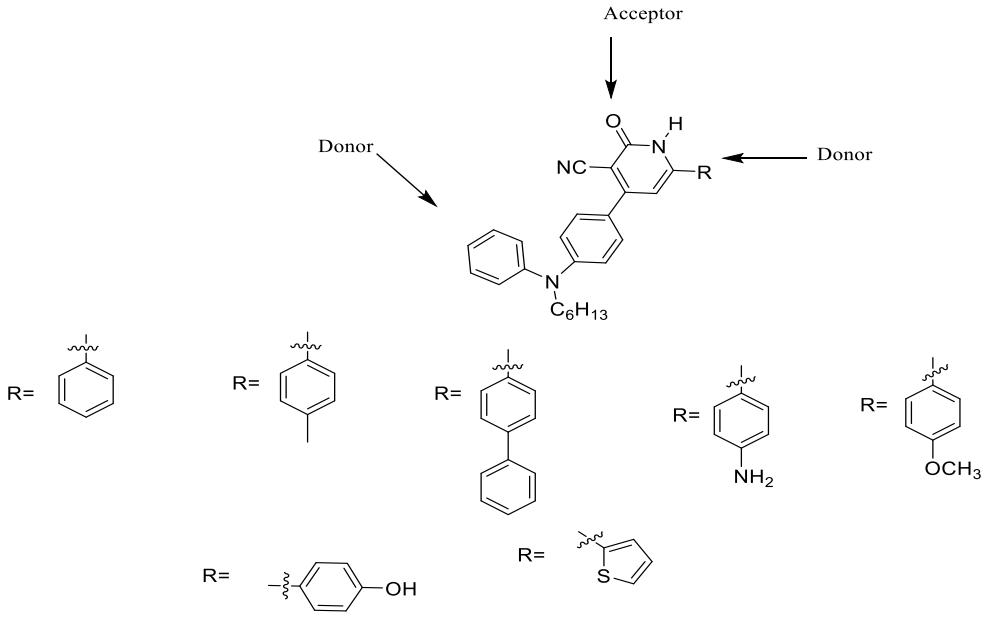

Figure 3.5. Design of diphenylamine-based cyanopyridone derivatives **C_{29-34}** (**Series-5**)

3.2.6 Design of *N*,*N*-dimethylaniline linked cyanopyridones (Series-6, C_{35-37})

Three new substituted cyanopyridones carrying *N*,*N*-dimethylaniline, *i.e.* **C_{35-37}** with D-A-D configuration were designed as shown in **Figure 3.6**. These cyanopyridone-based molecules consist of *N*,*N*-dimethylaniline as a fixed primary donor unit. Pyrene, triphenylamine, and *N*,*N*-dimethylaniline were selected as different varying donor groups. Cyanopyridone scaffold was chosen as a fixed electron-acceptor. It is expected that the designed molecules would show a good fluorescence. So, these molecules can be considered as potential emitters in OLEDs.

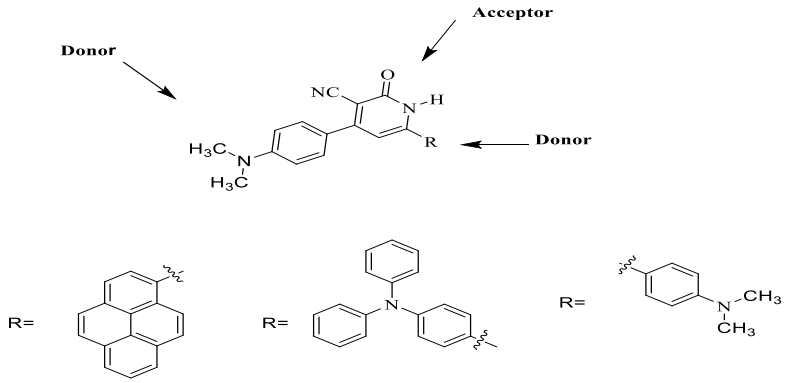

Figure 3.6. Design of *N*,*N*-dimethylaniline linked cyanopyridones **C_{35-37}** (**Series-6**)

3.2.7 Design of *N*,*N*-dimethylaniline substituted 2-(benzyloxy)nicotinonitriles (Series-7, C_{38-42})

Figure 3.7. depicts the structural design strategy of five D-A-D type cyanopyridine-based small molecules, *i.e.* **C_{38-42}** consisting of cyanopyridine as a fixed acceptor group, *N*,*N*-dimethylaniline as a fixed donor, and with a different secondary donor groups such as phenyl (**C_{38}**), tolyl (**C_{39}**), biphenyl (**C_{40}**), 4-methoxyphenyl (**C_{41}**), and 2-thienyl (**C_{42}**). The high electron-accepting cyanopyridine system helps to transporting the electron. The presence of cyano group on the pyridine ring enhances its electron-withdrawing nature. The designed molecules are anticipated to act as ideal emitters since they fulfill all the prerequisites.

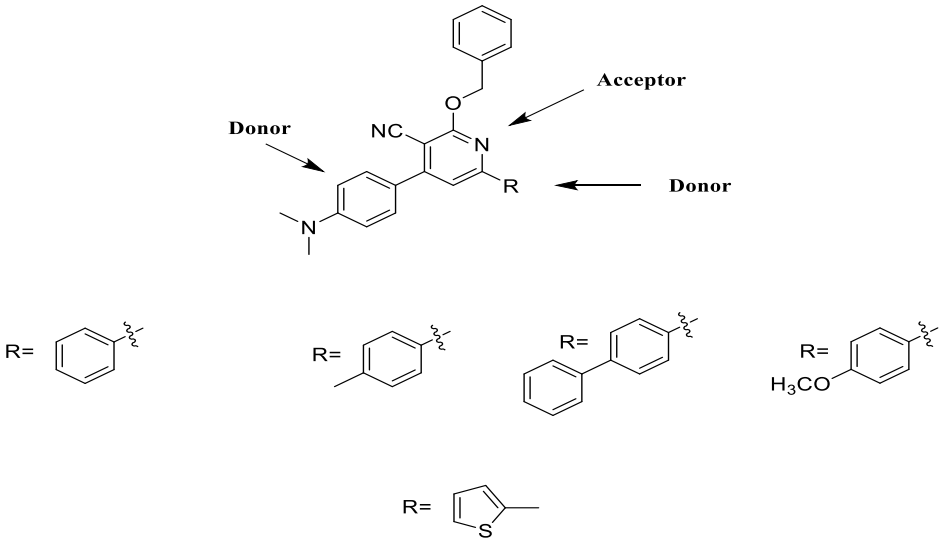

Figure 3.7. Design of *N*,*N*-dimethylaniline substituted 2-(benzyloxy)nicotinonitriles, **$C_{38\text{-}42}$** (**Series-7**)

3.3 EXPERIMENTAL

The materials used, experimental protocols, and purification techniques employed for the synthesis of newly designed compounds are given in the following section. It also includes structural characterization data.

3.3.1 Materials and methods

All the chemicals employed in the synthesis were purchased from Sigma-Aldrich and were used without any further purification. The solvents that were used in the reactions were of synthetic grade and those were purified by drying and distillation process. Final product was purified by recrystallization / column chromatography method and thereby obtained purified product was then taken for further characterizations like NMR, FTIR, and Mass spectrometry. The structure of the compound was confirmed by NMR spectroscopy, which was run in Bruker advance spectrometer using DMSO solvent with TMS as an internal standard. Bruker FTIR Alpha spectrophotometer was utilized to confirm the functional groups in the synthesized dyes and the mass spectra were obtained by making use of the electron spray ionization technique using ACQUITYTM UPLCTM H-Class PLUS Bio system mass spectrometer to confirm the molecular weight of the synthesized compounds.

3.3.2 Synthesis of C_{1-42}

The detailed synthetic strategy used for all the target molecules and respective purification techniques along with their characterization data are elaborated in the following section.

3.3.2.1 Synthesis of TPA substituted compounds C_{1-7} (Series-1)

The synthetic scheme employed for the preparation of compounds $\mathbf{C_{1-7}}$ starting from simple TPA has been depicted in **Scheme 3.1**. The steps involve the formylation of TPA through Vilsmeier-Haack reaction, followed by cyclization to give target compounds. Here, aryl/heteroaryl ketones, and ethyl cyanoacetate were used for the base catalyzed condensation reaction.

Synthesis of 4-(diphenylamino) benzaldehyde (2):

Phosphorus oxychloride (3.8 mL 0.04 mol) was added dropwise to a well-stirred 6.2 mL (0.08 mol) of *N*,*N*-dimethylformamide (DMF). The mixture was stirred at 0 ^{o}C for 1 hour and to this, a 10 g of (0.04 mol) of triphenylamine (***1)*** dissolved in dichloroethane was added slowly. The mixture was stirred at 90 ^{o}C for 2 hours to complete the reaction. The content was poured into100g of crushed ice, neutralized to pH7 with 2N NaOH solution, and extracted with dichloromethane (100 mL x 3). The combined extract was washed with brine 3-4 times, and the organic solvent was removed at reduced pressure. The residue was purified by using column chromatography with silica gel (ethylacetate: pet ether in 1:3); a yellowish solid of **2** was obtained with a 53% yield. Obtained spectral results matched with the reported data.

General procedure for the synthesis of C_{1-7}:

For the synthesis, a mixture of triphenylamine aldehyde (***2***, 1 g 1.18 mmol), aryl/hetero aryl ketone (1.71 mmol), ethyl cyanoacetate (0.48 g, 3.59 mmol), and ammonium acetate (2.48 g, 3.61 mmol) in dioxane was taken in a round bottom flask. The mixture was refluxed at 80 ^{o}C for 12 hours. After the reaction, the mixture was poured into 150 g of ice-cold water; the yellow solid separates out. Finally, the solid was purified by recrystallization from chloroform. Structures of $\mathbf{C_{1-7}}$ were confirmed by spectral studies.

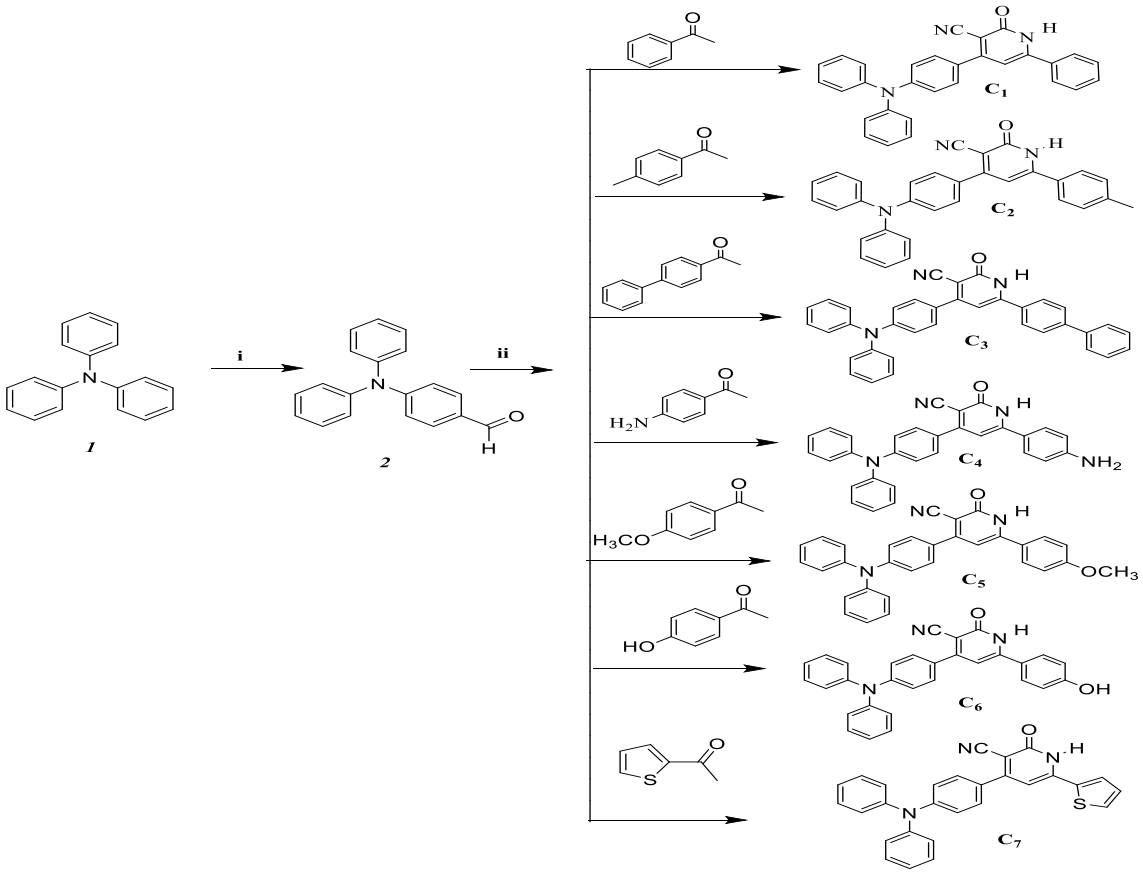

Scheme 3.1. Synthetic routes for $\mathbf{C_{1\text{-}7}}$: (**i**) $POCl_3$, DMF, RT, 12 hours (**ii**) aryl ketones, ammonium acetate, ethyl cyanoacetate 80 ^oC, 24 hours

4-(4-(Diphenylamino)phenyl)-1,2-dihydro-2-oxo-6-phenylpyridine-3-carbonitrile ($\mathbf{C_1}$):

FT-IR (ATR) υ_{max} in cm^{-1}: 2913(Ar-C-H), 2218(C≡N),1634(C=O), 1587(Ar-C=C); **^{1}H NMR** (DMSO-d_6,500MHz): δ 12.69(s,1H, CONH), 7.8(s,2H), 7.6(d,2H), 7.5(m,3H), 7.4(t,4H), 7.1(m,6H), 6.9(d,2H), 6.7(s,1H,pyridine-H); **^{13}C NMR** (DMSO, 125MHz): δ 150.30, 146.66, 131.59, 130.37, 130.22, 129.39, 128.31, 128.16, 126, 125.06, 120.47, 117.47; Melting point 350-357 ^oC, Yield 50%; **Mass (m/z)** value for $C_{30}H_{21}N_3O$ 439.17, obtained [M-H] 440.12.

4-4-(Diphenylamino)phenyl-1,2-dihydro-2-oxo-6-*p*-tolylpyridine-3-carbonitrile ($\mathbf{C_2}$):

FT-IR (ATR) υ_{max} in cm^{-1}: 2918(Ar-C-H), 2220(C≡N), 1627(C=O), 1592 (Ar C=C); **^{1}H NMR** (DMSO-d_6): δ 12.54(s,1H), 7.7(d,2H), 7.6(d,2H), 7.3(m,6H), 7.2(m,6H), 6.9(d,2H), 6.7(s,1H), 3.2(s,3H); **^{13}C NMR** δ 149.97, 146.69, 141.76, 130.36, 130.20, 129.97, 128.45, 128.05, 125.97, 125.01, 120.53, 117.53; Melting point 340-345 ^{o}C; Yield 40%; **Mass (m/z)** value for $C_{31}H_{23}N_3O$ 453.18, obtained [M-H] 454.18.

4-(4-(Diphenylamino)phenyl)-1,2-dihydro-6-biphenyl-2-oxopyridine-3-carbonitrile (C$_3$):

FT-IR (ATR) υ_{max} in cm^{-1}: 2960(Ar-C-H), 2215(C≡N), 1631(C=O), 1591(Ar-C=C); **^{1}H NMR** (DMSO-d_6, 500Hz): δ 12.72(s,1H,CONH), 8.0(d,2H), 7.8(d,2H), 7.7(d,2H), 7.6(d,2H), 7.5(t,2H), 7.4(m,4H), 7.3(t,2H), 7.1(d,5H), 6.8(s,1H);**^{13}C NMR** (DMSO, 125M Hz): δ 159.31, 150.02, 146.69, 143.04, 139.26, 130.35, 130.24, 129.56, 128.79, 128.71, 128.37, 127.46, 127.31, 125.99, 125.90, 125.02, 120.51, 117.48; Melting point 330-335 ^{o}C; Yield 40%; **Mass (m/z)** value for $C_{36}H_{25}N_3O$ 515.2, obtained [M-H] 516.14.

6-(4-Aminophenyl)-4-(4-(diphenylamino)phenyl)-1,2-dihydro-2-oxopyridine-3-carbonitrile (C$_4$):

FT-IR (ATR) υ_{max} in cm^{-1}: 2953(Ar-C-H), 2265(C≡N),1627(C=O), 1509(Ar-C=C); **^{1}H NMR** (DMSO-d_6): δ 12.18(s,1H), 7.6(t,2H), 7.36(t,4H), 7.1(m,6H), 6.9(d,2H), 6.6(d,3H), 5.9(s,2H); **^{13}C NMR**: δ 162.91, 152.69, 149.74, 146.78, 130.33, 130.03, 129.49, 129.09, 125.84, 124.89, 120.74, 118.05, 113.91; Melting point 345-350 ^{o}C; Yield 30%; **Mass (m/z)** value for $C_{30}H_{22}N_4O$ 454.18, obtained [M-H] 454.183.

4-(4-(Diphenylamino)phenyl)-1,2-dihydro-6-(4-methoxyphenyl)-2-oxopyridine-3-carbonitrile (C$_5$):

FT-IR (ATR) υ_{max} in cm^{-1}: 2955(Ar C-H), 2220(C≡N), 1679(C=O), 1594(Ar-C=C); **^{1}H NMR** (DMSO-d_6): δ 12.50(s,1H) 7.8(d,2H), 7.6(d,2H), 7.4(t,4H), 7.3(m,6H), 7.1(d,2H) 7.0(d,2H), 6.9(d,1H), 3.8(s,3H); **^{13}C NMR** (DMSO,125MHz): δ 162.78, 162.13, 159.31, 149.29, 146.72, 130.34, 130.17, 129.85, 128.59, 125.94,

124.98, 120.58, 117.63, 144.82; Melting point 345-350 ^{o}C; Yield 40%; **Mass (m/z)** value for $C_{31}H_{23}N_3O_2$ 469.18, obtained [M-H] 470.19.

4-(4-(Diphenylamino)phenyl)-1,2-dihydro-6-(4-hydroxyphenyl)-2-oxopyridine-3-carbonitrile (C$_6$):

FT-IR (ATR) υ_{max} in cm^{-1}: 2918(Ar-C-H), 2216(C≡N), 1636(C=O), 1588(Ar-C=C); **^{1}H NMR** (DMSO-d$_6$): δ 12.47(s,1H), 10.21(s 1H), 7.7(d,2H), 7.6(d,2H) 7.4(t 4H), 7.1(m 6H), 6.9(d,2H) 6.8(d,2H), 6.6(s,1H); **^{13}C NMR** (DMSO-d$_6$,125 MHz): δ 160.88, 149.86, 146.74, 130.13, 129.94, 125.91, 124.95, 120.64, 116.19; Melting point 335-340 ^{o}C; Yield 50%; Mass (m/z) for $C_{30}H_{21}N_3O_2$ 455.16, obtained [M-H] 455.169.

4-(4-(Diphenylamino)phenyl)-1,2-dihydro-2-oxo-6-(thiophen-2-yl)pyridine-3-carbonitrile (C$_7$):

FT-IR (ATR) υ_{max} in cm^{-1}: 2953 (Ar-C-H), 2213 (C≡N), 1637 (C=O), 1591 (Ar-C=C); **^{1}H NMR** (DMSO-d$_6$): δ 12.50(s,1H), 8.42(m,3H), 8.3(m,3H), 8.2(m,2H) 8.1(d,2H), 7.6(d,2H), 6.7(s,1H), 6.6(d,2H), 5.9(s,2H);**^{13}C NMR**: δ 146.74, 130.36, 130.12, 129.43, 125.92, 124.97; Melting point 350-357 ^{o}C; Yield 30%; **Mass (m/z)** for $C_{28}H_{19}N_3OS$ 445.12, obtained [M-H] 446.07.

3.3.2.2 Synthesis of pyrene-based compounds C$_{8-14}$ (Series-2)

Synthesis of series-2 compounds involves a single step wherein pyrenecarboxaldehyde (***1***) was condensed with different aryl/heteroaryl ketones and ethyl cyanoacetate in presence of a base to form **C$_{8-14}$** in good yield.

General procedure for the Synthesis of C$_{8-14}$:

A mixture of pyrenecarboxaldehyde (***1***, 1.18 mmol), heteroaryl/aryl ketone (1.7 mmol), ammonium acetate (3.59 mmol), and ethyl cyanoacetate (3.61 mmol) was dissolved in 40 mL of dioxane in a two necked round bottom flask. The reaction mixture was heated at 80 ^{o}C for 12 hours and the completion of the reaction was confirmed with the help of the TLC. Once the reaction was completed, the reaction mixture was poured onto the ice-cold water to get the yellow-coloured precipitate. Further, the compound was recrystallized from ethanol. Structures of **C$_{8-14}$** were confirmed by FTIR, ^{1}H NMR, and Mass spectral studies.

2-Oxo-6-phenyl-4-(pyrene-2-yl)-1,2-dihydropyridine-3carbonitrile (C$_8$):

FT-IR (ATR) υ_{max} in cm^{-1}: 2920 (Ar-C-H), 2218(C≡N), 1648(C=O), 1465(Ar-C=C); **^{1}H NMR** (DMSO-d_6,500MHz): δ 13.0(s,1H,CONH), 8.46(m,3H), 8.36(m,3H), 8.29(m,3H), 8.19((m,1H), 8.09(m,2H) 7.5(m,3H), 6.9(m,1H) Melting point 350-357 ^oC, Yield 50%; **Mass(m/z)** value calculated for $C_{28}H_{16}N_2O$ 396.45, obtained [M-H] 397.04.

2-Oxo-4-(pyrene-2-yl)-6-(p-tolyl)-1,2-dihydropyridine-3-carbonitrile (C$_9$):

FT-IR(ATR) υ_{max} in cm^{-1}:2910 (Ar-C-H), 2218(C≡N),1641(C=O) 1514(Ar-C=C); **^{1}H NMR** (DMSO-d_6):δ13.0(s,1H), 8.7(d,4H), 8.6(d,4H), 8.0(m,2H), 7.9(m,1H), 7.8(d,2H), 7.0(s,2H), 6.9(s,1H); Melting point 340-345 ^oC; Yield 40%; **Mass(m/z)** value calculated for $C_{29}H_{18}N_2O$, 410.48, obtained [M-H] 411.06.

6-([1,1^l-Biphenyl]-4-yl)-2-oxo-4-(pyrene-2-yl)-1,2-dihydropyridine-3-carbonitrile (C$_{10}$):

FT-IR (ATR) υ_{max} in cm^{-1}: 2951(Ar-C-H), 2217(C≡N), 1642(C=O), 1522(Ar C=C); **^{1}H NMR** (DMSO-d_6, 500Hz): δ 13.0(s,1H,CONH), 8.5(m,3H), 8.4(m,3H), 8.1(m,2H), 8.0(m,3H), 7.9(m,2H), 7.8(m,2H), 7.5(m,1H), 7.4(m,2H), 7.3(m,1H); Melting point 330-335 ^oC; Yield 40%; **Mass (m/z)** value calculated for $C_{34}H_{20}N_2O$ 472.55, obtained [M-H] 473.

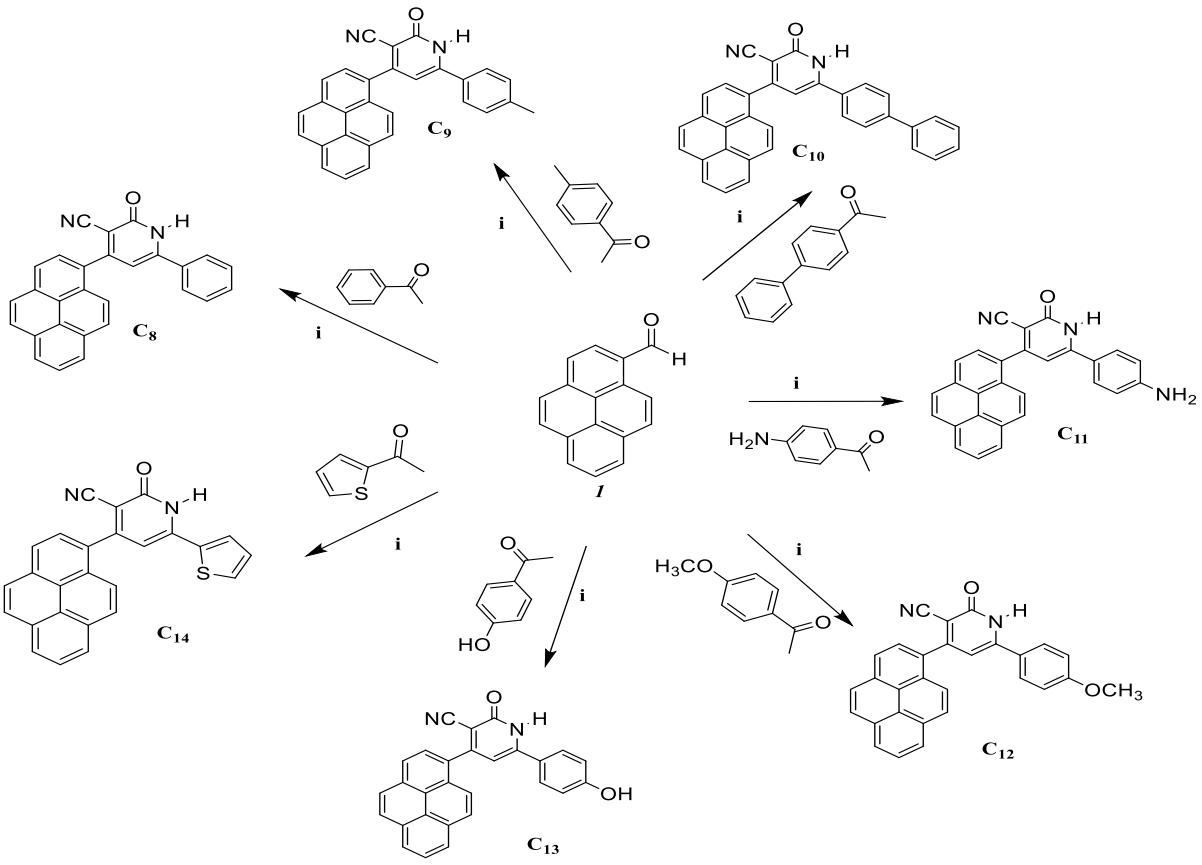

Scheme 3.2. Synthetic routes for **C_{8-14}**: (**i**) pyrenecarboxaldehyde, aryl/heteroaryl ketones, ammonium acetate, ethylcyanoacetate, 80 ^{o}C, 24 hours.

6-(4-Aminophenyl)-2-oxo-4-(pyren-2-yl)-1,2-dihydropyridine-3-carbonitrile (C$_{11}$):

FT-IR (ATR) υ_{max} in cm^{-1}: 2914(Ar C-H), 2218(C≡N), 1592(C=O), 1512(Ar C=C); **^{1}H NMR** (DMSO-d$_6$ 500Hz): δ 12.5(s,1H,CONH), 8.45(m,6H), 8.39(m,3H), 8.29(m,2H), 6.9(s,1H), 6.6(d,2H), 6.0(s,2H); Melting point 345-350 ^{o}C; Yield 30%; **Mass (m/z)** value calculated for $C_{28}H_{17}N_3O$ 411.46, obtained [M-H] 412 .

6-(4-Methoxyphenyl)-2-oxo-4-(pyren-2-yl)-1,2-dihydropyridine-3-carbonitrile (C$_{12}$):

FT-IR (ATR) υ_{max} in cm^{-1}: 2954(Ar C-H), 2211(C≡N), 1639(C=O), 1595(Ar C=C); ^{1}HNMR (DMSOd$_6$ 500Hz):δ12.8(s,1H,CONH),8.46(q,3H), 8.39(m,3H), 8.29(m,2H), 8.17(m,1H), 8.09(d,2H), 7.94(m,2H), 6.94(s,1H), Melting point 345-350 ^{o}C; Yield 40%; **Mass (m/z)** value calculated for $C_{29}H_{18}N_2O_2$ 426.48, obtained [M-H] 427.05.

6-(4-Hydroxyphenyl)-2-oxo-4-(pyren-2-yl)-1,2-dihydropyridine-3-carbonitrile (C$_{13}$):

FT-IR (ATR) υ_{max} in cm^{-1}: 2918(Ar-C-H), 2221(C≡N), 1635(C=O), 1503(Ar-C=C); **^{1}H NMR** (DMSO-d_6 500Hz): δ 12.7(s,1H CONH), 10.26(s,1H), 8.46(d,6H), 8.29(m,3H), 7.83(d,1H), 6.83(d,3H), Melting point 335-340 ^oC; Yield 50%; **Mass (m/z)** value calculated for $C_{28}H_{16}N_2O_2$ 412.45 obtained [M-H] 413.04.

2-Oxo-4-(pyren-2-yl)-6-(thiophen-2-yl)-1,2-dihydropyridine-3-carbonitrile (C$_{14}$):

FT-IR(ATR) υ_{max} in cm^{-1}: 2947(Ar-C-H), 2218(C≡N), 1641(C=O),1595(Ar-C=C); **^{1}H NMR** (DMSO-d_6 500Hz): δ 13.0(s,1H), 8.46(m,4H), 8.37(m,3H), 8.28(m,4H) 7.89(d,1H), 7.27(d,1H), Melting point 350-357 ^oC; Yield 30%; **Mass (m/z)** value calculated for $C_{26}H_{14}N_2OS$ 402.47, obtained [M-H] 403.00.

3.3.2.3 Synthesis of carbazole derivatives C$_{15\text{-}21}$ (Series-3)

In the present series, the adopted synthetic protocol involves alkylation of carbazole to give its *N*-alkylated derivative. Further, it is formulated following Vilsmeier-Haack reaction. Finally, carbazole aldehyde was converted to the target compounds, **C$_{15\text{-}21}$** through multicomponent condensation reaction as outlined in **Scheme 3.3**.

Synthesis of 9-hexyl-9H-carbazole (2):

Carbazole ***1*** (1 g, 5.9 mmol) was dissolved in 10 mL of DMF in an ice-cold condition. To the clear solution, sodium hydride (0.43 g, 17.29 mmol) was added slowly and stirred for about 30 minutes. Subsequently, 1- bromohexane (1.17 g, 7 mmol) was added drop-wise to the reaction mixture. Stirring was continued at room temperature for 12 h. The pale yellow solid separated out was filtered and further purified by means of column chromatography on 60-120 silica gel using hexane as an eluent to get a purified yellow solid.

Synthesis of 9-hexyl-9H-carbazole-3-carbaldehyde (3):

Initially, the Vilsmeier-Haack reagent was prepared. For this, freshly distilled DMF (1.5 mL) was taken in a two-necked round-bottom flask under an argon atmosphere in an ice-cold condition. To this, 1.8 mL of $POCl_3$ was added drop-wise with constant stirring at 0 °C. Then a solution of 9-Hexyl-9*H*-carbazole ***2*** (1 g) in

dichloroethane (10 mL) was added. The reaction mixture was allowed to attain room temperature and was continued stirring for 48 h. After completion of the reaction, the reaction mixture was poured into ice-cold water and neutralized by 5 N sodium hydroxide solution. The crude pale yellow liquid was purified to get a yellow liquid by means of column chromatography (Silica gel of mesh, 200-400) with hexane: ethyl acetate (7:3) as a mobile phase.

General procedure for the synthesis of $C_{15\text{-}21}$:

The 9-Hexyl-9*H*-carbazole-3-carbaldehyde (***3***, 2 g, 1.18 mmol) and aryl/heteroaryl ketone (1.7 mmol) was dissolved in 50 mL of dioxane taken in a two-necked round bottom flask. To the clear solution, ammonium acetate (2.48 g, 3.59 mmol), and ethyl cyanoacetate (0.48 g, 3.61 mmol) were added followed by the reaction mixture was heated for 12 h at 80 ^{o}C. The completion of the reaction was confirmed by TLC. Then, the reaction mixture was subjected to solvent extraction using ethyl acetate (50 mL x 4), and the obtained crude product was purified by column chromatography using hexane and ethyl acetate(1:1) as eluent on Silica gel of mesh 200-400. The purified compounds were spectroscopically analyzed to confirm their structures.

4-(9-Hexyl-9*H*-carbazol-3-yl)-2-oxo-6-phenyl-1, 2-dihydropyridine-3-carbonitrile (C$_{15}$):

FT-IR (ATR) υ_{max} in cm^{-1}: 2932(ArC-H), 2219(C≡N),1633(C=O), 1491(Ar-C=C); **^{1}H NMR** (DMSO-d$_6$,500MHz): δ 12.72(s,1H, CONH), 0.98(s,3H), 1.27(m,6H), 1.78(t,2H), 4.45(t,2H), 6.96(s,1H), 7.25(t,1H), 7.50(m,4H), 7.54((m,1H), 7.67(m,1H), 7.77(m,3H), 8.25(m,1H), 8.64(s,1H), 12.72(s,1H); **^{13}C NMR** (DMSO, 125MHz): δ 175.51, 162.30, 141.07, 131.07, 128.91, 126.43, 122.24, 120.74, 119.43, 109.74; Melting point 165-170 ^{o}C, Yield 50%; **Mass (m/z)** value for $C_{30}H_{27}N_3O$ 445.57, obtained [M-H] 446.22.

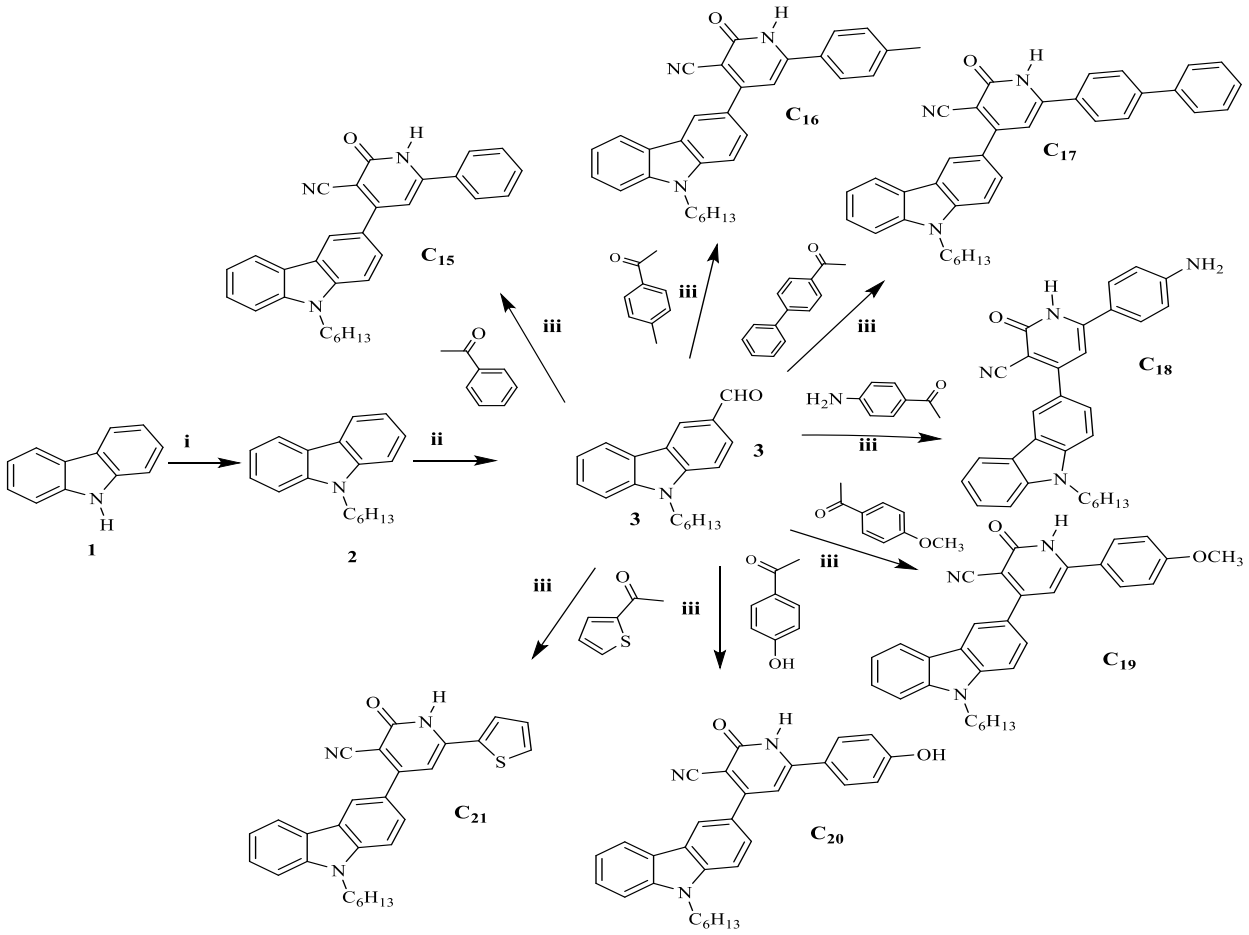

Scheme 3.3. Synthetic routes for **$C_{15\text{-}21}$:** (**i**) 1-Bromohexane, NaH, DMF, RT (**ii**) $POCl_3$,, DMF, RT (**iii**) aryl/heteroaryl ketone, NH_4Ac, and ethyl cyanoacetate 80 ^oC

4-(9-Hexyl-9*H*-carbazol-3-yl)-2-oxo-6-(*p*-tolyl)-1,2-dihydropyridine-3-carbonitrile (**C_{16}**):

FT-IR (ATR) υ_{max} in cm^{-1}: 2927 (Ar-C-H), 2218(C≡N),1632(C=O) 1503(Ar C=C);**^{1}H NMR** (DMSO-d_6 500MHz):δ 0.78(d,3H), 1.16(m,8H), 1.77(t,2H), 1.97(s,3H), 4.43(t,2H), 6.93(s,1H), 7.23(m,1H), 7.34(m,1H), 7.48(m,2H), 5.50(m,1H), 7.65(m,1H), 7.75(m,1H), 7.82(m,3H), 8.25(m,2H) 8.60(s,1H); **^{13}C NMR** δ 141.24, 140.58, 133.70, 129.50, 127.62, 126.37, 125.97, 122.22, 121, 119.40, 117.30; Melting point 210-215 ^oC; Yield 40%; **Mass (m/z)** value for $C_{31}H_{29}N_3O$ 459.59, obtained [M-H] 460.24.

6-([1,1'-Biphenyl]-4-yl)-4-(9-hexyl-9*H*-carbazol-3-yl)-2-oxo-1,2-dihydropyridine-3- carbonitrile (**C_{17}**):

FT-IR (ATR) υ_{max} in cm^{-1}: 2946(Ar-C-H), 2216(C≡N), 1630(C=O), 1482 (Ar-C=C); **^{1}H NMR** (DMSO-d_6, 500Hz): δ 1.31(d,3H),1.79(6H,t),1.83(t,2H), 4.49(d,2H), 7.02(m,1H), 7.26(m,1H), 7.30(m,1H), 7.42(m,3H), 7.50(m,3H) 8.05(m,2H), 8.26(s,1H), 8.66(s,1H), 12.7(s,1H); **^{13}C NMR** (DMSO, 125M Hz): δ 143.03, 141.56, 129.57, 128.70, 127.48, 122.74, 121.55, 110.23; Melting point 245-250 ^{o}C; Yield 40%; **Mass (m/z)** value for $C_{36}H_{25}N_3O$ 521.66, obtained [M-H] 522.14.

6-(4-Aminophenyl)-4-(9-hexyl-9*H*-carbazol-3-yl)-2-oxo-1,2-dihydropyridine-3-carbonitrile (C$_{18}$):

FT-IR (ATR) υ_{max} in cm^{-1}: 2925(Ar-C-H), 2216(C≡N), 1597 (C=O), 1509 (Ar-C=C); **^{1}H NMR** (DMSO-d_6): δ 0.79(t,3H), 1.23(6H.d),178(d,2H), 4.44(d,1H), 5.93(s,1H), 6.77(m,2H), 7.22(m,1H), 7.49(m,1H), 7.76(m,4H), 8.23(t,1H), 8.56(s,1H), 12.22(s,1H); **^{13}C NMR**: δ 163, 160.86, 153.59, 141.40, 129.55, 127.38, 122.66, 121.25, 119.81, 118.35, 113.92, 110.17, 104.11; Melting point 255-260 ^{o}C; Yield 30%; **Mass (m/z)** value for $C_{30}H_{28}N_4O$ 460.58, obtained [M-H] 461.23.

4-(9-Hexyl-9*H*-carbazol-3-yl)-6-(4-methoxyphenyl)-2-oxo-1,2-dihydropyridine-3-carbonitrile (C$_{19}$):

FT-IR (ATR) υ_{max} in cm^{-1}: 2926(Ar-C-H), 2217 (C≡N), 1631(C=O), 1603(Ar-C=C); **^{1}H NMR** (DMSO-d_6): δ 0.79(t,3H), 1.27(t,8H),1.79(s,2H), 3.30(t,3H), 4.45(s,2H), 6.90(m,1H), 7.07(m,2H), 7.24(m,1H), 7.49(m,1H), 7.51(m,1H), 7.65(m,1H), 7.75(m,1H), 7.85(m,2H), 8.24(d,1H), 8.60(s,1H), 12.56(s,1H); **^{13}C NMR** (DMSO,125MHz): δ 162.86, 161.07, 141.51, 129.89, 126.89, 122.71, 121.42, 119.89, 117.92, 114.86, 110.21, 109.88; Melting point 195-200 ^{o}C; Yield 40%; **Mass (m/z)** value for $C_{31}H_{29}N_3O_2$ 475.59, obtained [M-H] 476.22.

4-(9-Hexyl-9*H*-carbazol-3-yl)-6-(4-hydroxyphenyl)-2-oxo-1,2-dihydropyridine-3-carbonitrile (C$_{20}$):

FT-IR (ATR) υ_{max} in cm^{-1}: 2925(Ar-C-H), 2217 (C≡N), 1625(C=O), 1597 (Ar-C=C); **^{1}H NMR** (DMSO-d_6): δ 0.98(s,3H), 1.23(q,3H), 1.29(m,7H), 1.78(t,2H), 445(t,2H), 6.91(m,2H), 7.25(m,1H), 7.50(m,1H), 7.67(m,1H), 7.71(m,3H), 8.25(m,1H), 8.67(m,1H), 10.24(s,1H), 12.50(s,1H); **^{13}C NMR** (DMSO-d_6,125 MHz): δ 162.88, 161.70, 141.48, 130, 127.05, 126.88, 123.24,121.39, 119.87, 118.02,

116.22, 110.20; Melting point 245-250 ^{o}C; Yield 50%; **Mass (m/z)** for $C_{30}H_{27}N_3O_2$ 461.57, obtained [M-H] 462.20.

4-(9-Hexyl-9*H*-carbazol-3-yl)-2-oxo-6-(thiophen-2-yl)-1,2-dihydropyridine-3-carbonitrile(C_{21}):

FT-IR (ATR) υ_{max} in cm^{-1}: 2952(Ar C-H), 2200 (C≡N), 1635 (C=O), 1594 (Ar-C=C); **^{1}H NMR** (DMSO-d_6): δ 0.83(s,3H), 1.23(t,8H), 1.78(d,2H), 4.46((s,2H), 7.25(m,2H), 7.27(m,1H), 7.50(m,1H), 7.66(m,3H), 8.09(m,1H), 8.10(m,1H), 8.25(m,1H), 12.73(s,1H);**^{13}C NMR**: δ 141.45, 131.73, 129.41, 126.91, 122.71, 121.31, 119.88, 117.51, 110.20; Melting point 155-160 ^{o}C; Yield 30%; **Mass (m/z)** for $C_{28}H_{25}N_3OS$ 451.59, obtained [M-H] 452.17.

3.3.2.4 Synthesis of phenothiazine-based cyanopyridones $C_{22\text{-}28}$ (Series-4)

Synthetic roultes for the preparation of **$C_{22\text{-}28}$** are depicted in **Scheme 3.4**. Initially, phenothiazine was alkylated to give N-alkylated derivative, which was subsequently formylated folllowing Vilsmeier-Haack reaction. Finally, phenothiazine aldehyde, when treated with aryl/heteroaryl ketones and ethyl cyanoacetate in presence of a base underwent a smooth cyclization to give target compounds.

Synthesis of 10-hexyl-10H-Phenothiazine (2):

Phenothiazine (***1***, 1g, 5.9 mmol) was dissolved in 10 mL of DMF, taken in a two-necked round bottom flask. To this solution, sodium hydride (0.43 g, 17.29 mmol) was added slowly in an ice-cold condition and stirred for about 30 minutes. Subsequently, bromohexane (1.17 g, 7 mmol) was added in a drop-wise manner to the reaction mixture and the reaction was continued at room temperature for 12 h. Thereafter, the reaction mixture was poured into the crushed ice. The obtained colorless liquid was further purified by means of column chromatography on 60-120 silica gel using hexane as an eluent to get a pure product.

Synthesis of 10-hexyl-10H-phenothiazine-3-carbaldehyde (3):

In the beginning, required Vilsmeier-Haack reagent was prepared. To 1.5 mL of DMF taken in a two-necked round bottom flask, 1.8 mL of $POCl_3$ was added drop-wise in an ice-cold condition with constant stirring. Then, a solution of ***2*** (1 g) in dichloroethane (10 mL) was added. Stirring was continued for 48 h at RT. After the

completion of the reaction, the product was poured into ice-cold water and neutralized by 5 N NaOH solution. The obtained dark colored liquid was further purified by column chromatographic technique (60-120 silica gel, hexane-ethyl acetate).

General procedure for the synthesis of C_{22-28}:

10-Hexyl-10*H*-phenothiazine-3-carbaldehyde (***3***, 2 g**,** 1.18 mmol) and aryl/heteroaryl ketone (1.7 mmol) were dissolved in 40 mL dioxane taken in a two-necked round bottom flask. To the clear solution, ammonium acetate (2.48 g, 3.59 mmol), and ethyl cyanoacetate (0.48 g, 3.61 mmol) were added followed by heating the reaction mixture for 12 h at 80 ^{o}C. The reaction was monitored by TLC to check its completion. When the reaction was over, the content was subjected to solvent extraction using ethyl acetate solvent (50 mL x 3). The obtained product was purified by column chromatography (60-120 silica gel, pet ether-ethyl acetate) technique. Finally, their structures were confirmed using spectral techniques.

4-(10-Hexyl-10*H*-phenothiazin-3-yl)-2-oxo-6-phenyl-1,2-dihydropyridine-3-carbonitrile (**C_{22}**):

FT-IR (ATR) υ_{max} in cm^{-1}: 2931(ArC-H), 2321(C≡N), 1639(C=O), 1463(Ar-C=C); **^{1}H NMR** (DMSO-d_6, 500MHz): δ 12.69(s,1H, CONH), 0.82(t,3H), 1.14(m,4H), 1.24(m,2H), 1.68(m,2H), 3.92(2H,d), 6.82(s,1H), 6.99(t,1H), 7.05(m,1H), 7.20(3H,m), 7.52(m,3H), 7.60(m,1H), 7.92(m,2H), ;**^{13}C NMR** (DMSO,125MHz): δ 147.30, 144.20, 131.60, 130.07, 129.35, 128.62, 127.72, 124.15, 123.54, 117.29, 116.64, 15.87; Melting point 165-170 ^{o}C, Yield 50%; **Mass (m/z)** value for $C_{30}H_{27}N_3OS$ 477.63, obtained [M-H] 477.62.

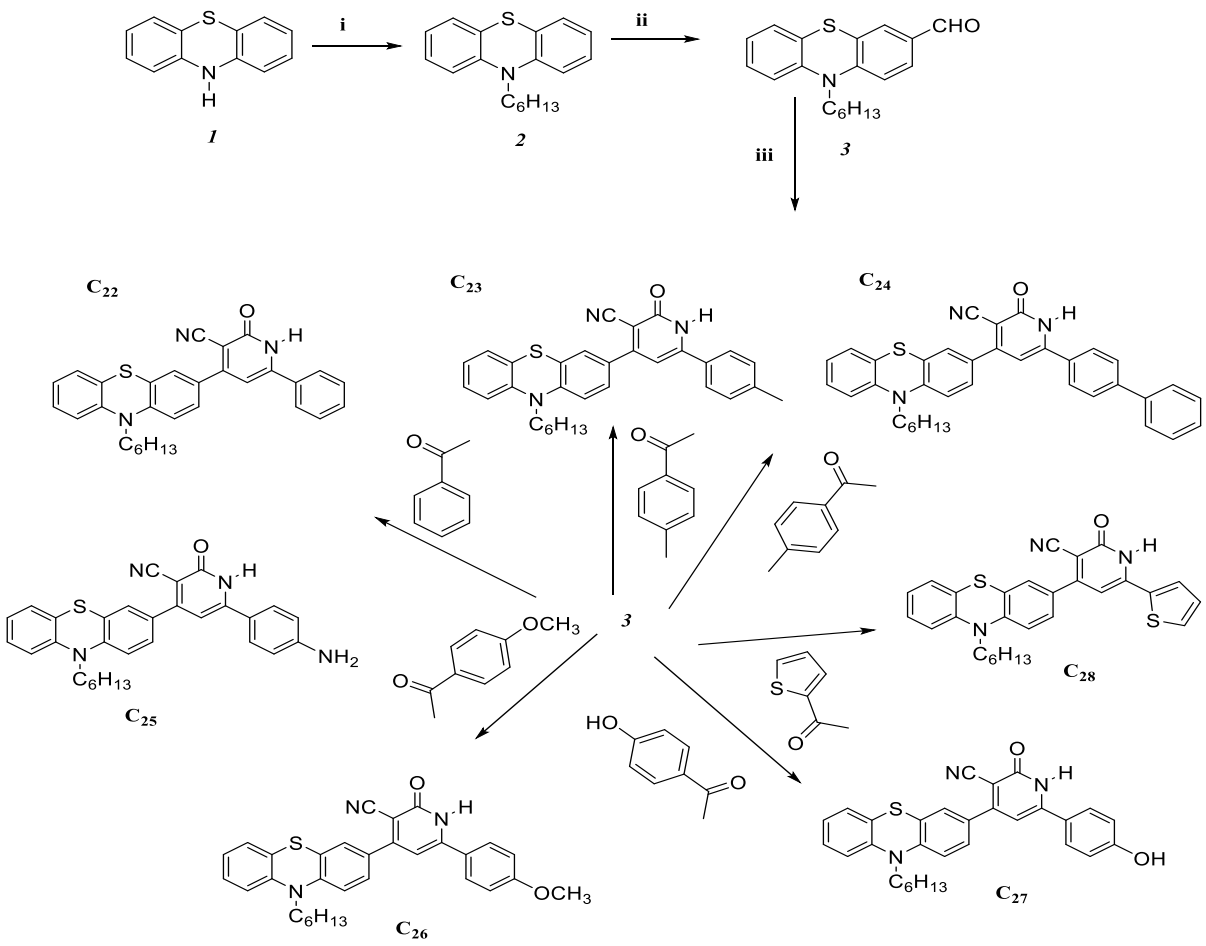

Scheme 3.4. Synthetic routes for **$C_{22\text{-}28}$**: (**i**) 1-Bromohexane, NaH, DMF, RT (**ii**) $POCl_3$, DMF, RT (**iii**) Aryl/heteroaryl ketones, ethyl cyanoacetate, NH_4Ac, 80 ^oC, and 24 h

4-(10-Hexyl-10*H*-phenothiazin-3-yl)-2-oxo-6-(p-tolyl)-1, 2-dihydropyridine-3-carbonitrile (**C_{23}**):

FTIR (ATR) υ_{max} in cm^1: 2929(Ar-CH), 2240(C≡N), 1638(C=O), 1493(ArC=C) ;**^{1}H NMR** ($DMSOd_6$, 500 MHz): δ 0.87(m,3H), 1.18(m,3H), 1.36(m,2H), 1.71(m,H), 2.48(m3H) ,6.79(s,1H), 7.05(m,1H), 7.15(m,1H), 7.20(m,2H), 7.31(m,1H), 7.53(m,1H), 7.79(m,1H), 12.62(m,1H), 3.94(m,2H), 7.24(m,2H), 7.83(m,1H); **^{13}C NMR** δ 147.25, 144.21, 141.79, 130.14, 129.93, 128.58, 127.71, 124.13, 123.52, 117.35, 116.63,115.85; Melting point 210-215 ^oC; Yield 40%; **Mass (m/z)** value for $C_{31}H_{29}N_3OS$ 491.65, obtained [M-H] 491.22.

6-([1,1'-Biphenyl]-4-yl)-4-(10-hexyl-10*H*-phenothiazin-3-yl)-2-oxo-1,2-dihydropyridine-3-carbonitrile (**C_{24}**):

FT-IR(ATR) υ_{max} in cm^{-1}:2928 (Ar-C-H), 2334 (C≡N),1637(C=O),1463 (Ar-C=C); **^{1}HNMR** (DMSO-d_6, 500Hz): δ 0.80(t,,3H), 1.21(4H,m), 132(m,2H), 1.66(m,2H), 3.99(t,1H), 6.97(m,1H), 6.99(m,1H), 7.07(m,1H), 7.14(m,1H), 7.39(m,1H), 7.56(m,1H), 7.64(m,1H), 7.74(m,2H), 7.81(m,1H), 7.84(1H,m) 7.86(m,2H), 8.00(m,2H), 8.02(m,2H), 12.72(s,1H); **^{13}CNMR** (DMSO,125MHz): δ 147.29, 144.20, 143.08, 139.27, 130.08, 129.56, 128.85, 127.72, 124.15, 123.54, 117.32, 116.64, 115.87; Melting point 245-250 ^{o}C; Yield 40%; **Mass (m/z)** value for $C_{36}H_{31}N_3OS$ 553.72, obtained [M-H] 553.60.

6-(4-Aminophenyl)-4-(10-hexyl-10*H*-phenothiazin-3-yl)-2-oxo-1,2-dihydropyridine-3-carbonitrile (**C_{25}**):

FT-IR (ATR) υ_{max} in cm^{-1}: 2870 (Ar-C-H), 2352 (C≡N), 1653 (C=O), 1596 (Ar-C=C); **^{1}H NMR** (DMSO-d_6): δ 0.80(m,6H), 1.21(6H.m), 1.67(m,2H), 1.71(t,2H), 3.93(t,2H), 5.93(s,1H), 6.62(m,2H), 7.04(m,1H), 7.11(m,1H), 7.20(m,3H), 7.38(m,1H), 7.47(m,1H), 7.20(m,3H), 7.38(m,3H), 7.47(m,1H), 7.54(m,1H), 7.55(m,1H), 7.67(2H,m), 12.21(s,1H); **^{13}C NMR** (DMSO,125MHz)**:** δ 163, 160.86, 153.59, 141.40, 129.55, 127.38, 122.66, 121.25, 119.81, 118.35, 113.92, 110.17, 104.11; Melting point 255-260 ^{o}C; Yield 30%; Mass (m/z) value for $C_{30}H_{28}N_4OS$ 492.64, obtained [M-H] 492.23.

4-(10-Hexyl-10H-phenothiazin-3-yl)-6-(4-methoxyphenyl)-2-oxo-1,2-dihydropyridine-3-carbonitrile (**C_{26}**):

FT-IR (ATR) υ_{max} in cm^{-1}: 2858 (Ar C-H), 2268 (C≡N), 1625(C=O), 1459(Ar-C=C); **^{1}H NMR** ($DMSOd_6$) 0.822(q,3H), 1.21(t,4H), 1.30(m,2H), 1.54(m,2H), 3.82(s,3H), 3.92(m,2H), 6.94(s,1H), 7.13(m,3H), 7.20(m,2H), 7.27(m,1H), 7.52(m,1H), 7.60(m,1H), 7.93(m,2H), 12.52(s,1H), 7.07(m,2H), 7.24(m,1H), 7.49(m,1H), 7.51(m,1H), 7.65(m,1H), 7.75(m,1H), 7.85(m,2H), 8.24(d,1H), 8.60(s,1H), 12.56(s,1H); **^{13}C NMR** (DMSO,125MHz): δ 162.86, 161.07, 141.51, 129.89, 126.97, 126.44, 122.71, 121.42, 119.89, 117.92, 114.84, 110.21,

105.96; Melting point 195-200 ^{o}C; Yield 40**%; Mass (m/z)** value for $C_{31}H_{29}N_3O_2S$ 507.65, obtained [M-H] 506.22.

4-(10-Hexyl-10*H*-phenothiazin-3-yl)-6-(4-hydroxyphenyl)-2-oxo-1,2-dihydropyridine-3-carbonitrile (**C_{27}**):

FT-IR (ATR) υ_{max} in cm^{-1}: 2856(ArC-H), 2231 (C≡N), 1632 (C=O), 1513 (Ar-C=C); **^{1}H NMR** ($DMSOd_6$): δ 0.82(s,3H), 1.25(s,4H), 1.39(s,2H), 1.69(s,2H), 3.92(s,2H), 6.71(s,1H), 6.83(d,2H), 6.99(1H,t), 7.06(1H,m), 6.83(d,2H), 6.99(t,1H), 7.06(1H,m), 7.17(m,3H), 7.51(m,1H), 7.57(1H,t), 7.78(2H,m), 7.51(m,1H), 7.57(t,1H), 7.78(2H,d), 10.19(s,1H), 12.47(1H,s); **^{13}C NMR** ($DMSOd_6$,125MHz): δ 62.69, 160.95, 158.68, 147.17, 144.23, 130.32, 128.51, 127.70, 124.11, 123.50, 117.56, 116.60, 115.82; Melting point 245-250 ^{o}C; Yield 50%; **Mass (m/z)** for $C_{30}H_{27}N_3O_2S$ 493.63 obtained [M-H] 493.20.

4-(10-Hexyl-10*H*-phenothiazin-3-yl)-6-(4-hydroxyphenyl)-2-oxo-1,2-dihydropyridine-3-carbonitrile (**C_{28}**):

FT-IR (ATR) υ_{max} in cm^{-1}: 2853(Ar-C-H), 2328(C≡N), 1638(C=O), 1467(Ar-C=C); **^{1}H NMR** ($DMSOd_6$): δ 0.84(m,3H), 1.20(m,5H), 1.22(m,2H), 1.23(m,2H), 3.92(2H,t), 6.99(1H,m), 7.05(m,1H), 7.14(2H,m), 7.48(2H,m), 7.54(m,1H), 7.57(m,1H), 7.48(m,2H), 7.54(m,1H), 7.57(m,1H), 7.85(m,1H), 8.05(m,1H), 12.68(s,1H); **^{13}C NMR** (DMSO,125MHz): δ 147.14, 144.27, 131.82, 130.01, 129.39, 128.51, 127.73, 124.18, 123.52, 117.07, 116.64, 15.95; Melting point 155-160 ^{o}C; Yield 30%; **Mass (m/z)** for $C_{28}H_{25}N_3OS_2$ 483.65 obtained [M-H] 482.17.

3.3.2.5. Synthesis of DPA-linked cyanopyridones $C_{29\text{-}34}$ (Series-5)

Scheme 3.5 depicts the synthetic routes followed for **$C_{29\text{-}34}$**. Here, the target compounds were obtained in three steps. The first step involves N-alkylation of DPA, the second step comprises the formylation of N-alkylated DPA using Vilsmeier-Haack reaction, and the final step consists of cyclocondensation of N-alkylated DPA with aryl/heteroaryl ketones to obtain final target products.

Synthesis of N-hexyl-N-phenylaniline (2):

Diphenylamine (***1***, 1 g, 5.9 mmol) was dissolved in 20 mL of DMF taken in a two-necked round bottom flask. To this, sodium hydride (0.5 g, 2 mmol) was added

slowly maintaining the temperature at 0 ^{o}C. Then, 1-bromohexane (1.47 g, 7.09 mmol) was added drop-wise to the flask, and the reaction was carried out at RT for 48 h. When the reaction was over, the content was neutralized with 2 N HCl. The product was isolated using solvent extraction technique. For this, DCM (50 mL x 3) was used. Finally, the isolated compound was further purified by column chromatography using silica gel of mesh 60-120 and hexane as an eluent.

Synthesis of 4-(hexyl (phenyl) amino benzaldehyde (3):

Initially, the Vilsmeir-Haack reagent was prepared by adding $POCl_3$ (1.1 mL, 12 mmol) drop-wise to the DMF (0.92 mL, 12 mmol) taken in a two-necked round bottom flask. To this reagent, *N*-alkylated DPA (1.0 g, 3.95 mmol) dissolved in dichloroethane (5 mL) was added while stirring and stirring was continued for 48 h at room temperature. The reaction was monitored by the TLC to avoid the di-formylation. Further, the reaction mixture was neutralized with 5 N NaOH maintaining ice-cold condition. The product was isolated following solvent extraction technique, for which 50 mL x 3 DCM was used. Finally, the obtained yellow product was further purified using column chromatography. For this purpose, silica gel of mesh 60-120 and pet ether/ethyl acetate were used.

General procedure for the synthesis of $C_{29\text{-}34}$:

A mixture of formylated DPA (***3,*** 2 g**,** 1.18 mmol), aryl/heteroaryl ketone (1.7 mmol), ammonium acetate (3.59 mmol), and 40 mL dioxane was taken in a two-necked round bottom flask. It is stirred to get a clear solution. Subsequently, ethyl cyanoacetate (0.48 g, 3.61 mmol) was added to this solution. The reaction mixture was refluxed at 80 ^{o}C for 24 h and was monitored by TLC to obtain a fluorescent polar spot. When the reaction was completed, the product was extracted with ethyl acetate (50 mL x 3) and the combined extract was distilled under reduced pressure to get yellow liquid. This was further purified using column chromatography with hexane/ethyl acetae as an eluent on silica gel of mesh 100-200. The structures of **$C_{29\text{-}34}$** were confirmed by FTIR, NMR and Mass spectral techniques.

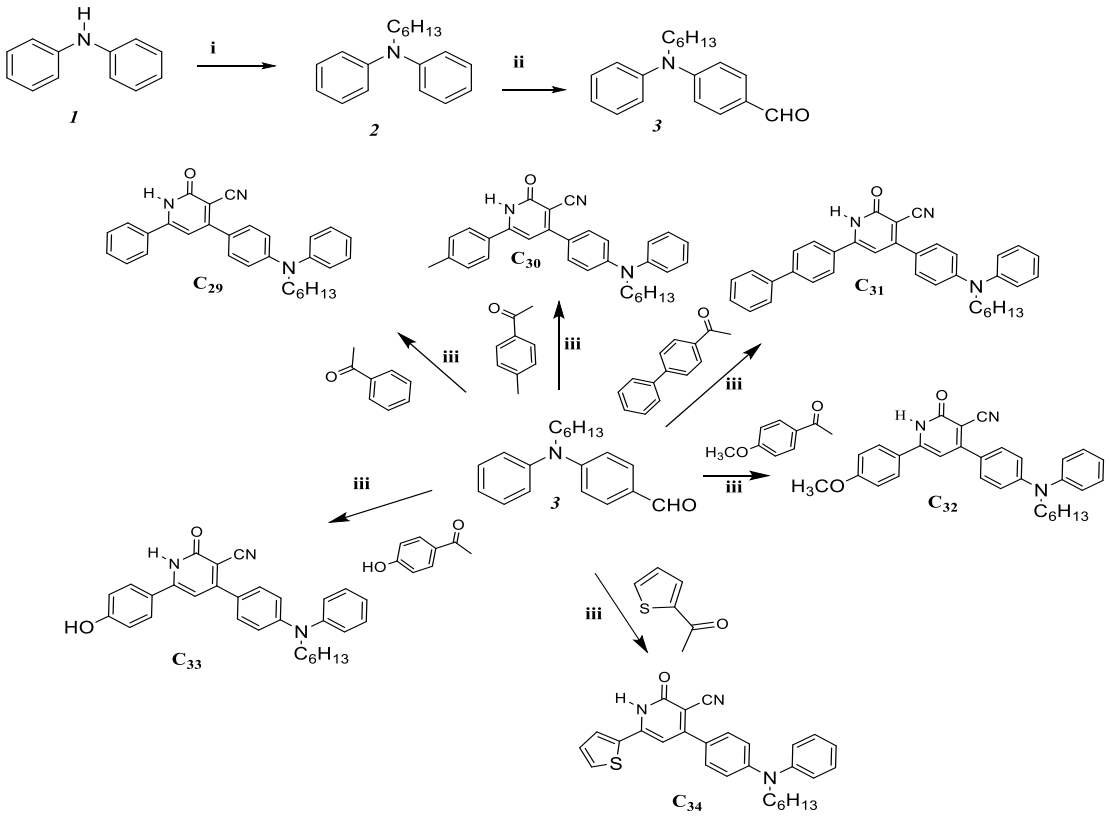

Scheme 3.5. Synthetic routes for **$C_{29\text{-}34}$:** (**i**) 1-Bromohexane, NaH, DMF, RT (**ii**) $POCl_3$, DMF, RT (**iii**) Ary/heteroaryl ketones, ammonium acetate, Ethyl acetate, 80 ^oC and 24 h

4-(4-(Hexyl(phenyl)amino)phenyl)-2-oxo-6-phenyl-1,2-dihydropyridine-3-carbonitrile (**C_{29}**):

FT-IR (ATR) υ_{max} in cm^{-1}: 2932(Ar-C-H), 2219(C≡N),1633(C=O), 1491(Ar-C=C); **^{1}H NMR** (DMSO-d_6, 500MHz): δ 12.72(s,1H, CONH), 0.98(s,3H), 1.27(m,6H), 1.78(t,2H), 4.45(t,2H), 6.96(s,1H), 7.25(t,1H), 7.50(m,4H), 7.54((m,1H), 7.67(m,1H), 7.77(m,3H), 8.25(m,1H), 8.64(s,1H) 12.72(s,1H); **^{13}C NMR** (DMSO, 125MHz): δ 175.51, 162.30, 141.07, 131.07, 128.91, 126.43, 122.24, 120.74, 119.43, 109.74; Melting point 165-170 ^oC, Yield 50%; **Mass (m/z)** value for $C_{30}H_{27}N_3O$ 445.57, obtained [M-H] 446.22.

4-(4-(Hexyl(phenyl)amino)phenyl)-2-oxo-6-(p-tolyl)-1,2-dihydropyridine-3-carbonitrile (**C_{30}**):

FT-IR (ATR) υ_{max} in cm^{-1}: 2927 (Ar-C-H), 2218(C≡N),1632(C=O) 1503 (Ar-C=C); **^{1}H NMR** (DMSO-d_6, 500MHz): δ 0.78(d,3H), 1.16(m,8H), 1.77(t,2H),

1.97(s,3H), 4.43(t,2H), 6.93(s,1H), 7.23(m,1H), 7.34(m,1H), 7.48(m,2H), 5.50(m,1H), 7.65(m,1H), 7.75(m,1H), 7.82(m,3H), 8.25(m,2H) 8.60(s,1H); **^{13}C NMR** δ 141.24, 140.58, 133.70, 129.50, 127.62, 126.37, 125.97, 122.22, 121, 119.40, 117.30; Melting point 210-215 ^{o}C; Yield 40%; **Mass (m/z)** value for $C_{31}H_{29}N_3O$ 459.59, obtained [M-H] 460.24.

6-([1,1'-Biphenyl]-4-yl)-4-(4-(hexyl(phenyl)amino)phenyl)-2-oxo-1,2-dihydropyridine-3-carbonitrile (**C_{31}**):

FT-IR (ATR) υ_{max} in cm^{-1}: 2946(Ar-C-H), 2216 (C≡N), 1630 (C=O), 1482 (Ar-C=C); **^{1}H NMR** (DMSO-d_6, 500Hz): δ 1.31(d,3H), 1.79(6H,t), 1.83(t,2H), 4.49(d,2H), 7.02(m,1H), 7.26(m,1H), 7.30(m,1H), 7.42(m,3H), 7.50(m,3H) 8.05(m,2H), 8.26(s,1H), 8.66(s,1H), 12.7(s,1H); **^{13}C NMR** (DMSO, 125M Hz): δ 143.03, 141.56, 129.57, 128.70, 127.48, 122.74, 121.55, 110.23; Melting point 245-250 ^{o}C; Yield 40%; **Mass (m/z)** value for $C_{36}H_{25}N_3O$ 521.66, obtained [M-H] 522.14.

4-(4-(Hexyl(phenyl)amino)phenyl)-6-(4-methoxyphenyl)-2-oxo-1,2-dihydropyridine-3-carbonitrile (**C_{32}**):

FT-IR (ATR) υ_{max} in cm^{-1}: 2925(Ar-C-H), 2216 (C≡N), 1597 (C=O), 1509 (Ar-C=C); **^{1}H NMR** (DMSO-d_6 500MHz): δ 0.79(t,3H), 1.23(6H.d),178(d,2H), 4.44(d,1H), 5.93(s,1H), 6.77(m,2H), 7.22(m,1H), 7.49(m,1H), 7.76(m,4H), 8.23(t,1H), 8.56(s,1H), 12.22(s,1H**)**; **^{13}C NMR** (DMSO,125MHz): δ 163, 160.86, 153.59, 141.40, 129.55, 127.38, 122.66, 121.25, 119.81, 118.35, 113.92, 110.17, 104.11; Melting point 255-260 ^{o}C; Yield 30%; **Mass (m/z)** value for $C_{30}H_{28}N_4O$ 460.58, obtained [M-H] 461.23.

4-(4-(Hexyl(phenyl)amino)phenyl)-6-(4-hydroxyphenyl)-2-oxo-1,2-dihydropyridine-3-carbonitrile (**C_{33}**):

FT-IR (ATR) υ_{max} in cm^{-1}: 2926(Ar C-H), 2217 (C≡N), 1631(C=O), 1603(Ar-C=C); **^{1}H NMR** (DMSO-d_6 500MHz): δ 0.79(t,3H), 1.27(t,8H),1.79(s,2H), 3.30(t,3H), 4.45(s,2H), 6.90(m,1H), 7.07(m,2H), 7.24(m,1H), 7.49(m,1H), 7.51(m,1H), 7.65(m,1H), 7.75(m,1H), 7.85(m,2H), 8.24(d,1H), 8.60(s,1H), 12.56(s,1H); **^{13}C NMR** (DMSO,125MHz): δ 162.86, 161.07, 141.51, 129.89, 126.89,

122.71, 121.42, 119.89, 117.92, 114.86, 110.21, 109.88; Melting point 195-200 ^{o}C; Yield 40%; **Mass (m/z)** value for $C_{31}H_{29}N_3O_2$ 475.59, obtained [M-H] 476.22.

4-(4-(Hexyl(phenyl)amino)phenyl)-2-oxo-6-(thiophen-2-yl)-1,2-dihydropyridine-3-carbonitrile (**C_{34}**):

FT-IR (ATR) υ_{max} in cm^{-1}: 2925(Ar-C-H), 2217 (C≡N), 1625 (C=O), 1597 (Ar-C=C); **^{1}H NMR** (DMSO-d_6, 500MHz): δ 0.98(s,3H), 1.23(q,3H), 1.29(m,7H), 1.78(t,2H), 445(t,2H), 6.91(m,2H), 7.25(m,1H), 7.50(m,1H), 7.67(m,1H), 7.71(m,3H), 8.25(m,1H), 8.67(m,1H), 10.24(s,1H), 12.50(s,1H); **^{13}C NMR** (DMSO-d_6,125 MHz): δ 162.88,161.70, 141.48, 130, 127.05, 126.88, 123.24,121.39, 119.87, 118.02, 116.22, 110.20; Melting point 245-250 ^{o}C; Yield 50%; **Mass (m/z)** for $C_{30}H_{27}N_3O_2$ 461.57, obtained [M-H] 462.20.

3.3.2.6 Synthesis of *N*,*N*-dimethylaniline-based cyanopyridones $C_{35\text{-}37}$ (Series-6)

N,*N*-Dimethylaniline-based cyanopyridones, **$C_{35\text{-}37}$** were synthesized in one step. Herein, 4-(*N*,*N*-dimethylaminophenyl)ethan-1-one was condensed with different aryl aldehydes and ethyl cyanoacetate in presence of ammonium acetate to form the target compounds. **Scheme 3.6** summarizes the synthetic pathways.

General procedure for the Synthesis of $C_{35\text{-}37}$:

A mixture of 4-(*N*,*N*-dimethylaminophenyl)ethan-1-one (***1***, 2 g, 1.7 mmol), different aromatic aldehyde (1.18 mmol), ammonium acetate (2.48 g, 3.59 mmol), and ethyl cyanoacetate (0.48 g, 3.61 mmol) was dissolved in 40 mL of dioxane in a two necked round bottom flask. The reaction mixture was heated at 80 ^{o}C for 12 h and the completion of the reaction was confirmed with the help of TLC. Once the reaction was completed, the reaction mixture was plunged onto the ice-cold water to get a yellow-coloured precipitate. Further, the compound was recrystallized from ethanol. Molecular structures of **$C_{35\text{-}37}$** were confirmed by FTIR, ^{1}H NMR, and Mass spectral studies.

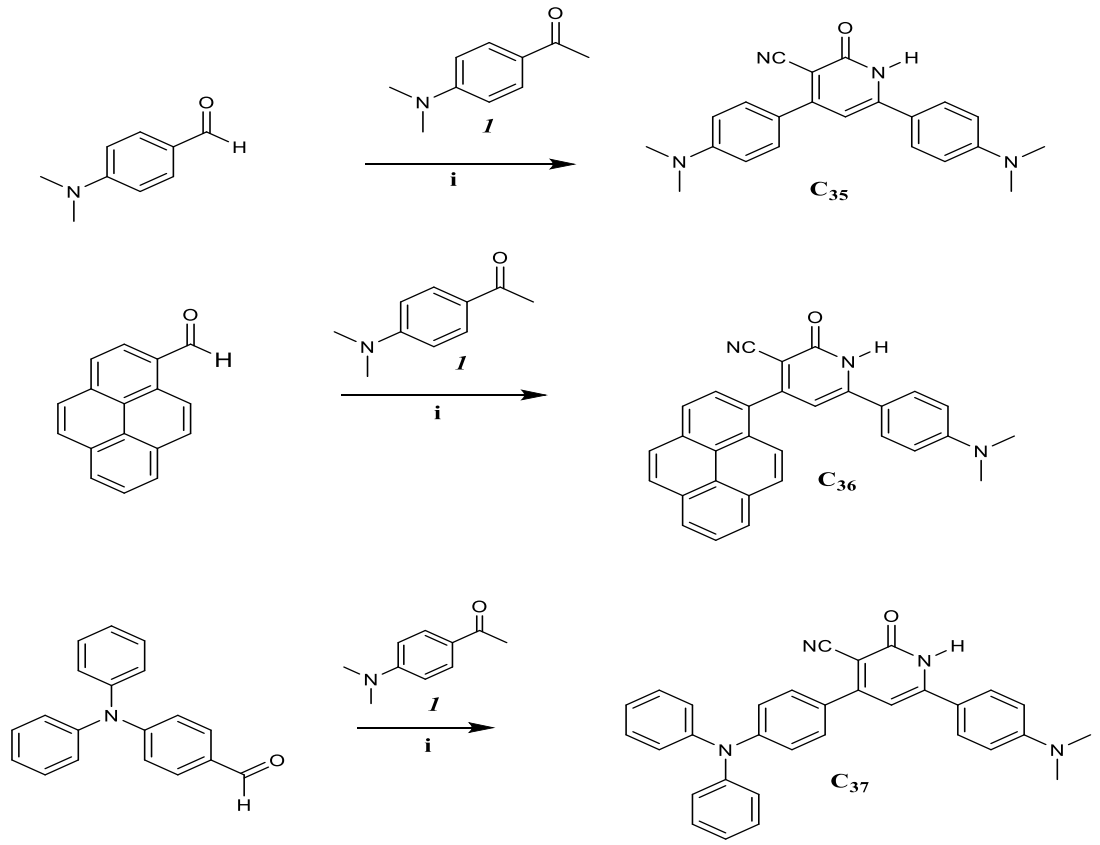

Scheme 3.6. Synthetic routes for **C_{35-37}**: (**i**) 4-(*N*,*N*-dimethylaminophenyl)ethan-1-one, ammonium acetate, ethyl cyanoacetate, 80 ^{o}C, 24 h

4,6-Bis(4-(dimethylamino)phenyl)-2-oxo-1,2-dihydropyridine-3-carbonitrile (C$_{35}$):

FT-IR (ATR) υ_{max} in cm^{-1}: 2932(ArC-H), 2219(C≡N),1633(C=O), 1491(Ar-C=C); **^{1}H NMR** (DMSO-d$_6$, 500MHz): δ 12.72(s,1H, CONH), 0.98(s,3H), 1.27(m,6H), 1.78(t,2H), 4.45(t,2H), 6.96(s,1H), 7.25(t,1H), 7.50(m,4H), 7.54((m,1H), 7.67(m,1H), 7.77(m,3H), 8.25(m,1H), 8.64(s,1H) 12.72(s,1H); Melting point 165-170 ^{o}C, Yield 50%; **Mass (m/z)** value for $C_{30}H_{27}N_3O$ 445.57, obtained [M-H] 446.22.

6-(4-(Dimethylamino)phenyl)-2-oxo-4-(pyren-1-yl)-1,2-dihydropyridine-3-carbonitrile (C$_{36}$):

FT-IR (ATR) υ_{max} in cm^{-1}: 2927 (Ar-C-H), 2218(C≡N),1632(C=O) 1503 (Ar C=C); **^{1}H NMR** (DMSO-d$_6$ 500 MHz): δ 0.78(d,3H), 1.16(m,8H), 1.77(t,2H), 1.97(s,3H), 4.43(t,2H), 6.93(s,1H), 7.23(m,1H), 7.34(m,1H), 7.48(m,2H), 5.50(m,1H), 7.65(m,1H), 7.75(m,1H), 7.82(m,3H), 8.25(m,2H) 8.60(s,1H); Melting

point 210-215 ^{o}C; Yield 40%; **Mass (m/z)** value for $C_{31}H_{29}N_3O$ 459.59, obtained [M-H] 460.24.

6-(4-(Dimethylamino)phenyl)-4-(4-(diphenylamino)phenyl)-2-oxo-1,2-dihydropyridine-3-carbonitrile (**C_{37}**):

FT-IR (ATR) υ_{max} in cm^{-1}: 2946 (Ar-C-H), 2216 (C≡N), 1630(C=O), 1482(Ar-C=C); **^{1}H NMR** (DMSO-d_6, 500Hz): δ 1.31(d,3H), 1.79(6H,t), 1.83(t,2H), 4.49(d,2H), 7.02(m,1H), 7.26(m,1H), 7.30(m,1H), 7.42(m,3H), 7.50(m,3H) 8.05(m,2H), 8.26(s,1H), 8.66(s,1H), 12.7(s,1H); Melting point 245-250 ^{o}C; Yield 40%; **Mass (m/z)** value for $C_{36}H_{25}N_3O$ 521.66, obtained [M-H] 522.14.

3.3.2.7 Synthesis of substituted nicotinonitriles C_{38-42} (Series-7)

The target compounds, *viz*. 2-(benzyloxy)-4-(4-(dimethylamino)phenyl)-6-substituted nicotinonitriles, **C_{38-42}** were synthesized by reacting benzyl bromide with substituted cyanopyridones (***2a-e***) using K_2CO_3 as a catalyst. The required intermediates, *i.e*. substituted cyanopyridones (***2a-e***) were obtained by condensing 4-(dimethylamino)benzaldehyde (***1***), aryl/heteroaryl ketones, and ethyl cyanoacetate in presence of ammonium acetate at 80 ^{o}C. **Scheme 3.7** gives their synthetic protocol.

General procedure for the synthesis of substituted cyanopyridones 2a-e:

A mixture of 4-(dimethylamino)benzaldehyde, (***1***,2g,1.7 mmol), aryl/heteroaryl ketones (1.18 mmol), ethyl cyanoacetate (0.48 g, 3.61 mmol), and ammonium aceate (2.48 g, 3.59 mmol) was dissolved 30 mL of dioxane. The mixture was heated at 80 ^{o}C for 24 h. After completion of the reaction, the content was plunged into ice cold water and the precipitated yellow solid was filtered. The compound was recrystallized from ethanol. Their spectral data matched with reported values.

General procedure for the synthesis of C_{38-42}:

A mixture of substituted cyanopyridone (***2a-e***, 5.6 mmol) and benzyl bromide (1 g, 1.2 mmol) was dissolved in 30 mL of DMF, taken in a two necked round bottom flask. To this, potassium carbonate (0.5 g, 1.18 mmol) was mixed. The reaction mixture was heated to 60 ^{o}C with stirring overnight. The obtained product was extracted with ethyl aceatate (50 mL x 3) and the extract was distilled under reduced

pressure to obtain the corresponding O-alkylated product. Finally, the further purification of the target compound was done by column chromatography on silica of mesh 100-200 using hexane: ethyl acetate as an eluent. Structures were confirmed by FTIR, ^{1}H NMR, and Mass spectral studies.

2-(Benzyloxy)-4-(4-(dimethylamino)phenyl)-6-phenylnicotinonitrile (C$_{38}$):

FT-IR (ATR) υ_{max} in cm^{-1}: 2200 (C≡N),1586 (Ar-C=C); **^{1}H NMR** (DMSO-d_6, 500MHz): δ 3.01(s,6H), 5.63(s,2H), 6.87(s,2H), 7.33(d,1H), 7.41(m,2H), 7.54(m,5H), 7.68(m,2H), 7.70((m,2H), 8.25(m,2H); Melting point 170 ^{o}C, Yield 55%; **Mass (m/z)** value for $C_{27}H_{23}N_3O$ 405.50, obtained [M-H] 406.

2-(Benzyloxy)-4-(4-(dimethylamino)phenyl)-6-(*p*-tolyl)nicotinonitrile (C$_{39}$):

FT-IR (ATR) υ_{max} in cm^{-1}: 2923 (Ar-C-H), 2218 (C≡N),1583 (Ar C=C); **^{1}H NMR** (DMSO-d_6 500MHz): δ 3.01(s,6H), 5.64 (s,2H), 6.87 (s,2H), 2.50(s,3H), 7.33(m,4H), 7.40(m,2H), 7.56(m,2H), 7.66(m,3H), 8.13(d,2H); Melting point 210-215 ^{o}C; Yield 40%; **Mass (m/z)** value for $C_{28}H_{25}N_3O$ 419.20, obtained [M-H] 420.

6-([1,1'-Biphenyl]-4-yl)-2-(benzyloxy)-4-(4(dimethylamino)phenyl)nicotinonitrile (C$_{40}$):

FT-IR (ATR) υ_{max} in cm^{-1}: 2857 (Ar-C-H), 2219 (C≡N),1527 (Ar-C=C); **^{1}H NMR** (DMSO-d_6, 500MHz): δ 3.31(s,3H), 5.68(1H,s), 1.83(t,2H), 6.88(s,1H), 7.34(m,2H), 7.40(m,2H), 7.70(t,1H), 7.78(m,2H), 8.36(d,1H); Melting point 245-250 ^{o}C; Yield 40%; **Mass (m/z)** value for $C_{33}H_{27}N_3O$ 412, obtained [M-H] 413.

2-(Benzyloxy)-4-(4-(dimethylamino)phenyl)-6-(4-methoxyphenyl)nicotinonitrile (C$_{41}$):

FT-IR (ATR) υ_{max} in cm^{-1}: 2923 (Ar-C-H), 2212 (C≡N),1527 (Ar-C=C); **^{1}H NMR** (DMSO-d_6, 500MHz): δ 3.03(s,6H), 3.84(3H,s), 5.64(s,2H), 6.87(s,2H), 7.09(s,2H), 7.32(m,2H), 7.40(m,1H), 7.54(m,2H), 7.56(m,2H), 7.68(m,3H), 8.20(m,2H); Melting point 245-250 ^{o}C; Yield 40%; **Mass (m/z)** value for $C_{28}H_{25}N_3O_2$ 435.53, obtained [M-H] 436.

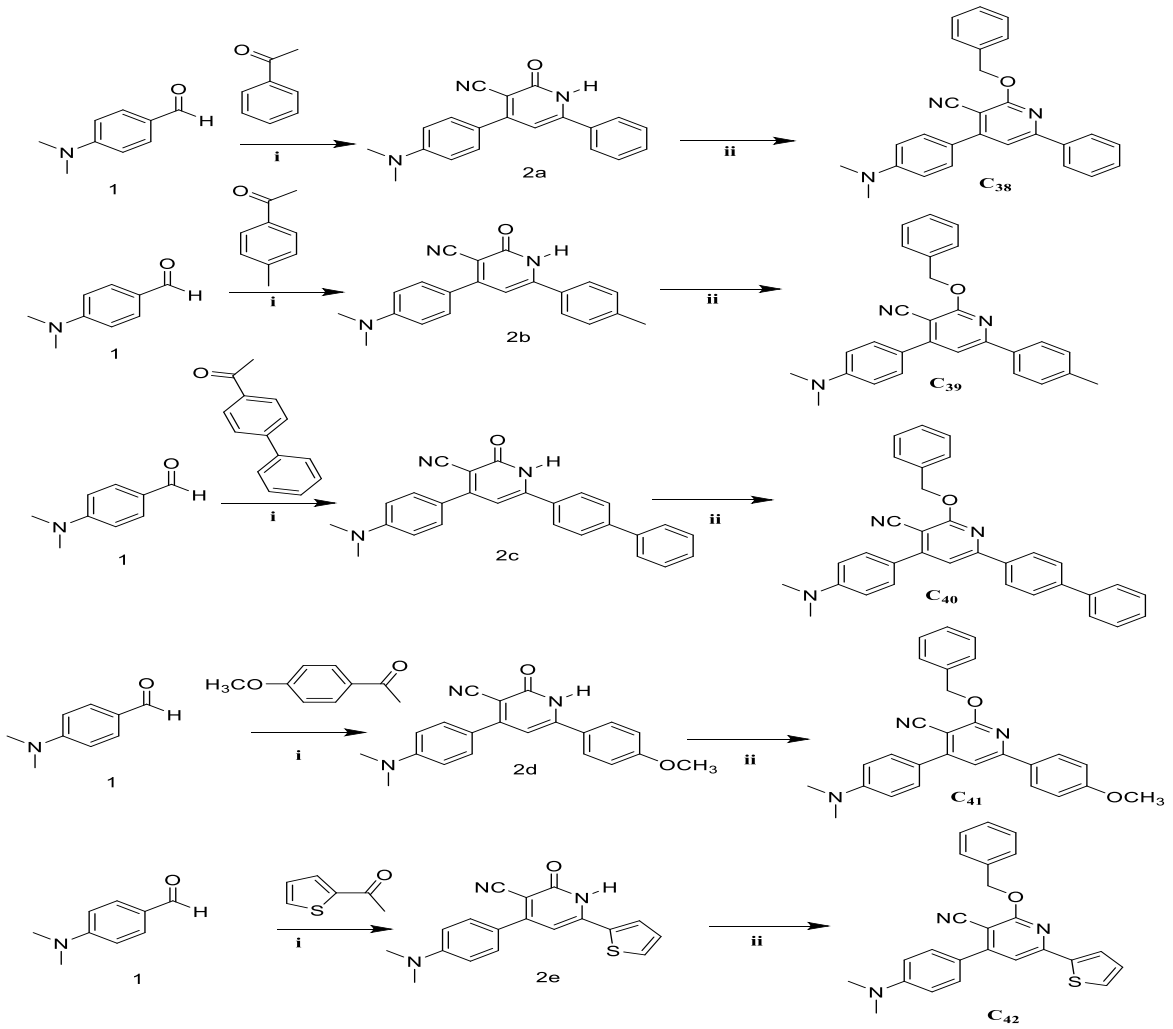

Scheme 3.7. Synthetic routes for **C_{38-42}**: (**i**) Aryl/heteroaryl ketones, ammonium acetate, Ethyl cyanoacetate, 80 ^{o}C and 24 h (**ii**) Benzyl bromide, K_2CO_3, DMF, 60 ^{o}C, overnight

2-(Benzyloxy)-4-(4-(dimethylamino)phenyl)-6-(thiophen-2-yl)nicotinonitrile (C$_{42}$):

FT-IR (ATR) υ_{max} in cm^{-1}: 2922 (Ar-C-H), 2218 (C≡N),1583(Ar-C=C); ^{1}H NMR (DMSO-d_6, 500MHz): δ 3.33(s,3H), 5.58(2H,s), 7.23(s,1H), 7.35(sm1H), 7.41(m,1H), 7.57(m,1H), 7.62(m,1H), 7.70(m,1H), 7.81(m,1H), 8.07(d,1H); Melting point 245-250 ^{o}C; Yield 40%; **Mass (m/z)** value for $C_{25}H_{21}N_3OS$ 412, obtained [M-H] 411.52.

3.3.3 Results and discussion

All the designed molecules were synthesized following standard synthetic protocols. The reaction parameters such as temperature, solvent, reaction rate, the concentration of reactants and catalyst were optimized in order to get a good yield. Their structures were confirmed by spectral techniques. In the following section, the structural characterization of few selected representative molecules has been discussed.

3.3.3.1 Compounds $C_{1\text{-}7}$ (Series-1)

Figure 3.8. displays the **FTIR** spectrum of representative compound $\mathbf{C_1}$ which shows sharp bands at 2218 and 1634 cm^{-1} due to stretching vibrations of cyano and carbonyl functionalities, respectively, indicating the formation of cyanopyridone ring. Further its **^{1}H-NMR** spectrum (**Figure 3.9**.) depicts highly down fielded a broad singlet at δ 12.95 ppm accounting for the NH of lactam ring; the appearance of subsequent aromatic signals elucidate the structure.

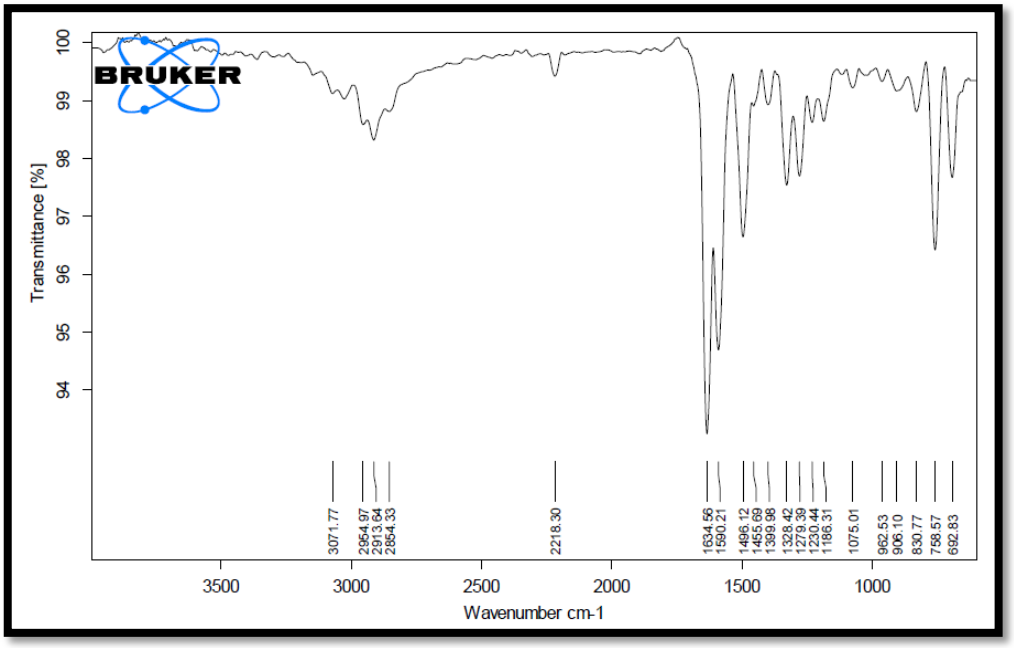

Figure 3.8. FTIR spectrum of $\mathbf{C_1}$

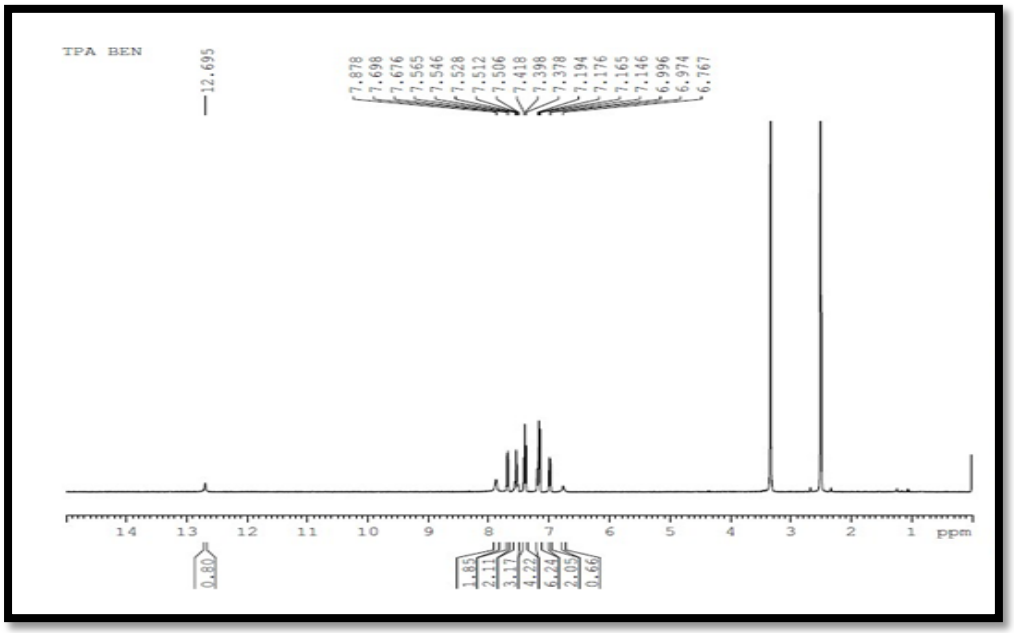

Figure 3.9. ^{1}H NMR spectrum of **C_1**

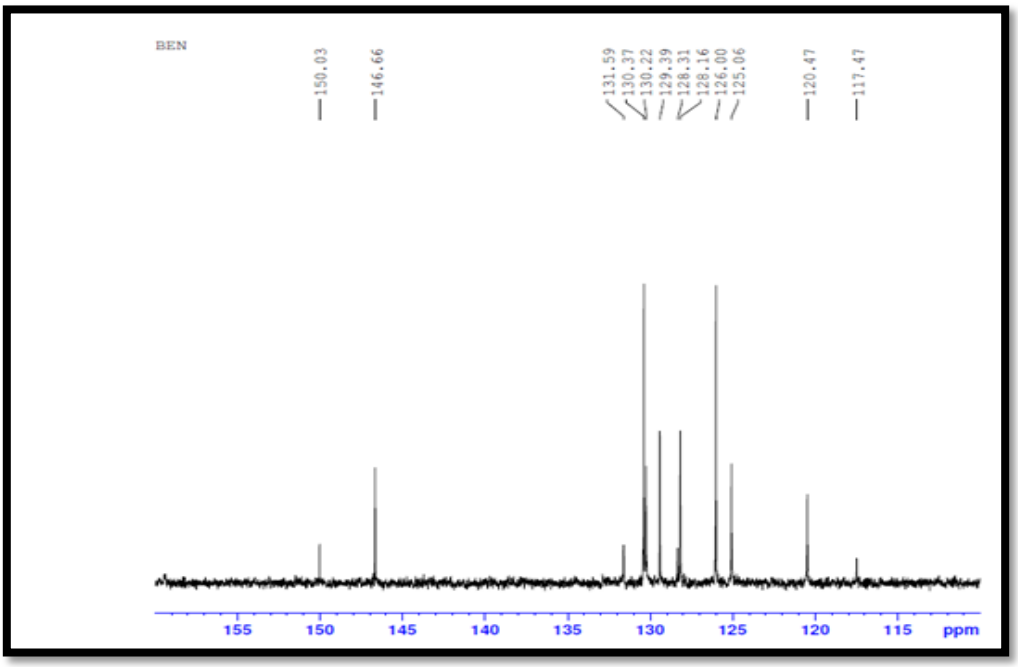

Figure 3.10. ^{13}C NMR spectrum of **C_1**

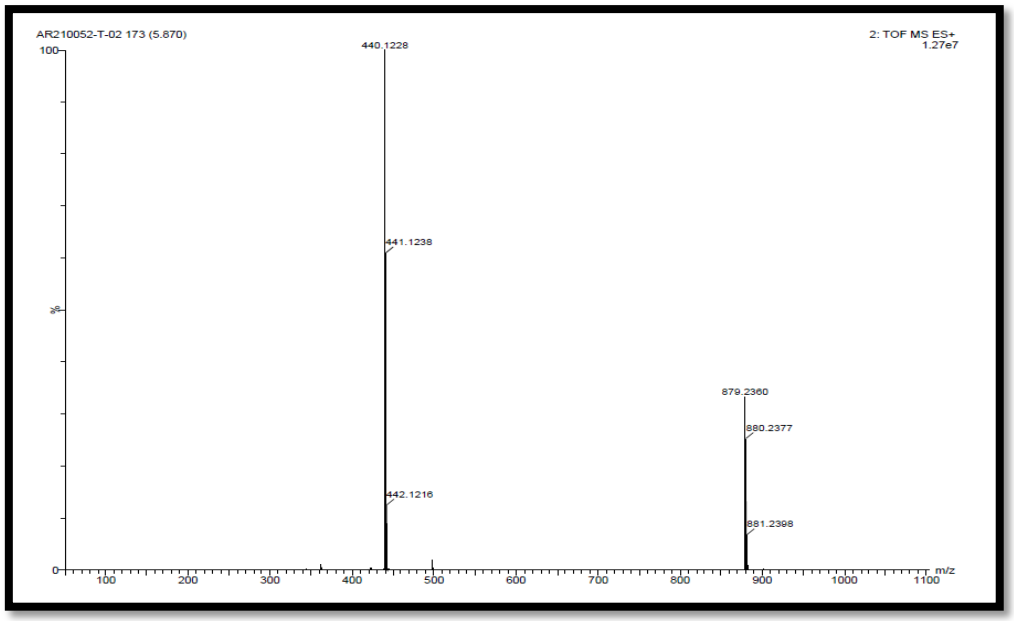

Figure 3.11. LCMS spectrum of **C_1**

In its **^{13}C NMR** spectrum (**Figure 3.10**.), number of distinct signals obtained in the higher frequency region are due to secondary and tertiary carbon atoms present in the structure. Particularly, carbonyl carbon and carbon bearing cyano group resonate at 150.30 and 146.0 ppm, respectively. Further, its **mass spectrum** (**Figure 3.11**.) displayed the distinct [M+H] peak that is in good agreement with the calculated mass of $C_{30}H_{21}N_3O$, conforming the chemical structure of the synthesized molecule.

3.3.3.2 Compounds $C_{8\text{-}14}$ (Series-2)

Figures 3.12 to **3.14** show **FTIR**, **^{1}H NMR**, and **LCMS** spectra of **C_{10}**, respectively. The **FTIR** spectrum of **C_{10}** showed prominent stretching bands at 2217 and 1642 cm^{-1} indicating the presence of cyano and carbonyl groups, respectively. Its **^{1}H NMR** spectrum showed a sharp highly down fielded signal at δ 13 ppm due to NH proton and the remaining aromatic protons resonated in between δ 7 and 8 ppm. Further **LCMS** spectrum was carried out for these molecules and obtained [M+1] peak matched with the calculated mass of $C_{34}H_{20}N_2O$ conforming the chemical structure of the synthesized molecule.

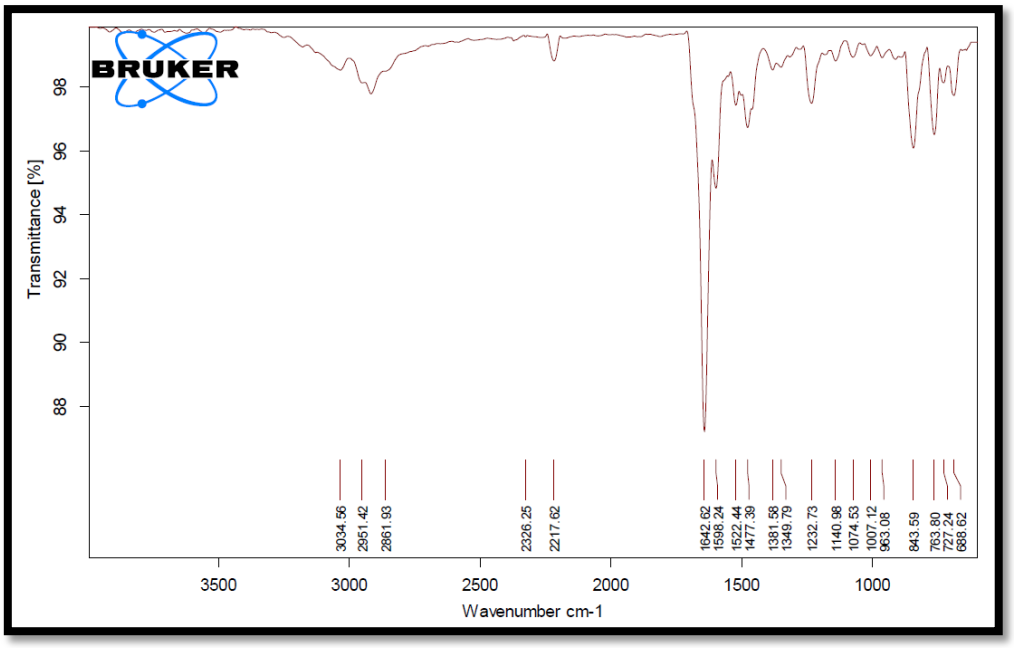

Figure 3.12. FTIR spectrum of **C_{10}**

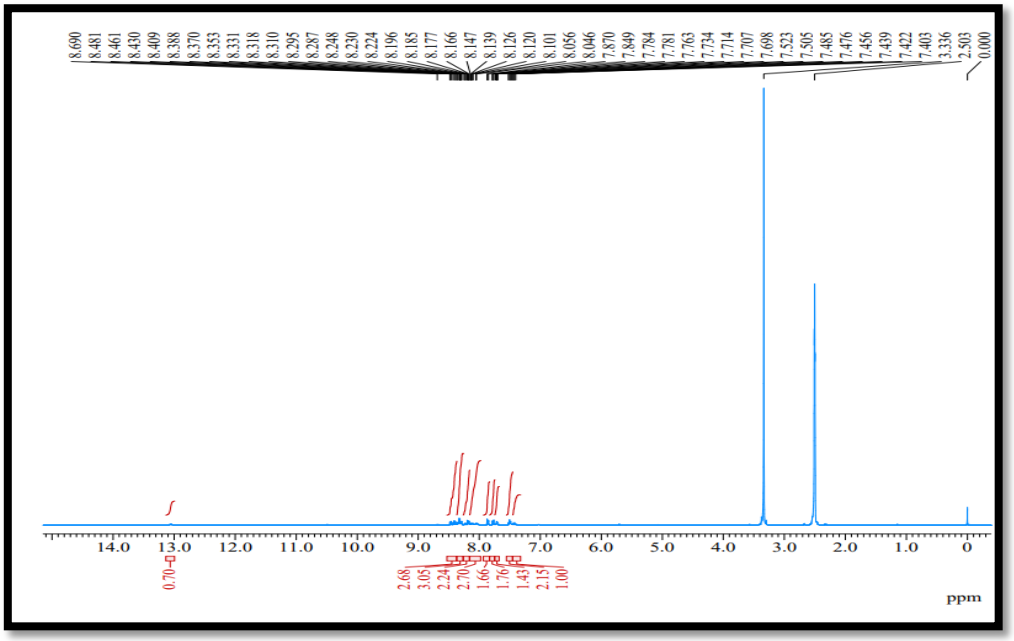

Figure 3.13.[1]H NMR spectrum of **C_{10}**

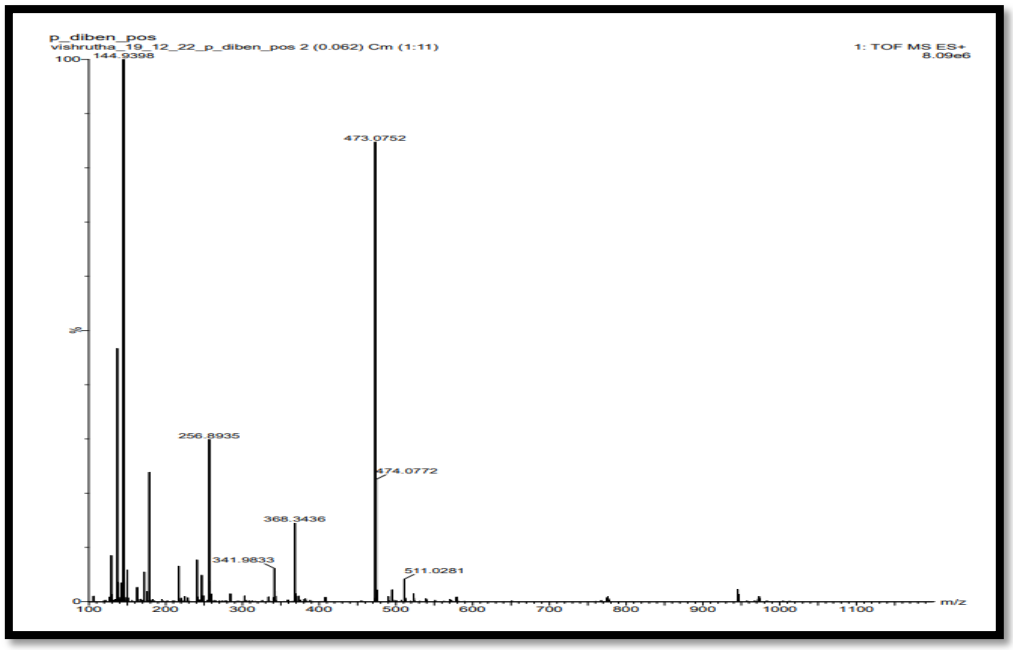

Figure 3.14. LCMS spectrum of **C_{10}**

3.3.3.3 Compounds $C_{15\text{-}21}$ (Series-3)

Figure 3.16 shows the **^{1}H NMR** spectrum of **C_{15}**. All the aromatic protons resonated in between δ 7.25 and 8.64 ppm as multiplet. Further, appearance of a peak between δ 0.98 and 4.45 ppm, is due to presence of hexyl chain in the structure. The **^{13}C NMR** spectrum of **C_{15}** displayed the characteristic signals at downfield region (**Figure 3.17**). The carbonyl carbon atom and carbon containing cyano group resonated at δ 175.51 and 162.30 ppm, respectively. All the aliphatic carbons of hexyl chain appeared in the region of δ 13.00-42.47 ppm. Further, the **FTIR** spectrum (**Figure 3.15**) of **C_{15}** showed carbonyl vibration at 1633 cm^{-1}, whereas peak at 2219 cm^{-1} corresponds to cyano group of the molecule. **Figure 3.18** gives the **mass spectrum** of **C_{15}.** It exhibited the $[M+H]^{+}$ peak at 446.22, which is in good agreement with the calculated molecular weight of 445.57, which confirms the chemical structure of the synthesized **C_{15}**.

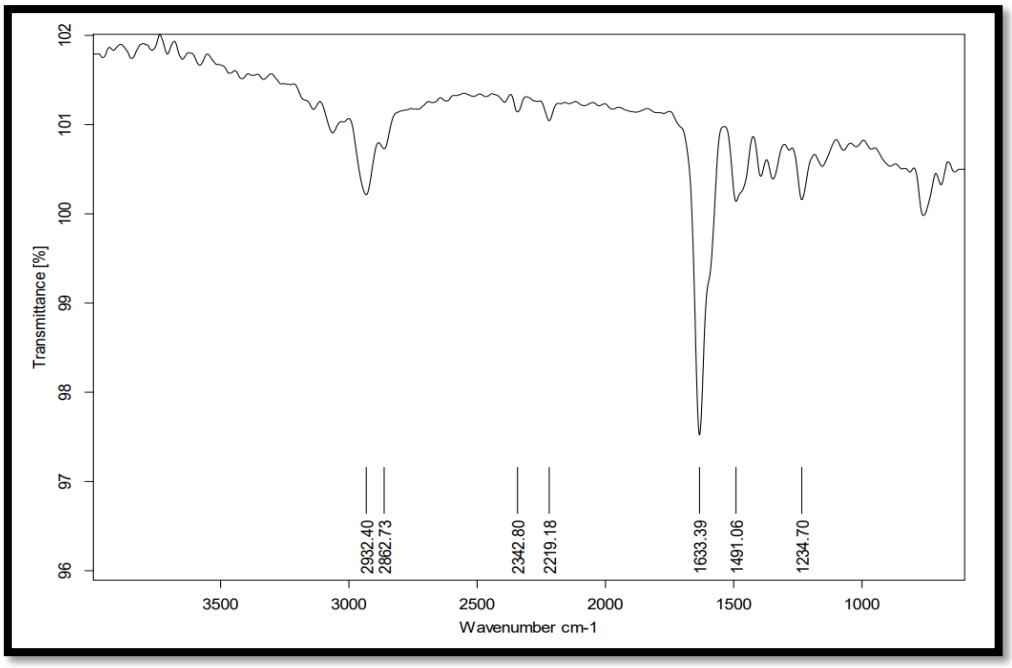

Figure 3.15. FTIR spectrum of **C_{15}**

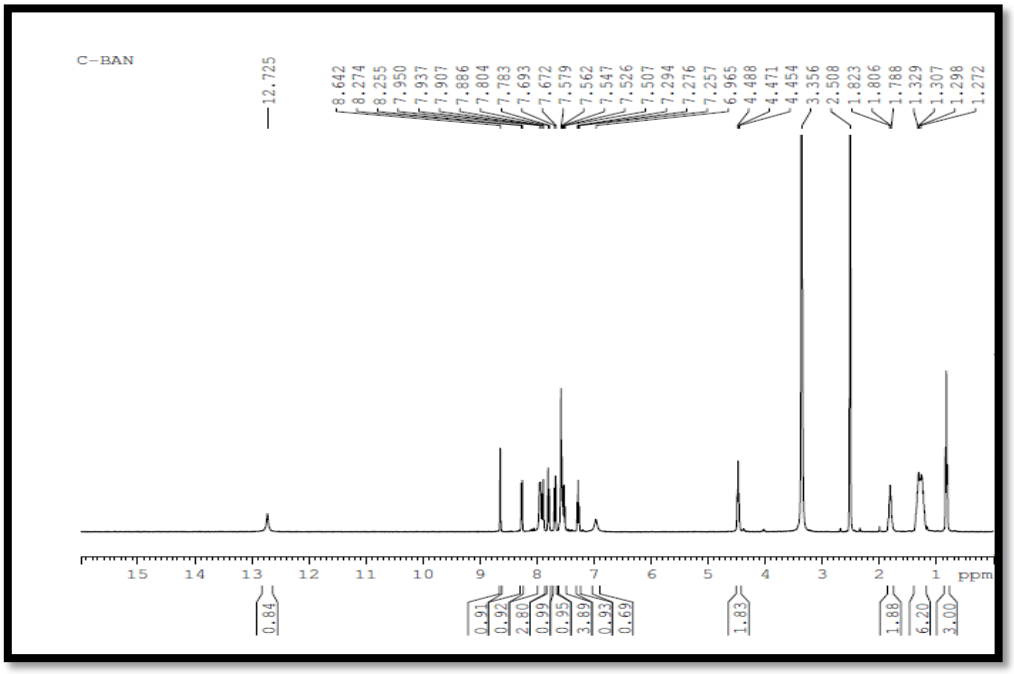

Figure 3.16. ^{1}H NMR spectrum of **C_{15}**

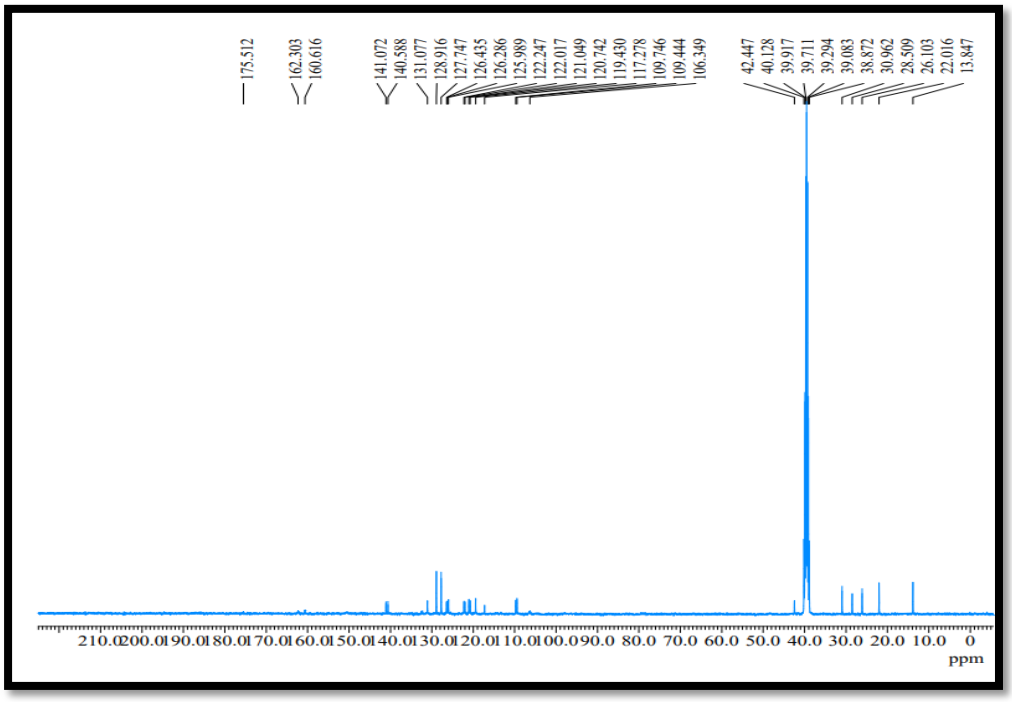

Figure 3.17.^{13}C NMR spectrum of **C_{15}**

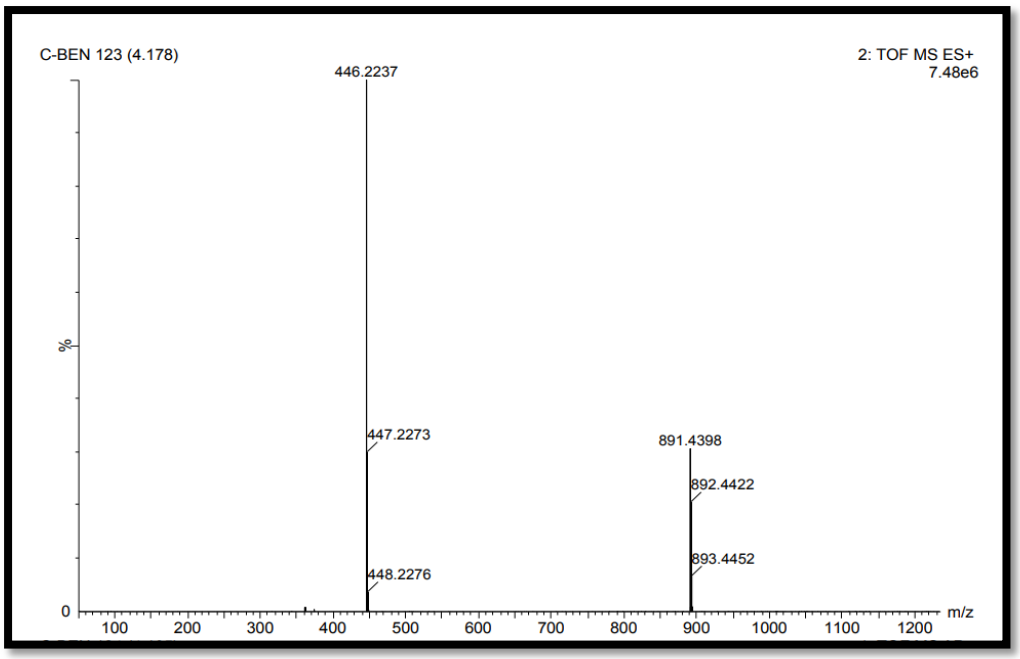

Figure 3.18. LCMS spectrum of **C_{15}**

3.3.3.4 Compounds $C_{22\text{-}28}$ (Series-4)

The **^{1}H NMR, ^{13}C NMR, FTIR** and **Mass spectra** of the selected compound **C_{22}** are depicted in **Figures 3.19, 3.20, 3.21** and **3.12**, respectively. In its **^{1}H NMR** spectrum, all the aromatic protons of phenothiazine, cyanopyridone, and phenyl groups appeared in between δ 6.82 and 7.92 ppm as medium multiplet. Also, the peaks in the region of δ 3.92 to 0.82 ppm correspond to primary and secondary protons of hexyl side chain. The **^{13}C NMR** spectrum of **C_{22}** displayed the characteristic signals, which are found at downfield region. The carbonyl carbon atom of acid group resonated at δ 147.30 ppm, while signals due to aromatic carbons were observed between δ 129.35 to 116.64 ppm. Further, **FTIR** spectrum of the molecule showed the characteristic C=O vibration band at 1639 cm^{-1}. In addition, the band obtained at 2931 cm^{-1} is due to presence of C≡N functional group in the compound. The structure of **C_{22}** was further confirmed by its **mass spectrum**, which showed its M+H at 477.27.

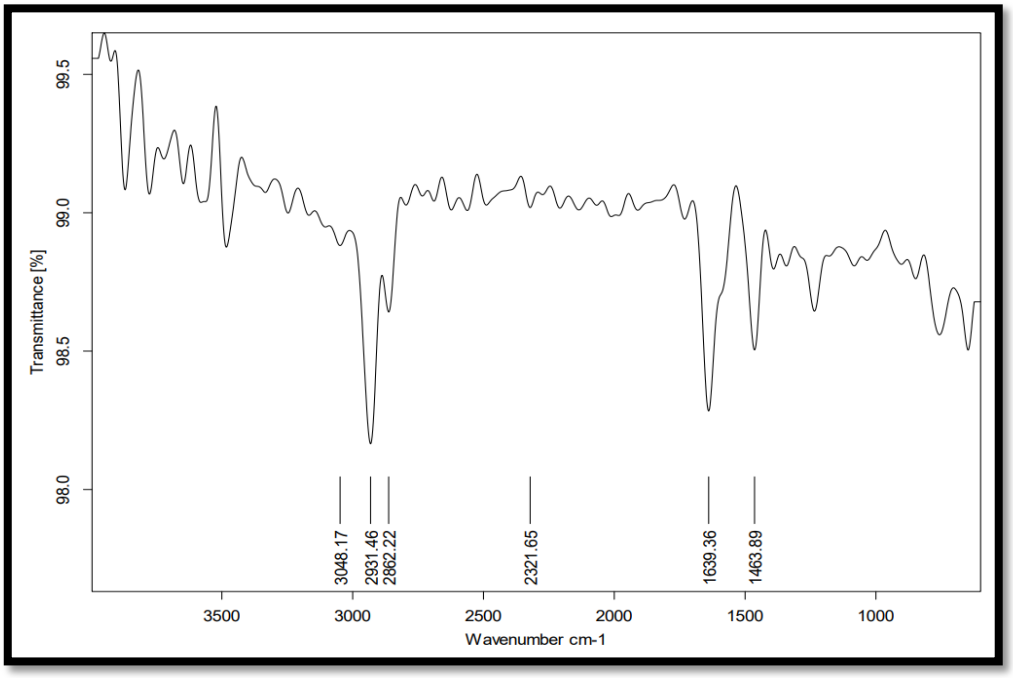

Figure 3.19. FTIR spectrum of **C_{22}**

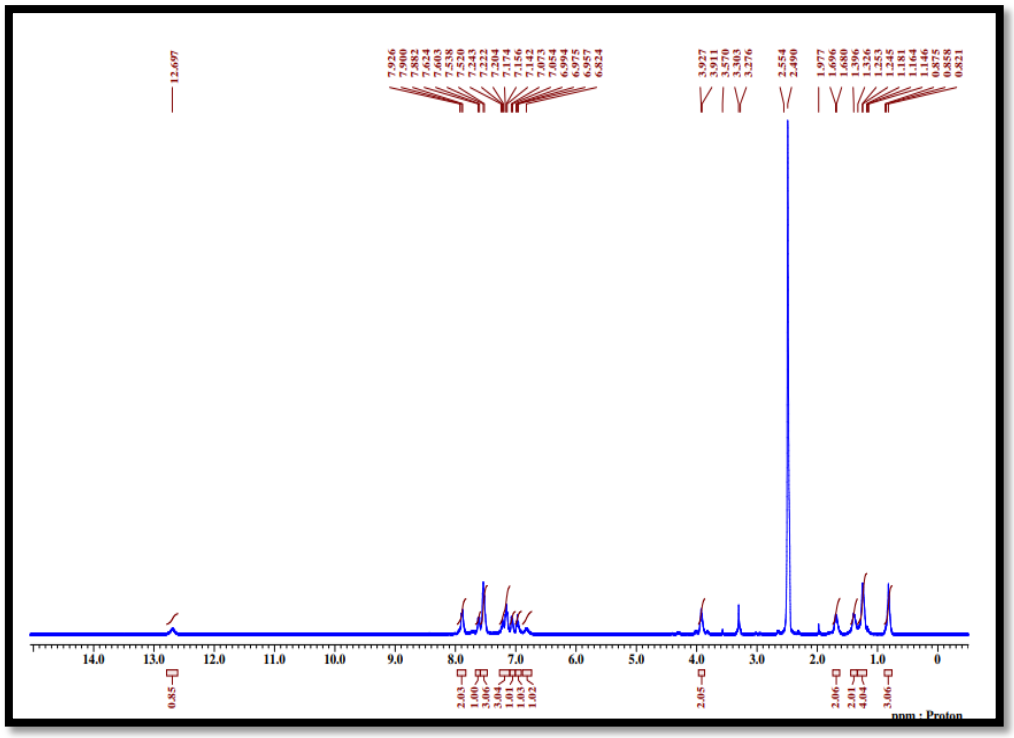

Figure 3.20. ^{1}H NMR spectrum of **C_{22}**

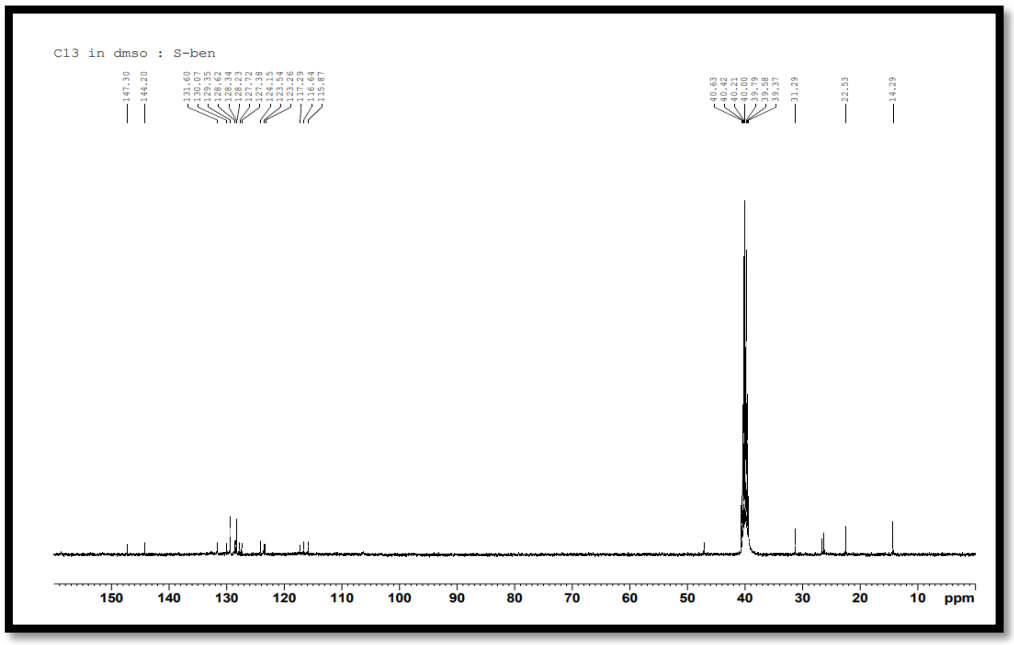

Figure 3.21. ^{13}C NMR spectrum of **C_{22}**

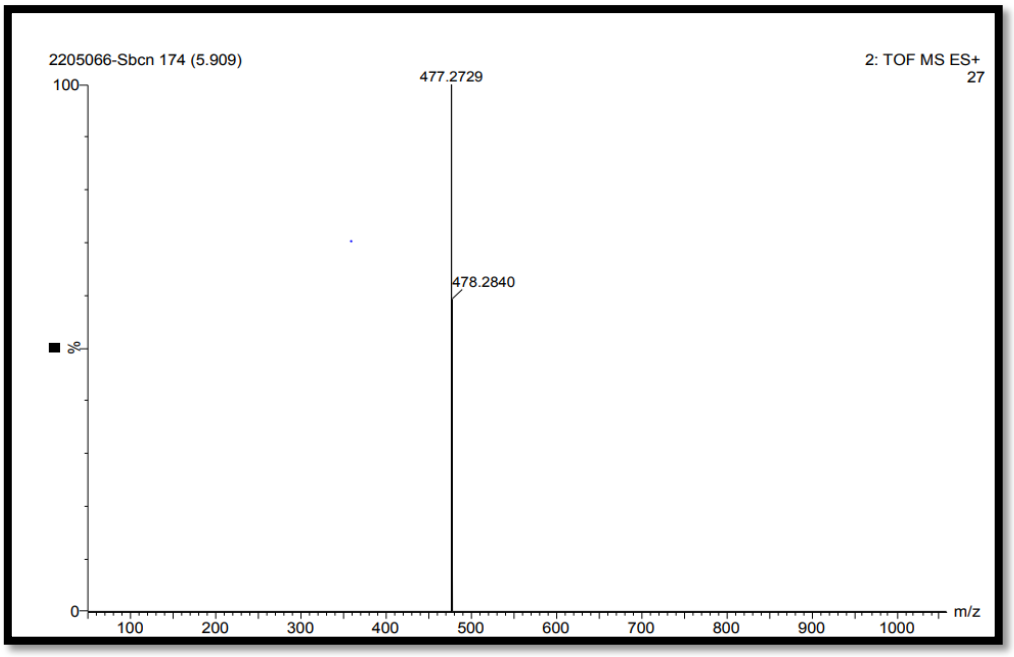

Figure 3.22. LCMS spectrum of **C_{22}**

3.3.3.5 Compounds $C_{29\text{-}34}$ (Series-5)

Figures 3.23, **3.24, 3.25**, and **3.26** depict the **FTIR**, **^{1}H NMR**, **^{13}C NMR**, and **Mass** spectra of **C_{29}**, respectively.

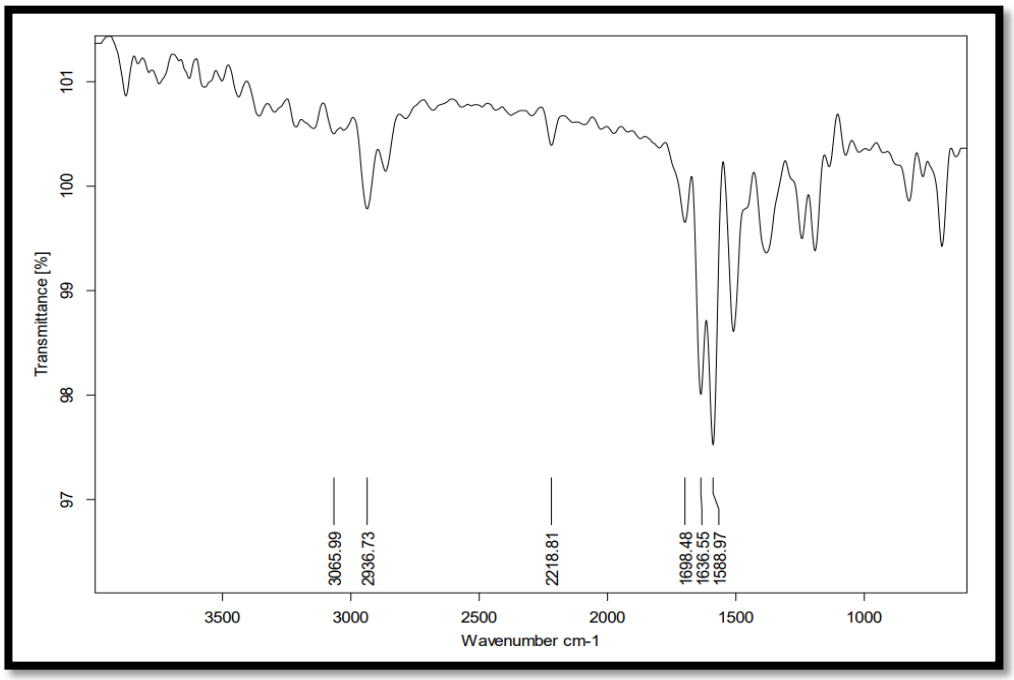

Figure 3.23. FTIR spectrum of **C_{29}**

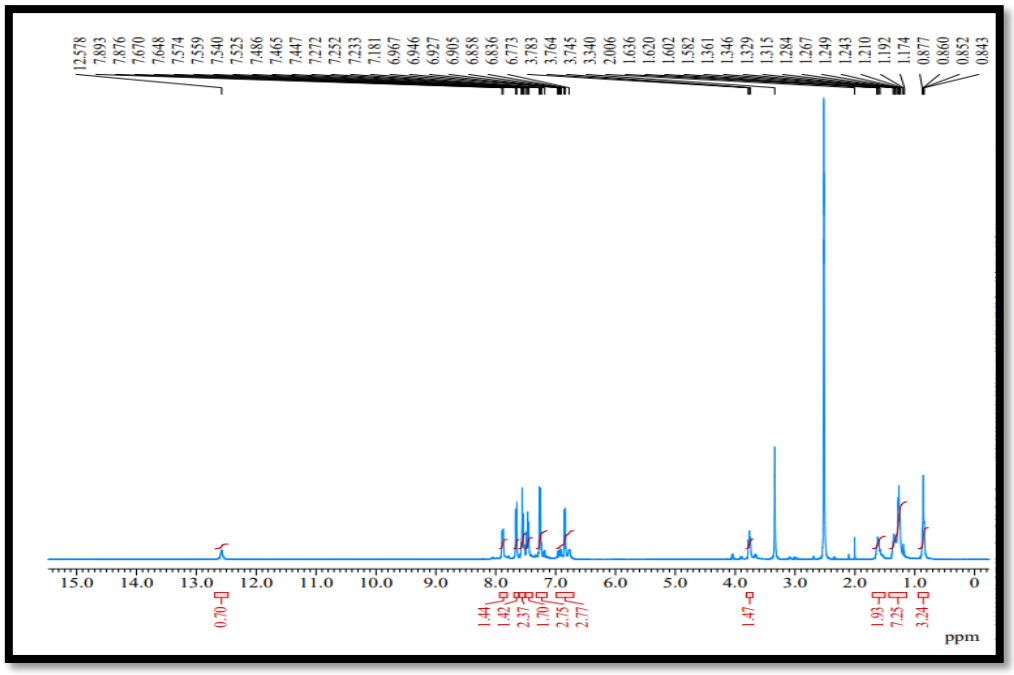

Figure 3.24. ^{1}H NMR spectrum of **C_{29}**

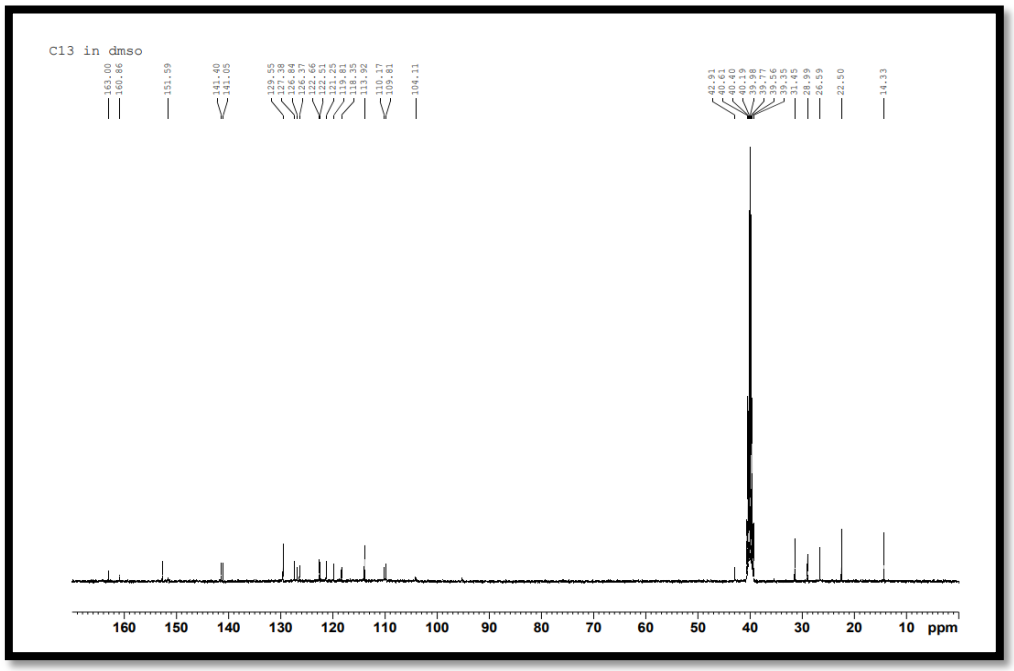

Figure 3.25. ^{13}C NMR spectrum of **C_{29}**

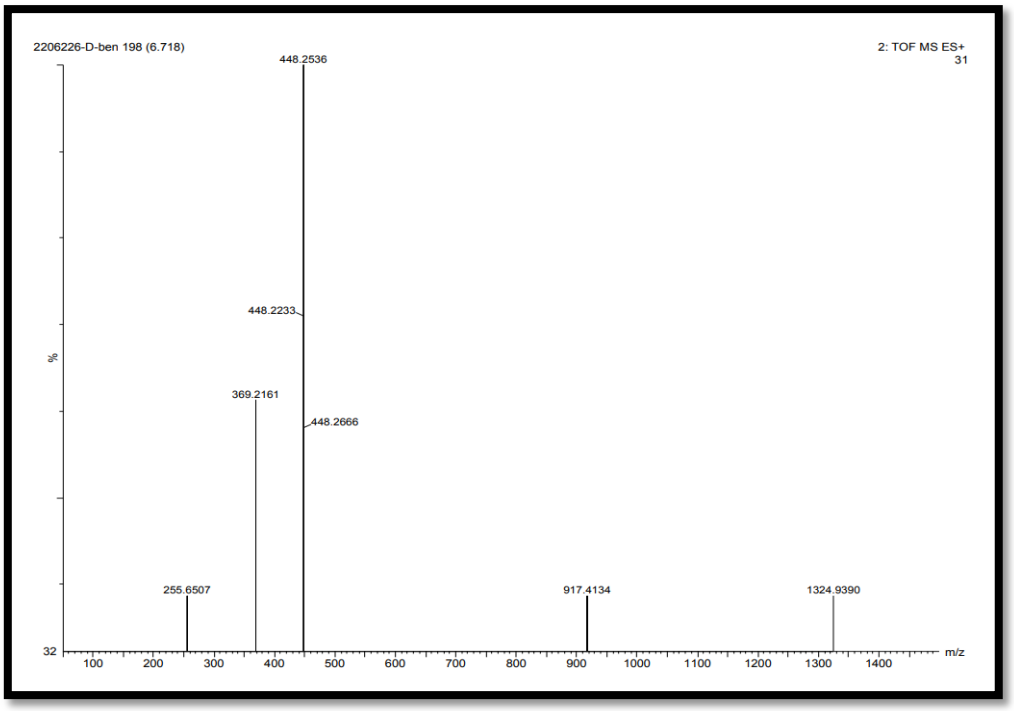

Figure 3.26. LCMS spectrum of **C_{29}**

In its **^{1}H NMR** spectrum, the peak appeared at δ 12.57 is due to presence of NH proton. The presence of alkyl chain protons appeared between δ 0.873 and 3.76 ppm. The aromatic protons of diphenylamine, cyanopyridone, and phenyl groups appeared between δ 6.96 and 7.69 ppm. The **^{13}C NMR** spectrum of **C_{29}** displayed the characteristic signals which appeared at downfield. The carbonyl carbon atom of acid group resonated at δ 167.97 ppm, while the carbon in imine bond showed signals at 190.90 and 168.33 ppm. The aliphatic carbon atoms displayed peaks in the region δ 14.01-52.64, as in the case of **C_{29}**. Further, FTIR spectrum displayed a broad peak at 2218.81 cm^{-1} due to cyano group of cyanopyridone and showed a sharp peak at 1698 cm^{-1}, which is attributed to carbonyl group of pyridone. The obtained **mass spectrum** confirmed that the molecular weight of **C_{29}** is 448.25, which matched with its calculated molecular weight.

3.3.3.6 Compounds $C_{35\text{-}37}$ (Series-6)

^{1}H NMR spectrum of **C_{35}** is depicted in **Figure. 3.28**. In its spectrum, **C_{35}** showed sharp singlet at δ 3 ppm, which is due to presence aliphatic NH_2 proton. The appeared peak at δ 12.2 ppm is due the NH proton of the cyanopyridone ring.

Aromatic protons showed peaks between δ 6.40 and 7.88 ppm.

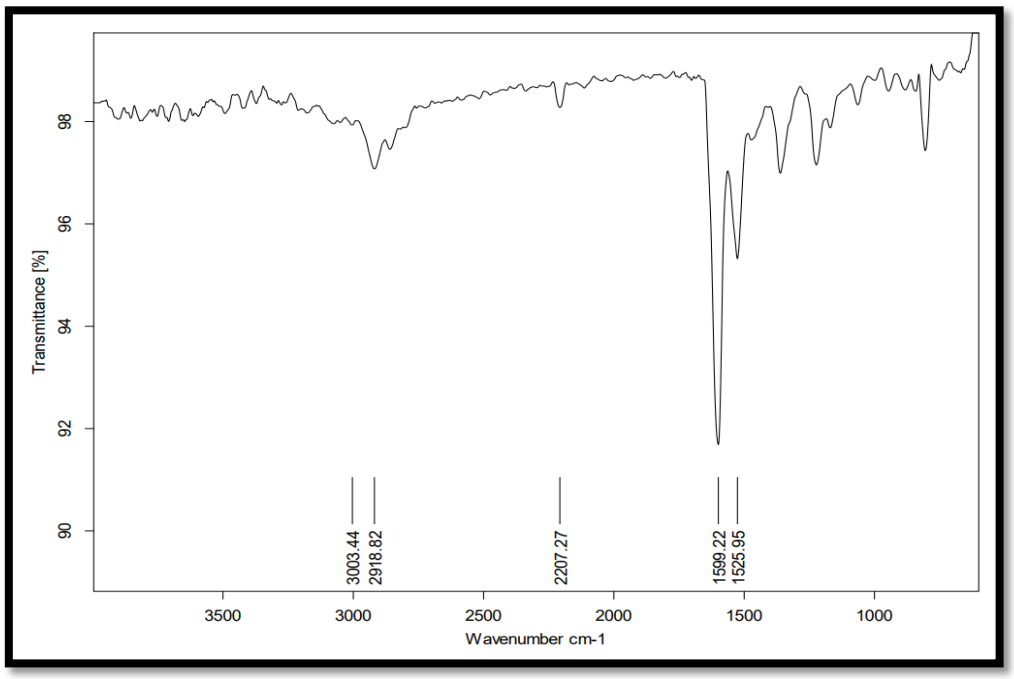

Figure 3.27. FTIR spectrum of **C_{35}**

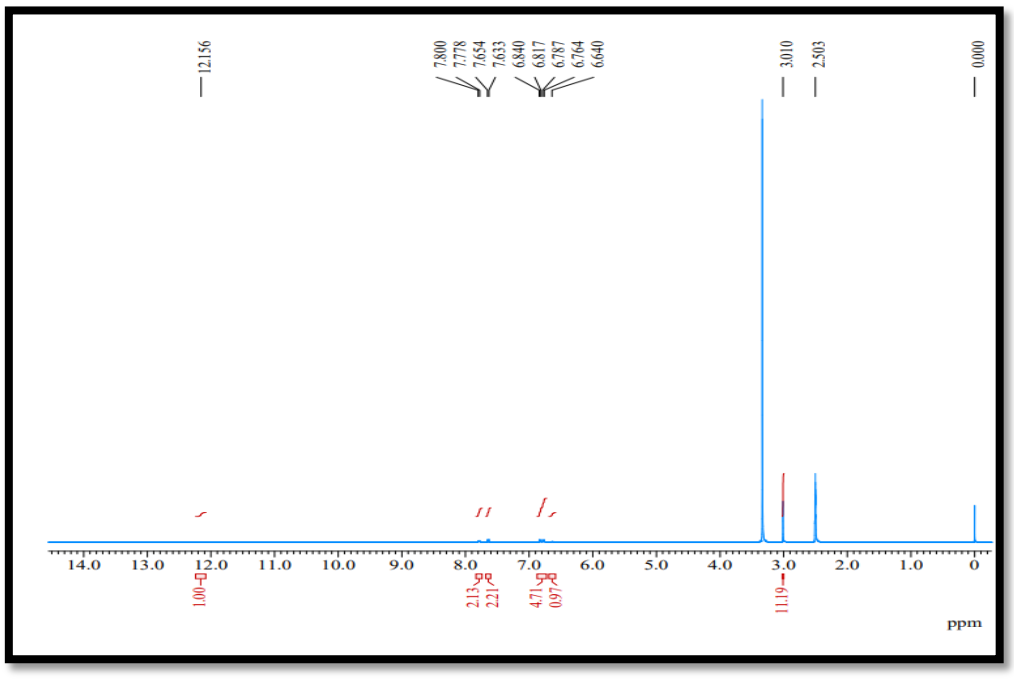

Figure 3.28.^{1}H NMR spectrum of **C_{35}**

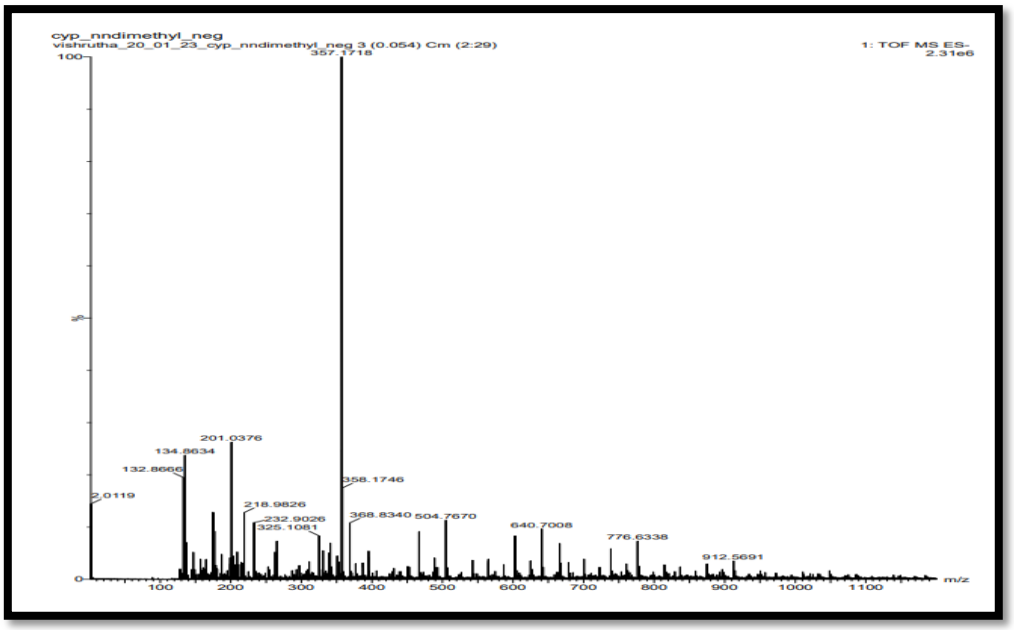

Figure 3.29. LCMS spectrum of **C_{35}**

Its **FTIR** spectrum (**Figure 3.22**) displayed sharp peaks at 1599 and 2207 cm^{-1} due to the presence of the carbonyl group and cyano group of the molecule. Further, its **mass spectrum** conformed the molecular weight of the synthesized compound **C_{35}**.

3.3.3.7 Compounds $C_{38\text{-}42}$ (Series-7)

FTIR, **^{1}H-NMR**, and **Mass** spectrometry of **C_{38}** are depicted in **Figures 3.30-3.31**,and **3.32** respectively. In the **FTIR** spectrum, **C_{38}** showed an absorption band at 2414 cm^{-1} indicating the presence of the cyano group of the central pyridine core and the absence of any absorption in the range of 1650-1680 cm^{-1} suggested the successful alkylation of pyridone to O-alkylated pyridine. As expected, the set of **^{1}H NMR** signals appeared between δ 6.87 and 8.25 ppm accounts for aromatic protons; a singlet appeared at δ 3.01 ppm is due to presence of six dimethyl protons of **C_{38}**. **Mass** data unambiguously matched with calculated molecular mass of $C_{27}H_{23}N_3O$.

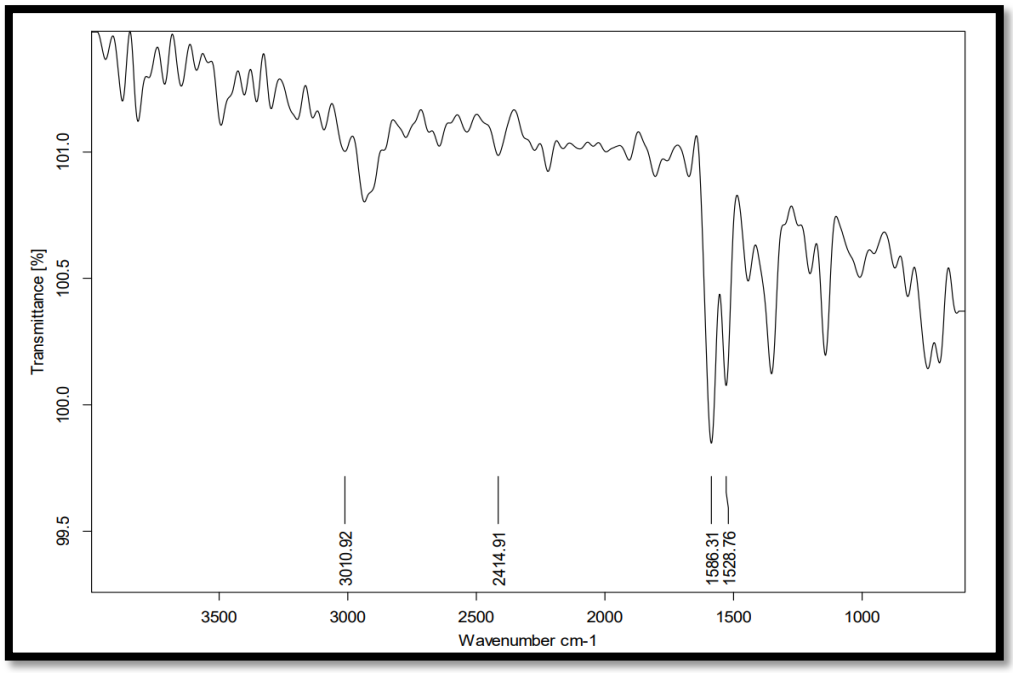

Figure 3.30. FTIR spectrum of **C_{38}**

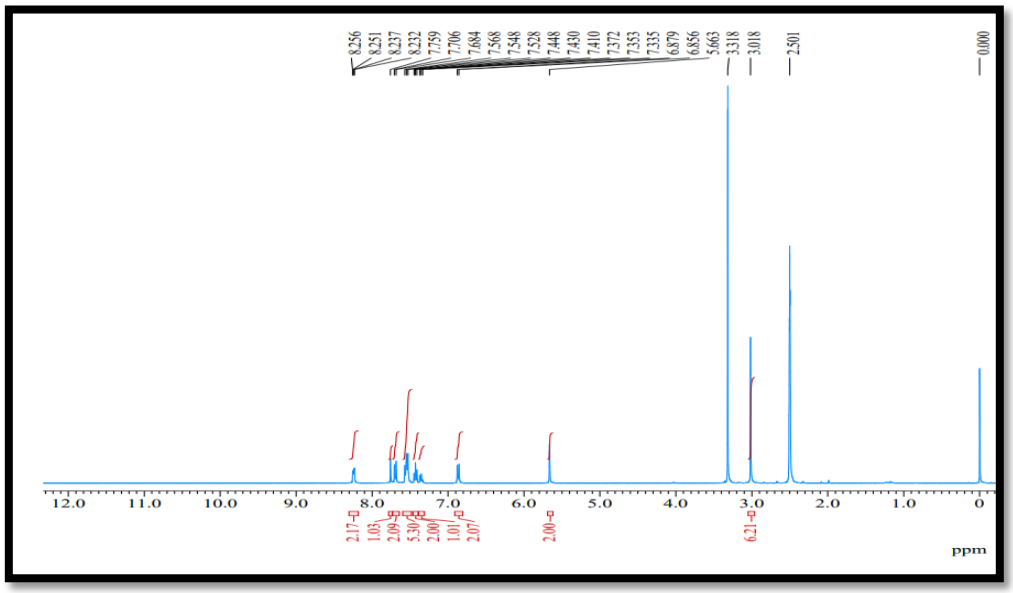

Figure 3.31. ^{1}H NMR spectrum of **C_{38}**

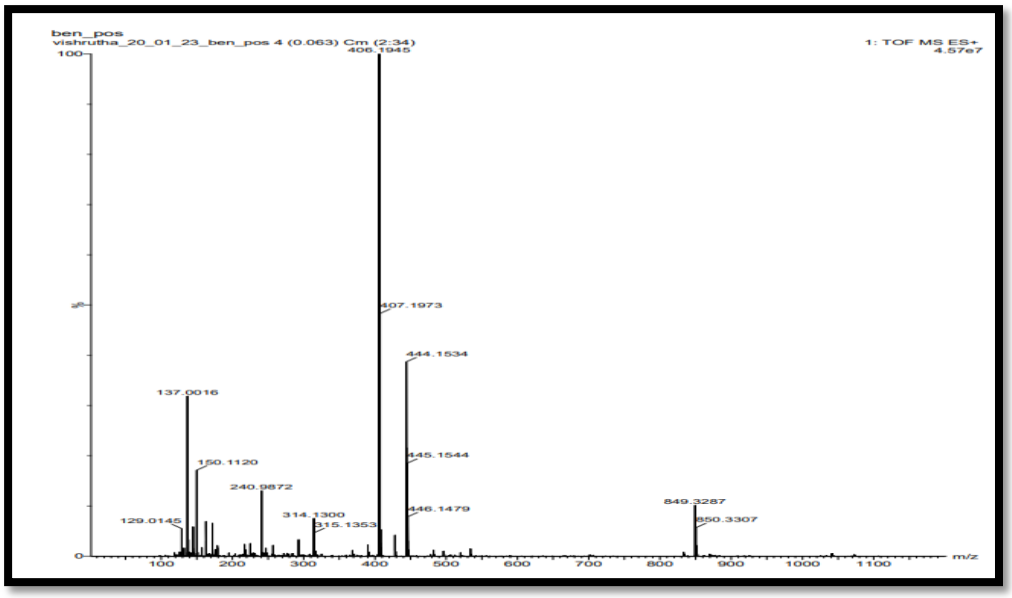

Figure 3.32. LCMS spectrum of **C_{38}**

3.4 CONCLUSIONS

In conclusion, seven series comprising forty-two cyanopyridones/ cyanopyridines with D-A-D configuration (**C_{1-42}**) were successfully designed as potential emitters for OLED applications. All the compounds possess cyanopyridone as an effective acceptor and different donor groups attached to its 4th and 6th positions. They were synthesized successfully adopting standard methodologies. The optimized synthetic routes were well established with respect to yield, solvent, temperature, reaction time, concentration, and other reaction parameters. In addition, their purification techniques have been developed. Their structures were confirmed by **^{1}H NMR**, **^{13}C NMR**, **FTIR**, and **Mass** spectroscopy.

PHOTOPHYSICAL, ELECTROCHEMICAL, THERMAL AND THEORETICAL INVESTIGATIONS

Abstract

This chapter comprises in-depth studies on the linear optical, electrochemical, and thermal properties of newly synthesized compounds. It also includes solvatochromic study with different solvents of varied polarities. Further, it involves their computational studies using DFT software, encompassing geometric optimizations, and calculations of HOMO-LUMO energy levels. Additionally, it consists of investigations into the correlation between the structural characteristics of these compounds and their respective properties.

4.1 PHOTOPHYSICAL INVESTIGATION

Studying the photophysical properties of organic compounds primarily involves conducting UV-Vis absorption and emission spectral analyses. These collected optical data play a crucial role in assessing their viability as light-emitting materials for OLED applications.

4.1.1 Introductions

The UV-Vis absorption spectroscopy involves the measurement of absorbance of light by a compound as a function of wavelength in the UV-visible range. When a molecules is subjected to incident light, it absorbs a photon and get excited from ground state (HOMO level) to an electronic excited state (LUMO level). Fluorescence is a complementary technique to UV-Vis absorption. It occurs in the same wavelength range, but results from an excited state, emitting a photon of a lower energy than it absorbed. Further, photophysical studies of any material can evaluate the important data like optical band gap, molar extinction coefficient (ε), Stokes shift, quantum yield of organic molecules. These are valuable parameters used for selecting such materials as emitters for OLED applications. Therefore, all the newly synthesized organic compounds, $\mathbf{C_{1\text{-}42}}$ were subjected to UV- Vis and fluorescence spectral studies in order to evaluate their suitability for their applications in OLEDs. These generated optical data give valuable information, which are highly useful in designing new emitters. Further, their solvatochromic behavior, *i.e*. interaction of the

molecule with the solvents, was investigated by measuring absorption and emission maxima in different solvents of varied polarities in order to know the ICT in the molecules.

4.1.2 Materials and methods

The UV-Vis absorption spectra of the compounds were recorded at room temperature using Analytik Jena SPECORD S 600 spectrophotometer. Further, the fluorescence emission spectra were obtained using Jasco FP 6200 spectrophotometer.

4.1.3 Experimental

The UV-Vis absorption measurements were performed in dichloromethane solutions at a concentration of 10^{-5} M. From the absorption spectra, emission spectra were obtained by exciting the molecules at the wavelength corresponding to their absorption maxima using the same concentration. In addition, the emission spectra of the compounds were obtained in thin film states. From these spectral data, various optical properties like optical band gap, Stokes shift, quantum yield, and molar extinction coefficient were calculated. The Stokes shift values were calculated by using Eq **4.1**.

$$(\gamma_a\text{-}\gamma_f) = \left[\frac{1}{\lambda a} - \frac{1}{\lambda f}\right] \times 10^7 \ldots\ldots\ldots\ldots\ldots\ldots \quad (\mathbf{4.1})$$

4.1.4 Results and discussion

Results of photochemical studies of new compounds have been discussed series-wise in the following section.

4.1.4.1 TPA substituted compounds $C_{1\text{-}7}$ (Series-1)

The absorbance and fluorescence spectra of $\mathbf{C_{1\text{-}7}}$ are depicted in **Figure 4.1**, and the corresponding data are summarized in **Table 4.1**. Apparently, all the molecules exhibited three intense absorption bands in DCM ($C=10^{-5}$ M) corresponding to π to π* localized electronic transfer of the triphenylamine group (~295 nm) and π to π* electronic transition of the second donor group (~230 nm). In contrast, the peaks at ~390 nm occur due to the intramolecular donor to acceptor charge transition (**Table 4.1**). The minimal impact of the secondary donor groups is evident in the absorption spectra, as shown by the nearly equal bands at ~390 nm. All the compounds, except

C_4 and **C_7**, have the same intramolecular charge transfer (ICT) absorption because of the similar donor strength of the secondary donor group (**Figure 4.1a**). The slight red-shifts observed in **C_4** and **C_7** may be attributed to the strong donor strength of the second donor groups, *viz*. aniline and thiophene units, respectively. Further, we calculated the Stokes shift value as well as the optical band gap using absorption and emission spectral data. The obtained optical band gaps are in the range 2.39~2.44 eV. Whereas, the Stokes shift are observed in the range of 6726~8247 cm^{-1}. Notably, among all, the compounds **C_7** and **C_8** showed the highest Stokes shift indicated the enhanced light-emission ability due to the strong electron-withdrawing cyanopyridone group and electron-donating phenyl and biphenyl unit in the visible region. Their optical band gaps were ~2.4 eV (**Table 4.1**). The observed single emission band in their DCM fluorescence spectra, devoid of fine vibronic structure, reveals the disordered nature of the excited state. On changing the auxiliary donor group, the emission maxima appear in the range of 551 to 565 nm having a full width at half maxima (FWHM) of ~60 nm. Among all the compounds, **C_3** and **C_7** demonstrated bathochromic shifts, which may owe to the strong donor strength of the second donor groups, *i.e.* biphenyl and thiophene moieties, respectively. Compared to the observed spectra in DCM, the thin-film emission bands are widened (FWHM~88 nm) with slight bathochromic shifts (<5 nm) in the emission maxima, revealing the weak intermolecular aggregation in their thin-film state (**Figure 4.1b**). The thin-film emission maxima are in the range of 557 to 569 nm (**Table 4.1**). Interestingly, all the compounds have demonstrated high quantum yields (Φ_F) in thin-film states, which is a crucial prerequisite for their good performance in OLEDs (**Table 4.1**)[44].

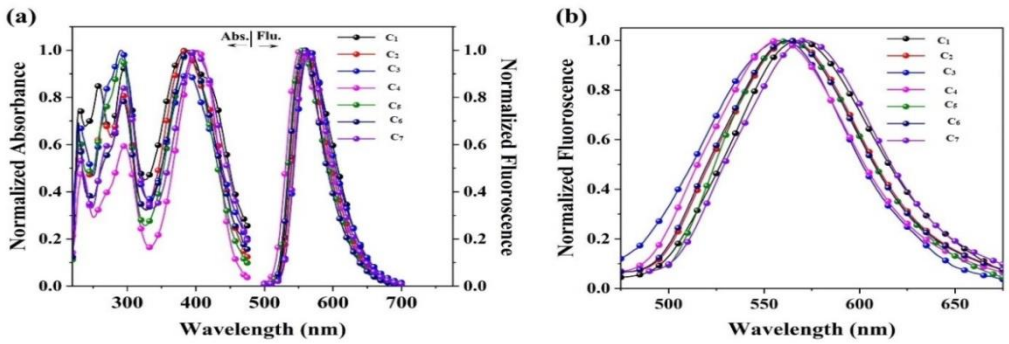

Figure 4.1. Absorbance and fluorescence spectra of **$C_{1\text{-}7}$** in (**a**) solution in DCM and (**b**) thin-film state.

Table 4.1. Photophysical data of $\mathbf{C_{1\text{-}7}}$ in DCM and thin-film state

Compds	λ_A[a] **(nm)**	λ_A[b] **(nm)**	λ_E[a]**(FWHM) (nm)**	λ_E[b]**(FWHM) (nm)**	E_g^{opt} **(eV)**[b]	**Δλ (cm^{-1})**	Φ_F[b]
$\mathbf{C_1}$	259, 295, 384	393	562 (62)	568 (88)	2.42	8247	0.22
$\mathbf{C_2}$	266, 294, 385	391	560 (58)	565 (89)	2.40	8116	0.35
$\mathbf{C_3}$	230, 291, 387	394	565 (60)	571 (87)	2.39	8140	0.39
$\mathbf{C_4}$	233, 295, 402	408	551 (62)	557 (85)	2.41	6726	0.31
$\mathbf{C_5}$	229, 291, 390	398	556 (57)	562 (84)	2.44	7458	0.24
$\mathbf{C_6}$	229, 294, 389	396	558 (55)	564 (88)	2.41	7785	0.36
$\mathbf{C_7}$	232, 295, 397	406	564 (61)	569 (89)	2.38	7458	0.28

λ_A: Absorption maxima λ_E: Emission maxima; **FWHM**: Full width at half-maximum; $\mathbf{E_g^{opt}}$**:** Optical band gap; Δλ: Stokes shift; Φ_F: Fluorescence quantum yields
[a] Recorded in DCM (10^{-5} M) at room temperature, [b] Recorded in thin-film state

Further, the ICT of $\mathbf{C_{1\text{-}7}}$ was investigated by measuring their solvatochromic behaviour using different solvents of varied polarities, and their optical values are portrayed in **Table 4.2.** From the data, it is evident that all the compounds exhibited intense absorption spectra and are slightly affected by the solvent polarities (**Table 4.2**, and **Figures 4.2** to **4.8**), varying from less polar solvent toluene to high polar solvent ethanol, indicating the non-polar nature of the ground state. Significantly, their emission spectra showed bathochromic shifts with increasing solvent polarity in all the cases except ethanol due to its weak interaction with the chromophores (**Table 4.2**). The Stokes shift value is a key parameter of a compound and it gives valuable information about luminescence property.

Table 4.2. Photophysical data of $\mathbf{C_{1\text{-}7}}$ in solvents of varying polarities

Compds	**Toluene**			**Ethyl Acetate**			**Acetone**			**Ethanol**			**Acetonitrile**		
	λ_A	λ_E	Δλ	λ_A	λ_E	Δλ	λ_A	λ_E	Δλ	λ_A	λ_E	Δλ	λ_A	λ_E	Δλ
$\mathbf{C_1}$	392	505	5708	382	545	7829	383	548	7861	379	544	8002	380	560	8458
$\mathbf{C_2}$	390	503	5760	383	530	7241	383	554	8059	381	555	8228	383	563	8347
$\mathbf{C_3}$	393	510	5837	389	534	6980	388	550	7591	385	486	5397	387	562	8046
$\mathbf{C_4}$	400	491	4633	397	504	5347	403	542	6363	412	531	5439	402	561	7050
$\mathbf{C_5}$	392	497	5389	386	530	7038	386	554	7856	386	558	7985	386	563	8144
$\mathbf{C_6}$	393	498	5364	387	525	6792	387	554	7789	412	558	6350	402	562	7082
$\mathbf{C_7}$	403	508	5128	393	514	5990	394	535	6689	392	464	3958	394	556	7395

λ_A: Absorption maxima in nm; λ_E: Emission maxima in nm; Δλ: Stokes shift in cm^{-1}

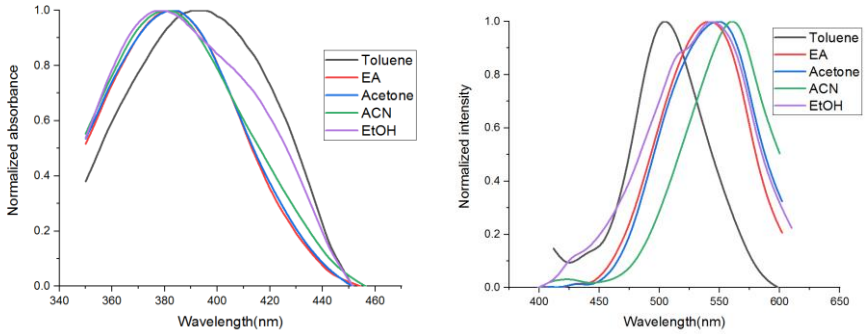

Figure 4.2. UV and PL spectra of $\mathbf{C_1}$ in different solvents

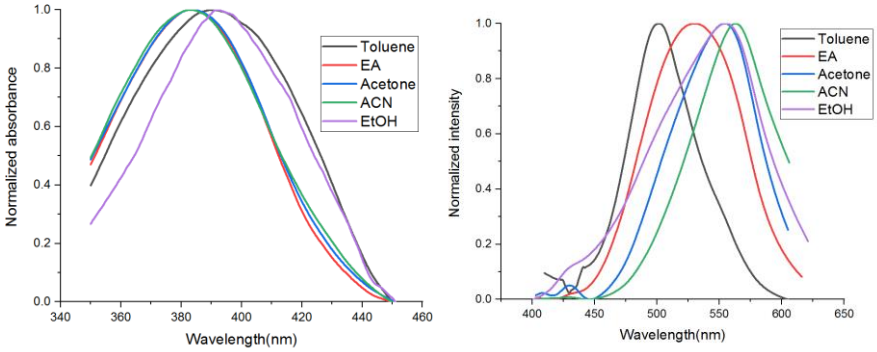

Figure 4.3. UV and PL spectra of $\mathbf{C_2}$ in different solvents

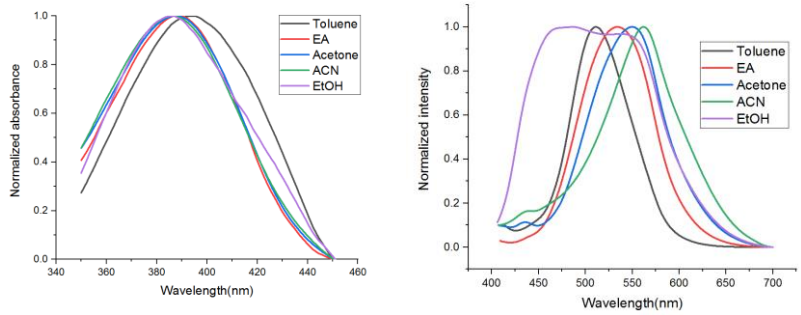

Figure 4.4. UV and PL spectra of $\mathbf{C_3}$ in different solvents

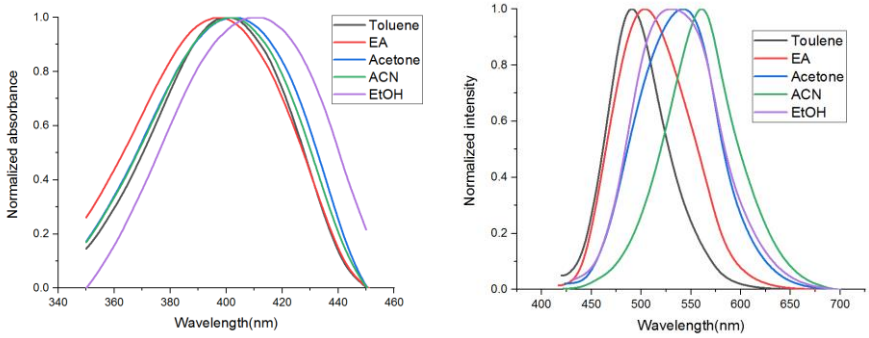

Figure 4.5. UV and PL spectra of $\mathbf{C_4}$ in different solvents

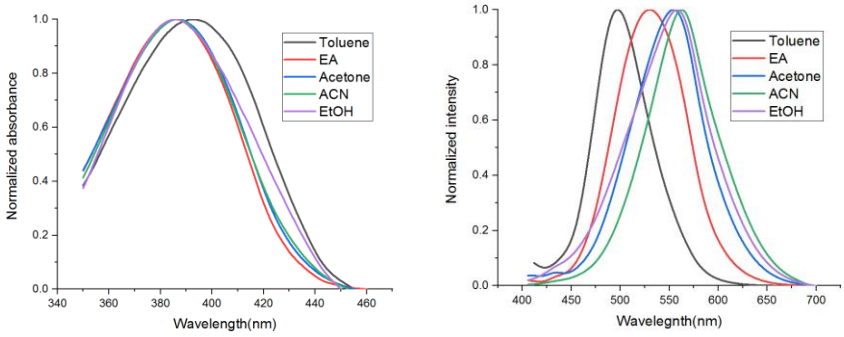

Figure 4.6. UV and PL spectra of $\mathbf{C_5}$ in different solvents

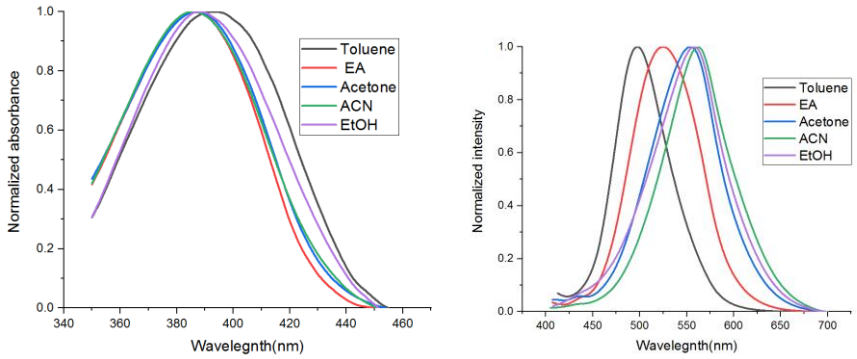

Figure 4.7. UV and PL spectra of $\mathbf{C_6}$ in different solvents

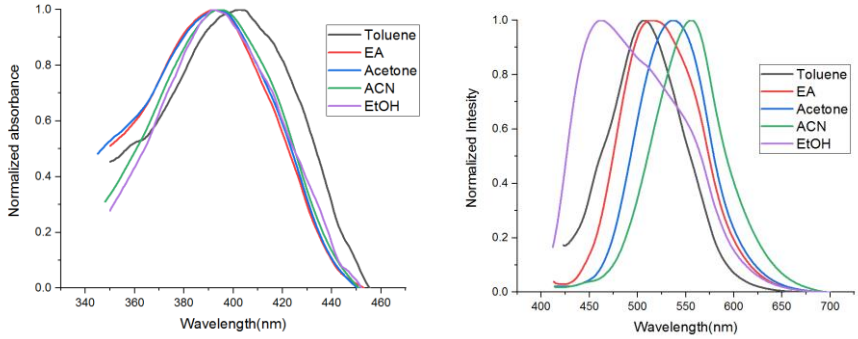

Figure 4.8. UV and PL spectra of $\mathbf{C_7}$ in different solvents

4.1.4.2 Pyrene-based compounds $C_{8\text{-}14}$ (Series-2)

The absorption spectra of $\mathbf{C_{8\text{-}14}}$ are depicted in **Figure 4.9**, and the corresponding optical data are tabulated in **Table 4.3**. Their absorption spectra displayed three bands; the high energy band appears at 242 nm, which is owing to the π-π* transition of the auxiliary donor group, and the second band appears at 330 nm because of the π-π* transition of the pyrene ring and the low energy band transition is due to the intramolecular charge transition from donor to acceptor group. The ICT band values range from 368 to 398 nm. The peak value depends on the strength of the

auxiliary donor group, *i.e.*, phenyl (**C_8**), tolyl (**C_9**), biphenyl (**C_{10}**), 4-aminophenyl (**C_{11}**), 4-methoxyphenyl (**C_{12}**), 4-hydroxyphenyl (**C_{13}**), and 2-thienyl (**C_{14}**). Among the series, the compounds with 4-aminophenyl (**C_{11}**) and 2-thienyl (**C_{14}**) substitutions showed absorptions in the longer wavelength regions due to their strong electron-donating nature. Further, synthesized compounds exhibited high Stokes shifts (**Table 4.3**), which were determined by taking the difference between absorption and emission maxima. Compound **C_8** has a highest stokes shift among the compounds, which is due to the enhanced light-emission ability to strong electron-withdrawing nature of cyanopyridone group and electron-donating phenyl unit in the visible region. The large stoke shift is beneficial for reducing the self-quenching that is results from molecular self-absorption. The optical band gaps of the **$C_{8\text{-}14}$** were calculated using absorption spectra. The acquired band gap of **$C_{8\text{-}14}$** showed the decreasing pattern in the order of **C_8**(2.76 eV)> **C_{13}**(2.75 eV)> **C_9**(2.72 eV)>**C_{12}**(2.72 eV)> **C_{11}**(2.69 eV)> **C_{10}**(2.65 eV)> **C_{14}**(2.64 eV). The emission spectra of the dyes, recorded in the solution (DCM) and solid thin film state, are shown in **Figure 4.9**, and the data are tabulated in **Table 4.9** All the compounds gave only a single emission band without any fine vibronic structure, indicating the floppy nature in the excited state. Further, changing the auxiliary electron donating groups makes the photoluminescence (PL) spectra range from 478 to 506 nm possessing a full width at half maxima (FWHM) of ~70 nm**,** indicating that enhanced colour purity in the device**.** Amongst the tested compounds, **C_{10}** and **C_{14}** displayed the bathochromic shift in the emission values. This is due to the biphenyl and thienyl systems which act as strong electron-donating moieties. Their emission maxima in the solid thin film state were measured to be between 522 and 536 nm. In addition, they displayed high quantum yields (28-42 %) in the solid thin film state.

For deeper insights into the ICT phenomenon, the solvatochromic behaviour of **$C_{8\text{-}14}$** was investigated in five solvents with increasing polarity order: toluene, acetone, ethyl acetate, acetonitrile, and ethanol. The absorption spectra of the dyes are not much affected by the solvent polarity, indicating the non-polar nature of their ground states. In contrast, the emission maxima of the dyes shift accordingly with the increase in the solvent polarity, as shown in **Table 4.4** and **Figure 4.10** to **4.16**.

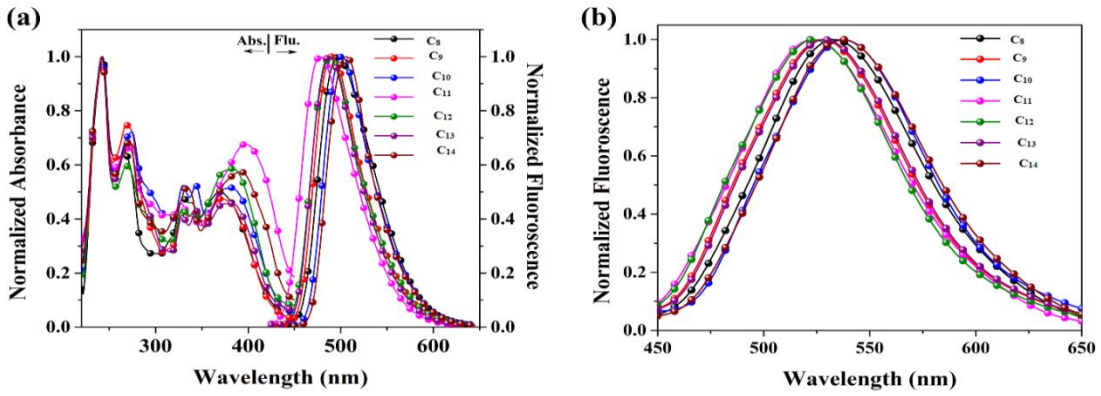

Figure 4.9. Absorbance and fluorescence spectra of $\mathbf{C_{8\text{-}14}}$ (a) in solution (b) in thin film state

Table 4.3. Photophysical data of the fluorophores $\mathbf{C_{8\text{-}14}}$ in DCM and solid thin film state

Compds	λ_A (nm)[a]	λ_E (FWHM) (nm)[a]	λ_E (FWHM) (nm)[b]	E_g^{opt} (eV)	$\Delta\lambda$ (cm^{-1})	Φ_F
$\mathbf{C_8}$	242,330,368	497(77)	532(84)	2.72	7213	0.28
$\mathbf{C_9}$	242,329,371	491(70)	528(81)	2.76	6628	0.37
$\mathbf{C_{10}}$	242,330,381	503(74)	537(82)	2.65	6492	0.27
$\mathbf{C_{11}}$	242,328,398	478(71)	522(80)	2.69	4398	0.34
$\mathbf{C_{12}}$	241,330,383	489(77)	524(83)	2.72	5757	0.42
$\mathbf{C_{13}}$	241,330,379	487(72)	529(84)	2.75	5852	0.24
$\mathbf{C_{14}}$	242,333,393	506(76)	536(81)	2.64	6082	0.26

λ_A: Absorption maxima; λ_E: Emission maxima;
FWHM: Full width at half-maximum;
$\mathbf{E_g^{opt}}$**:** Optical band gap;
$\Delta\lambda$: Stokes shift; Φ_F: Fluorescence quantum yields
[a] Recorded in DCM (10^{-5} M) at room temperature
[b] Recorded in a solid thin-film state

Table 4.4. Photophysical data of the $\mathbf{C_{8\text{-}14}}$ in various solvents of increasing polarity

Comp	Toluene			Ethyl Acetate			Acetone			Ethanol			Acetonitrile		
	λ_A	λ_E	$\Delta\lambda$	λ_A	λ_E	$\Delta\lambda$	λ_A	λ_E	$\Delta\lambda$	λ_A	λ_E	$\Delta\lambda$	λ_A	λ_E	$\Delta\lambda$
$\mathbf{C_8}$	370	472	5840	366	488	683	367	501	7287	364	530	8604	366	502	7402
$\mathbf{C_9}$	396	470	3975	367	479	637	368	497	7053	364	525	8424	367	517	7905
$\mathbf{C_{10}}$	433	473	1953	384	487	550	382	504	6336	433	543	4678	382	525	7130
$\mathbf{C_{11}}$	426	474	2421	402	492	455	405	509	5044	412	527	5296	401	503	5056

C_{12}	425	465	2024	369	462	545	372	488	6389	373	517	7467	372	504	7040
C_{13}	397	483	4484	370	456	509	372	485	6263	370	510	7419	370	504	7185
C_{14}	386	469	4584	338	454	755	401	473	3796	387	530	6971	387	513	6346
λ_A: Absorption maxima in nm; λ_E: Emission maxima in nm; $\Delta\lambda$: Stokes shift in cm^{-1}															

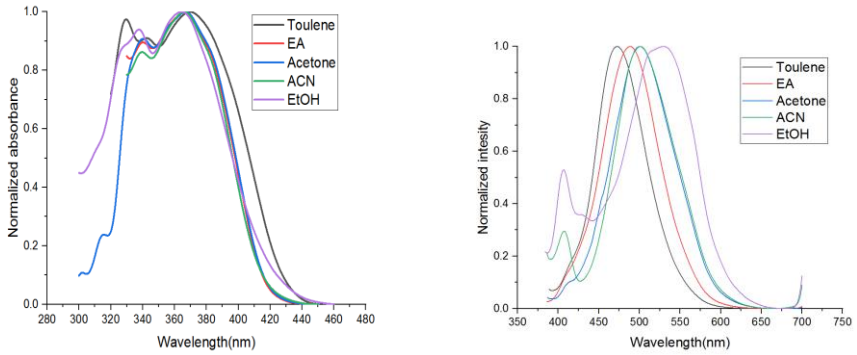

Figure 4.10. UV and PL spectra of **C_8** in different solvents

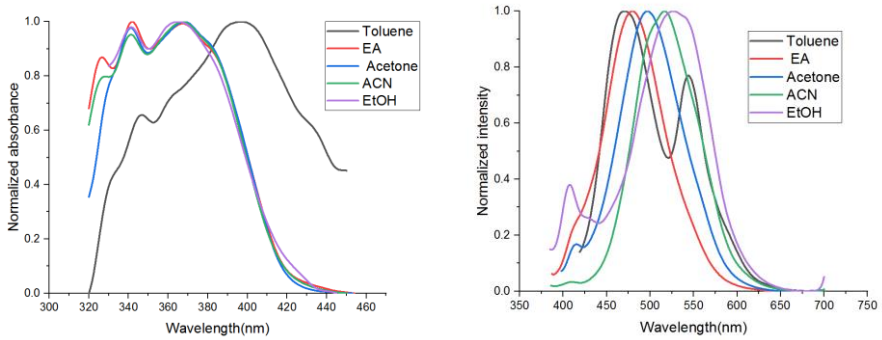

Figure 4.11. UV and PL spectra of **C_9** in different solvents

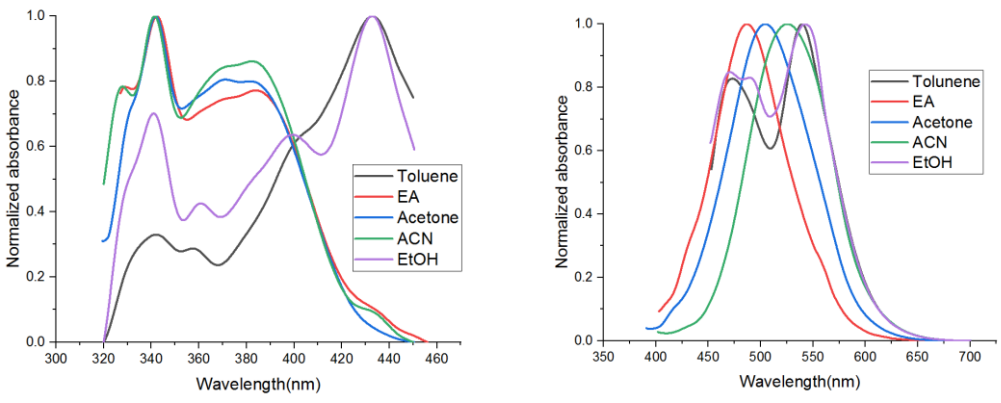

Figure 4.12. UV and PL spectra of **C_{10}** in different solvents

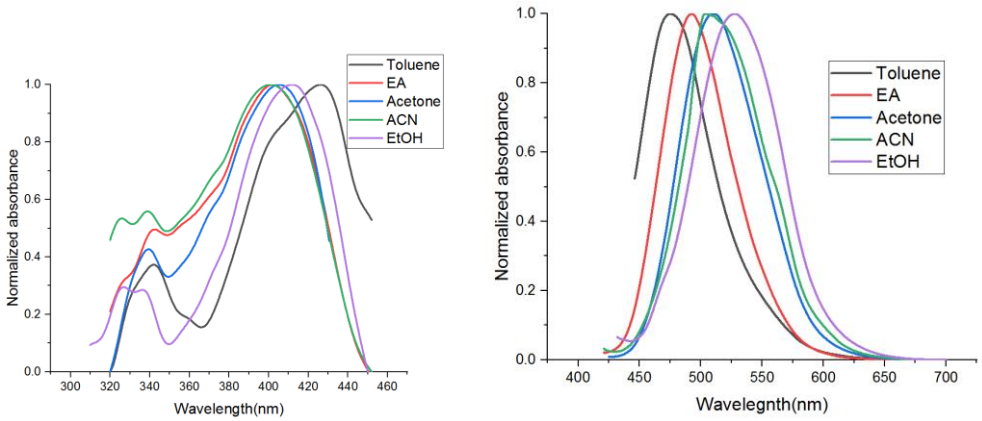

Figure 4.13. UV and PL spectra of $\mathbf{C_{11}}$ in different solvents

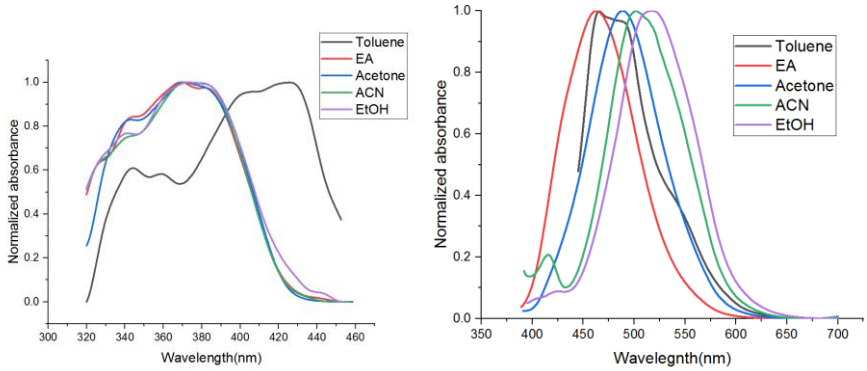

Figure 4.14. UV and PL spectra of $\mathbf{C_{12}}$ in different solvents

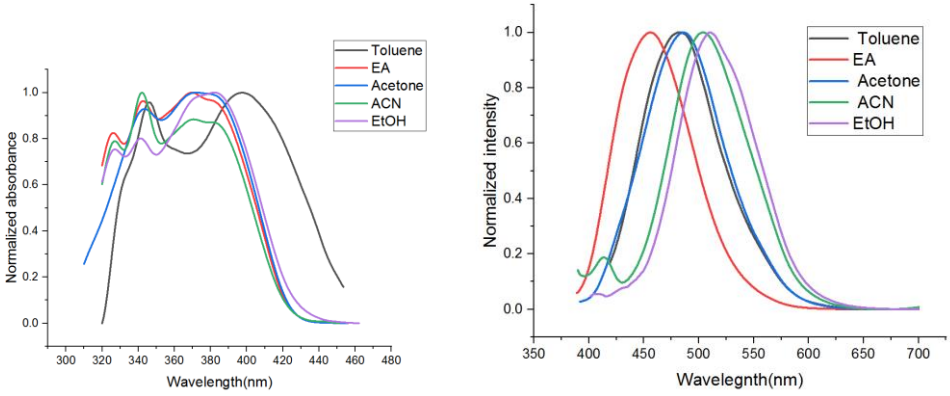

Figure 4.15. UV and PL spectra of $\mathbf{C_{13}}$ in different solvents

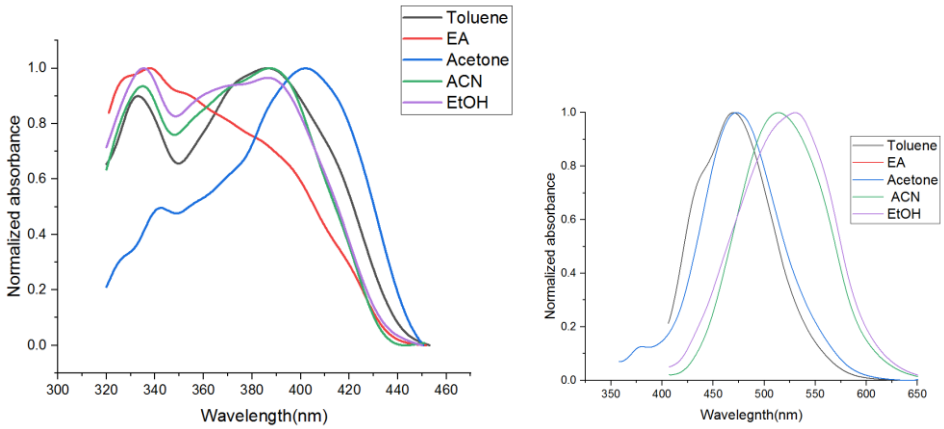

Figure 4.16. UV and PL spectra of **C_{14}** in different solvents

4.1.4.3 Carbazole derivatives $C_{15\text{-}21}$ (Series-3)

The absorption and emission spectra of **$C_{15\text{-}21}$** are shown in **Figure 4.17** and the corresponding photophysical data are tabulated in **Table 4.5**. All of them showed a good quantum yield in the range of 10-40% in the thin film state. Their absorption spectra displayed distinct absorption bands which are attributed to π-π* transition and ICT interactions between donor and acceptor units. The two prominent absorption bands were observed at 270 and 236 nm, the former is due to the π-π* electronic transition occurring within the carbazole scaffold itself and the latter is owing to the presence of the secondary donor groups. The phenyl rings with electron-donating auxochromic groups like hydroxy, amino, methoxy, and methyl strengthen the auxiliary behaviour of the secondary electron-donating moiety. These auxiliary secondary donors are 4-tolyl, 4-biphenyl, 4-aminophenyl, 4-methoxyphenyl, and 4-hydroxyphenyl moieties.

In addition, comparatively a weaker absorption peak was detected in the range of 374 to 391 nm. The bands at 374 (**C_{15}**), 376 (**C_{16}**), 383 (**C_{17}**), 391 (**C_{18}**), 380 (**C_{19}**), 377 (**C_{20}**), 391 nm (**C_{21}**) correspond to ICT transition from aryl/heteroaryl group to cyanopyridone core. The auxochromic groups in the secondary donors have a significant impact on the absorption and emission of the molecules. Interestingly, the molecules containing amino and thienyl substituents display a positive shift in the ICT transition towards a longer wavelength (red region), suggesting that the additional donors play a significant role in facilitating the ICT process. Their optical band gap was determined from the solution state absorption spectra and the values were found

to be 2.85 (**C_{15}**) 2.83 (**C_{16}**) 2.84 **(C_{17}**) 2.78 (**C_{18}**) 2.89 (**C_{19}**), 2.93 (**C_{20}**) and 2.79 eV (**C_{21}**).

In respect of emission behaviour, **$C_{15\text{-}21}$** exhibited a solitary emission peak falling within the range of 468 to 510 nm. The compounds **C_{17}**, and **C_{18}** showed the highest emission intensity due to the significant electron-donating characteristics of their secondary groups.

Normally, the magnitude of the Stokes shift is determined by the electronic structure of the molecule and is a basic characteristic of a luminous material. It gives information about the difference in the structure and properties of the molecules between the ground and excited states. The calculated values of Stokes shift for **$C_{15\text{-}21}$** were found to be 6737**,** 6434, 6307, 4207, 5865, 6075, and 5967 cm^{-1}, respectively. The observed large Stokes shift signifies the effective ICT properties in these π-conjugated structures and it is a most advantageous feature for a desired emitter in the fabrication of OLEDs. Among these entire compound, compound containing, phenyl group as donor group and cyanopyridone as a acceptor core showed a maximum Stokes shift, suggesting a significant charge transfer from donor moiety to the respective acceptor groups.

For the solvatochromic study, **$C_{15\text{-}21}$** were dissolved in solvents of varied polarities, *viz*. toluene, acetone, ethyl acetate, acetonitrile, and ethanol, and their absorption and emission spectra were recorded. Their absorption spectral analysis indicated that the polarity of the solvent had no discernible impact on the compound, suggesting a non-polar ground state nature. However, the emission spectra exhibited a notable redshift, implying an interaction between the solvents and the molecule's ground state. The observed red-shift emission in polar solvents can be attributed to a diminished energy gap between the compound's ground and excited states. This reduced energy gap arises from the presence of the donor and acceptor moieties involved in conjugation, resulting in the electron cloud being delocalized towards the acceptor side from the donor side. Consequently, an internal charge-transfer state is established in addition to the locally excited state. The enhanced polarity of polar solvents favours the formation of the internal charge-transfer state. As a consequence,

the energy difference between the ground and excited states diminishes in polar solvents, leading to a red-shifted emission.

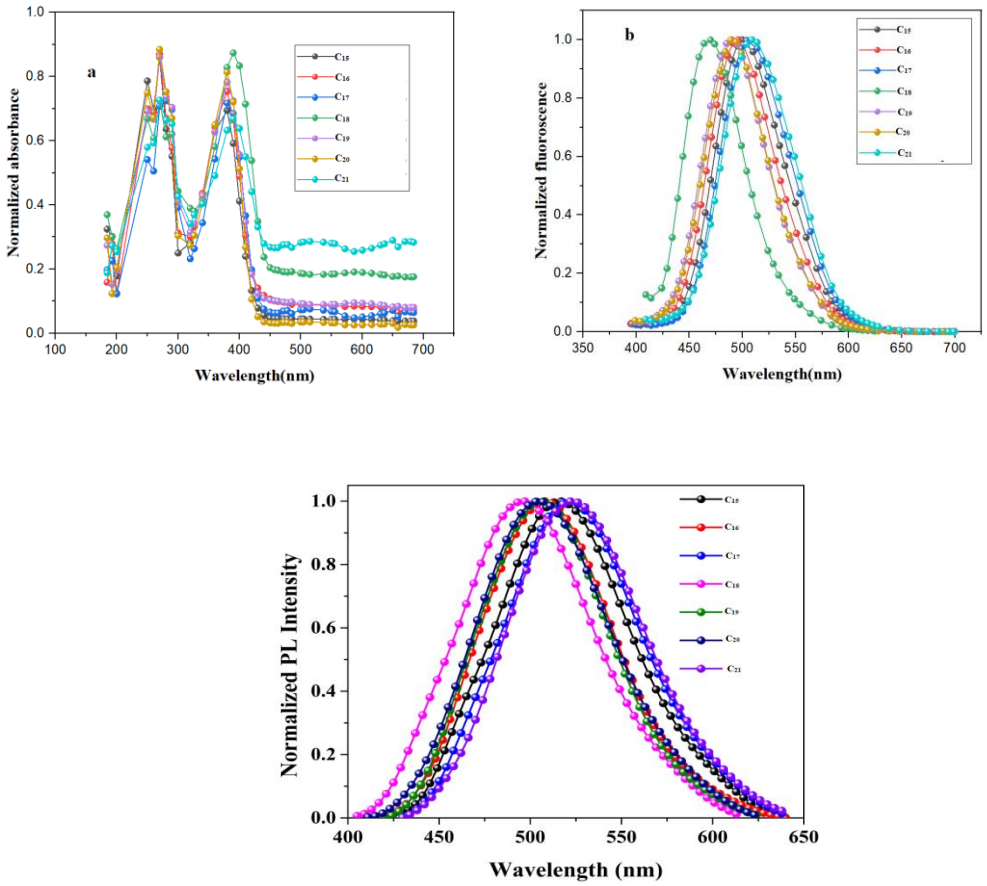

Figure 4.17. (a) Absorption spectra of **C_{15-21}** in solution state (b) fluorescence spectra of **C_{15-21}** in solution state (c) fluorescence spectra of **C_{15-21}** in thin film state

Table 4.5. Photophysical data of **C_{15-21}** in DCM and solid thin-film state

Compds	**λ_A[a] (nm)**	**λ_E[a](FWHM) (nm)**	**λ_E[b](FWHM) (nm)**	**E_g^{opt} (eV)**	**$\Delta\lambda$ (cm^{-1})**	**Φ_F**
C_{15}	236,270,374	500(77)	516(87)	2.85	6737	0.36
C_{16}	234,270,376	496(79)	508(85)	2.83	6434	0.41
C_{17}	236,275,383	505(86)	521(88)	2.84	6307	0.63
C_{18}	236,269,391	468(67)	496(89)	2.78	4207	0.24
C_{19}	236,269,380	489(79)	506(83)	2.89	5865	0.58
C_{20}	236,271,377	489(75)	503(87)	2.93	6075	0.31

C_{21}	236,271,391	510(87)	523(88)	2.79	5967	0.29

λ_A: Absorption maxima λ_E: Emission maxima; **FWHM**: Full width at half-maximum; $\mathbf{E_g^{opt}}$**:** Optical band gap; Δλ:Stokesshift; Φ_F: Fluorescence quantum yields

[a] Recorded in DCM (10^{-5} M)at room temperature

[b] Recorded in solid thin-film state

Table 4.6. Photophysical data of $\mathbf{C_{15\text{-}21}}$ in solvents of varying polarities

Fluoro-phore	Toluene			Ethyl acetate			Acetone			Ethanol			Acetonitrile		
	λ_A	λ_E	Δλ	λ_A	λ_E	Δλ	λ_A	λ_E	Δλ	λ_A	λ_E	Δλ	λ_A	λ_E	Δλ
C_{15}	372	457	4999	367	486	6671	368	507	7450	369	448	4778	369	523	7979
C_{16}	373	451	4636	369	480	6266	369	500	7100	371	513	7461	372	522	7724
C_{17}	381	465	4741	374	491	2871	374	510	7130	377	515	7107	380	531	7483
C_{18}	384	461	4349	391	469	4253	401	485	4319	393	510	5837	404	503	4871
C_{19}	375	443	4093	371	454	4927	373	493	6525	374	502	6817	371	523	7833
C_{20}	369	448	4778	370	445	6535	372	488	6389	374	505	6935	379	510	6777
C_{21}	384	456	4111	370	456	5097	374	491	6371	381	469	4924	386	531	7074

λ_A: Absorption maxima in nm; λ_E: Emission maxima in nm; Δλ: Stokes shift in cm^{-1}

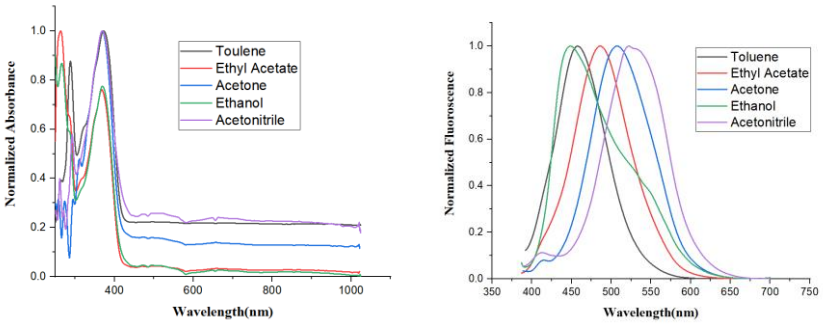

Figure 4.18. UV and PL spectra of $\mathbf{C_{15}}$ in different solvents

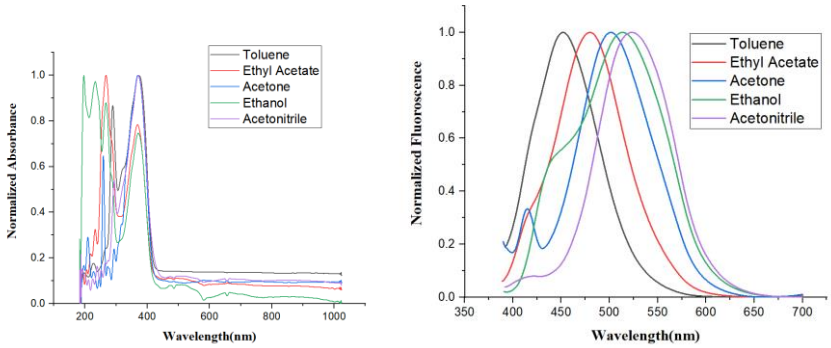

Figure 4.19. UV and PL spectra of $\mathbf{C_{16}}$ in different solvents

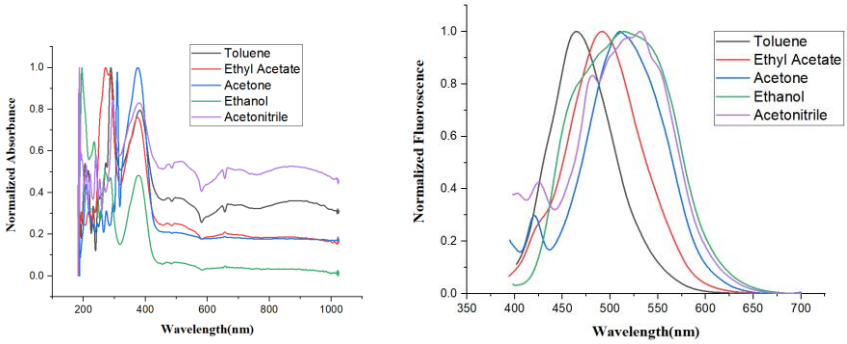

Figure 4.20. UV and PL spectra of **C_{17}** in different solvents

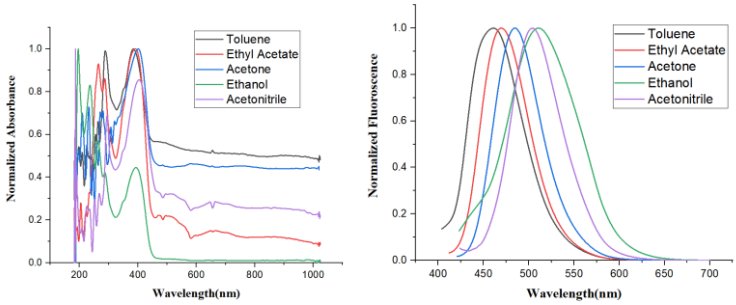

Figure 4.21.UV and PL spectra of **C_{18}** in different solvents

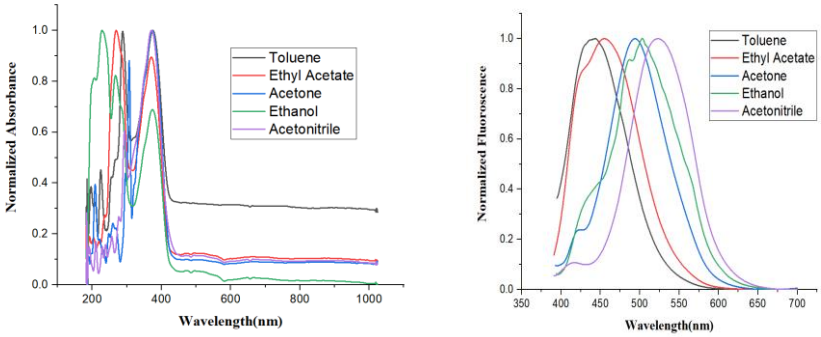

Figure 4.22.UV and PL spectra of **C_{19}** in different solvents

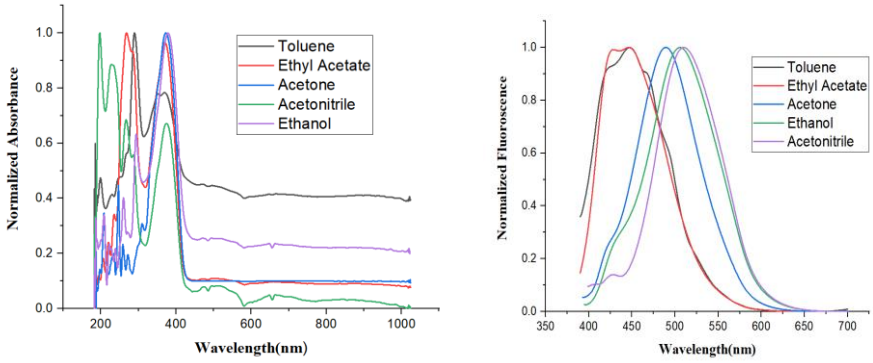

Figure 4.23.UV and PL spectra of **C_{20}** in different solvents

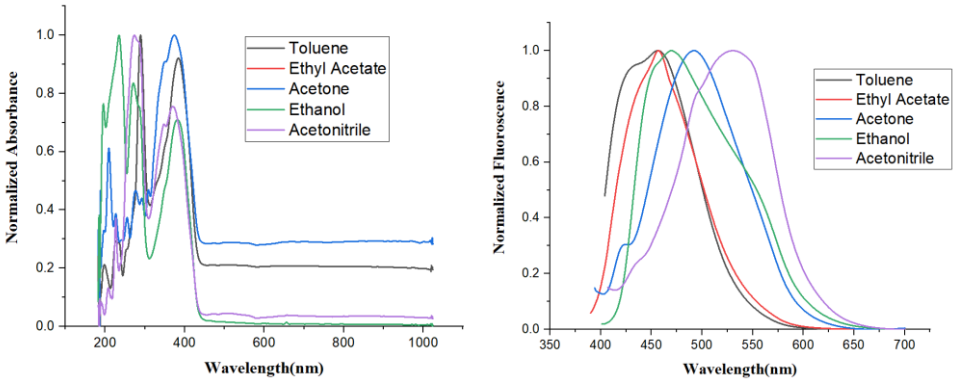

Figure 4.24. UV and PL spectra of $\mathbf{C_{21}}$ in different solvents

4.1.4.4 Phenothiazine-based cyanopyridones $C_{22\text{-}28}$ (Series-4)

The absorption and emission spectra of $\mathbf{C_{22\text{-}28}}$ are depicted in **Figure 4.25** and the respective spectral data are summarized in **Table 4.7.** Their absorption spectra exhibited three distinct peaks. These peaks originate from the presence of three aromatic groups within the molecules. The electron-rich phenothiazine group is responsible for the peak observed at 294 nm, indicating a π-π* transition within this specific group. The presence of secondary donor groups, such as phenyl ($\mathbf{C_{22}}$), tolyl ($\mathbf{C_{23}}$), biphenyl ($\mathbf{C_{24}}$), 4-aminophenyl ($\mathbf{C_{25}}$), 4-methoxyphenyl ($\mathbf{C_{26}}$), 4-hydroxyphenyl ($\mathbf{C_{27}}$), and 2-thienyl ($\mathbf{C_{28}}$) contributes to the peak observed at 250 nm. The peak appeared at a higher wavelength region can be attributed to an ICT transition from donor to acceptor group. Here, the strength of the secondary donor group has influenced the ICT. Notably, the compounds with thiophene and amine substitutions give a red-shift in the absorption. This is due to the strong electron-donating nature of the molecules.

In general, the knowledge of the material's optical band gap holds great significance in assessing its electrical conductivity and plays a fundamental role in organic electronics. Normally, it serves as a critical factor in selecting appropriate organic semiconducting materials for the production of stable and efficient OLEDs.

The band gap values were calculated from absorption data using the formula 1240/λ. The obtained band gap values of $\mathbf{C_{22\text{-}28}}$ are in between 2.66 to 2.95 eV.

In the emission spectra of **C_{22-28},** compounds exhibited a single emission peak within the wavelength range of 486 to 497 nm. However, molecules containing thiophene and biphenyl substitution displayed a red-shift in their emission, which can be attributed to their strong electron-donating nature.

Further, Stokes shift values were calculated using absorption data. They were found to in the range of 3097 to 6576 cm^{-1}. All these compounds showed a high Stokes shift value this is because of presence of strong donor group cyanopyridone core in **C_{22-28}**. These large stoke shift indicate the good light emission properties in the compounds.

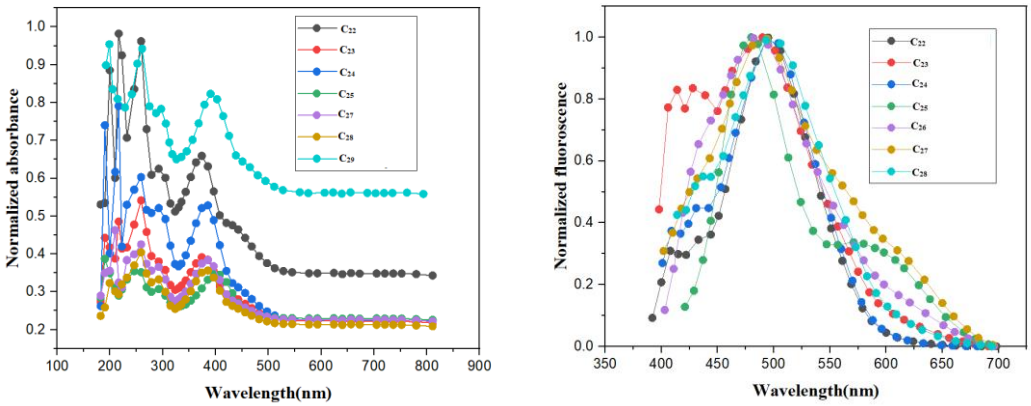

Figure 4.25. Absorbance and fluorescence spectra of **C_{22-28}** in solution

Table 4.7. Photophysical data of **C_{22-28}** in DCM

Comps	λ_A^a (nm)	λ_E^a (FWHM) (nm)	E_g^{opt} (eV)	$\Delta\lambda$ (cm^{-1})	Φ_F
C_{22}	255,296,374	496(88)	2.95	6576	0.10
C_{23}	255,294,377	491(144)	2.55	6158	0.05
C_{24}	255,294,382	497(97)	2.85	6057	0.45
C_{25}	254,292,403	479(76)	2.71	3937	0.34
C_{26}	255,294,383	486(129)	2.72	5533	0.46
C_{27}	257,292,383	490(152)	2.66	5701	0.32
C_{28}	258,258,395	497(133)	2.82	5195	0.50

λ_A: Absorption maxima λ_E: Emission maxima; **FWHM**: Full width at half-maximum; $\mathbf{E_g^{opt}}$**:** Optical band gap; $\Delta\lambda$: Stokes shift; Φ_F: Fluorescence quantum yields
[a] Recorded in DCM (10^{-5} M)at room temperature

In solvatochromic studies of $\mathbf{C_{22\text{-}28}}$, their absorption properties remain unaffected by changing the solvent polarity. However, when examining the emission spectra, an interesting observation was made; as the solvent polarity increases, a blue-shift was observed. This indicates that the ground state of the molecules is more polar than the excited state. It can be inferred that polar solvents stabilize the ground state to a greater extent than the excited state, resulting in an increased energy gap between the excited and ground states. Consequently, this energy gap shift leads to the observed blue-shift in the emission spectra.

Table 4.8. Photophysical data of $\mathbf{C_{22\text{-}28}}$ in solvents of varying polarities

comps	Toluene			Ethyl Acetate			Acetone			Methanol			Acetonitrile		
	λ_A	λ_E	$\Delta\lambda$	λ_A	λ_E	$\Delta\lambda$	λ_A	λ_E	$\Delta\lambda$	λ_A	λ_E	$\Delta\lambda$	λ_A	λ_E	$\Delta\lambda$
$\mathbf{C_{22}}$	372	457	4999	375	486	6090	375	507	6942	364	448	5151	373	523	7689
$\mathbf{C_{23}}$	374	567	9101	376	555	8577	375	502	6746	370	509	7380	364	512	7941
$\mathbf{C_{24}}$	375	570	9122	379	490	5977	379	508	6700	375	507	6942	371	456	5024
$\mathbf{C_{25}}$	400	559	7110	398	564	7395	408	496	4348	404	494	4509	410	475	3337
$\mathbf{C_{26}}$	382	564	8447	383	559	8220	383	498	6029	382	505	6376	374	490	6329
$\mathbf{C_{27}}$	376	559	8706	382	565	8478	383	554	8059	382	504	6336	380	500	6315
$\mathbf{C_{28}}$	387	559	7950	396	558	7331	389	486	5130	388	509	6126	389	453	3631

λ_A: Absorption maxima in nm; λ_E: Emission maxima in nm; $\Delta\lambda$: Stokes shift in cm^{-1}

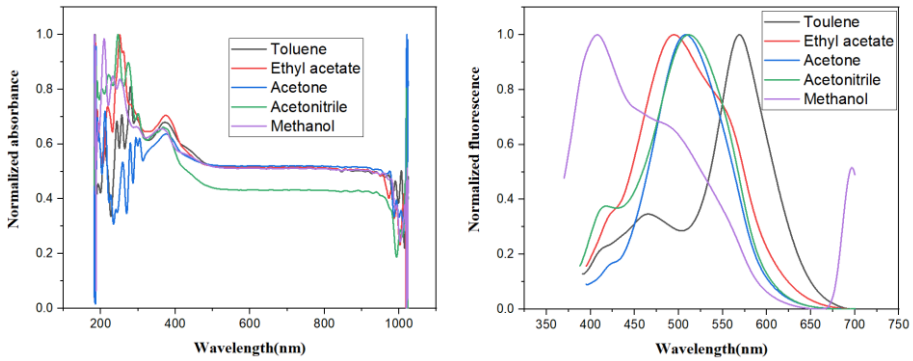

Figure 4.26. UV and PL spectra of $\mathbf{C_{22}}$ in different solvents

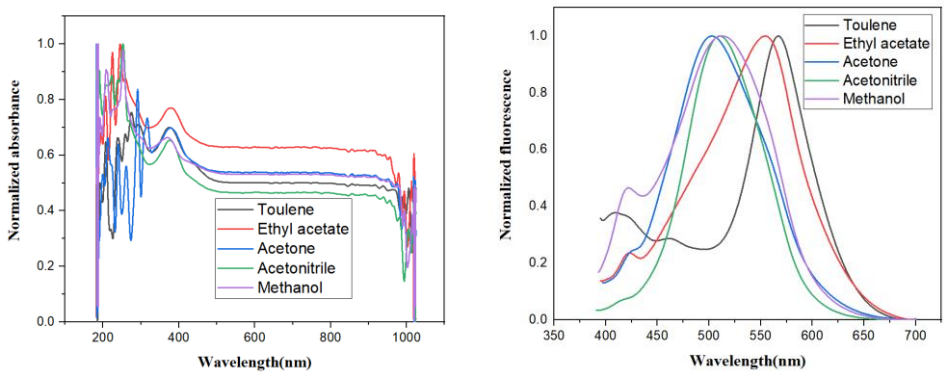

Figure 4.27. UV and PL spectra of **C_{23}** in different solvents

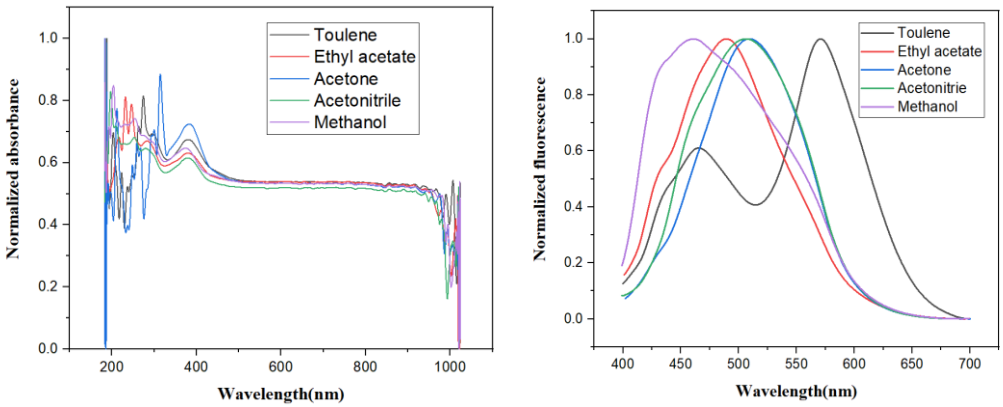

Figure 4.28. UV and PL spectra of **C_{24}** in different solvents

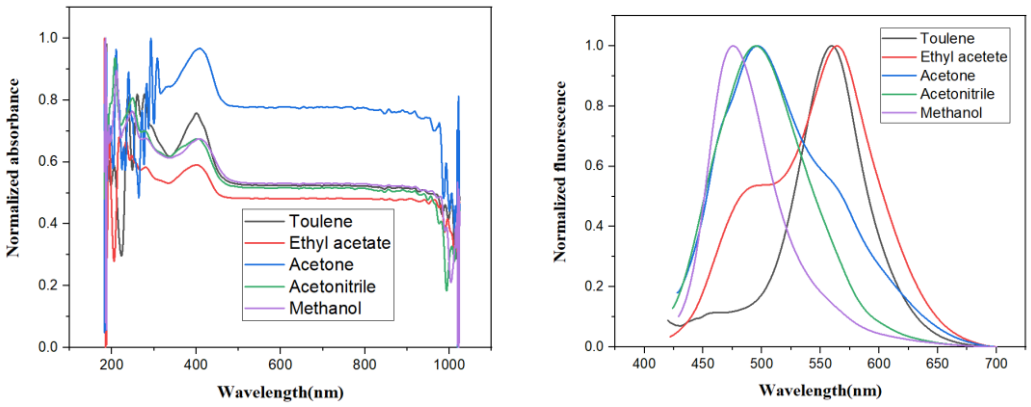

Figure 4.29. UV and PL spectra of **C_{25}** in different solvents

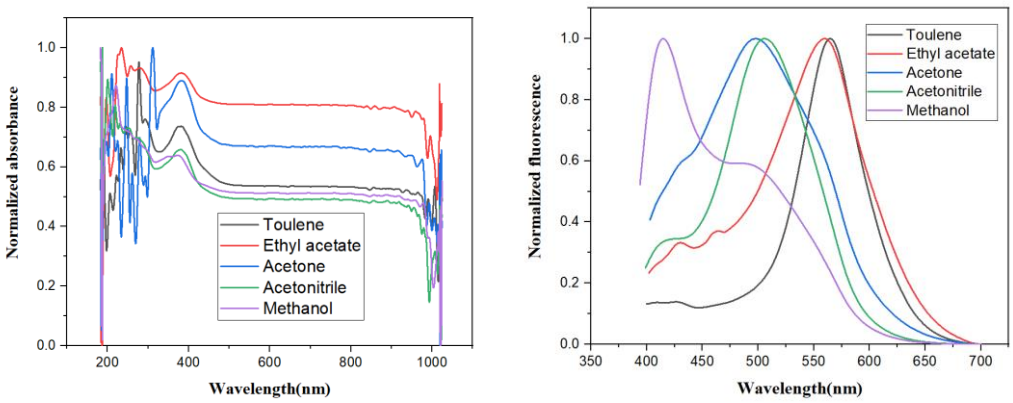

Figure 4.30. UV and PL spectra of **C_{26}** in different solvents

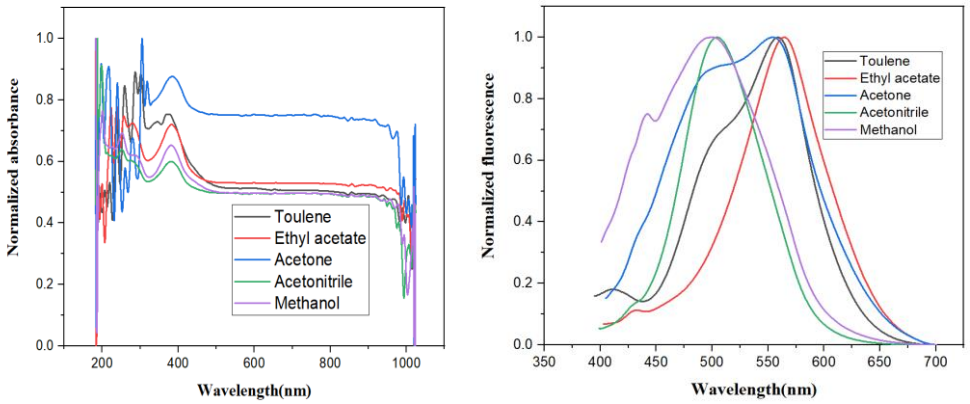

Figure 4.31. UV and PL spectra of C_{27} in different solvents

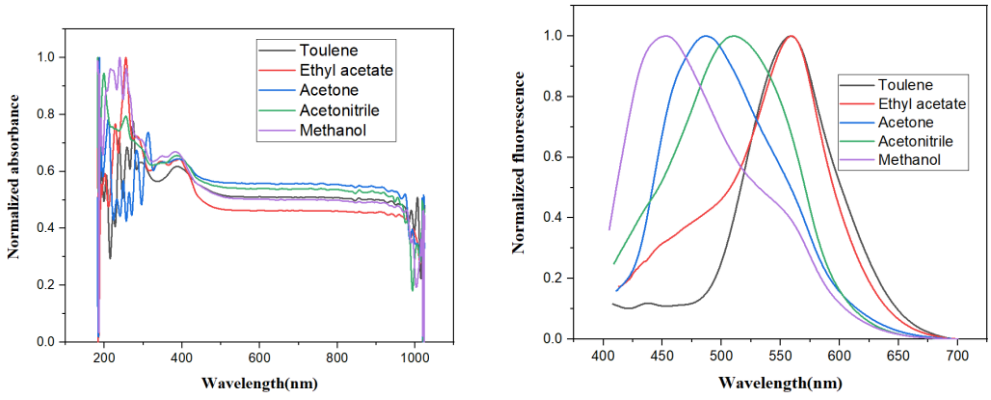

Figure 4.32. UV and PL spectra of **C_{28}** in different solvents

4.1.4.5 DPA-linked cyanopyridones $C_{29\text{-}34}$ (Series-5)

The UV-VIS absorption and fluorescence emission spectra of **$C_{29\text{-}34}$** are given in **Figure 4.33**. The resulting data are summarized in **Table 4.9**. It was observed that absorbance maxima were in descending order, **C_{34}** (400 nm)>**C_{32}** (388 nm)>**C_{33}** (385

nm)>**C_{31}** (383nm)>**C_{30}** (382 nm)>**C_{29}** (377 nm). It is worth noting that **C_{34}** exhibited a unique characteristic of a blue-shift in comparison to other compounds of the series. This variation in spectral pattern could be attributed to the electron-donating nature of the thiophene scaffold in the molecule.

The emission wavelengths of these compounds are in the order: **C_{31}** (554nm)>**C_{34}**(555 nm)>**C_{30}**(553 nm)>**C_{32}**(548 nm)>**C_{33}**(547 nm)>**C_{29}**(547 nm). Notably**,** **C_{31}** exhibited a red-shift in the λ_E values compared to the other molecules in the series. This is owing to the strong electron-donating nature of biphenyl group. Their calculated Stokes shift values are **C_{29}** (8243 cm^{-1})>**C_{30}** (80948 cm^{-1})>**C_{31}** (8091 cm^{-1})>**C_{32}** (7692 cm^{-1})>**C_{33}** (7525 cm^{-1})>**C_{34}** (67718 cm^{-1}). The large values of the Stokes shift indicate the presence of an effective intra molecular charge transfer property in the **$C_{29\text{-}34}$** molecules. Out these 6 compounds **C_{29}**, **C_{30}**, and **C_{31}** showed a highest Stokes shift vales this due to presence strong donor phenyl, tolyl, biphenyl groups and strong cyanopyridone acceptor unit. The calculated optical band gap values for **$C_{29\text{-}34}$** are 2.65, 2.60, 2.55, 2.80, 2.60, and 2.59 eV, respectively.

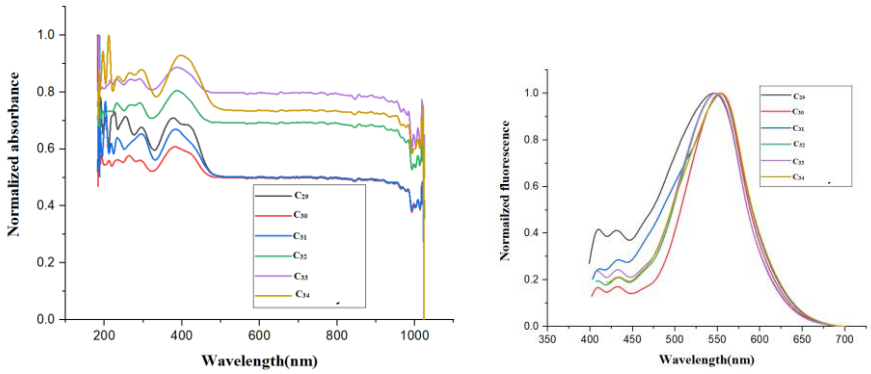

Figure 4.33. Absorbance and fluorescence spectra of the **$C_{29\text{-}34}$** in DCM

Table 4.9. Photophysical data of **$C_{29\text{-}34}$** in DCM

Compds	**λ_A[a] (nm)**	**λ_E[a](FWHM) (nm)**	**E_g^{opt} (eV)**	**$\Delta\lambda$ (cm^{-1})**	**Φ_F**
C_{29}	377	547(114)	2.65	8243	0.24
C_{30}	382	553(90)	2.60	8094	0.34

C_{31}	383	555(118)	2.55	8091	0.23
C_{32}	388	548(87)	2.80	7525	0.45
C_{33}	385	547(91)	2.60	7692	0.20
C_{34}	400	554(98)	2.59	7692	0.44

λ_A: Absorption maxima λ_E: Emission maxima; **FWHM**: Full width at half-maximum; $\mathbf{E_g^{opt}}$**:** Optical band gap; $\Delta\lambda$: Stokes shift; Φ_F: Fluorescence quantum yields
[a] Recorded in DCM (10^{-5} M)at room temperature

In solvatochromic studies, the absorption properties of the compounds remain unaffected with changes in solvent polarity. From the emission data, it is interesting to note that, as the solvent polarity increases, blue-shift has been observed in all the compounds. This observation indicated that the ground state of the molecules is more polar than the excited state. It can be inferred that polar solvents stabilize the ground state to a greater extent than the excited state, resulting in an increased energy gap between the excited and ground states. Consequently, this energy gap shift leads to the observed blue shift in the emission spectra.

Table 4.10. Photophysical data of **$C_{29\text{-}34}$** in solvents of varying polarities

Comp	**Toluene**			**Ethyl Acetate**			**Acetone**			**Methanol**			**Acetonitrile**		
	λ_A	λ_E	$\Delta\lambda$	λ_A	λ_E	$\Delta\lambda$	λ_A	λ_E	$\Delta\lambda$	λ_A	λ_E	$\Delta\lambda$	λ_A	λ_E	$\Delta\lambda$
C_{29}	383	500	6109	376	517	7253	380	504	6474	367	416	3209	376	451	4422
C_{30}	367	496	6434	384	525	6994	382	519	6910	374	481	5947	380	505	6513
C_{31}	384	499	6001	383	521	6915	384	511	6472	375	451	4493	383	460	4370
C_{32}	385	492	5648	385	521	6780	385	529	7070	379	473	5243	384	504	6200
C_{33}	374	490	6329	382	515	6760	385	516	6594	380	478	5395	383	500	6109
C_{34}	400	500	500	389	504	5865	397	513	5695	387	474	4742	396	462	3607

λ_A: Absorption maxima in nm; λ_E: Emission maxima in nm; $\Delta\lambda$: Stokes shift in cm^{-1}

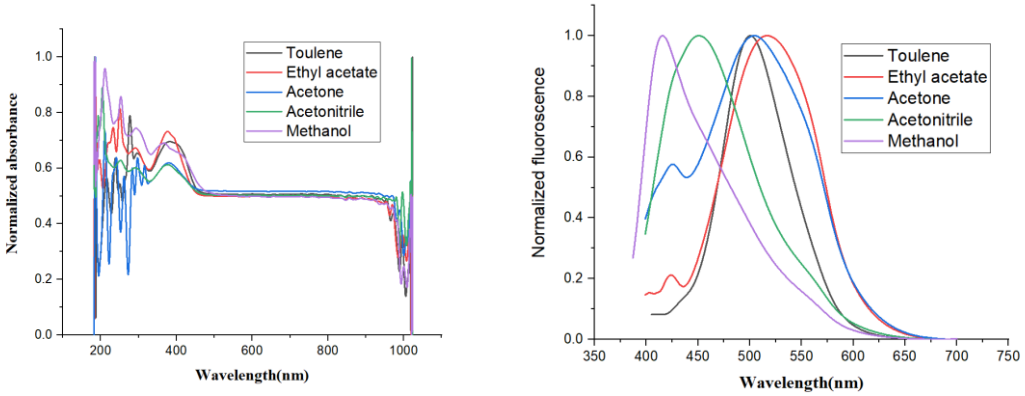

Figure 4.34. UV and PL spectra of C_{29} in different solvents

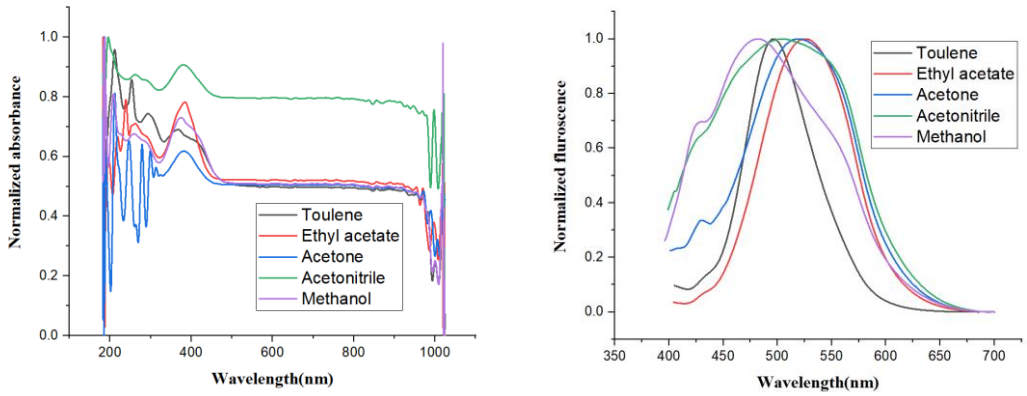

Figure 4.35. UV and PL spectra of C_{30} in different solvents

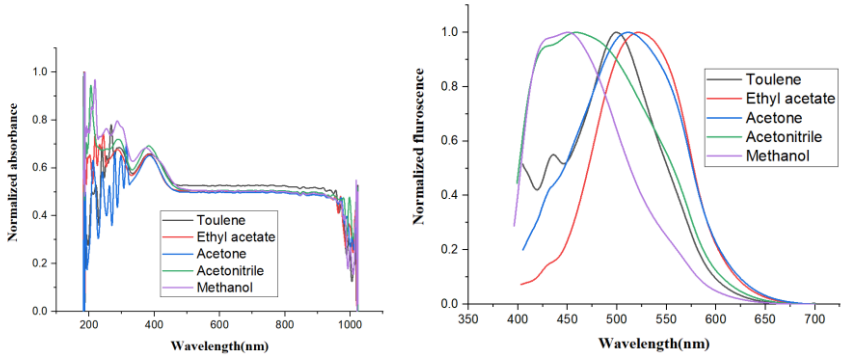

Figure 4.36. UV and PL spectra of C_{31} in different solvents

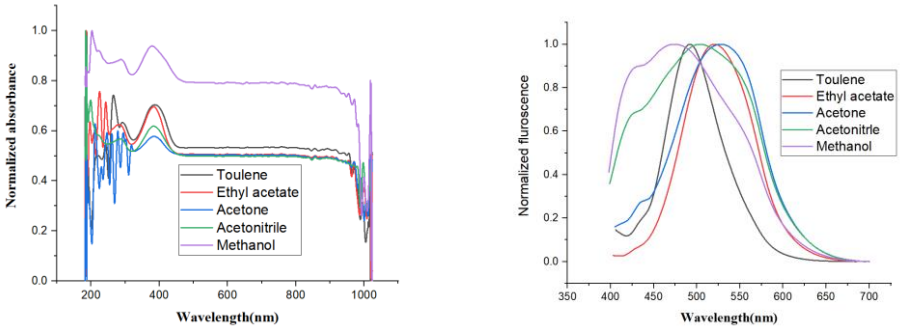

Figure 4.37. UV and PL spectra of C_{32} in different solvents

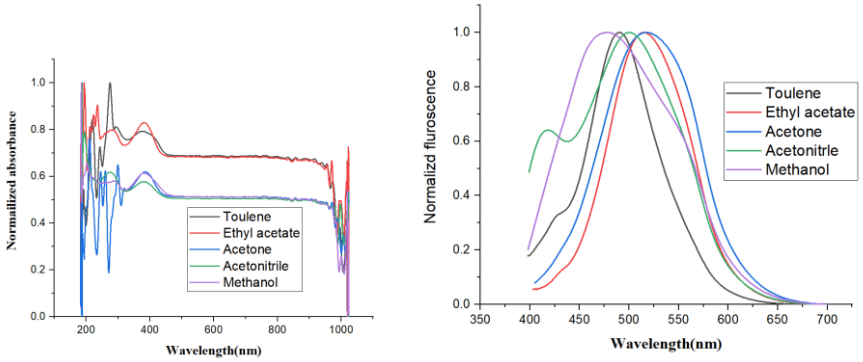

Figure 4.38. UV and PL spectra of $\mathbf{C_{33}}$ in different solvents

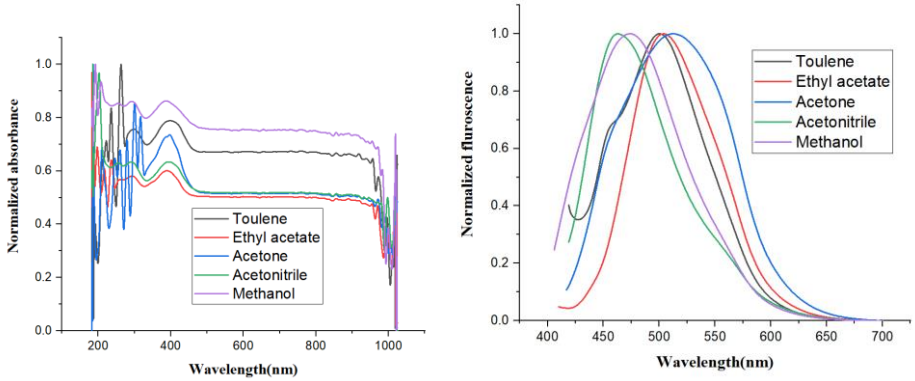

Figure 4.39. UV and PL spectra of C_{34} in different solvents

4.1.4.6 *N,N*-dimethylaniline-based cyanopyridones $\mathbf{C_{35\text{-}37}}$ (Series-6)

Figure 4.40 shows UV-VIS absorption and fluorescence emission spectra of $\mathbf{C_{35\text{-}37}}$. The observed data are listed in **Table 4.11**. They displayed the absorption maxima at 421, 433, and 429 nm, respectively. Further, the recorded λ_E values for $\mathbf{C_{35\text{-}37}}$ are 496, 513, 522 nm, respectively. Notably, $\mathbf{C_{37}}$ displayed the highest emission because of the strong donor strength of triphenylamine group. Further, their calculated Stokes shift values are 3591($\mathbf{C_{35}}$), 3601($\mathbf{C_{36}}$), and 4152 cm^{-1}($\mathbf{C_{37}}$). In the series, $\mathbf{C_{37}}$ demonstrated the most significant shift, indicating a pronounced intramolecular charge transfer (ICT) phenomenon within the molecule. Furthermore, the calculated band gap values follow a decreasing order 2.58($\mathbf{C_{37}}$), 2.61($\mathbf{C_{36}}$) and 2.66 eV($\mathbf{C_{35}}$).

The solvatochromic study of $\mathbf{C_{35\text{-}37}}$ in different solvents of varied polarities indicated that the solvent polarity had no distinct impact on the compound, suggesting their non-polar ground state nature. From the emission data, it is evident that all the compounds exhibited a notable red-shift, showing an interaction between the solvent

and the molecule's ground state. The observed red-shift emission in polar solvents can be attributed to a diminished energy gap between the compound's ground and excited states. This reduced energy gap arised from the presence of the donor and acceptor moieties involved in conjugation, resulting in the electron cloud being delocalized towards the acceptor side from the donor side. Consequently, an internal charge-transfer state has been established in addition to the locally excited state. The enhanced polarity of solvents facilitated the formation of the internal charge-transfer state. As a consequence, the energy difference between the ground and excited states diminished in polar solvents, leading to a red-shifted emission.

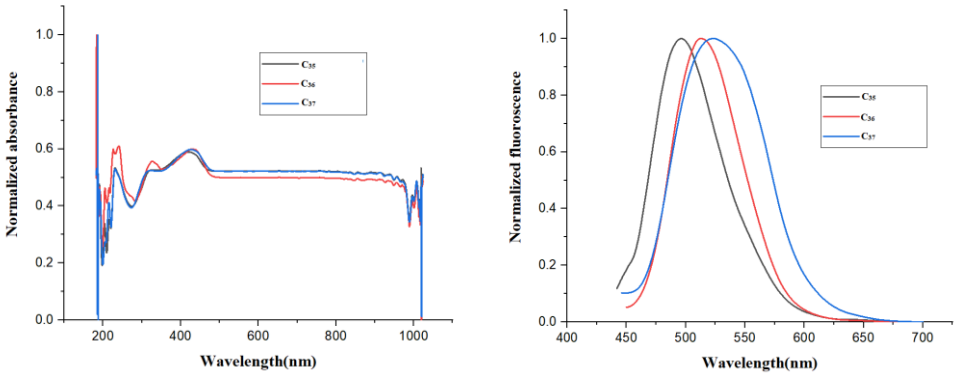

Figure 4.40. Absorbance and fluorescence spectra of **$C_{35\text{-}37}$** in DCM

Table 4.11. Photophysical data of **$C_{35\text{-}37}$** in DCM

Compound	**λ_A[a] (nm)**	**λ_E[a](FWHM) (nm)**	**E_g^{opt} (eV)**	**$\Delta\lambda$ (cm^{-1})**	**Φ_F**
C_{35}	421	496(72)	2.66	3591	0.20
C_{36}	433	491(71)	2.61	3601	0.35
C_{37}	429	497(93)	2.58	4152	0.45

λ_A: Absorption maxima λ_E: Emission maxima; FWHM: Full width at half-maximum; E_g^{opt}: Optical band gap; $\Delta\lambda$:Stokes shift; Φ_F: Fluorescence quantum yields
[a] Recorded in DCM (10^{-5} M) at room temperature

Table 4.12. Photophysical data of C_{35-37} in solvents of varying polarities

Fluorophore	Toluene			Ethyl Acetate			Acetone			Methanol			Acetonitrile		
	λ_A	λ_E	$\Delta\lambda$	λ_A	λ_E	$\Delta\lambda$	λ_A	λ_E	$\Delta\lambda$	λ_A	λ_E	$\Delta\lambda$	λ_A	λ_E	$\Delta\lambda$
C_{35}	400	480	4166	400	491	4633	421	522	4595	417	515	4563	415	517	4754
C_{36}	450	489	1772	422	510	4088	423	535	4949	426	549	5259	426	545	5125
C_{37}	480	481	1870	407	499	4529	419	522	4770	421	538	5165	422	543	5280

λ_A: Absorption maxima in nm; λ_E: Emission maxima in nm; $\Delta\lambda$: Stokes shift in cm^{-1}

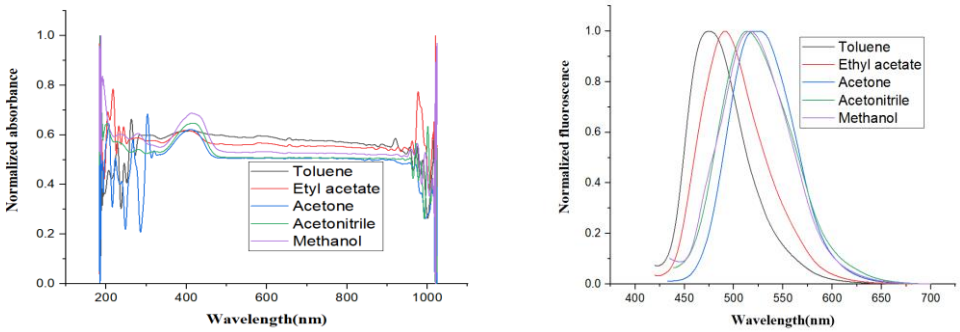

Figure 4.41. UV and PL spectra of C_{35} in different solvents

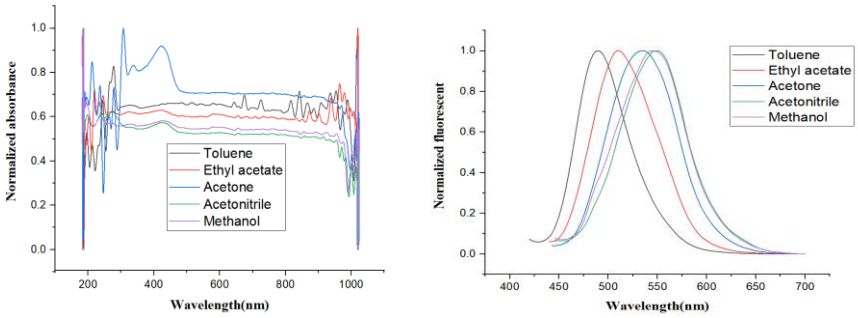

Figure 4.42. UV and PL spectra of C_{36} in different solvents

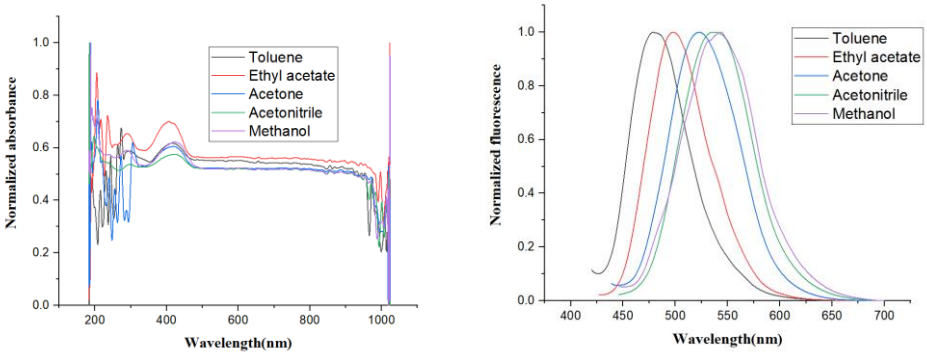

Figure 4.43. UV and PL spectra of C_{37} in different solvents

4.1.4.7 Substituted nicotinonitriles C_{38-42} (Series-7)

The absorption and emission spectra of C_{38-42} are shown in Figure 4.44 and the corresponding data are summarized in Table 4.13. From the absorption spectra, it is clear that C_{38-42} displayed λ_A at 378, 375,387, 421 and 382 nm, respectively. Their emission spectra showed λ_E at 497, 491, 505, 484, and 501 nm, respectively. In the series, C_{40} exhibited the highest emission because of the strong donor strength of the biphenyl group. Because of presence of electron-donating benzyloxy group on pyridine ring, aromaticity of the central core is lost. Consequently, blue-shift was observed in the compounds of the series. Further, their calculated Stokes shift values were found to be 6334(C_{38}), 6300(C_{39}), 6037(C_{40}), 3091(C_{41}), and 6217 cm^{-1}(C_{42}). The obtained high Stokes shift indicated the effective ICT property in these π-conjugated structures and it is a most require features for a desired emitter in the fabrication of OLEDs. Finally, the band gap values of the compounds were calculated. Their decreasing order is: 2.93(**C_{38}**), 2.93(**C_{40}**), 2.88(**C_{39}**), 2.91(C_{42}), and (2.91 eV (**C_{41}**).

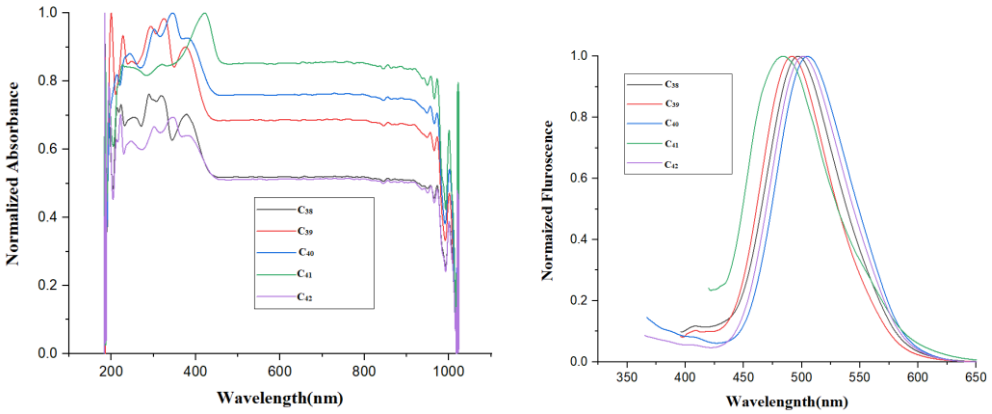

Figure 4.44. Absorbance and fluorescence spectra of the **C_{38-42}** in DCM

Table 4.13. Photophysical data of **C_{38-42}** in DCM

Compds	**λ_A[a] (nm)**	**λ_E[a](FWHM) (nm)**	**E_g^{opt} (eV)**	**Δλ (cm^{-1})**	**Φ_F**
C_{38}	378	497(71)	2.93	6334	0.22
C_{39}	375	491(74)	2.88	6300	0.27
C_{40}	387	505(80)	2.93	6037	0.30

C_{41}	421	484(85)	2.71	3091	0.35
C_{42}	382	501(82)	2.91	6217	0.39

λ_A: Absorption maxima λ_E: Emission maxima; FWHM: Full width at half-maximum; E_g^{opt}: Optical band gap; $\Delta\lambda$:Stokes shift; Φ_F: Fluorescence quantum yields
[a] Recorded in DCM (10^{-5} M) at room temperature

4.2 ELECTROCHEMICAL INVESTIGATION

Electrochemical investigation on organic materials offers precise insight into their oxidation and reduction behaviors. These studies are quite useful in estimating critical properties like HOMO and LUMO energies, band gap, and oxidation-reduction potentials. This information helps in assessing the semiconducting characteristics of these materials. In the present work, cyclic voltammetry (CV) was employed to delve into the electronic properties of **$C_{1\text{-}42}$**. The following section focuses on the comprehensive electrochemical analysis of newly synthesized compounds, including the discussion on experimental data.

4.2.1 Materials and methods

Electrochemical measurements were performed on AUTOLAB electrochemical workstation. The required supporting electrolyte, *i.e.* *n*-butyl ammonium hexafluorophosphate (n-Bu)$_4$N$^+$(PF_6) was procured from Sigma Aldrich Company whereas acetonitrile was purchased from Merck.

4.2.2 Experimental

CV experiments were conducted for **$C_{1\text{-}42}$** at a scan rate of 100 mV/s using 10^{-3} M solution in anhydrous acetonitrile. The solution was coated on the glassy carbon electrode, which acts as a working electrode, Ag/AgCl was used as a reference electrode, and a platinum electrode was employed as a counter electrode. Ferrocene was used as an internal standard to calibrate the redox potentials. Here, 0.1 M tetra-*n*-butylammonium tetrafluoroborate (in acetonitrile) was selected as a supporting electrolyte.

4.2.3 Results and discussion

Results of electrochemical measurements of $\mathbf{C_{1\text{-}42}}$ have been summarised in **Tables 4.14** to **4.20** and the corresponding data were discussed elaborately series-wise in the following section.

4.2.3.1 TPA substituted compounds $\mathbf{C_{1\text{-}7}}$ (Series-1)

Energy level alignment of the interfaces is typically crucial for the injection of charge carriers from adjacent transport layers into the emissive layer. As a result, understanding the HOMO and LUMO energy levels is vital.

The cyclic voltammograms of $\mathbf{C_{1\text{-}7}}$ are displayed in **Figure 4.45**, and the corresponding data are tabulated in **Table 4.14**. In these emitters, the oxidation and the reduction behaviour arise due to the presence of electron-donating and electron-withdrawing groups. The first oxidation and reduction potential values were used to estimate the HOMO and LUMO energies by assuming the oxidation potential of ferrocene is 4.8 eV. The data in eV were obtained by using the formulae:$\mathrm{E_{HOMO}} = -\mathbf{e}(\mathrm{E_{onset}^{oxd}} + 4.4\ \mathrm{eV})$, and $\mathrm{E_{LUMO}} = -\mathbf{e}(\mathrm{E_{onset}^{red}} + 4.4\ \mathrm{eV})$, respectively.

During the oxidation cycle, all the molecules exhibited two irreversible oxidation waves (relative to the Ag/AgCl electrode), which can be attributed to the strong electron-donating nature of triphenylamine moiety and the other donor group. The molecules exhibit first oxidation waves between 0.785 and 0.950 V, corresponding to HOMO energies –5.70 to –5.55 eV. The observed high-lying HOMO values suggested that the energy barrier between the emissive layer (consisting of the fluorophores) and the commonly used hole-transport materials is relatively small, which assists in effective hole injection into the emissive layer. Among all the compounds $\mathbf{C_3}$,$\mathbf{C_5}$,$\mathbf{C_6}$ and $\mathbf{C_7}$ has an ideal HOMO and LUMO levels, which effectively transfer the hole from hole transporting layer to HOMO of the compound and electrons from electron transporting layers to LUMO of the molecules. This is may be due to presence of electron donating TPA, biphenyl ($\mathbf{C_3}$), 4-aminophenyl ($\mathbf{C_4}$), 4-hydroxylphnyl ($\mathbf{C_6}$), and thiophene ($\mathbf{C_7}$) groups along with the strong electron-withdrawing cyanopyridone core. In addition to the oxidation waves, two waves were also observed during the reduction cycles owing to the presence of

electron-withdrawing carbonyl and pyridine groups in the fluorophores. These signals correspond to reduction potentials between –1.481 and –1.261 V. The corresponding low-lying LUMO energies detected in the range of –3.538 to –3.318 eV facilitate the passage of electrons into the emissive layer from the electron-transport materials. The band gap values were determined by the difference between the HOMO and LUMO levels of the molecules, which are in the range of 2.10-2.33 eV.

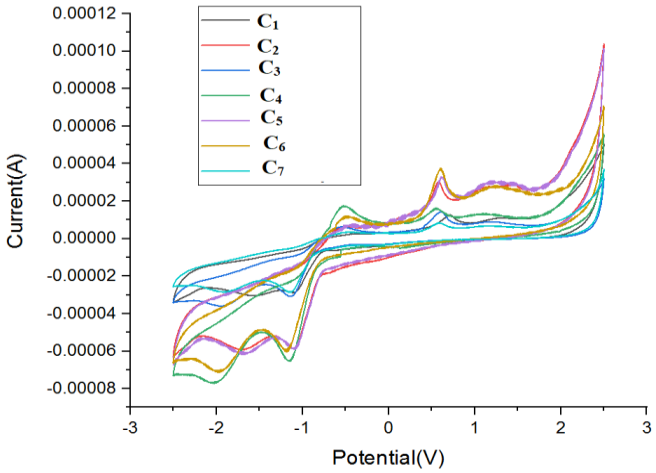

Figure 4.45. Cyclic voltammograms of **C_{1-7}**

Table 4.14. Electrochemical data of **C_{1-7}**

Compds	E^{ox}_{onset} (V)	E^{red}_{onset} (V)	E_{HOMO}[b](eV)	E_{LUMO}[c](eV)	E_g^{CV} (eV)
	CV measurements [a]				
C_1	0.950	–1.261	–5.70	–3.538	2.21
C_2	0.785	–1.324	–5.55	–3.475	2.10
C_3	0.879	–1.426	–5.69	–3.373	2.30
C_4	0.808	–1.481	–5.68	–3.318	2.29
C_5	0.839	–1.324	–5.69	–3.475	2.16
C_6	0.808	–1.473	–5.63	–3.326	2.33
C_7	0.863	–1.450	–5.63	–3.349	2.31

4.2.3.2 Pyrene-based compounds C_{8-14} (Series-2)

The obtained cyclic voltammograms of **C_{8-14}** are displayed in **Figure 4.46,** and the corresponding data are summarized in **Table 4.15**. All the fluorophores showed oxidation and reduction peaks owing to the presence of electron-donating groups and electron-withdrawing groups. Their second oxidation and reduction potential values were used to calculate the HOMO and LUMO energies of the

molecules. The data in eV were obtained by using the formulae:$E_{HOMO} = -\mathbf{e}(E^{oxd}_{onset} + 4.4\ eV)$, and $E_{LUMO} = -\mathbf{e}(E^{red}_{onset} + 4.4\ eV)$, respectively. The HOMO of these molecules were found to be –5.60(**C_8**), –5.46(**C_9**), –5.56(**C_{10}**), –5.60(**C_{11}**), –5.53(**C_{12}**), –5.50(**C_{13}**), and –5.74 eV(**C_{14}**). The observed high-lying HOMO values indicated that the energy barrier between the emissive layer of the dyes and the commonly used hole-transport materials is relatively small, which boosts effective hole injection into the emissive layer. The LUMO levels of the molecules were calculated to be –3.49(**C_8**), –3.38(**C_9**), –3.49(**C_{10}**), –2.91(**C_{11}**), –2.99(**C_{12}**), –3.27(**C_{13}**), and –3.52 eV(**C_{14}**). Among all the compound, 4-aminophenyl substituted compound showed small separation between HOMO and hole transporting layer. And small separation between the LUMO and electron transport layer. This is due to the high electron donating nature of the pyrene, 4-aminophenyl groups and electron withdrawing nature of cyanopyridone core. This results in effective hole and electron recombination. From their HOMO and LUMO energy levels, the band gaps were calculated, and the obtained data are 2.1(**C_8**), 2.07(**C_9**), 2.06(**C_{10}**), 2.68(**C_{11}**), 2.53(**C_{12}**), 2.22(**C_{13}**), and 2.22 eV (**C_{14}**).

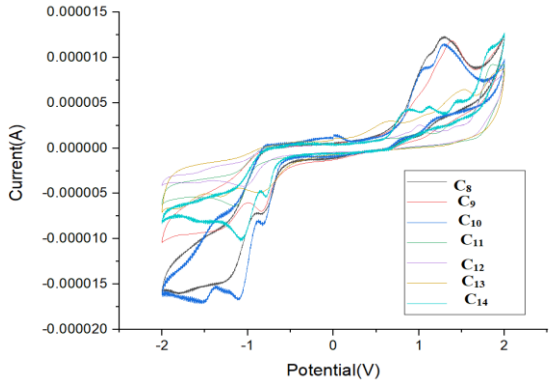

Figure 4.46. Cyclic voltammograms of $C_{8\text{-}14}$

Table 4.15. Electrochemical data of **$C_{8\text{-}14}$**

Compds	**E^{ox}_{onset} (V)**	**E^{red}_{onset} (V)**	**E_{HOMO} [b] (eV)**	**E_{LUMO} [c] (eV)**	**E_g^{CV} (eV)**
	CV measurements				
C_8	1.198	-0.931	-5.60	–3.49	2.11
C_9	1.061	-1.018	–5.46	–3.38	2.07
C_{10}	1.159	–0.906	-5.56	-3.49	2.06
C_{11}	1.198	-1.529	-5.60	-2.91	2.68
C_{12}	1.316	–1.405	–5.53	–2.99	2.53

C_{13}	1.100	-1.129	-5.50	-3.27	2.22
C_{14}	1.342	-0.880	-5.74	-3.52	2.22

4.2.3.3 Carbazole derivatives $C_{15\text{-}21}$ (Series-3)

Figure 4.47 depicts the cyclic voltammograms of **$C_{15\text{-}21}$** and **Table 4.16** summarizes the electrochemical data. The measured CV data revealed that molecules undergo both reversible oxidation and reduction processes, resulting in the formation of stable cation and anion radicals. This suggests that the emitters possesse bipolar transporting properties. The presence of an electron-donating group at 4^{th} and 6^{th} positions of the cyanopyridone core has led to the observation of two oxidation potential peaks in the CV sketches. Here, the second oxidation potential was used to calculate the HOMO level, for which Eq **4.2** was used.

$$E_{HOMO} = -(E^{oxd}_{onset} + 4.8\ eV) \quad \textbf{(4.2)}$$

From the calculations, the HOMO levels of the molecules were found to be in the range of –5.697 to –5.356 eV. These results indicated that the molecules possess a low energy barrier between the HOMO and hole-transporting materials, which results in the effective hole injection into the emissive layer. The electron-withdrawing nature of the cyano and carbonyl groups of the cyanopyridone core credit to the two reduction potential peaks in the CV curves. The LUMO levels of the molecules were calculated using the Eq **4.3**.

$$E_{LUMO} = -(E^{red}_{onset} + 4.8\ eV) \quad \textbf{(4.3)}$$

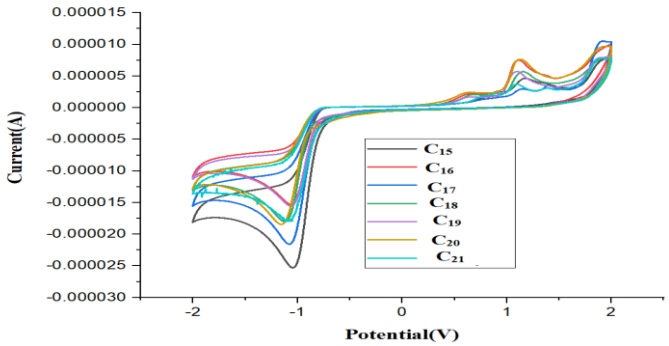

Figure 4.47. Cyclic voltammograms of **$C_{15\text{-}21}$**

Table 4.16. Electrochemical data of $\mathbf{C_{15\text{-}21}}$

Compds	E^{ox}_{onset} (V)	E^{red}_{onset} (V)	$E_{HOMO}{}^{b}$(eV)	$E_{LUMO}{}^{c}$(eV)	$E_g{}^{CV}$ (eV)
	CV measurements				
$\mathbf{C_{15}}$	1.040	−1.458	−5.440	−2.942	2.49
$\mathbf{C_{16}}$	0.982	−1.379	−5.382	−3.020	2.36
$\mathbf{C_{17}}$	1.297	−1.451	−5.697	−2.948	2.74
$\mathbf{C_{18}}$	0.975	−1.458	−5.375	−2.941	2.43
$\mathbf{C_{19}}$	0.956	−1.437	−5.356	−2.926	2.39
$\mathbf{C_{20}}$	0.988	−1.470	−5.388	−2.929	2.45
$\mathbf{C_{21}}$	0.982	−1.431	−5.382	−2.968	2.41

The obtained values are in the range of –2.926 to –3.020 eV. $\mathbf{C_{19}}$ has ideal HOMO and LUMO levels, facilitating an effective charge injection. The reason may be due to presence of carbazole,4-methoxylphenyl groups and electron-withdrawing cyanopyridone group. Finally, the electrochemical band gap of the molecules was calculated by taking the difference of HOMO and LUMO energy levels, which were found to be 2.49, 2.36, 2.74, 2.43, 2.39, 2.45, and 2.41 eV for $\mathbf{C_{14\text{-}21}}$, respectively.

4.2.3.4 Phenothiazine-based cyanopyridones $C_{22\text{-}28}$ (Series-4)

The CV curves of $\mathbf{C_{22\text{-}28}}$ are given in **Figure 4.48** and their calculated electrochemical data are summarized in **Table 4.17**.

Their HOMO and LUMO energy levels were calculated by making use of Eq **4.4** and Eq **4.5**.

$$E_{HOMO} = -[4.8 - E_{\frac{1}{2'}\frac{Fe^{+}}{Fe}} + E_{Oxd}] \text{.....(4.4)}$$

$$E_{LUMO} = -[4.8 - E_{\frac{1}{2'}\frac{Fe^{+}}{Fe}} + E_{Red}] \text{.....(4.5)}$$

The obtained data indicated that all the compounds exhibited irreversible oxidation and reduction potentials, primarily due to the presence of electron-donating and electron-withdrawing groups within the molecules. The estimated energy levels

for the HOMO and LUMO of **C_{22-28}** are in the range of −5.61 to −5.74 eV and −2.88 to −3.113 eV, respectively, with a band gap range 2.58 to 2.97 eV. All the compounds display ideal HOMO and LUMO levels which almost matches with the standard hole transporting and electron transporting layer, which facilitate the effective charge transportation. It is evident that the calculated band gap values are consistently smaller than the optical band gap values observed for all the materials.

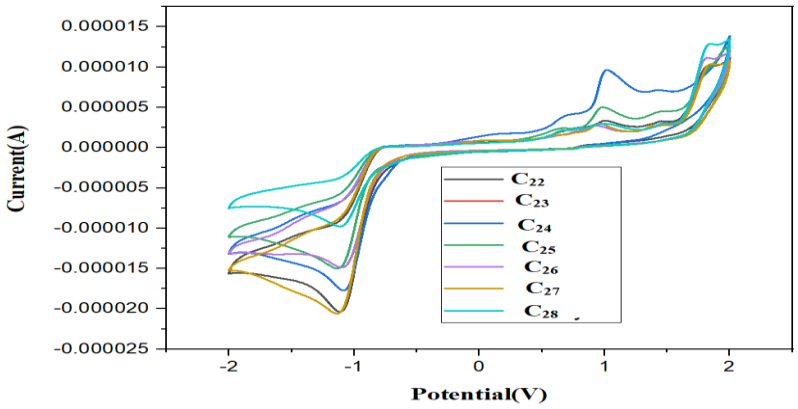

Figure 4.48. Cyclic voltammagrams of **C_{22-28}**

Table 4.17. Electrochemical data of **C_{22-28}**

Compds	**E^{ox}_{onset} (V)**	**E^{red}_{onset} (V)**	**$E_{HOMO}{}^{b}$(eV)**	**$E_{LUMO}{}^{c}$(eV)**	**$E_g{}^{CV}$ (eV)**
	CV measurements				
C_{22}	1.257	−1.346	−5.657	− 3.054	2.60
C_{23}	1.218	−1.346	−5.618	−3.054	2.56
C_{24}	1.336	−1.320	−5.736	−3.080	2.65
C_{25}	1.270	−1.424	−5.670	−2.975	2.97
C_{26}	1.297	−1.287	−5.697	−3.113	2.58
C_{27}	1.244	−1.516	−5.644	−2.884	2.76
C_{28}	1.349	−1.398	−5.749	−3.002	2.74

4.2.3.5 DPA-linked cyanopyridones $C_{29\text{-}34}$ (Series-5)

Figure 4.49 displays the CV curves of **$C_{29\text{-}34}$**, while **Table 4.18** summarized the corresponding electrochemical data. It is evident that all the compounds exhibited irreversible oxidation and reduction waves at the onset, occurring within the range of 0.844 to 0.818 V and –1.391 to –1.489 V, respectively. All the compounds are ideal HOMO and LUMO levels which are almost matching with the standard emitters. The HOMO and LUMO energy levels were calculated using the formulae given in the previous series. The calculated band gap values were found to be in the range of 2.36 to 2.26 eV. Notably, these calculated electrochemical band gap values are smaller than the optical band gaps observed for all the materials.

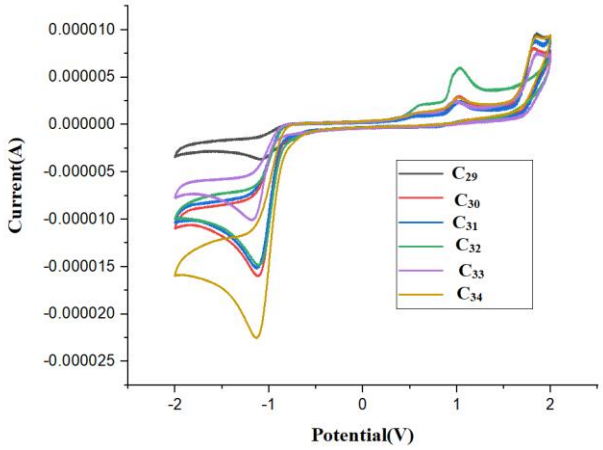

Figure 4.49. Cyclic voltammograms of **$C_{29\text{-}34}$**

Table 4.18. Electrochemical data of **$C_{29\text{-}34}$**

Molecules	E^{ox}_{onset} **(V)**	E^{red}_{onset} **(V)**	$E_{HOMO}{}^{b}$**(eV)**	$E_{LUMO}{}^{c}$**(eV)**	$E_g{}^{CV}$ **(eV)**
	CV measurements				
C_{29}	0.870	−1.391	−5.270	−3.008	2.26
C_{30}	0.870	−1.431	−5.270	−2.968	2.30
C_{31}	0.844	−1.451	−5.244	−2.294	2.29
C_{32}	0.870	−1.411	−5.270	−2.988	2.28
C_{33}	0.818	−1.496	−5.218	−2.903	2.31
C_{34}	0.876	−1.489	−5.276	−2.910	2.36

4.2.3.6 *N,N*-dimethylaniline-based cyanopyridones $C_{35\text{-}37}$ (Series-6)

Figure 4.50 contains the CV voltagramms of $\mathbf{C_{35\text{-}37}}$ and the corresponding measurement data are summarized in **Table 4.19**. The results of the CV measurements indicated that $\mathbf{C_{35\text{-}37}}$ undergo both reversible oxidation and reduction processes, leading to the the formation of stable cation and anion radicals. This suggests that the molecules have bipolar transporting properties. The presence of electron-donating groups at 4th and 6th positions of the cyanopyridone core led to the appearance of two oxidation potential peaks in the cyclic voltammograms. The cyano and carbonyl groups in the cyanopyridone core, being electron-withdrawing in nature, contributed to two reduction potential peaks in the CV curves. The HOMO and LUMO energy levels of all the compounds were calculated using the Eq. **4.4** and **4.5**. The redox potentials obtained are agreement that of standard layers. Thus from the results it is clear that all the compounds display suitable HOMO and LUMO energy levels, facilitating an adequate charge transfer processes. Finally, electrochemical band gaps were determined by taking the difference between the HOMO and LUMO energy levels. The calculated band gap values for $\mathbf{C_{35\text{-}37}}$ were 2.66, 2.61, and 2.58 eV, respectively.

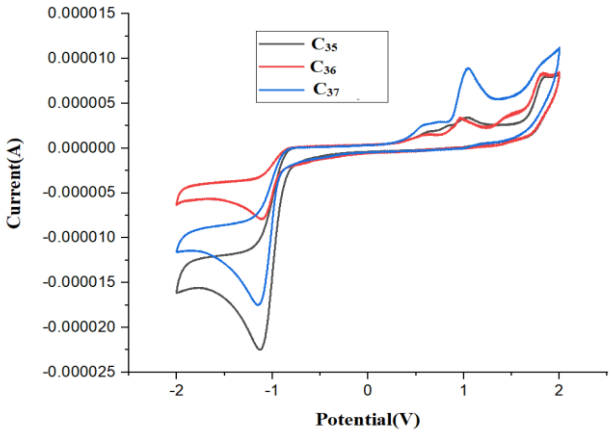

Figure 4.50. Cyclic voltammograms of $\mathbf{C_{35\text{-}37}}$

Table 4.19. Electrochemical data of $\mathbf{C_{35\text{-}37}}$

Molecules	E^{ox}_{onset} (V)	E^{red}_{onset} (V)	E_{HOMO}[b](eV)	E_{LUMO}[c](eV)	E_g^{CV} (eV)
	CV measurements				
$\mathbf{C_{35}}$	0.904	−1.463	−5.304	−2.636	2.63
$\mathbf{C_{36}}$	0.804	−1.444	−5.204	−2.955	2.95
$\mathbf{C_{37}}$	0.890	−1.424	−5.290	−2.975	2.31

4.2.3.7 Substituted nicotinonitriles $\mathbf{C_{38\text{-}42}}$ (Series-7)

Figure 4.51 and **Table 4.20** display the experimentally obtained CV curves and their corresponding electrochemical data, respectively. From the results, it is evident that all the compounds of this series undergo both reversible oxidation and reduction processes, leading to the formation of stable cation and anion radicals. This indicated that the molecules have bipolar transporting properties. The presence of an electron-donating group, *i.e. N,N*-dimethylaniline at 4th position and other varied donors like phenyl, 4-methoxyphenyl, biphenyl, 4-hydroxyphenyl and thiophene at position-6 of the cyanopyridone core led to the identification of two oxidation potentials in the cyclic voltammograms. The cyano and carbonyl groups in the central core, due to electron-withdrawing behaviour, contributed to two reduction potential levels in the CV curves. Using Eqs.**4.4** and **4.5**, the HOMO and LUMO levels of $\mathbf{C_{38\text{-}42}}$ were determined. Their electrochemical band gaps were calculated by taking the difference between the HOMO and LUMO energy levels. The calculated band gap values for $\mathbf{C_{38\text{-}42}}$ were 2.27, 2.64, 2.37, 2.53, and 2.42 eV, respectively.

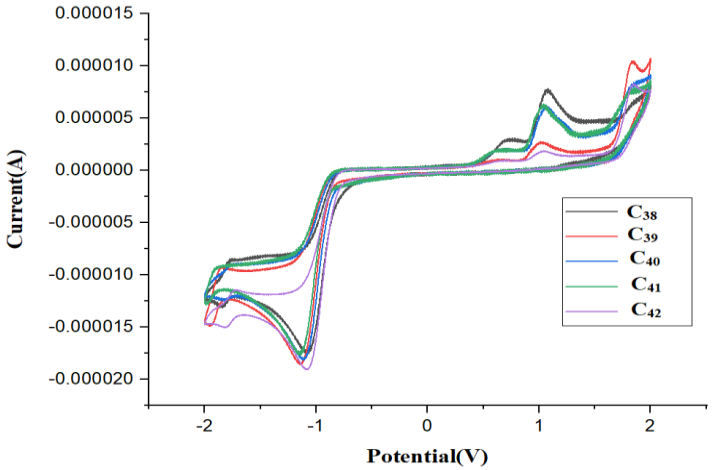

Figure 4.51. Cyclic voltammograms of **C_{38-42}**

Table 4.20. Electrochemical data of **C_{38-42}**

Molecules	E^{ox}_{onset} (V)	E^{red}_{onset} (V)	E_{HOMO} [b](eV)	E_{LUMO} [c](eV)	E_g^{CV} (eV)
	CV measurements				
C_{38}	0.916	−1.353	−5.316	−3.046	2.27
C_{39}	0.870	−1.772	−5.270	−2.627	2.64
C_{40}	0.904	−1.470	−5.304	−2.930	2.37
C_{41}	0.876	−1.654	−5.276	−2.530	2.53
C_{42}	0.904	−1.510	−5.304	−2.887	2.42

4.3 THERMAL INVESTIGATION

Thermal stability is one of the important requirements for an efficient OLED with high lifetime. During device operation, a large amount of Joule heat is usually generated from high current density. Hence, materials with high thermal stability are mandatory for OLED applications. Further, high thermal stability facilitates the formation of uniform amorphous films upon evaporation, which helps in improving the long-term stability of organic molecule-based LED devices. The present study evaluated the thermal stability of the newly synthesized molecules using the thermogravimetric analysis (TGA) technique.

4.3.1 Materials and methods

TGA was carried out on a Perkin Elmer TGA 400 Analyzer under a nitrogen atmosphere over a temperature range of 100-600°C at a heating rate of 10 °C min^{-1}.

4.3.2 Experimental

By using the TGA technique the thermal stability of the molecules was determined; the TGA was carried out under a nitrogen atmosphere at a heating rate of 10 ^{o}C/ min.

4.3.3 Results and discussion

Results of thermal studies of newly synthesized **C_{1-42}** have been discussed series-wise in the following section.

4.3.3.1 TPA substituted compounds C_{1-7} (Series-1)

Figure 4.52 depicts the thermograms of **C_{1-7}** recorded in the TGA analyzer. From the curves, the decomposition temperatures (T_d) of **C_{1-7}** were found to be 395.5, 393.95, 154.58, 400.42, 423.21, 182.93, and 390.72, respectively. The compounds **C_3** and **C_6** showed a small weight loss near 190 ^{o}C, this may be due to partial thermal decomposition/degradation of certain linkages, however the weight loss was found to be about 10% only. The high thermal resistance is mainly due to a rigid aromatic heterocyclic core, *i.e*. cyanopyridone, which brings about extra stability through hydrogen bonding. Among them, **C_4** possesses added stability owing to the presence of the amino group in the donor moiety, enabling excessive molecular interaction. Consequently, these stable molecules can form uniform film upon evaporation, which increases the efficiency and long-term stability of OLED devices.

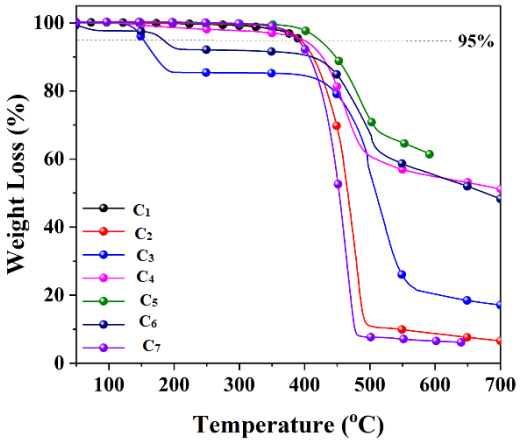

Figure 4.52. Thermograms of $\mathbf{C_{1\text{-}7}}$

4.3.3.2 Pyrene-based compounds $C_{8\text{-}14}$ (Series-2)

The TGA data obtained for $\mathbf{C_{8\text{-}14}}$ are shown in **Figure 4.53**. As per the TGA results, the compounds displayed T_d values at 150, 430, 410, 470, 430, 110, and 110 ^oC respectively. From the results, it is clear that all compounds of the series except $\mathbf{C_8}$, $\mathbf{C_{13}}$, and $\mathbf{C_{14}}$ did not show any weight loss. The weight loss observed for $\mathbf{C_8}$, $\mathbf{C_{13}}$, and $\mathbf{C_{14}}$ was minimal, which may be due to partial degradation of certain linkages. The presence of a rigid heteroaromatic core, *i.e.*, cyanopyridone moiety has provided extra stability through intermolecular hydrogen bonding. So, they can form stable device when they are fabricated in OLEDs as emitters.

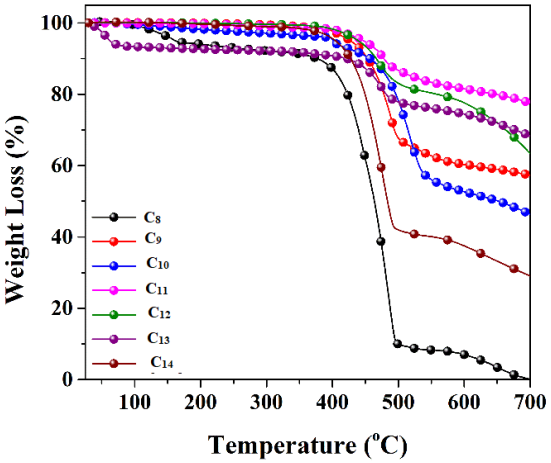

Figure 4.53. Thermograms of $\mathbf{C_{8\text{-}14}}$

4.3.3.3 Carbazole derivatives $C_{15\text{-}21}$ (Series-3)

Figure 4.54 depicts thermograms of $\mathbf{C_{15\text{-}21}}$ obtained in TGA measurements. The thermal data revealed that all the molecules except $\mathbf{C_{17}}$ and $\mathbf{C_{20}}$ exhibited impressive thermal stability. The observed T_d are 384 ^oC ($\mathbf{C_{15}}$), 334 ^oC ($\mathbf{C_{16}}$), 153 ^oC ($\mathbf{C_{17}}$), 245 ^oC ($\mathbf{C_{18}}$), 226 ^oC ($\mathbf{C_{19}}$), 161 ^oC ($\mathbf{C_{20}}$), and 378 ^oC ($\mathbf{C_{21}}$). Notably, a rigid cyanopyridone scaffold in the molecules imparted additional thermal stability owing to its strong hydrogen bonding properties. However, $\mathbf{C_{17}}$ and $\mathbf{C_{20}}$ demonstrated a slight weight loss at around 150 ^oC, which could be attributed to the presence of volatile impurities or residual moisture in the materials. These compounds might have showed a partial thermal decomposition due to favourable structure.

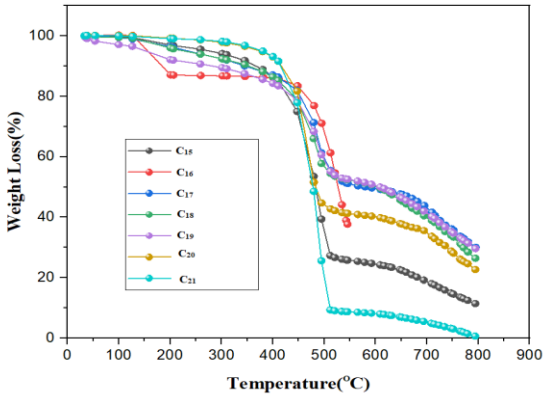

Figure 4.54. Thermograms of $\mathbf{C_{15\text{-}21}}$

4.3.3.4 Phenothiazine-based cyanopyridones $C_{22\text{-}28}$ (Series-4)

The generated TGA thermograms of $\mathbf{C_{22\text{-}28}}$ are presented in **Figure 4.55**. T_d data of the compounds are 311 ^oC ($\mathbf{C_{22}}$), 367 ^oC ($\mathbf{C_{23}}$), 373 ^oC ($\mathbf{C_{24}}$), 310 ^oC ($\mathbf{C_{25}}$), 312 ^oC ($\mathbf{C_{26}}$), 144 ^oC ($\mathbf{C_{27}}$), and 301 ^oC ($\mathbf{C_{28}}$). The thermal analysis data confirmed that all the compounds possess high thermal stability except $\mathbf{C_{27}}$, which shows a minimal weight loss near 210 ^oC. Remarkably, among the molecules analysed, $\mathbf{C_{23}}$ displayed the highest level of thermal stability. Here, the weight loss in case of $\mathbf{C_{27}}$ may be attributed to thermal decomposition/degradation of certain linkages in the molecules. The exceptional stability enables these compounds to form uniform films during the

evaporation process while fabrication, which is a critical factor in enhancing the efficiency and long-term stability of OLED devices.

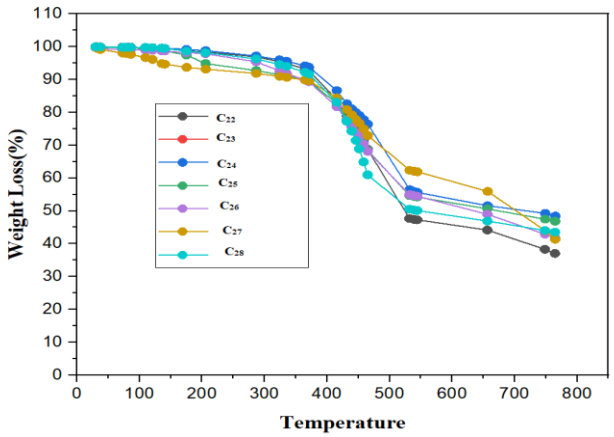

Figure 4.55. Thermograms of **C_{22-28}**

4.3.3.5 DPA-linked cyanopyridones C_{29-34} (Series-5)

Figure 4.56 shows the TGA curves obtained for **C_{29-34}**. As per the analysis, T_d values obtained are 300 ^oC (**C_{29}**), 383 ^oC (**C_{30}**), 318 ^oC (**C_{31}**), 381 ^oC (**C_{32}**), 146 ^oC (**C_{33}**), and 138 ^oC (**C_{34}**). The first four compounds of the series exhibited very good thermal stability while **C_{33}**, and **C_{34}** underwent about 5% weight loss near 140 ^oC. The exceptional stability of the compounds might be due to its unique structure, particularly the presence of cyanopyridone core gives high thermal stability through interactions like intermolecular hydrogen bonding. However, a slight weight loss in case of **C_{33}**, and **C_{34}** may be attributed to thermal degradation of weak linkages in the molecules. Thus, most of the compounds of this series are potential emitters for their applications in long lifetime OLEDs.

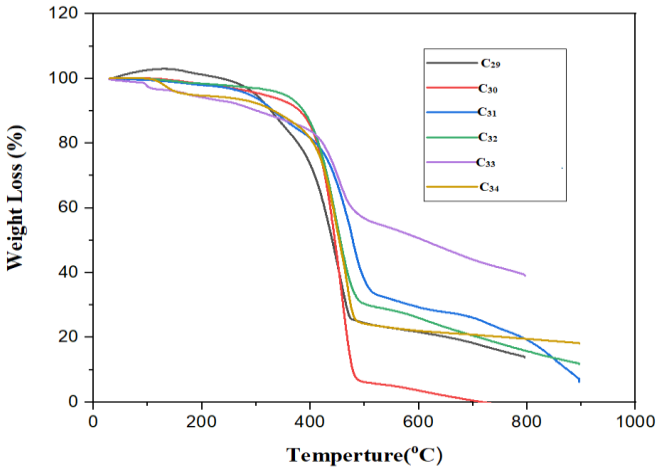

Figure 4.56. Thermograms of $\mathbf{C_{29\text{-}34}}$

4.3.3.6 *N*,*N*-Dimethylaniline-based cyanopyridones $\mathbf{C_{35\text{-}37}}$ (Series-6)

The thermograms obtained for $\mathbf{C_{35\text{-}37}}$ are given in **Figure 4.57**. According to the analysis, T_d values observed for the compounds of this series are 157 °C ($\mathbf{C_{35}}$), 384 °C ($\mathbf{C_{36}}$), and 400 °C ($\mathbf{C_{37}}$). Among them, $\mathbf{C_{36\text{-}37}}$ showed a good thermal stability due to strong intermolecular interactions, as explained earlier. While $\mathbf{C_{35}}$ containing *N*,*N*-dimethylaniline on both sides of cyanopyridone displayed a minor weight loss at around 150 °C. This may be due to its partial degradation at that temperature. Thus, fabrication of OLEDs with $\mathbf{C_{36\text{-}37}}$ as emitters would lead to stable devices.

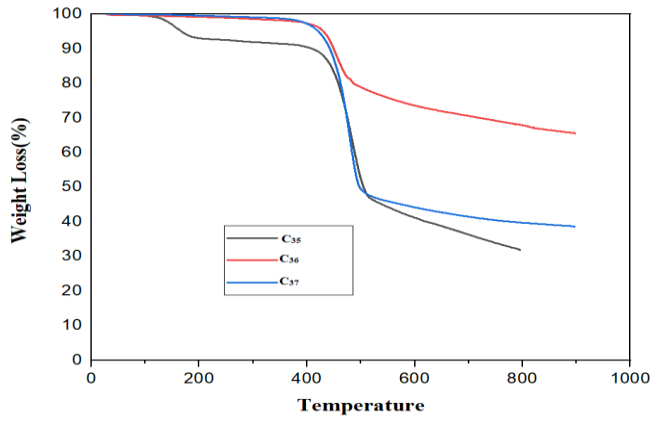

Figure 4.57. Thermograms of $\mathbf{C_{35\text{-}37}}$

4.4 THEORETICAL INVESTIGATION

In contemporary organic electronics research, computational analyses play a pivotal role by elucidating the intricate connection between the molecular electronic structure and the performance of optoelectronic devices. In the context of our current study, theoretical calculations are invaluable for obtaining essential information about the optimized ground state structures of newly synthesized compounds. This, in turn, aids in comprehending the distribution and energy levels of frontier molecular orbitals within new molecules.

4.4.1 Simulations

In our current research, Density Functional Theory (DFT) simulations were utilized to investigate the electronic properties of the molecules. These calculations were conducted on isolated molecules in a vacuum environment. For the quantum chemical stimulations, the Gaussian 09 program tailored to our specific requirements was employed. The geometry optimization was carried out using the Becker three-parameter exchange functional and the Lee-Yang-B3LY exchange correlation functional, along with a 6-31G (d,p) basis set for C, H, N, S and O. All these calculations were performed in a vacuum.

4.4.2 Results and discussion

The simulation results *viz.* optimized geometry, HOMO, LUMO and band gap energies of representative structures have been discussed in the following section.

4.4.2.1 TPA substituted compounds $C_{1\text{-}7}$ (Series-1)

Theoretical calculations were performed to obtain insights into the spatial distribution at the HOMO and LUMO levels of **$C_{1\text{-}7}$**, to develop a better understanding of structure-function relationships from a molecular and morphological perspective. The obtained frontier molecular orbital surfaces of the HOMO and LUMO are shown in **Figure 4.58** and their DFT simulation data are summarized in **Table 4.21**. As can be seen in **Figure 4.58**, the HOMO levels of all the molecules are concentrated on the donor group, *i.e.* TPA, while their LUMO surfaces are localized on the central cyanopyridone core. Here, the non-mixing of the HOMO and LUMO has clearly indicated that the emission of these molecules is mainly attributed to the ICT process,

which was further proved by the observed positive solvatochromic shift. These compounds are yellow emitters. The calculated band gaps of $\mathbf{C_{1\text{-}7}}$ were found to be 3.05, 3.07, 2.98, 3.18, 3.15, 3.12, and 2.90 eV. It was observed that the band gap values calculated from the DFT study were higher than that of experimentally determined values. This is because of various factors such as influence of polarity of solvents, counterions, pH, temperature, ionic strength, structural variation of the electrodes during the electron transfer process, *etc.*

Compds.	**Optimized geometry**	**HOMO**	**LUMO**
C_1	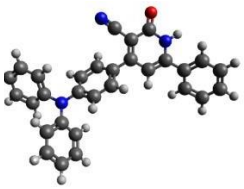	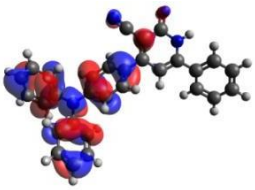	
C_2	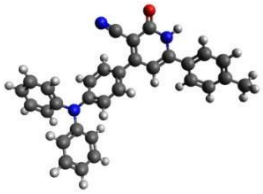	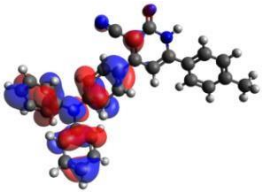	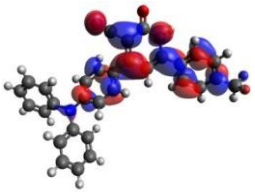
C_3	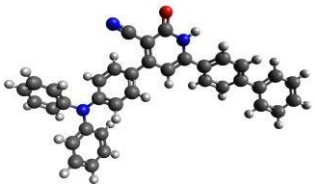	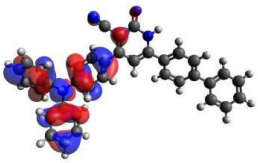	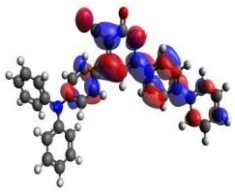
C_4	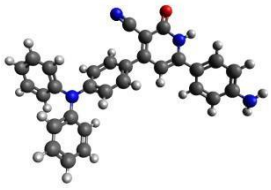	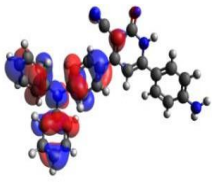	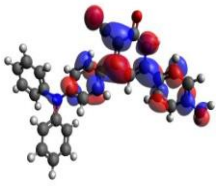
C_5	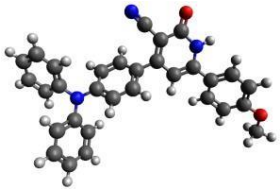	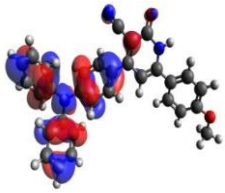	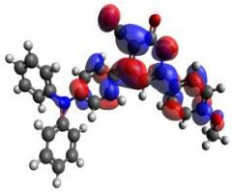

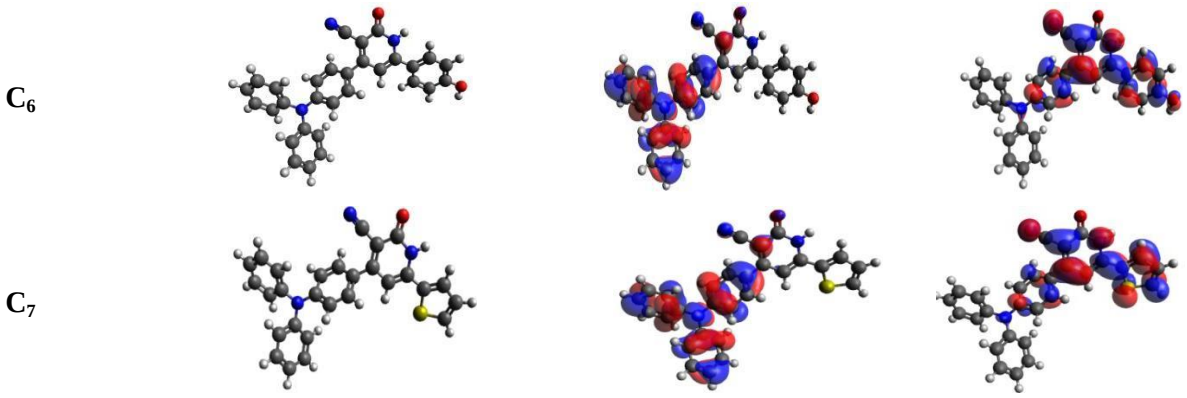

Figure 4.58. Frontier molecular orbital surfaces of HOMO and LUMO of $\mathbf{C_{1\text{-}7}}$

Table 4.21. DFT simulations data of $\mathbf{C_{1\text{-}7}}$

Compds	E_{HOMO} (eV)	E_{LUMO} (eV)	E_g (eV)
$\mathbf{C_1}$	−5.21	−2.16	3.05
$\mathbf{C_2}$	−5.18	−2.11	3.07
$\mathbf{C_3}$	−5.19	−2.21	2.98
$\mathbf{C_4}$	−5.11	−1.93	3.18
$\mathbf{C_5}$	−5.16	−2.01	3.15
$\mathbf{C_6}$	−5.18	−2.06	3.12
$\mathbf{C_7}$	−1.19	−2.29	2.90

4.4.2.2 Pyrene-based compounds $C_{8\text{-}14}$ (Series-2)

The optimized molecular geometries and HOMO, LUMO levels of $\mathbf{C_{8\text{-}14}}$ as calculated from DFT studies are portrayed in **Figure 4.59**, and their corresponding data are tabulated in **Table 4.22**. The results revealed that the delocalized electrons in the HOMO state are distributed significantly over the donor group, *i.e.* pyrene ring and the excited state electron density is distributed much over the acceptor unit, *i.e.* cyanopyridone core. Here, the delocalization of the electron density between occupied FMO is inductive of the stable donor-acceptor type interactions in the structure suggesting that the atoms in the HOMO readily provide electrons. At the same time, LUMO readily receives them effectively. Further, the observed non-mixing of HOMO

and LUMO confirmed that the emission of **C_{8-14}** is mainly due to ICT process. These compounds are green emitters. The calculated band gap values are 3.23(**C_8**), 3.25(**C_9**), 3.18(**C_{10}**), 3.34(**C_{11}**), 3.31(**C_{12}**), 3.29(**C_{13}**), and 3.09 eV(**C_{14}**). The observed band gap values are higher than that of experimentally found values.

Compds.	**Optimized geometry**	**HOMO**	**LUMO**
C_8	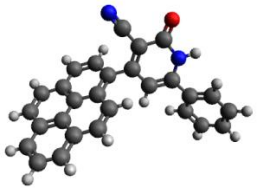	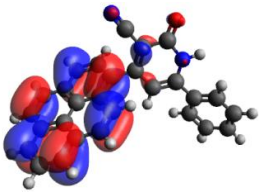	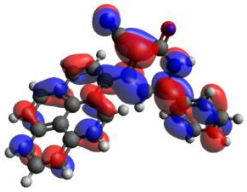
C_9	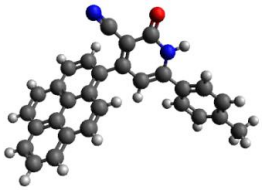	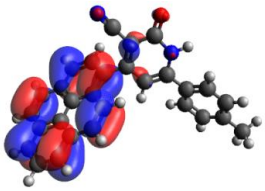	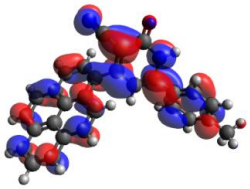
C_{10}	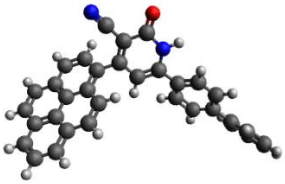	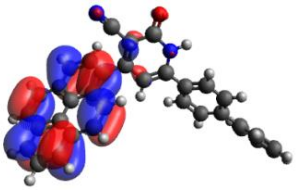	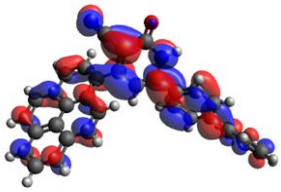
C_{11}	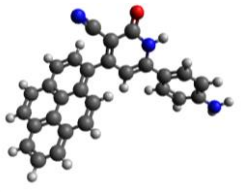	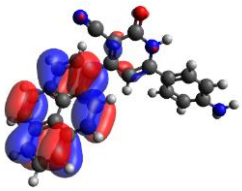	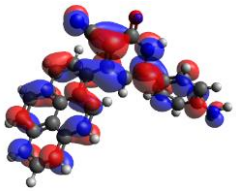
C_{12}	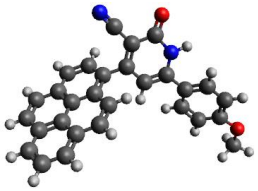	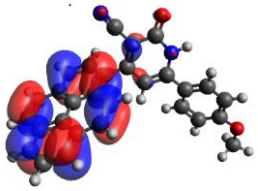	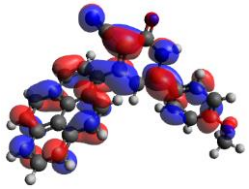
C_{13}	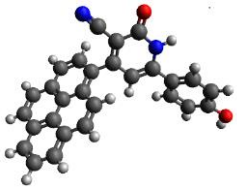	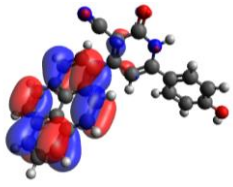	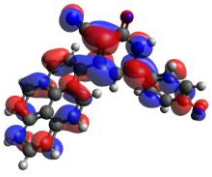

C_{14}

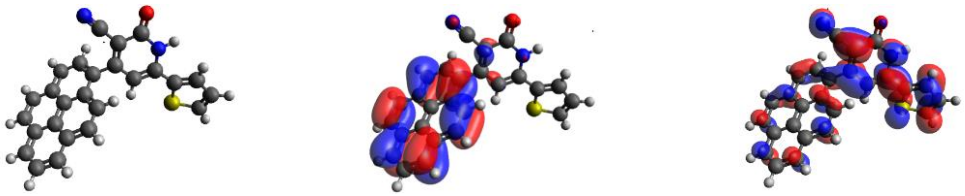

Figure 4.59. Frontier molecular orbital surfaces of HOMO and LUMO of **C_{8-14}**

Table 4.22. DFT simulations data of **C_{8-14}**

Compds	E_{HOMO} (eV)	E_{LUMO} (eV)	E_g (eV)
C_8	−5.56	−2.32	3.23
C_9	−5.54	−2.28	3.25
C_{10}	−5.54	−2.35	3.18
C_{11}	−5.45	−2.11	3.34
C_{12}	−5.51	−2.20	3.31
C_{13}	−5.53	−2.24	3.29
C_{14}	−5.56	−2.47	3.09

4.4.2.3 Carbazole derivatives C_{15-21} (Series-3)

Figure 4.60 shows electron distributions in HOMO, LUMO levels along with optimized geometries of **C_{15-21}**. The calculated HOMO, LUMO energy levels and band gaps are summarized in **Table 4.23**. The outcomes of the investigation unveiled a distinct localization of the HOMO primarily on electron-donating carbazole unit, whereas the LUMO exhibited dispersion across the central electron-withdrawing cyanopyridone moiety. Notably, the absence of orbital mixing strongly implies that the emission of the molecules predominantly arises from intramolecular charge transfer (ICT) process. This observation is further substantiated by the noticeable positive solvatochromic shift observed. These compounds are cyan emitters. The band gap values as calculated using DFT studies are 3.47(**C_{15}**), 3.50(**C_{16}**), 3.39(**C_{17}**), 3.61(**C_{18}**), 3.57(**C_{19}**), 3.55(**C_{20}**), and 3.29 eV(**C_{21}**). These values are slightly higher than the experimentally determined band gaps.

Compds.	Optimized geometry	HOMO	LUMO
C_{15}	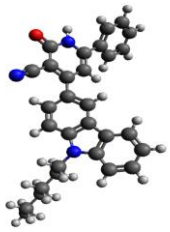	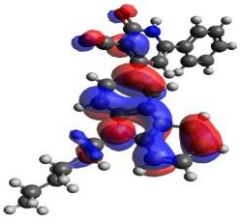	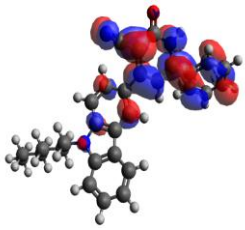
C_{16}	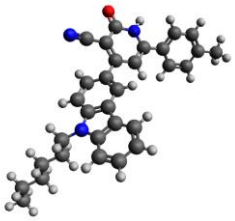	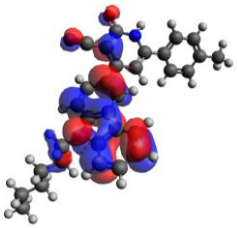	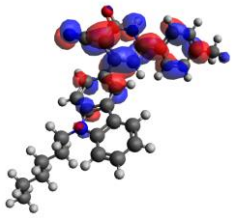
C_{17}	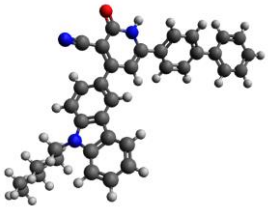	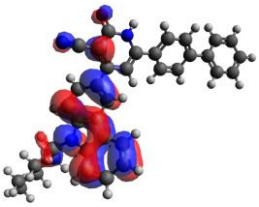	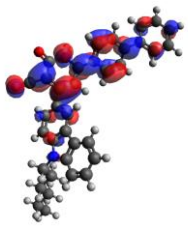
C_{18}	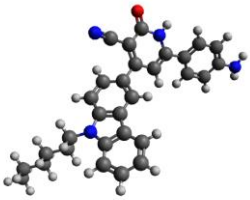	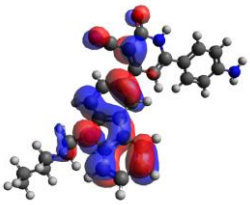	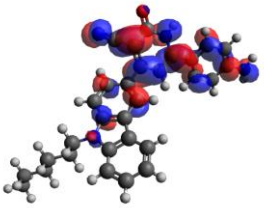
C_{19}	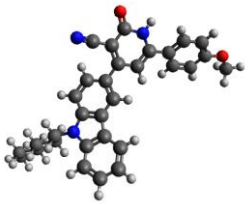	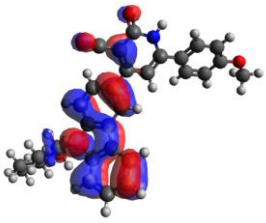	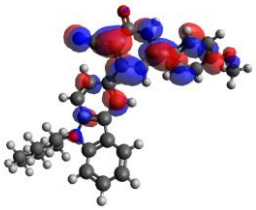
C_{20}	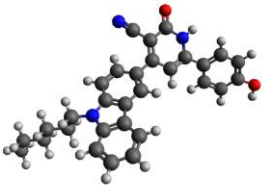	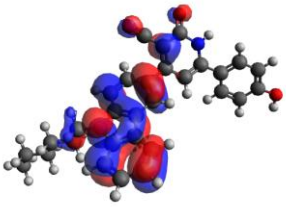	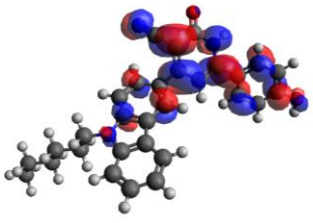

C_{21}

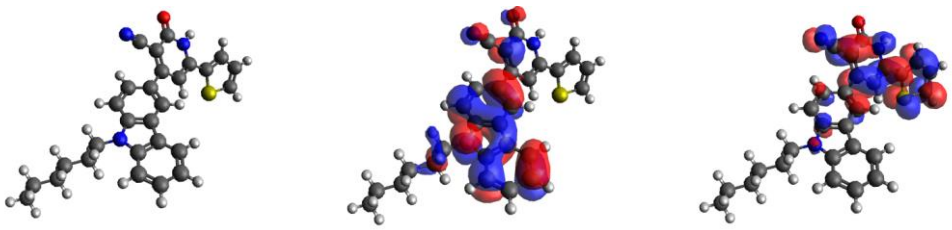

Figure 4.60. Frontier molecular orbital surfaces of HOMO and LUMO of **$C_{15\text{-}21}$**

Table 4.23. DFT simulations data of **$C_{15\text{-}21}$**

Compds	E_{HOMO} (eV)	E_{LUMO} (eV)	E_g (eV)
C_{15}	−5.57	−2.10	3.47
C_{16}	−5.54	−2.04	3.50
C_{17}	−5.56	−2.16	3.39
C_{18}	−5.46	−1.85	3.61
C_{19}	−5.52	−1.95	3.57
C_{20}	−5.54	−1.98	3.55
C_{21}	−5.57	−2.28	3.29

4.4.2.4 Phenothiazine-based cyanopyridones $C_{22\text{-}28}$ (Series-4)

Figure 4.61 shows the electron distributions in HOMO, LUMO and optimized geometries of **$C_{22\text{-}28}$,** while **Table 4.24** displays the corresponding calculated data. According to the theoretical simulations, the HOMO is primarily localized within the phenothiazine donor, whereas the LUMO is predominantly distributed across the central electron-withdrawing cyanopyridone core. This localization results in significant intramolecular charge transfer transition within the molecules, leading to efficient light emission in the bluish-green spectral region. The calculated band gap values of **$C_{22\text{-}28}$** are 2.91, 2.95, 2.85, 3.07, 3.02, 3.00, and 2.75 eV, respectively. These values were found to be slightly higher than the experimentally determined data.

Compds.	Optimized geometry	HOMO	LUMO
C_{22}	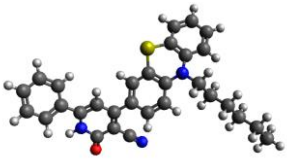	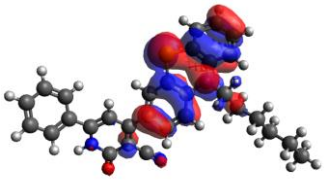	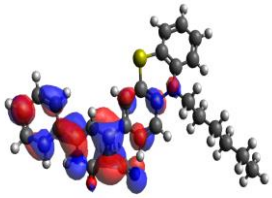
C_{23}	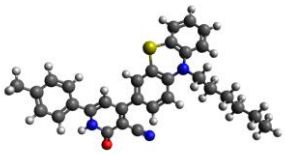	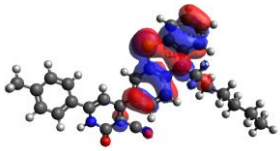	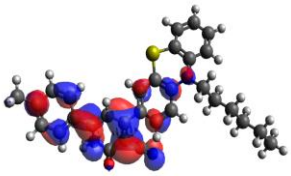
C_{24}	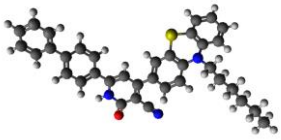	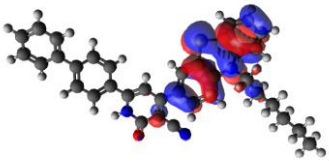	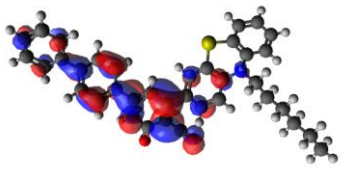
C_{25}	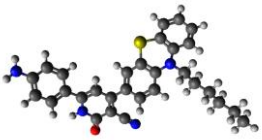	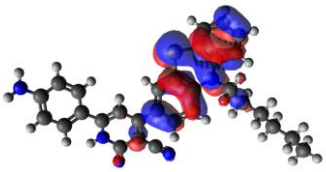	
C_{26}	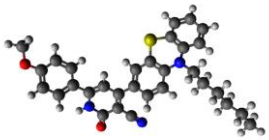	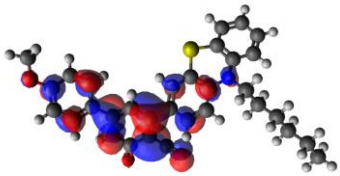	
C_{27}	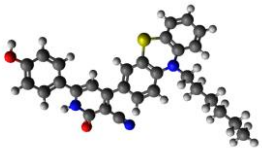	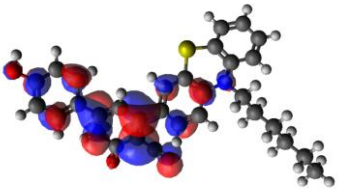	

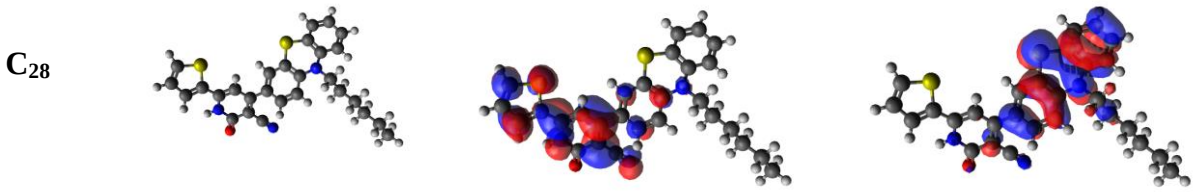

Figure 4.61. Frontier molecular orbital surfaces of HOMO and LUMO of $\mathbf{C_{22\text{-}28}}$

Table 4.24. DFT simulations data of $\mathbf{C_{22\text{-}28}}$

Compds	E_{HOMO} (eV)	E_{LUMO} (eV)	E_g (eV)
$\mathbf{C_{22}}$	−5.11	−2.19	2.91
$\mathbf{C_{23}}$	−5.09	−2.13	2.95
$\mathbf{C_{24}}$	−5.09	−2.24	2.85
$\mathbf{C_{25}}$	−5.02	−1.95	3.07
$\mathbf{C_{26}}$	−5.07	−2.05	3.02
$\mathbf{C_{27}}$	−5.09	−2.08	3.00
$\mathbf{C_{28}}$	−5.11	−2.35	2.75

4.4.2.5 DPA-linked cyanopyridones $C_{29\text{-}34}$ (Series-5)

Figure 4.62 depicts electron cloud density distributions within the HOMO and LUMO levels of $\mathbf{C_{29\text{-}34}}$. It also shows their optimized geometries. **Table 4.25** contains their calculated HOMO, LUMO energy levels and band gaps. From the results, it is clear that, in the HOMO state, electrons are notably delocalized within the donor group, *i.e.* DPA, while in the excited state, electron density is predominantly concentrated within the electron-accepting cyanopyridone unit. It is evident that the electrons within the HOMO are readily available for transfer, thus making it as a good donor, while the LUMO efficiently accepts these electrons. Here, the non-overlapping HOMO and LUMO clearly indicated that the observed emission is originated mainly by ICT transition within these flurophores. The calculated band gap values of $\mathbf{C_{29\text{-}34}}$ are 3.27, 3.30, 3.19, 3.37, 3,34, and 3.10 eV, respectively. These values are higher than that of experimentally obtained data.

Compds.	Optimized geometry	HOMO	LUMO
C_{29}	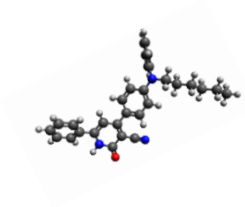	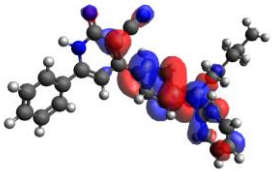	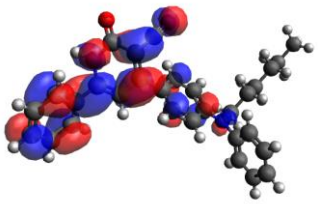
C_{30}	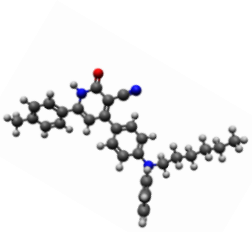	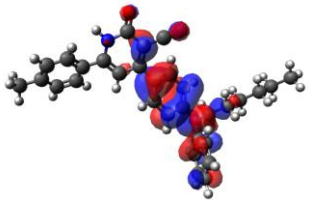	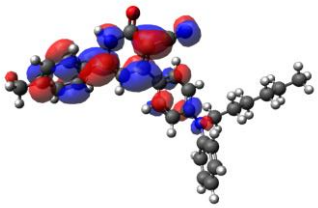
C_{31}	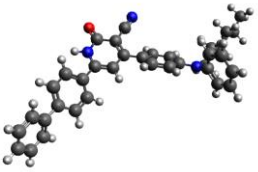	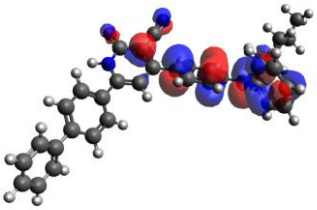	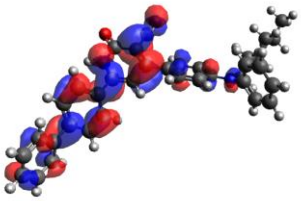
C_{32}	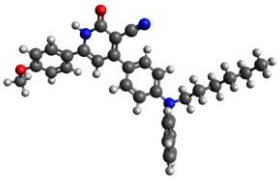	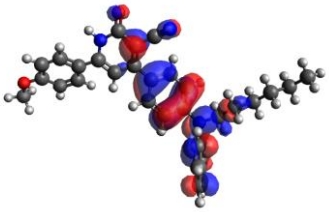	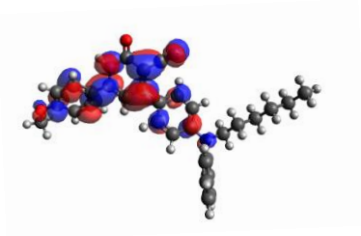
C_{33}	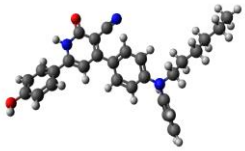	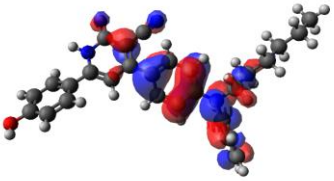	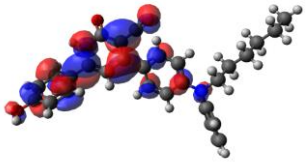
C_{34}	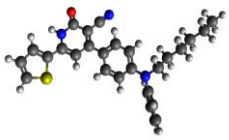	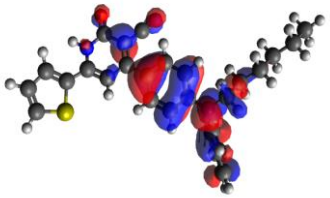	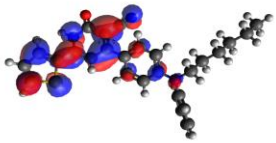

Figure 4.62. Frontier molecular orbital surfaces of HOMO and LUMO of $\mathbf{C_{29\text{-}34}}$

Table 4.25. DFT simulations data of $\mathbf{C_{29\text{-}34}}$

Compds	E_{HOMO} (eV)	E_{LUMO} (eV)	E_g (eV)
$\mathbf{C_{29}}$	−5.29	−2.02	3.27
$\mathbf{C_{30}}$	−5.27	−1.96	3.30
$\mathbf{C_{31}}$	−5.27	−2.07	3.19
$\mathbf{C_{32}}$	−5.25	−1.88	3.37
$\mathbf{C_{33}}$	−5.25	−1.91	3.34
$\mathbf{C_{34}}$	−5.30	−2.20	3.10

4.5 CONCLUSIONS

All the newly synthesized compounds, *viz*. $\mathbf{C_{1\text{-}42}}$ have been subjected to photophysical, electrochemical, thermal and theoretical studies. Their optical studies revealed that $\mathbf{C_{1\text{-}7}}$ (**Series-1**) displayed absorption maxima at 384-402 nm, and emission maxima at 551-564 nm, emitting bright yellow light. Compounds of **Series-**2 to **Series-**7 showed λ_A in the range of 368-398, 374-391, 374-403, 377-400, 421-433, and 375-421 nm, while their λ_E values were found to be 478-506 (green emission), 468-510 (cyan emission), 479-497 (blue emission), 547-555 (yellow emission), 491-497 (greenish blue), and 484-501(green emission) nm range, respectively. Further, their solvatochromic studies confirmed the presence of ICT phenomenon in all the compounds. The range of optical band gaps of **Series-1** to **Series-7** are 2.39-2.44, 2.64-2.76, 2.78-2.93, 2.55-2.95, 2.55-2.80, 2.58-2.66, and 2.71-2.93 eV, respectively. Their thermal studies revealed that $\mathbf{C_{1\text{-}2}}$, $\mathbf{C_4}$, $\mathbf{C_5}$, $\mathbf{C_7}$ (393-423 ^oC), $\mathbf{C_{8\text{-}12}}$ (410-470 ^oC, $\mathbf{C_{15\text{-}16}}$, $\mathbf{C_{18}}$, $\mathbf{C_{21}}$ (334-384 ^oC), $\mathbf{C_{22\text{-}24}}$, $\mathbf{C_{26\text{-}28}}$ (301-373 ^oC), $\mathbf{C_{29\text{-}32}}$ (300-381 ^oC), $\mathbf{C_{36\text{-}37}}$ (384-400 ^oC) are thermally stable without weight loss. As per the electrochemical studies, the band gaps range were found to be 2.10-2.33 (**Series-1**), 2.07-2-68 (**Series-2**), 2.36-2.74 (**Series-3**), 2.58-2.76 (**Series-4**), 2.28-2.36 (**Series-5**), 2.31-2.63 (**Series-6**), and 2.37-2.53 eV (**Series-7**), respectively. Further, their DFT calculations confirmed a favorable charge separation between the HOMO

and LUMO levels. Both optical and DFT studies established the presence of ICT behavior in all the compounds. Conclusively, all the synthesized compounds meet the necessary requirements of good emitters to be used in OLED devices.

OLED FABRICATION STUDIES

5.1 DEVICE FABRICATION

Abstract

This chapter deals with the fabrication studies of selected four series of newly synthesized ***C_{1-28}*** *as an emissive layer in OLED devices. Their device parameters such as EQE, current efficiency, and power efficiency have been discussed. Also, it deliberates a detailed account of the structure-device performance study.*

5.1.1 Introduction

An OLED is a light-emitting diode in which the emissive electroluminescent layer is a film of organic compound that emits light in response to an electric current. At present OLEDs are being widely used to create digital displays in devices such as television screens, computer monitors, and portable systems. Nevertheless, current challenges in this area are the development of ideal light-emitting device materials, engineering of the device structure, and their optimizations to get more efficient and long-life devices.

Certainly, the emissive layer is a vital component that determines the overall efficiency of the device. Till today a large variety of luminescent materials has been developed, to improve the device performance. Presently, one of the major challenges is the development of efficient fluorophores with high charge transport properties as well as the preserved solid-state emission for high-performance non-doped OLEDs. In the present work, compounds of **Series-1** (**C_{1-7}**), **Series-2** (**C_{8-14}**), **Series-3** (**C_{15-21}**), and **Series-4** (**C_{22-28}**) were chosen for device fabrication studies. Their optical studies confirmed that the first series emits yellow light, the second series shows green light emission, and the third series exhibits a cyan emission and the fourth series exhibits a bluish-green emission.

5.1.2 Materials and methods

F_4TCNQ (2,3,5,6-tetrafluoro-7,7,8,8-tetracyanoquinodimethane, LUMTEC) α-NPD (4,4’-bis[*N*-(1-naphthyl)-N-phenyl-L-amino]-biphenyl, LUMTEC) TPBi (2,2',2''-(1,3,5-benzenetriyl)-*tris*(1-phenyl-1-*H*-benzimidazole), LUMTEC), LiF (lithium fluoride, Sigma-Aldrich) and Al (aluminium, Alfa Aesar) were purchased

from sigma Aldrich. Fabrications of OLEDs were carried out by thermal evaporation and spin coater technique.

5.1.3 Experimental

Pre-patterned indium tin oxide (ITO) (thickness ~120 nm, sheet resistance ~15 Ω/cm^2) coated glass substrates were used as anodes. Prior to device fabrication, the ITO substrates were systematically cleaned with acetone, isopropyl alcohol, and deionized water with a sonication process sequentially, and dried in an oven at 120 °C. This is followed by UV-ozone treatment of the ITO substrates for 20 min to eliminate any organic impurities and to modify the work function of ITO. The substrates were finally transferred to a vacuum deposition system. All organic materials and cathode layers were deposited by thermal evaporation at a base pressure of $5x10^{-6}$ Torr. On the ITO substrate, the organic layers, metal contacts as per the device architectures were deposited sequentially without breaking the vacuum. F_4TCNQ (2,3,5,6-tetrafluoro-7,7,8,8-tetracyanoquinodimethane, LUMTEC) was used as hole-injection layer (HIL), α-NPD (4,4'-bis[N-(1-naphthyl)-N-phenyl-L-amino]-biphenyl, LUMTEC) was used as the hole-transport leyer (HTL), TPBi (2,2',2"-(1,3,5-benzenetriyl)-tris(1-phenyl-1-*H*-benzimidazole), LUMTEC) was used as hole/exciton-blocking layer (HBL), LiF (lithium fluoride, Sigma-Aldrich) was used as electron-injection layer (EIL), and Al (aluminium, Alfa Aesar) was used as the cathode. All the organic materials were used as received without further purification. The deposition rate of organic materials was maintained at 0.5 Å s^{-1}, whereas the deposition rates of LiF and Al were 0.1 Å s^{-1} and 6 Å s^{-1}, respectively. The deposition rates and thickness of the deposited layers were controlled *in situ* by a quartz crystal thickness monitor placed near the substrate. The cathode was deposited on the top of the structure through a shadow mask. The light-emitting area was 1.6 mm as defined by the overlap of the cathode and anode.

5.1.4 Results and discussion

Devices were constructed employing our samples with and without dopants. From the experiments, current density-voltage-luminance (J-V-L), normalized EL spectra, current efficiency-current density, and power efficiency-current density

characteristics including colour coordinates (CIE) of the fabricated OLEDs have been generated. Also, the hole-only and electron-only devices were fabricated to know the mobility of holes and electrons.

The results of device performance studies of **Series-1** to **Series-4** have been discussed in the following section.

5.1.4.1 Device performance of $C_{1\text{-}7}$ (Series-1)

The underlying issue pertaining to the charge transport properties of the materials was investigated using the SCLC (space-charge limited currents) method of the single-carrier devices, for which we used the device architectures of ITO / α-NPD (10 nm)/ **$C_{1\text{-}7}$** (100 nm)/ α-NPD (10 nm)/ Al (100 nm) for the hole-only devices (HODs) and ITO/ TPBi (10 nm)/ **$C_{1\text{-}7}$** (100 nm)/TPBi (10 nm)/LiF (1 nm)/Al (100 nm) for the electron-only devices (EODs). To ensure the hole-only currents in HODs, α-NPD was used adjacent to the cathode Al to block the electrons. In the same way, TPBi was also used in the EODs near the anode, ITO, to avoid the hole injection. **Figure 5.1** shows the striking differences between the current density versus voltage (J-V) characteristics of single-carrier devices. The HODs rapidly generate a current signal as the voltage increases, whereas EODs are relatively slow. The results indicate that the hole-transport capacities are superior to electron-transport capacities in all tested materials. The hole mobility in most organic semiconductor materials is usually two to three orders of magnitude greater than the electron mobility.

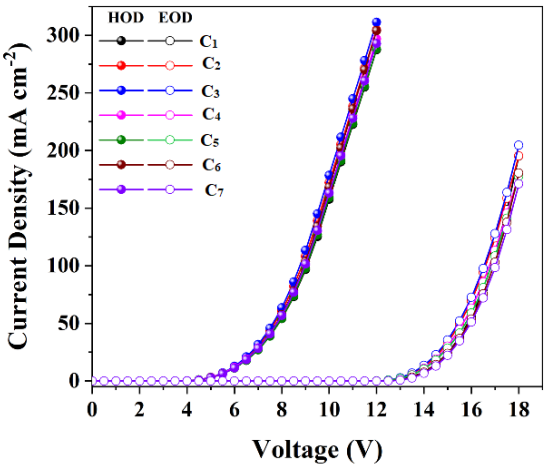

Figure 5.1. Current density *vs* voltage curves of the hole-only and electron-only devices

On the strength of constructive photophysical properties and favourable HOMO-LUMO energy levels of new **C_{1-7}**, we got inspired to explore their possible performance in OLED devices as yellow emitters. Hence, as the final part of the investigation, two different multi-layer device architectures were fabricated using vacuum deposition to make non-doped and doped OLED devices with fluorophores **C_{1-7}** as emitters. **Figure 5.2** depicts an OLED architecture diagram and the alignment of the energy levels of the fluorophores and other materials used in OLED fabrications. It is important to note that the device configurations were meticulously designed to prevent exciton loss and maintain the balance of electron and hole transport. Initially, non-doped multilayer OLEDs with the configuration **device I**: ITO (120 nm)/F_4TCNQ (4 nm)/ α-NPD (30 nm)/ **C_{1-7}**(35 nm)/ TPBi (30 nm)/ LiF (0.5 nm)/ Al (150 nm) were investigated. Here, a patterned ITO-coated glass substrate served as a transparent anode. F_4TCNQ served as a HIL, effectively injecting holes into the HTL from the ITO anode. An optimal thickness of F4TCNQ was used for better hole injection, as previously reported.α-NPD was selected as the hole-transport material because of its high HOMO energy (similar to the fluorophores). In addition, α-NPD with a higher LUMO level contributes to efficient electron-blocking when the energy levels of the materials used in OLEDs are considered (**Figure 5.2**). TPBi was used as ETL and HBL to block holes and excitons effectively. This allows for more efficient electron injection into the emitting material and better confinement of the remaining holes in the emitting layer that did not recombine with the electrons. To improve electron injection, we used a bilayer cathode composed of LiF and Al in the OLED device architectures; here, LiF works as an electron injection material. **Figure 5.2** depicts the OLED device characteristics. **Table 5.1** summarizes the device performance data. The non-doped devices (**device I**) display high current densities but low brightness at the same applied voltage (**Figure 5.3 a**), resulting in low device efficiencies (**Table 5.1** and **Figure 5.3**). This is because there is a leakage of charge at the electrodes, which is caused by an imbalance in the transport of charge carriers. Since the energy barrier for hole injection into the emitter is much lower (<0.15 eV) than that for electron injection (>0.62 eV), hole injection occurs superficially into the emitter layer, while only a small amount of electrons are injected by TPBi. Therefore, hole-only currents are primarily responsible for the observed current density in

devices. Besides, the steady-state electroluminescence (EL) spectra (**Figure 5.3b**) of the non-doped devices are red-shifted compared to their PL spectra counterparts recorded in the thin-film state. This can be inferred from the solid-state aggregation, which hampers the film morphology. Hence, the unbalanced charge injection and transport in the emissive layer and aggregation caused the quenching of fluorophores in the emissive layer of the non-doped devices, resulting in low performance and poor colour purity [47,48,49,50].

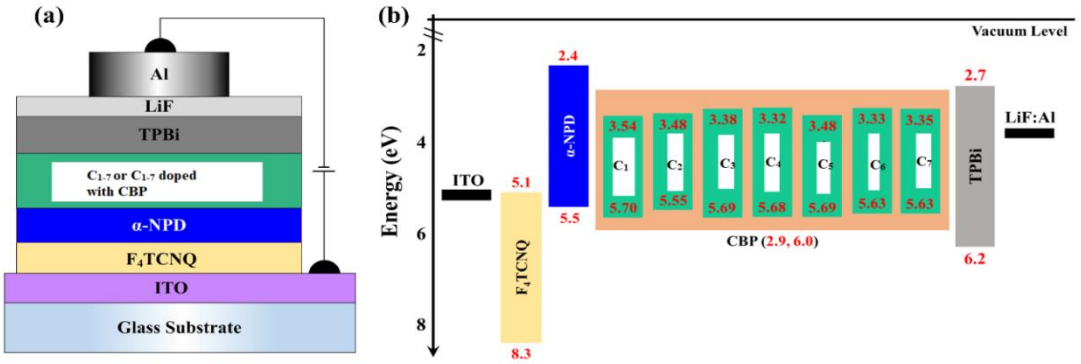

Figure 5.2. (**a**) Schematic diagram of the device architecture and (**b**) energy levels of the materials used in the OLEDs

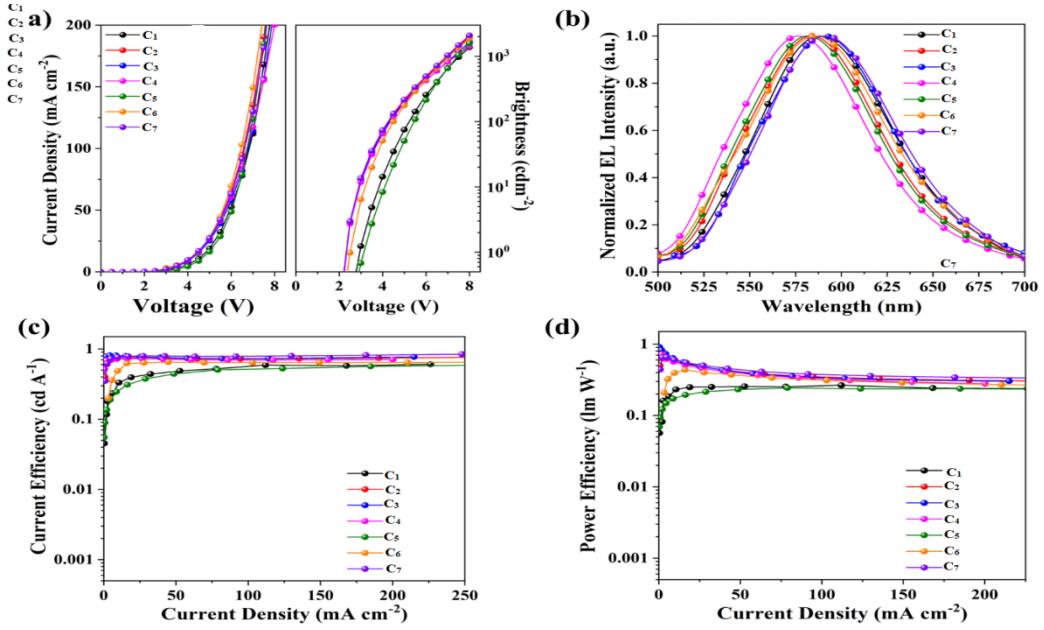

Figure 5.3. (**a**) Current density-voltage-luminance (J-V-L), (**b**) normalized EL spectra, (**c**) current efficiency-current density, and (**d**) power efficiency-current density characteristics of the OLEDs with configuration **device I**

To overcome aggregation-induced quenching and further improve device performance, we used fluorophores as dopants in the wide energy host material, CBP (4,4′-bis(N-carbazolyl)-1,1′-biphenyl), with the following device architecture, **device II**: ITO (120 nm)/F_4TCNQ (4 nm)/ α-NPD (30 nm)/ CBP: 3 wt% of $\mathbf{C_{1\text{-}7}}$ (35 nm)/ TPBi (30 nm)/ LiF (0.5 nm)/ Al (150 nm). CBP is the primary charge carrier in doped devices (**Type II**), and the excitons in CBP can be efficiently transferred to the dopant emitters ($\mathbf{C_{1\text{-}7}}$). Smaller dopant concentration was used for facile charge transport and to prevent concentration quenching in the devices, thus, ensuring the EL colour purity. **Figure 5.4** depicts the current density-voltage-luminance (J-V-L) characteristics of the OLEDs with configuration **II**. **Table 5.1** summarizes the relevant device performance data. When $\mathbf{C_{1\text{-}7}}$ fluorophores were used as dopants in the CBP host (device **II**), the EL spectra displayed hypsochromic shifts in comparison to the analogous devices **I**, indicating that aggregation is prevented in devices **II**. **Figure 5.4b** depicts the EL spectra of the devices at 8 V. OLEDs with device architecture **II** consistently showed stable yellow EL spectra when ITO was biased positively. This was consistent with the observed PL spectra, indicating that the emission originated in the emitting layer rather than the interface exciplex. EL spectra of the devices had FWHM of ~62 nm. In addition, as illustrated in **Figure 5.4e**, the EL spectra of the OLEDs exhibit the same profile with no variation in the shape or EL spectral peak at different driving voltages. As a result, the devices display exceptional spectral stability over a broad voltage range. The Commission Internationale de L'Eclairage (CIE) 1931 standard chromaticity coordinates of the fluorophores were established using the EL spectra of the devices at 10 V. The CIE coordinates are listed in **Table 5.1**.

The current density characteristics as a function of the applied voltage show good diode behaviour. All the devices with configuration **II** exhibit lower current densities with an associated increase in luminance with respect to the equivalent devices with configuration **I**. This is because, in device **II**, CBP as a host serves as the primary charge carrier and ensures a balanced charge carrier transport. In addition, the dopant molecules efficiently capture the excitons created in the host layer (CBP); subsequently, the emission originates from the dopant molecules. In addition, devices **II** display low drive voltages, corresponding to 100 cdm^{-2}, compared to the

counterpart device **I**. Thus, the devices with $\mathbf{C_{1\text{-}7}}$ fluorophores as dopants (**device II**) outperform their configuration I counterparts (**Table 5.1**). The results show that recombination is confined deep within the host layer (CBP), highlighting the importance of balanced charge carrier transport at low fluorophore concentrations (device **II**). Intriguingly, among the series of synthesized fluorophores, the device doped with $\mathbf{C_3}$ shows the best performance with high EQE (5.32%), current efficiency (10.72 cd A^{-1}), and luminance efficiency (7.87 lm W^{-1}). These findings suggest that the synthesized fluorophores could be used in OLED applications.

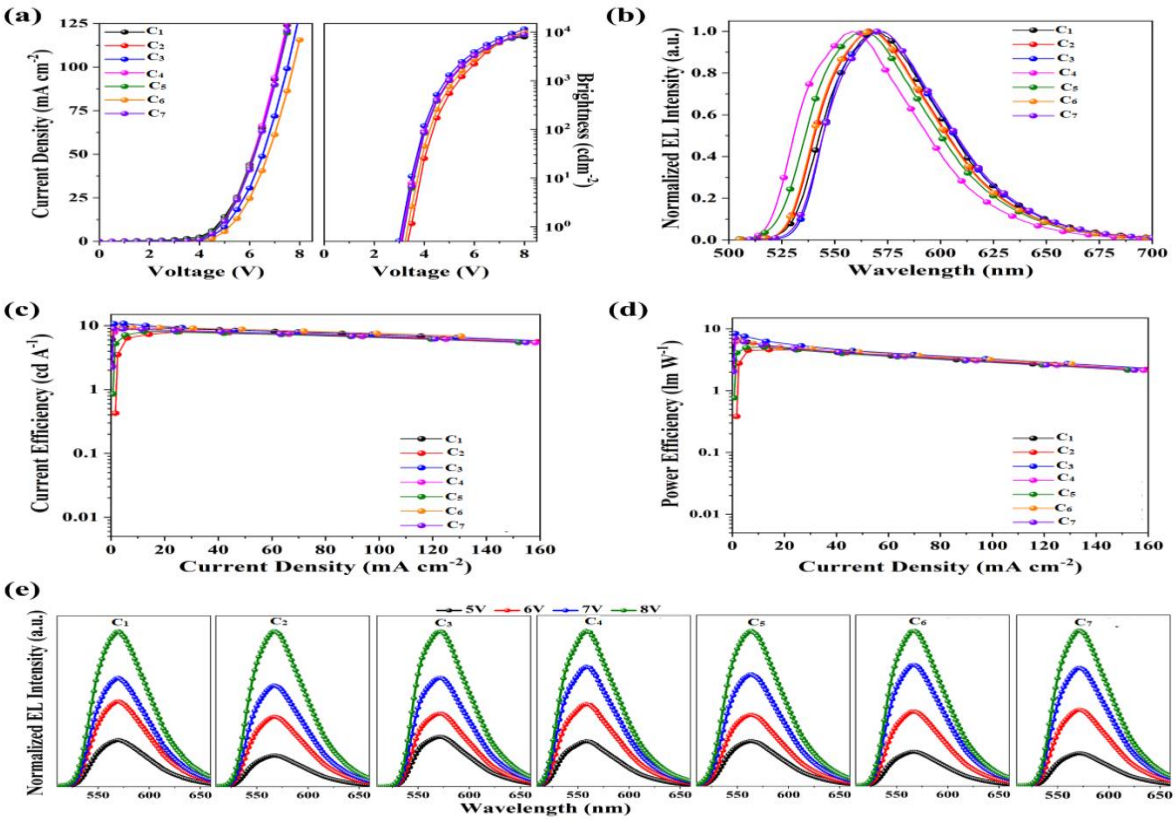

Figure 5.4. (**a**) Current density-voltage-luminance(J-V-L), (**b**) normalized EL spectra, (**c**) current efficiency-current density, (**d**) power efficiency-current density and normalized EL spectra-Voltage characteristics of the OLEDs with configuration **device II**

Table 5.1. Electroluminescence characteristics of the fabricated OLEDs

Compd.	Conc. [wt.%]	V_o [V][a]	η_c (cd A^{-1})[b]	η_p (lm W^{-1})[b]	η_{EQE} (%)[b]	L_{max} (cd m^{-2})[c]	λ_{EL} (nm)[d]	CIE[e]
C_1	3	3.93	5.64/9.26	5.55/6.75	3.03/4.12	7968	570 (63)	(0.484, 0.513)
	100	5.17	0.41/0.59	0.25/0.27	0.21/0.32	1372	587 (88)	(0.522,0.473)
C_2	3	4.22	4.76/7.92	3.47/4.59	3.38/5.11	10251	566 (63)	(0.474, 0.523)
	100	4.25	0.74/0.76	0.55/0.63	0.38/0.47	1988	584 (87)	(0.504, 0.889)
C_3	3	3.84	8.05/10.72	6.39/7.87	**4.77/5.32**	11542	573 (62)	(0.491, 0.506)
	100	4.29	0.79/0.81	0.59/0.91	0.41/0.54	1657	591 (88)	(0.529, 0.468)
C_4	3	3.92	6.56/8.69	5.09/6.11	4.02/4.42	9561	558 (63)	(0.430, 0.564)
	100	4.34	0.72/0.73	0.52/0.72	0.37/0.48	1418	577 (89)	(0.480, 0.511)
C_5	3	3.94	4.58/7.96	3.39/5.01	3.24/4.26	8706	563 (64)	(0.455, 0.541)
	100	5.38	0.36/0.59	0.21/0.24	0.19/0.27	1577	582 (91)	(0.499, 0.495)
C_6	3	4.11	8.89/9.33	6.83/7.02	4.41/5.18	9942	567 (61)	(0.471, 0.525)
	100	4.47	0.62/0.65	0.42/0.44	0.22/0.29	1876	585 (91)	(0.507, 0.486)
C_7	3	3.92	7.38/8.86	5.76/6.64	4.26/4.31	8916	571 (62)	(0.492, 0.505)
	100	4.21	0.77/0.84	0.58/0.66	0.37/0.42	2092	590 (89)	(0.531, 0.465)

[a] turn-on voltage at a luminance of 100 cd m^{-2}

[b] current efficiency (η_c), power efficiency (η_p) and external quantum efficiency (η_{EQE}) measured @ 100 cd m^{-2} and maximum values

[c] Maximum luminance at 8 V

[d] El spectra maximum at 8 V

[e] CIE colour coordinate

5.1.4.2 Device performance of $C_{8\text{-}14}$ (Series-2)

The ability of the dyes to carry charge carriers was investigated using single-carrier devices. Hole-only-devices (HODs) had the device architecture of ITO/ α-NPD (10 nm)/ **$C_{8\text{-}14}$** (100 nm)/ α-NPD (10 nm)/ Ag (100 nm) and the electron-only-devices (EODs) had the architecture ITO/ TPBi (10 nm)/ **$C_{8\text{-}14}$** (100 nm)/TPBi (10 nm)/LiF (0.5 nm)/Al (100 nm) (Figure 5.5). Here ITO was used as an anode. α-NPD in HODs was used to ensure the hole-only currents and to block the electrons, whereas TPBi was used to provide the electron-only currents in EODs and block holes. In addition, LiF and Al were used as electron-injection layer (EIL) and cathode, respectively. The current density-voltage (J-V) characteristics of the fabricated single charge-carrier devices (Figure 5.5c) show remarkable differences. In response to an increase in voltage, the current in HODs responds faster than that in EODs. This is in line with the fact that, in the vast majority of organic semiconductors, the mobility of holes is

typically higher than the mobility of electrons. According to the findings, the hole-transport capabilities of all the dyes are significantly higher than the electron-transport capabilities[1-10].

The favourable HOMO-LUMO energies and beneficial photophysical characteristics of the dyes, **C_{8-14}** motivated us to look into their possible uses in optoelectronic devices. Hence, as the final stage of the investigation, the potential of the dyes as prospective green emittiers in multilayer OLEDs was investigated utilizing two device architectures (**A** and **B**). The dyes were employed as sole-emitters in multilayer undoped OLEDs with the device architecture **A**: ITO (120 nm)/F_4TCNQ (4 nm)/ α-NPD (30 nm)/ **C_{8-14}** (35 nm)/ TPBi (30 nm)/ LiF (0.5 nm)/ Al (150 nm); while as dopant emitters with the device architecture **B**: ITO (120 nm)/F_4TCNQ (4 nm)/ α-NPD (30 nm)/ CBP: x wt% of **C_{8-14}** (x=3, 10) (35 nm)/ TPBi (30 nm)/ LiF (0.5 nm)/ Al (150 nm). Schematics of the architectures and molecular energy alignment of the dyes and other materials utilized in OLEDs are shown in **Figure 5.6.** The device architectures were carefully engineered to avoid exciton loss and maintain electron-hole equilibrium. In our case, for transparent anode, we employed pre-patterned ITO coated glass. An optimum thickness of F_4TCNQ was employed as the hole-injection layer (HIL) as it has the ability to efficiently inject holes into the hole-transport layer (HTL). As the HOMO energies of α-NPD is similar to the dyes, it was used as HTL. In addition, the high LUMO level of α-NPD will effectively block the electrons (**Figure 5.6a**), which makes it an efficient electron-blocking layer (EBL). TPBi facilitates electron injection into the emitting layer (EML). In addition, it also blocks and confines the holes to the EML. Hence, it plays a dual role as an electron-transporting layer (ETL) and hole/exciton-blocking material (HBL). To improve electron injection, we employed a LiF/Al as bilayer cathode.

The undoped devices with configuration **A** show high current densities but a low luminance (**Figure 5.7a**), which results in low device efficiencies (**Table 5.2**). The imbalanced charge injection and transport in the EML leaks charges at the electrodes, resulting in high current densities in devices with configuration **A**. However, the devices showed low performance and brightness at the same applied voltages, leading to low performance. Since the hole-injection energy barrier from α-

NPD to the EML is substantially lower (<0.24 eV) than that for electron injection (>0.82 eV) from TPBi to the EML, α-NPD injects holes easily to the EML compared to electron injection from TPBi to the EML. As a result, the hole-only current is the primary factor that drives the current density of devices with configuration **A**. Also, the steady-state electroluminescence (EL) spectra (**Figure 5.7b**) of the undoped devices (**A**) are bathochromically shifted compared to their thin-film PL spectra counterparts (**Figure 4.9**). This suggests aggregation-induced self-quenching occurs in devices **A** (undoped devices) with dyes as sole emitters. The imbalanced charge injection, transport and aggregation-induced quenching of dyes in the EML of devices **A** (undoped) result in poor device performance and colour purity.

To prevent aggregation-induced quenching, improve device performance, and achieve effective charge-carrier balance in OLEDs (devices **B**), we employed dyes as dopants in CBP, a wide energy host. CBP shows promise as an attractive host for realizing an efficient host-guest system due to its advantageous energy level alignment, bipolar nature, triplet energy, and thermal stability. The device performance, stability, and lifetime of the OLEDs rely heavily on the optimal dopant concentration in the EML. Hence, a device with 3 wt% and 10 wt% of $\mathbf{C_8}$ in CBP was utilized to confirm the effect of dopant concentration. The device containing 3 wt% $\mathbf{C_8}$ has a low turn-on voltage of 3.46 V, η_{EQE} of 4.56%, a luminance (L_{max}) of 7968 cd m^{-2}, a green emission (535nm), with chromaticity coordinates of (0.325, 0.640) as shown in **Figure 5.8** and **Table 5.2**. With an increase in $\mathbf{C_8}$ concentration from 3 wt% to 10.0 wt%, the η_{EQE} decreases drastically from 4.56% to 3.28%, respectively. Also, when comparing devices with 3 and 10 wt% dopant concentration, the device with 10 wt% dopant concentration exhibited bathochromically shifted EL spectra (**Figure 5.8b**). Triplet quenching mechanisms, such as triplet-polaron annihilation, triplet-triplet annihilation, and electric field-oriented dissociation of excitons, can be triggered by higher dopant concentrations in the host, leading to a drastic decrease in exciton generation and inducing more current transport in the EML, both of which are detrimental to device performance. The increase in current transport in the EML is evident from the increase in the current density as the $\mathbf{C_8}$ (dopant) concentration increases in the CBP host.

In order to ensure the EL colour purity and improve the performance of the device, a lower concentration of dopants (3%) was chosen for easy charge transmission and to minimize concentration quenching. In devices with configuration **B** (doped), hypsochromic shifts in the EL spectra were seen when $\mathbf{C_{8\text{-}14}}$ dyes were utilized as dopants in CBP host, in contrast to the analogous devices **A** (Undoped), showing that aggregation is suppressed in devices with configuration **B** (**Figure 5.9 and Table 5.2**). This suggests that the formation of aggregates is hindered at lower dopant concentrations. The devices with configuration **B** exhibited stable green EL spectra (**Figure 5.9b**), consistent with the notion that the emission originates from the EML as opposed to the interface exciplex. In addition, no emission was seen either from the CBP host or the adjacent charge-transport layers. This suggests that there is an effective energy transfer between the host and dopant, as well as effective charge confinement. As can be seen in **Figure 5.9b**, the EL spectra of the OLEDs maintained the same profile throughout a wide range of applied voltages, indicating outstanding spectral stability. The chromaticity coordinates of the dyes at 10 V are tabulated in **Table 5.2**. The devices show diode-like current density characteristics as a function of applied voltage. However, devices with configuration **B** have a lower current density and higher brightness than their corresponding counterparts (**A**). In addition, devices **B** have lower drive voltages than devices **A**, as CBP (host) provides a balanced charge carrier transport. Furthermore, the excitons created in the host are efficiently captured by the dopant molecules, making them the source of the emission. As a result, devices with configuration **B** using $\mathbf{C_{8\text{-}14}}$ dyes as dopants are superior to their counterparts (**A**). At low doping concentrations of dyes, devices **B** exhibit balanced charge carrier transport, and recombination is well contained inside the host layer (CBP). In addition, the enhanced inclination for crystallinity hinders the film morphology of the dyes, which is likely responsible for the poor device performance in the case of devices **A** as well as device with high dopant concentrations (10 wt.% of $\mathbf{C_8}$). The device with 3 wt.% $\mathbf{C_{11}}$ as dopant performs best among the synthesized series of dyes with efficiencies of 5.91% (η_{EQE}), 14.38 cd A^{-1} (η_C), and 12.04 lm W^{-1} (η_P). The CIE coordinates of (0.270, 0.655) are comparable with that of reported molecules (**Table 5.2**). In addition, the obtained efficiencies of the fabricated devices in this work are either comparable or higher than that of the recently reported OLEDs using

fluorescent green emitters (**Table 5.2**). These data suggest that the dyes can be conveniently utilized in OLED applications.

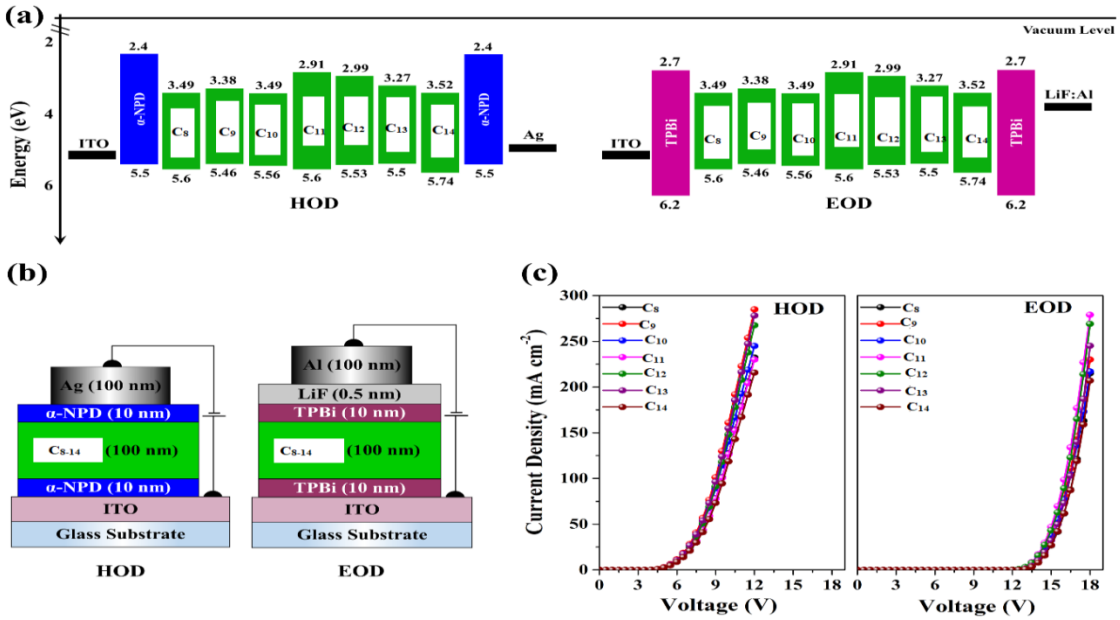

Figure 5.5. (**a**) Energy levels of the materials used, (**b**) schematic diagrams, and (**c**) current density *vs* voltage curves of the single carrier devices (hole-only and electron-only devices)

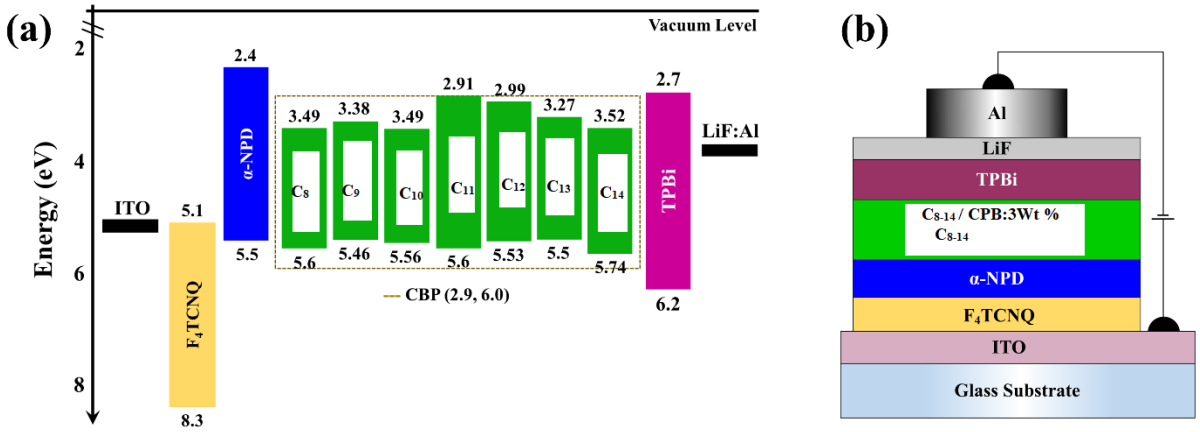

Figure 5.6. (**a**) Energy levels of the materials used, and (**b**) a schematic diagram of the OLEDs

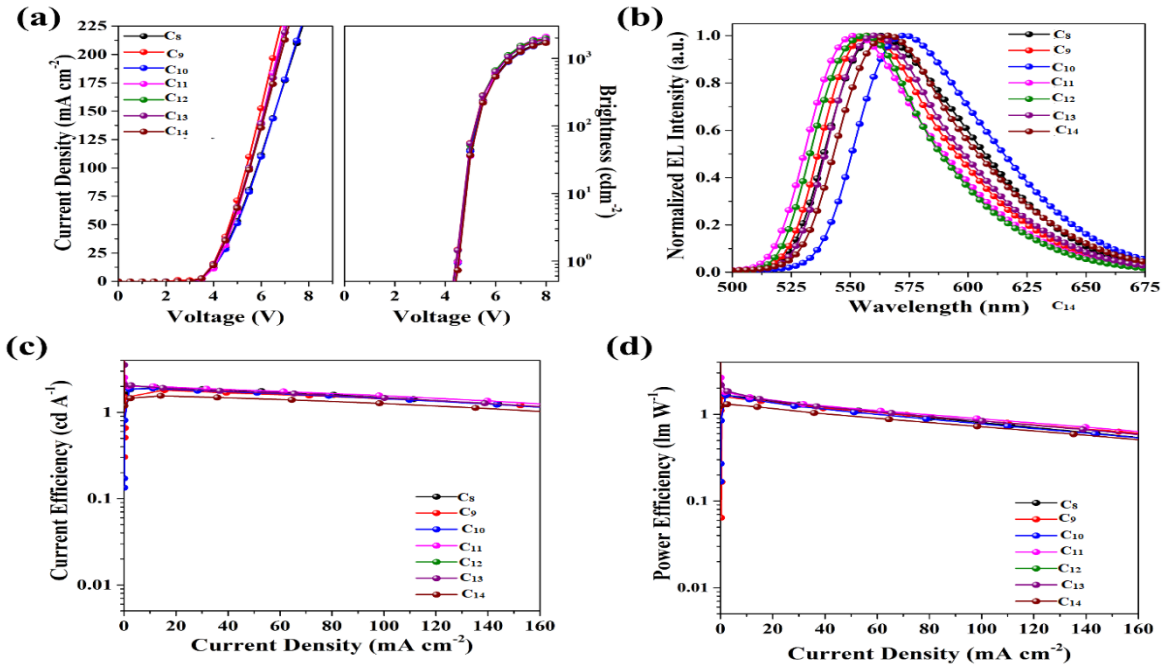

Figure 5.7. (**a**) J-V-L (**b**) EL spectra, (**c**) CE-J, and (**d**) PE-J characteristics of the OLEDs with configuration **device A**

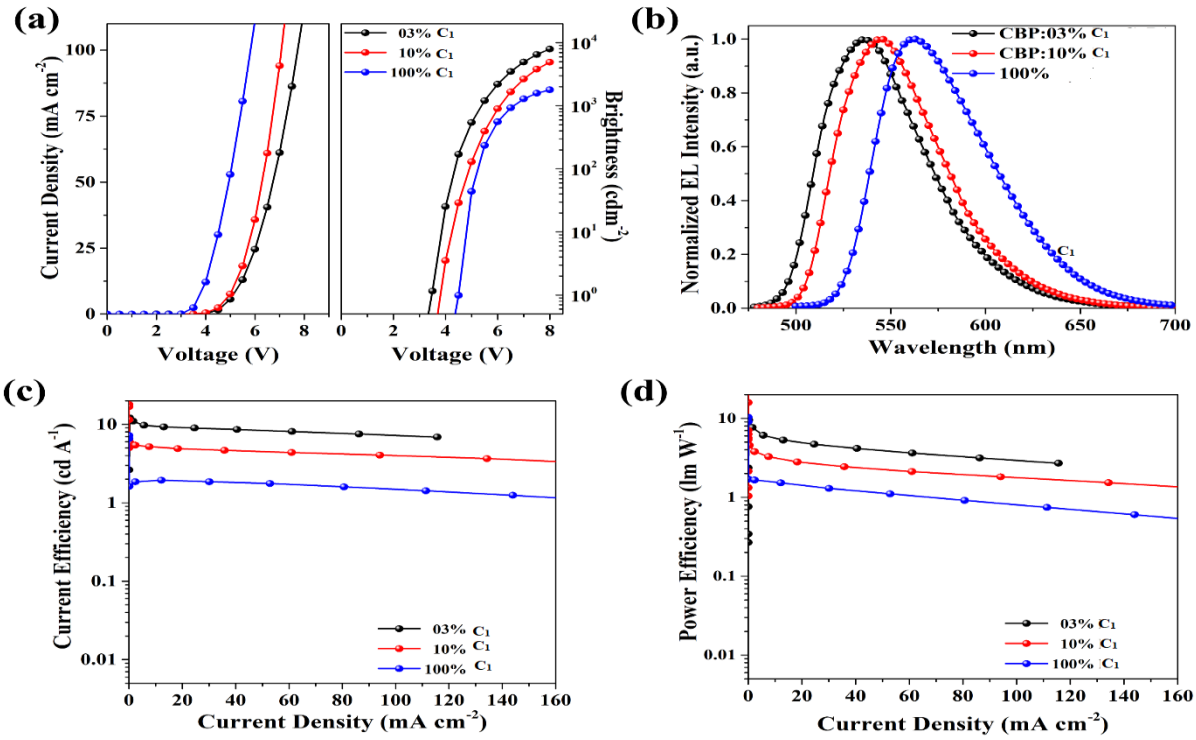

Figure 5.8. (**a**) J-V-L (**b**) EL spectra, (**c**) CE-J, and (**d**) PE-J characteristics of the OLEDs with different concentrations of $\mathbf{C_{8\text{-}14}}$ in CBP host

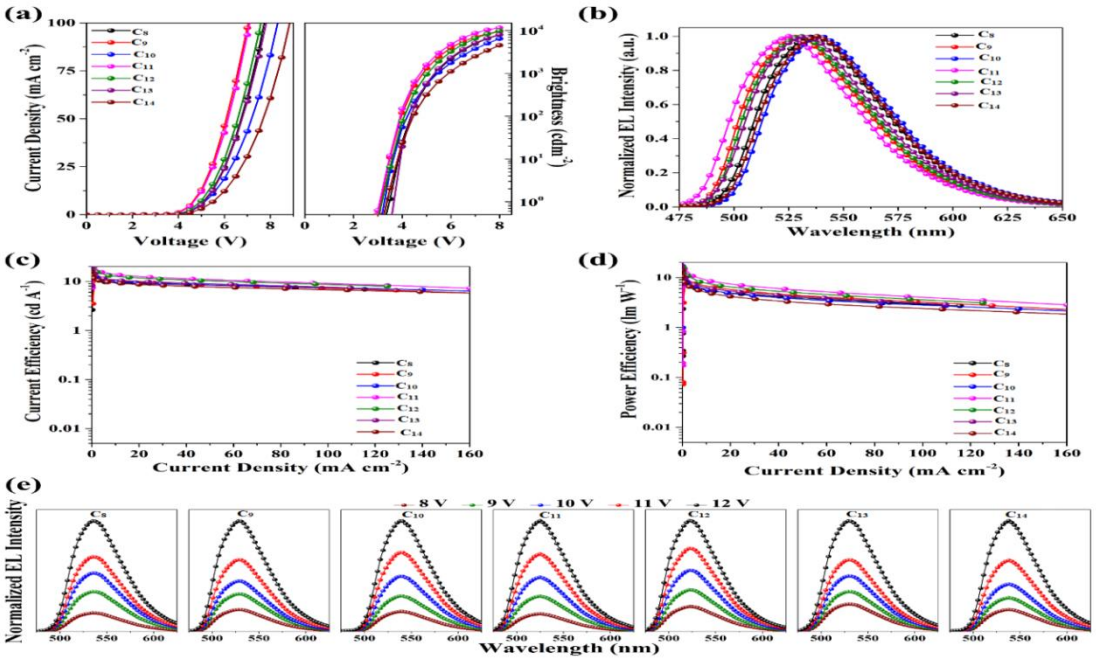

Figure 5.9. (**a**) J-V-L (**b**) EL spectra, (**c**) CE-J, and (**d**) PE-J (**e**) EL spectra-Voltage characteristics of the OLEDs with configuration **device B**

Table 5.2. Electroluminescence data of the $\mathbf{C_{8\text{-}14}}$ based OLED devices with different doping concentrations within the CBP host matrix

Emitter	Dopant Conc. (wt.%)	V_o (V)[a]	$CE_{100}/PE_{100}/EQE_{100}$ (cd A^{-1}, lm W^{-1}, %)[b]	$CE_{max}/PE_{max}/EQE_{max}$ (cd A^{-1}, lm W^{-1}, %)[c]	L_{max} (cd m^{-2})[d]	λ_{EL} (nm)[e]	CIE[f]
C_8	3	3.46	8.96/7.87/3.89	10.08/8.63/4.56	7968	535	(0.325, 0.640)
	10	3.57	5.56/4.08/2.93	5.89/4.64/3.28	4912	544	(0.366, 0.616)
	100	4.31	1.61/0.98/0.67	1.89/1.28/0.78	1792	561	(0.473, 0.524)
C_9	3	3.09	11.32/9.02/4.34	12.36/10.39/4.82	9383	530	(0.288, 0.657)
	100	4.14	1.65/1.01/0.72	1.94/1.41/0.88	1920	558	(0.447, 0.548)
C_{10}	3	3.27	8.64/7.62/3.63	9.89/8.48/4.41	6442	541	(0.342, 0.632)
	100	4.22	1.55/0.95/0.64	1.82/1.19/0.71	1702	573	(0.516, 0.481)
C_{11}	3	3.06	12.57/10.88/5.16	**14.38/12.04/5.91**	11678	526	(0.270, 0.655)
	100	4.11	1.72/1.09/0.83	2.02/1.54/0.95	2090	552	(0.421, 0.572)

C_{12}	3	3.16	12.11/10.13/4.72	13.99/11.84/5.52	9974	529	(0.263, 0.657)
	100	4.16	1.69/1.04/0.79	1.99/1.48/0.91	1972	556	(0.426, 0.568)
C_{13}	3	3.63	9.93/8.25/4.16	11.18/9.82/4.61	8082	532	(0.298, 0.651)
	100	4.56	1.64/1.00/0.68	1.93/1.35/0.81	1871	561	(0.461, 0.535)
C_{14}	3	3.38	8.38/7.17/3.51	9.42/8.31/4.09	4565	539	(0.333, 0.637)
	100	4.26	1.35/0.83/0.54	1.55/1.06/0.62	1686	566	(0.481, 0.517)

[a] Turn-on voltage at a luminance of 1 cd m^{-2}
[b] CE, PE, EQE at 100 cd m^{-2}
[c] Maximum CE, PE and EQE
[d] Maximum luminance at 8 V
[e] EL spectra maximum at 8 V
[f] CIE color coordinate at 8 V

5.1.4.3 Device performance of $C_{15\text{-}21}$(Series-3)

Single-carrier devices were used to evaluate the carrier-transport capabilities of the synthesized dyes **$C_{15\text{-}21}$**. The device architecture of the hole-only-devices (HODs) and electron-only-devices (EODs) are ITO/ α-NPD (10 nm)/ **$C_{15\text{-}21}$** (50 nm)/ α-NPD (10 nm)/ Ag (100 nm) and ITO/ TPBi (10 nm)/ **$C_{15\text{-}21}$** (50 nm)/TPBi (10 nm)/LiF (0.5 nm)/Al (100 nm), respectively (Figure 3). Here, ITO (indium tin oxide) was employed as an anode. α-NPD (4,4'-bis[N-(1-naphthyl)-N-phenyl-L-amino]-biphenyl) was used both as a hole-transporting layer (HTL) and electron-blocking layer (EBL) in HODs. In EODs, TPBi (2,2′,2"-(1,3,5-benzenetriyl)-tris(1-phenyl-1-H-benzimidazole)) was used as both electron-transporting layer (ETL) and hole-blocking layer (HBL) to facilitate electron-only current**.** Additionally, LiF (lithium fluoride) and Al (aluminium) were employed as electron-injection layer (EIL) and cathode, respectively. The current density-voltage (J-V) characteristics of the fabricated HODs and EODs are shown in **Figure 5.10**. The hole and electron current densities increased with voltage and showed a comparable trend. As shown in **Figure 5.10**, distinct variations can be seen in the J-V characteristics of HODs and EODs. When the voltage is increased, the current in HODs responds more quickly than in

EODs. This is consistent with the observation that the mobility of holes is often more significant than that of electrons in organic semiconductors**.**. Among these seven dyes, **C_{15-21}** has the best hole-transporting property, and **C_{19}** has the best electron-transporting property. The results show that all dyes have much greater hole-transport capabilities than electron-transport capabilities. The studies also show that OLED devices using **C_{15-21}** can efficiently balance holes and electrons, which will lead to balanced exciton formation and recombination in the emitting layer and, ultimately, good device performance [25-35].

The high-intensity emission and favourable HOMO-LUMO energies of new **C_{15-21}** dyes prompted us to investigate their use in OLEDs. Thus, solution-processed multilayer device architectures were used to test the adaptability of the dyes **C_{15-21}** as potential cyan emitters in OLEDs. **Figure 5.11** displays the schematic of the solution-processed OLEDs and molecular energy level alignments. To avoid aggregation-induced concentration quenching, ensure efficient charge trapping by suitable HOMO and LUMO energy, and achieve effective charge-carrier balance in OLEDs, we used 3 wt% of dyes as dopants in the wide energy host material, CBP (4,4′-bis(*N*-carbazolyl)-1,1′-biphenyl). Low dopant concentrations allowed easy charge transmission and prevented concentration quenching ensuring EL colour purity. ITO (120 nm)/ PEDOT: PSS (35 nm)/ CBP: 3wt% **C_{15-21}** (35 nm)/ TPBi (30 nm)/ LiF (0.5 nm)/ Al (150 nm). Pre-patterned ITO-coated glass substrates were used as transparent anodes. PEDOT: PSS (poly(3,4-ethylenedioxythiophene)-poly(styrenesulfonate)) was employed as a hole-injection layer (HIL), which facilitates in smoothening of the ITO surface, and hence reduces the turn-on voltage and probability of any electric shorts**.** TPBi plays a dual role as an ETL by effectively injecting electrons into the emitting layer (EML) and as HBL confines the holes to EML. We used a LiF/Al bilayer cathode to boost electron injection. The energy level alignment, bipolar nature, triplet energy, and thermal stability of CBP make it a promising host for an efficient host-guest system.CBP acts as the major charge carrier and efficiently transfers excitons to dopant emitters. **Table 5.3** shows device performance data, and **Figure 5.12** shows device characteristics of the OLEDs. The devices display diode-like behaviour (**Figure 5.12a**). All the devices (**Figure 5.12a**) have lower current densities and high brightness. The devices exhibited lower driving voltages (**Table 5.3**) because the host

CBP balances charge carrier transport and contains recombination in the host layer. The devices doped with 3 wt.% $\mathbf{C_{15\text{-}21}}$ outperform the other dyes as dopants (**Table 5.3**) in terms of efficiency (13.16 cd A^{-1}, 9.85 lm W^{-1}, and 5.41%). The EL spectra of the devices are shown in Figure **5.12b**. When ITO was biased positively, all the devices had stable cyan EL spectra (**Figure 5.12b**), supporting the idea that the emission comes from the EML rather than the interface exciplex. EL spectra of the devices had FWHM of ~64 nm. Since the dopants efficiently trap the excitons produced in the host, no emission was seen from the CBP host or surrounding charge-transport layers. This suggests effective host-dopant energy transfer and charge containment. **Figure 5.12e** shows that the EL spectra remained constant over a wide range of applied voltages, demonstrating excellent spectral stability. **Table 5.3** lists the CIE 1931 standard chromaticity coordinates at 10 V. These results provide evidence that the dyes are suitable for use in OLEDs.

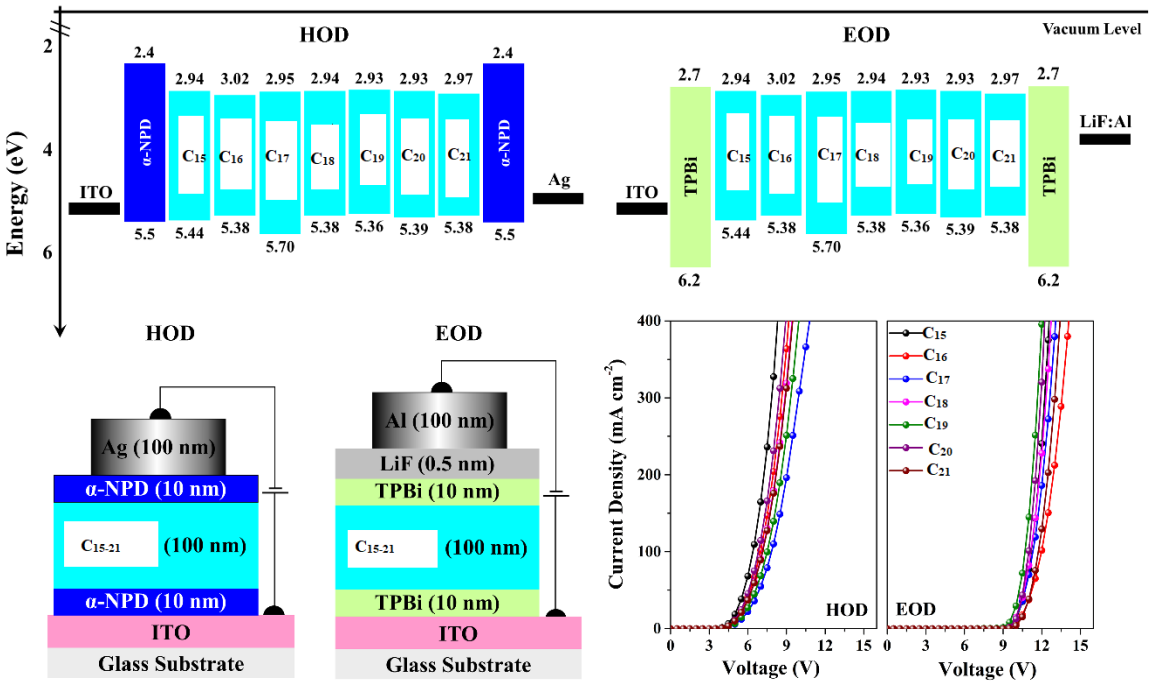

Figure 5.10. Energy level diagram and schematic of the device architectures of single carrier devices

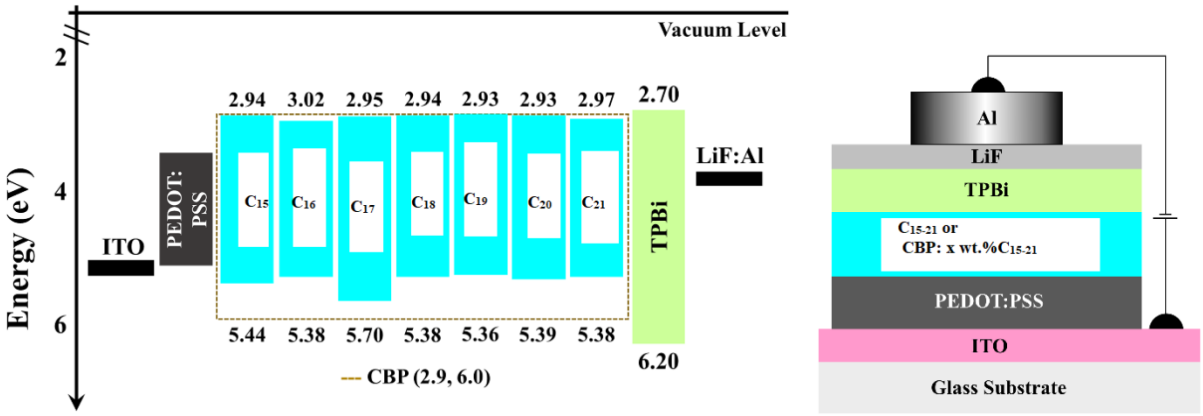

Figure 5.11. Energy level diagram and schematic of the device architectures of solution-processed OLEDs

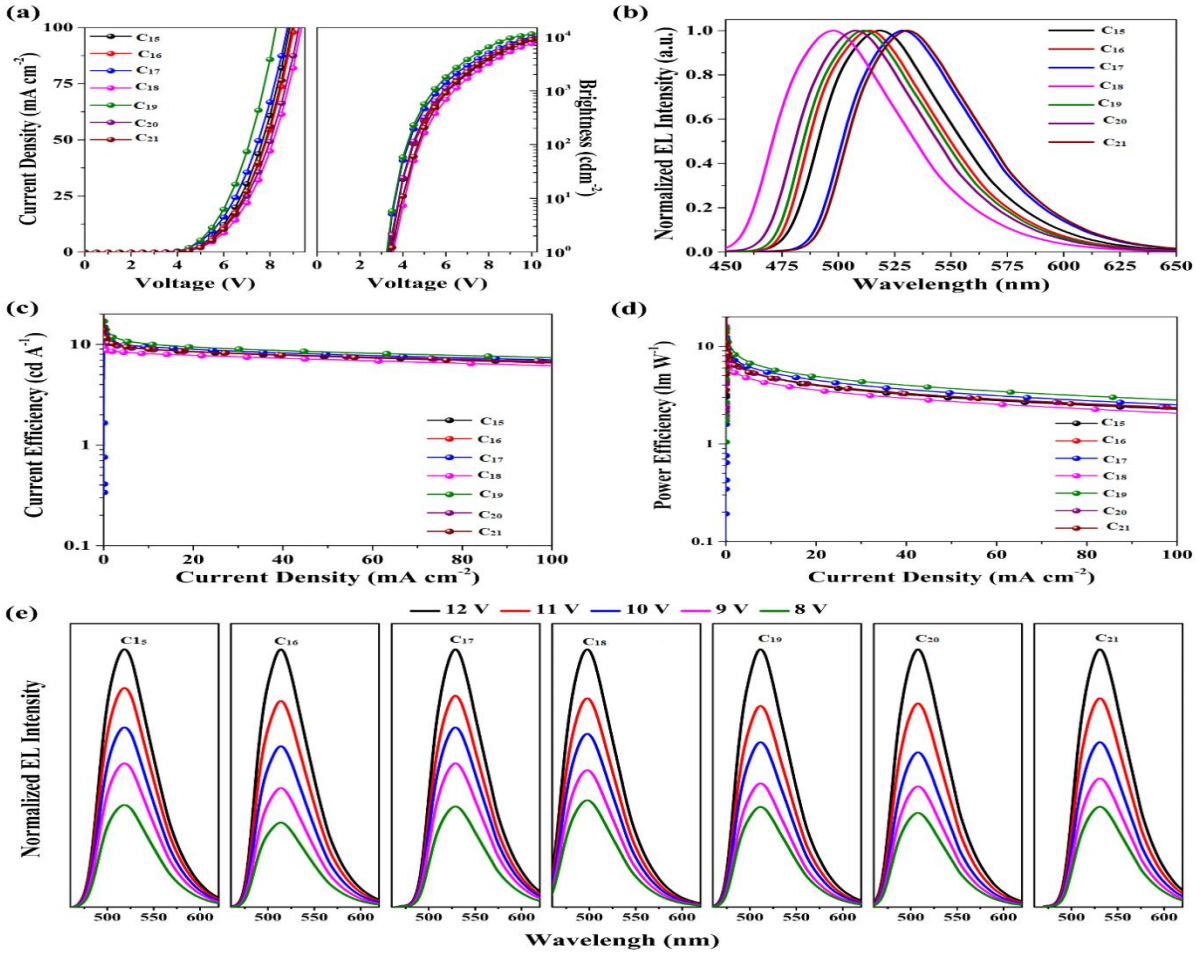

Figure 5.12. (**a**) J-V-L (**b**) EL spectra, (**c**) CE-J, and (**d**) PE-J (**e**) EL-V characteristics of the OLEDs.

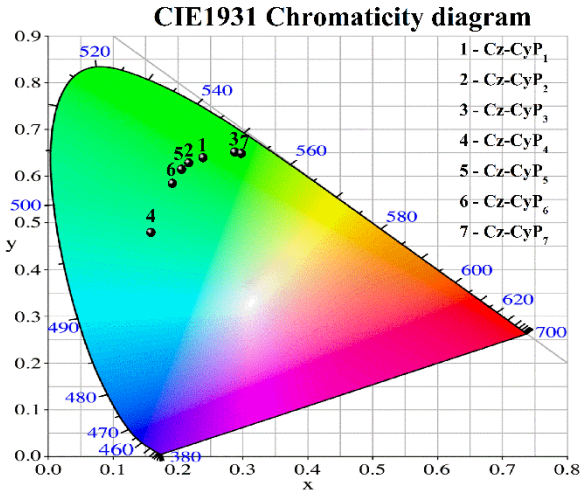

Figure 5.13. Chromaticity diagram of the OLEDs

Table 5.3. Electroluminescence data of the **C_{15-21}** based OLED devices in CBP host matrix

Emitter	V_{100}/ V_{1000} (V)[a]	$CE_{100}/PE_{100}/EQE_{100}$ (cd A^{-1}, lm W^{-1}, %)[b]	$CE_{1000}/PE_{1000}/EQE_{1000}$ (cd A^{-1}, lm W^{-1}, %)[c]	L_{max} (cd m^{-2})[d]	λ_{EL} (nm)[e]	CIE[f]
C_{15}	4.42/6.05	10.66/7.42/4.30	8.78/4.40/3.22	8540	519	(0.239, 0.644)
C_{16}	4.04/6.00	10.98/8.49/4.93	8.84/4.65/3.68	9170	514	(0.217, 0.633)
C_{17}	4.15/5.61	11.62/8.66/5.07	9.40/5.29/3.94	10130	528	(0.288, 0.656)
C_{18}	4.70/6.34	8.64/5.58/3.92	8.01/3.99/3.04	7570	498	(0.159, 0.484)
C_{19}	4.09/5.39	13.16/9.85/5.41	10.09/5.91/4.18	11390	511	(0.206, 0.619)
C_{20}	4.37/5.87	10.55/7.61/4.49	9.03/4.88/3.72	9620	506	(0.192, 0.589)
C_{21}	4.61/6.07	11.14/7.90/4.64	8.89/4.59/3.51	8890	530	(0.298, 0.653)

[a] Turn-on voltage at a luminance of 100/1000 cd m^{-2}
[b] CE, PE, EQE at 100 cd m^{-2}
[c] CE, PE, EQE at 1000 cd m^{-2}
[d] Maximum luminance at 10 V
[e] EL spectra maximum at 10 V
[f] CIE color coordinate at 10 V

5.1.4.3 Device performance of C_{22-28}(Series-4)

The study investigated compounds **C_{22-28}** as potential bluish-green emitters in OLEDs. Intricate multilayer device setup was used, it was processed *via* solutions. The device's architecture featured various layers: ITO (120 nm)/ PEDOT: PSS (35 nm)/ CBP: 3wt% **C_{15-21}** (35 nm)/ TPBi (30 nm)/ LiF (0.5 nm)/ Al (150 nm). Starting with ITO-coated glass acting as the anode, followed by PEDOT: PSS facilitating hole injection, then the CBP host material doped with 3wt% **C_{22-28}** as the emitting layer,

succeeded by TPBi for electron transport, and concluding with a LIF/Al bilayer serving as the cathode. CBP played a pivotal role in transferring charge and efficiently channelling excitons to the dopant emitters.

To maintain the integrity of the emitted colors and prevent concentration quenching, a meticulous approach involved using a low dopant concentration of 3wt% within the CBP host materials. This not only facilitated smooth charge transmission but also averted any compromise in the purity of emitted light. **Table 5.4** shows device performance data, and **Figure 5.14** shows device characteristics of the OLEDs.

The device setup, with its distinctive layers, showcased a diode-like behaviour (**Figure 5.14a**) and demonstrated lower current densities paired with high brightness across all variations (**Figure 5.14a**). These attributed were to the balanced charge carrier transport and effective recombination containment within the CBP host layer. Moreover, the emitted light spectra, maintaining stability and consistency in the bluish-green range, strongly indicated that the emission primarily originated from the EML rather than any interface-related sources. The FWHM of ~100 nm further validated the efficient trapping of excitons by the dopant within the host, ensuring negligible emission from the CBP host or the surrounding charge-transport layers. This substantiated the effectiveness of host-dopant energy transfer and contained charge carriers within the layer. In essence, the comprehensive analysis of the OLEDs, encompassing their performance data and spectral characteristics, strongly support the suitability of these molecules, particularly **$C_{22\text{-}28}$**, for integration into OLED technologies.

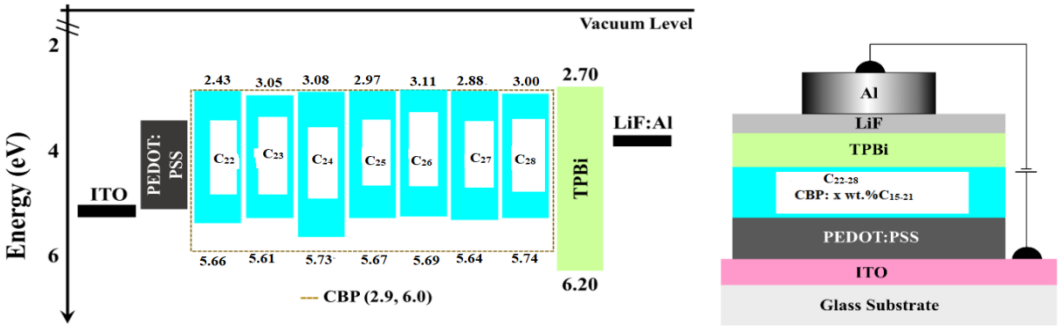

Figure 5.14. Energy level diagram and schematic of the device architectures of solution-processed OLEDs

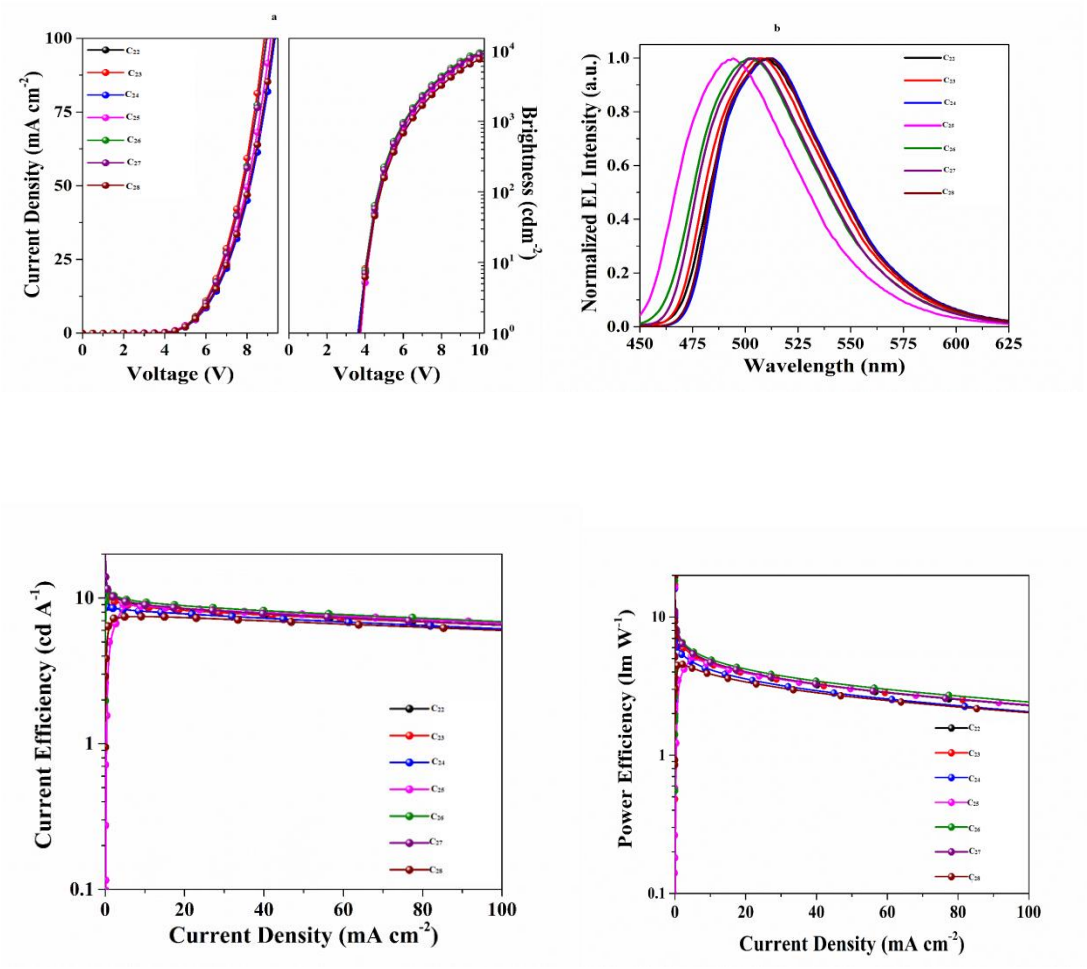

Figure 5.15 (**a**) J-V-L (**b**) EL spectra, (**c**) CE-J, and (**d**) PE-J characteristics of the OLEDs

Table 5.4. Electroluminescence data of the $\mathbf{C_{22\text{-}28}}$ based OLED devices in the CBP host matrix

Emitter	V (V)[a]	CE/PE/EQE (cd A^{-1}, lm W^{-1}, %)[b]	L_{max} (cd m^{-2})[c]	λ_{EL} (nm)[d]	CIE[e]
$\mathbf{C_{22}}$	4.59	8.91/4.72/4.33	8903	510	(0.202, 0.601)
$\mathbf{C_{23}}$	4.58	8.68/4.64/4.21	9154	506	(0.191, 0.588)
$\mathbf{C_{24}}$	4.71	8.08/4.16/3.92	7570	514	(0.205, 0.621)
$\mathbf{C_{25}}$	4.69	8.79/4.57/4.03	8680	494	(0.151, 0.435)
$\mathbf{C_{26}}$	4.54	9.36/4.97/4.62	9352	502	(0.175, 0.531)
$\mathbf{C_{27}}$	4.62	9.02/4.78/4.49	8891	504	(0.177, 0.555)
$\mathbf{C_{28}}$	4.73	7.46/3.86/3.69	7581	512	(0.200, 0.614)

[a] Turn-on voltage at a luminance of 100 cd m^{-2}
[b] CE, PE, EQE at 100 cd m^{-2}
[c] Maximum luminance at 10 V
[d] EL spectra maximum at 10 V
[e] CIE color coordinate at 10 V

5.2 CONCLUSIONS

The selected four series (**Series 1-4**) of newly synthesized organic compounds were subjected to OLED fabrication studies as emissive layers. The electroluminescence performance of synthesized molecules in a doped OLED device displayed encouraging results. OLED device configuration, *i.e.* ITO (120 nm)/F_4TCNQ (4 nm)/ α-NPD (30 nm)/ CBP: x wt% of Series-1/Series-2 (35 nm)/ TPBi (30 nm)/ LiF (0.5 nm)/ Al (150 nm) was done for emitters of **Series-1** and **Series 2**. Further, the device configuration, *i.e.* ITO (120 nm)/ PEDOT: PSS (35 nm)/ CBP: 3wt% of Series-3/Series-4 (35 nm)/ TPBi (30 nm)/ LiF (0.5 nm)/ Al (150 nm) was constructed for fluorophores of **Series-3** and **Series-4**. Among them, a doped devices composed of **C_3**, **C_{11}**, **C_{19}** and **C_{26}** as an emissive layer display the EQE of 5.32(CE: 10.72 cd/A, PE: 7.87 lm/W), 5.91(CE: 14.38 cd/A, PE: 12.04 lm/W)**,** 5.41(CE: **13.16/9 cd/A,** PE: 9.85 lm/W) and 4.62%, (CE: 9.36 cd/A, PE: 4.97 lm/W), respectively. Evidently, the observed results suggest that new design strategies for emitters offer efficient materials for OLEDs with improved efficiency. Proper tailoring of the donor attached to the heterocyclic core could further improve the quantum yield of the materials, leading to enhanced device efficiency.

SUMMARY, CONCLUSIONS, AND SCOPE FOR FUTURE WORK

Abstract

This chapter contains a summary of the entire research carried out and the important conclusions drawn from the present research work. It also includes a brief account of the scope for further work.

6.1 SUMMARY

The development of efficient organic π-conjugated small molecules has been crucial in the advancement of electronic applications in recent years. These compounds have played a major role in electronic devices such as organic light-emitting diodes (OLEDs), organic field-effect transistors (OFETs), organic light-emitting transistors (OLETs), organic solid-state lasers, organic solar cells (OSCs), and biomedical devices. These devices owe their significance to the well-structured molecular arrangements of these compounds. The simplicity in their synthesis, easy purification methods, adaptability for solution and vacuum deposition during fabrication, and the ability to fine-tune their functional properties through relatively straightforward structural engineering make them highly desirable.

Over the last decade, OLEDs have gained a lot of attention for their potential use in advanced lighting and flat panel displays. Scientists have been working to create new emissive materials that meet market demands, such as high luminescence in solid form, excellent film-forming properties, heat stability, and color purity. However, there is still plenty of room for further refinement and innovation in the development of new OLED emissive materials for broader applications in OLED devices.

In this context, the present research work has mainly focused on the molecular design and synthesis of interesting push-pull type structural entities based on cyanopyridone core, which would favour the formation of thermally stable small molecules with exciting optical and electronic properties for application in OLEDs as effective emitters. Currently, there are no reports available on these types of molecules.

A comprehensive literature review was conducted to explore the design principles of new heterocyclic structures. Based on a donor-acceptor strategy, seven new series (**Series 1-7**) were designed. They were all D-A-D configured structures containing powerful electron-withdrawing cyanopyridone (**Series-1** to **6**) and nicotinonitrile (**Series-7**) cores at the center, along with different auxiliary donor moieties. They include fixed donor units, *viz.* triphenylamine **(Series-1),** pyrene **(Series-2)**, carbazole **(Series-3),** phenothiazine **(Series-4**), *N,N*-diphenylamine **(Series-5),** and *N,N*-diphenylaniline **(Series-6** and **-7)** and varied auxiliary donors such as thienyl, tolyl, 4-hydroxy phenyl, anisolyl, phenyl, biphenyl, *etc*. The synthesis of these designed molecules was achieved through several straightforward and multistep protocols, and their structures were confirmed using spectral techniques. As well, their photophysical and electrochemical properties were studied through experimental methods. Also, theoretical simulations was carried out to gauge their potential in optoelectronic devices. On the basis of the material's properties, luminogens of four series (**Series-1** to **4**) were employed as active emissive components to fabricate multilayer OLED devices, and their performance in the devices was studied in detail.

6.2 CONCLUSIONS

On the basis of experimental results, the following significant conclusions have been drawn from the present research work.

1. Based on the literature survey, seven new series of (forty-two) compounds carrying cyanopyridone, and cyanopyridine heterocyclic core appended to different fixed donor group with a varying axillary donor group were successfully designed and synthesized through multi-step synthetic routes. The reaction conditions were rationally optimized with respect to many parameters to get compounds with maximum yield. Further, purification methods were developed.
2. The chemical structures of all the newly synthesized intermediates as well as target compounds were established by various spectral techniques.
3. From their photophysical, electrochemical, thermal, and molecular modelling studies, it is clear that the synthesized molecules ($\mathbf{C_{1\text{-}42}}$) possess all the prerequisites to act as potential emitters.

4. From the optical characterization, it is evident that all the compounds display strong absorption at 384-402 nm (**Series-1**), 368-398 nm (**Series-2**), 374-391 nm (**Series-3**), 374-403 nm (**Series-4**), 377-400 nm (**Series-5**) , 421-433 nm (**Series-6**), and 375-421 nm (**Series-7**) and emission at 551-564 nm (**Series-1**, yellow) 478-506 nm (**Series-2,** green), 468-510 nm (**Series-3,** cyan), 479-497 nm (**Series-4,** bluish green), 547-555 nm (**Series-5**), 491-497 nm (**Series-6**), and 484-501 nm (**Series-7**) nm. In addition, the range of optical band gaps of **Series-1** to **Series-7** are 2.39-2.44, 2.64-2.76, 2.78-2.93, 2.55-2.95, 2.55-2.80, 2.58-2.66, and 2.71-2.93 eV, respectively. Whereas, Stokes shifts are in the range of 4000-9780 cm^{-1}. This large stoke shift is beneficial for reducing the self-quenching that is resulting from molecular self-absorption. The quantum yield as calculated in solution state is of the order of 10-50%.
5. Their thermal study demonstrates that most of the compounds, *i.e.* $\mathbf{C_{1-2}}$, $\mathbf{C_4}$, $\mathbf{C_5}$, $\mathbf{C_7}$ (393-423 ^oC), $\mathbf{C_{8-12}}$ (410-470 ^oC), $\mathbf{C_{15-16}}$, $\mathbf{C_{18}}$, $\mathbf{C_{21}}$ (334-384 ^oC), $\mathbf{C_{22-24}}$, $\mathbf{C_{26-28}}$ (301-373 ^oC), $\mathbf{C_{29-32}}$ (300-381 ^oC), $\mathbf{C_{36-37}}$ (384-400 ^oC) show good thermal stability without weight loss. Among $\mathbf{C_{1-42}}$, pyrene-substituted compounds have high T_d due to their rigid structure.
6. According to the theoretical studies (by Gaussian 09 software), and geometry optimizations (by Lee-Yang-Parr B3LYP exchange correlation functional with 6-31G (d,p) basis set), all the synthesized compounds possess ICT behaviour.
7. As established by their electrochemical study, all the compounds exhibit significant redox properties and have low-lying LUMO levels with narrow energy bandgaps. The bandgap range for each series is as follows: 2.10-2.33 (**Series-1**), 2.07-2-68 (**Series-2**), 2.36-2.74 (**Series-3**), 2.58-2.76 (**Series-4**), 2.28-2.36 (**Series-5**), 2.31-2.63 (**Series-6**), and 2.37-2.53 eV (**Series-7**). In this, all of them have ideal HOMO and LUMO levels, that match the standard hole transporting and electron transporting layers, which aid in efficient charge transportation.
8. Among the fabricated multi-layer OLED devices employing $\mathbf{C_{1-28}}$ as emissive materials, device structures with $\mathbf{C_3}$, $\mathbf{C_{11}}$, $\mathbf{C_{19}}$, and $\mathbf{C_{26}}$ exhibited high current efficiency of 10.72, 14.38, 13.16, and 9.36 cd/A, good power efficiency of 7.87, 12.04, 9.95, and 4.97 lm/W, and fairly good EQE of **5.32%, 5.91%, 5.41, and 4.62%**, respectively. The devices showed different emissions, *i.e.* **Series-1**

emitted yellow colour, **Series-2** gave the green light, **Series-3** produced bluish-green radiations, and **Series-4** radiated bluish-green light.

6.3 SCOPE FOR FUTURE WORK

Organic emitters based on π-conjugated skeletons are emerging as promising next-generation materials for optoelectronic devices. To optimize the performance of OLEDs based on such emitters, a balanced distribution of injected charge carriers (holes and electrons) is required. The control of parameters such as optical characteristics, energy gap, ionization potential, or electron affinity by adjusting the length of π-conjugation or by introducing electron-donating or accepting substituents plays a key role. There are many factors to consider in the design of organic emitters, and even a slight change in any of these factors can affect other parameters. OLEDs have many favorable features such as high brightness and efficiency, low driving voltage, and low production cost, making them the most competitive candidate for next-generation lighting sources with energy-saving capability.

For the first time, OLEDs were fabricated by using cyanopyridone-based small molecules. With adequate tailoring of donors and accepters, it would be possible to further improve the quantum yield of the materials and hence further enhancement of device efficiency. It may also lead to optimization of desired properties of good emitters. By changing the device architecture, *i.e.* by choosing appropriate HTM and ETM, it is possible to further enhance the device performance. Further, these investigated molecules and their intermediates may find applications in various other fields including medicinal chemistry.

REFERENCE

1. Abbotto, A.S. Bradamante, Pagani G.A. (2001) .‘‘Pyridoneimines and Pyridonemethides: Substituent- and Solvent-Tunable Intramolecular Charge Transfer and Geometric Isomeris”.J. Org. Chem. 66 8883–8892.
2. Baldo, M.A, Lamansky S, Burrows PE, Thompson ME, Forrest SR. “Very high-efficiency green organic light-emitting devices based on electrophosphorescence”. *Appl Phys Lett*. 1999;75(1).
3. Baheti, A. Lee, C.P. Thomas , K.R. Ho, K.C. (2011) “Pyrene-based organic dyes with thiophene containing π-linkers for dye-sensitized solar cells: Optical, electrochemical and theoretical investigations. *Phys Chem Chem Phys*. 13(38):17210-17221.
4. Chen, L.X. Chen, (2019) ‘‘Organic Solar Cells: Recent Progress and Challenges’’, ACS Energy Lett. 4 2537–2539.
5. Chidirala, S. Ulla, H. Valaboju, A. Kiran, M.R. Mohanty, M.E. Satyanarayan, M.N. Umesh, G. Bhanuprakash, K. Rao, V.J. (2016). “Pyrene-Oxadiazoles for Organic Light-Emitting Diodes: Triplet to Singlet Energy Transfer and Role of Hole-Injection/Hole-Blocking Materials. *J Org Chem*, 81(2),603-614.
6. Chen, J.J. Wang, I.J. (1995). “ Synthesis and colour assessment of some 3-cyano-4-pyrenyl-6-substituted-2-pyridone derivatives”. *Dye Pigment*,29(4):305-313.
7. Duan, L. Hou, T.W. Lee, J. Qiao, D. Zhang, G. Dong, L. Wang, Y. Qiu, (2010). “Solution processable small molecules for organic light-emitting diodes’’, J. Mater. Chem. 20 6392–6407.
8. Duan, L. Qiao, J. Sun, Y. Qiu, Y. (2011). “Strategies to Design Bipolar Small Molecules for OLEDs: Donor-Acceptor Structure and Non-Donor-Acceptor Structure”. Adv. Mater. 23 1137–1144.
9. Fernandes, J.M. Raveendra Kiran, M, Ulla, H. Satyanarayan, M.N. Umesh, G. (2014). “Investigation of hole-injection in α-NPD using capacitance and impedance spectroscopy techniques with F4TCNQ as hole-injection layer: Initial studies”. *Superlattices Microstruct*. 76:385-393.
10. Gao, Z.J. Yeh, T.H. Xu, J.J. Lee, C.C. Chowdhury, A.Wang, B.C. Liu, S.W. Chen, C.H. (2020). “Carbazole/Benzimidazole-Based Bipolar Molecules as the Hosts for Phosphorescent and Thermally Activated Delayed Fluorescence Emitters for Efficient OLEDs’’, ACS Omega. 5 10553–10561.
11. Goes, M. Verhoeven, J.W. Hofstraat, H. Brunner, K. (2003). “OLED and PLED Devices Employing Electrogen- cence.” *Chemphyschem A Eur J Chem Phys Phys Chem*. 4(4):349-358.
12. Hong, L. Yao, H. Cui, Y. Ge, Z. Hou, J. (2020) “Recent advances in high-efficiency organic solar cells fabricated by eco-compatible solvents at relatively large-area scale’’, APL Mater. 8 120901.
13. Jeong, S. Kim, M.K. Kim, S.H. Hong, J.I. (2013) “ Efficient deep-blue emitters based on triphenylamine-linked” 14(10):2497-2504.
14. Jiang, Y.. Liu, Y. Liu, Y, Lin, X. Gao, H. K.. Lai, W.Y. Huang, W. (2020). ‘‘Organic solid-state lasers: a materials view and future development’’ Chem. Soc. Rev. 49 5885–5944.

15. Khalifa, N.M. Omar, M.A. Sediek, A.A. (2015) “Synthesis and characterization of some novel substituted pyridones and iminopyridines derived from pyrene moiety”. *Russ J Gen Chem*.;85(12):2839-2844.
16. Kulhánek, J. Bureš, F. (2012) ,‘‘Imidazole as a parent π-conjugated backbone in charge-transfer chromophores’’, J. Org. Chem. 8 25–49.
17. Kajjam, A.B. Giri, S. (2017) ‘‘Triphenylamine-based donor–π–acceptor organic phosphors: synthesis, characterization and theoretical study’’, Mater. Chem. Front. 1 512–520.
18. Kulkarni, A.P, Kong , X .Jenekhe, S.A. (2006) “High-performance organic light-emitting diodes based on intramolecular charge-transfer emission from donor-acceptor molecules: Significance of electron-donor strength and molecular geometry”. *Adv Funct Mater*. 16(8):1057-1066.
19. Kang, S. Huh, J.S, Kim, J.J, Park, J.(2020) “Highly efficient deep-blue fluorescence OLEDs with excellent charge balance based on phenanthro[9,10-: D] oxazole-anthracene derivatives”. *J Mater Chem C*. 8(32):11168-11176.
20. Kajjam, A.B, Giri, S. Sivakumar, V. (2017) “Triphenylamine-based donor-π-acceptor organic phosphors: Synthesis, characterization and theoretical study”. *Mater Chem Front*.;1(3):512-520.
21. Kim, Y.H. Yoon, D.K. Lee, E.H. Jung, H.T. 2006 “Photoluminescence properties of a perfluorinated supramolecular columnar liquid crystal with a pyrene core: Effects of the ordering and orientation of the columns”. *J Phys Chem B*. 110(42):20836-20842.
22. Kang, S. Huh, J.S, Kim, J.J. Park, J. (2020) “Highly efficient deep-blue fluorescence OLEDs with excellent charge balance based on phenanthro[9,10-d]oxazole-anthracene derivatives’’, J. Mater. Chem. C. 8 11168–11176.
23. Liu, K. Ouyang, B. Guo, X. Guo, Y. Liu, Y. (2022) .‘‘Advances in flexible organic field-effect transistors and their applications for flexible electronics.’’ Npj Flex. Electron. 6 1–19.
24. Lin, S.L. Chan, L.H. Lee, R.H. et al. (2008) “Highly efficient carbazole-π-dimesitylborane bipolar fluorophores for nondoped blue organic light-emitting diodes”. *Adv Mater*.;20(20):3947-3952.
25. Ledwon, P. Motyka, R. Ivaniuk, K. et al. (2019): “The effect of molecular structure on the properties of quinoxaline-based molecules for OLED applications”. *Dye Pigment*.173108008.
26. Liu, R. Ran, H. Zhao, Z. et al. (2018)“Synthesis and Optical Properties of Donor-Acceptor-Type 1,3,5,9-Tetraarylpyrenes: Controlling Intramolecular Charge-Transfer Pathways by the Change of π-Conjugation Directions for Emission Color Modulations”. *ACS Omega*.;3(5):5866-5875.
27. Liu, X.K. Zheng, C,J,Lo, M.F. et al. (2013). “Novel blue fluorophor with high triplet energy level for high performance single-emitting-layer fluorescence and phosphorescence hybrid white organic light-emitting diodes”. *Chem Mater*.;25(21):4454-4459.
28. Nezakati, T. Seifalian, A. Tan, A. Seifalian, A.M. (2018) “Conductive Polymers: Opportunities and Challenges in Biomedical Applications’’, Chem. Rev. 118 6766–6843.
29. Paquin, F. Rivnay, J. Salleo, A. Stingelin, N. Silva, C. (2015) “Multi-phase semicrystalline microstructures drive exciton dissociation in neat plastic

semiconductors". *J Mater Chem C*.;3:10715-10722.
30. Pilicode, N. Acharya, M. P. Naik, S.M. Adhikari, A.V. (2019) "New blue light emitting cyanopyridine based conjugated polymers: From molecular engineering to PLED applications", J. Photochem. Photobiol. Chem. 378 38–45.
31. Qin, Z. Gao, H. Dong, H. Hu, W. (2021) ''Organic Light-Emitting Transistors Entering a New Development Stage'', Adv. Mater. 33 2007149.
32. Reddy, S.S, Sree, V.G. Gunasekar, K. et al.(2016) "Highly Efficient Bipolar Deep-Blue Fluorescent Emitters for Solution-Processed Non-Doped Organic Light-Emitting Diodes Based on 9,9-Dimethyl-9,10-dihydroacridine/Phenanthroimadazole Derivatives". *Adv Opt Mater*.;4(8):1236-1246.
33. Sohn, S. Hyun Koh, B. Baek, J.Y. et al. (2017). "Synthesis and characterization of diphenylamine derivative containing malononitrile for thermally activated delayed fluorescent emitter". *Dye Pigment*.;140:14-21.
34. Singh, M. Jou, J.H. Sahoo, S. Krucaite, G. Grigalevicius, S. Wang, C.W. (2018). "High light-quality OLEDs with a wet-processed single emissive layer'', Sci. Rep. 8 7133.
35. Scott, J.C. Karg, S. Carter, S.A. (1997) "Bipolar charge and current distributions in organic light-emitting diodes". *J Appl Phys*.;82(3):1454-1460.
36. Shirota ,Y. Kinoshita, M. Noda, T. Okumoto K. Ohara, T. (2000) "A novel class of emitting amorphous molecular materials as bipolar radical formants: 2-{4-[Bis(4-methylphenyl)amino]phenyl}-5(dimesitylboryl)thiophene and 2-{4-[Bis(9,9-dimethylfluorenyl)amino]phenyl}-5-(dimesitylboryl)thiophene [9]. *J Am Chem Soc*.;122(44):11021-11022.
37. Song, J. Lee, H. Jeong, E.G. Choi, K.C. Yoo, S. (2020) "Organic Light-Emitting Diodes: Pushing Toward the Limits and Beyond'', Adv. Mater. 32 1907539.
38. Tagare, J. Ulla, H. Kajjam, A.B. Satyanarayan, M.N. Vaidyanathan, S. (2017) "Star-Shaped Phenanthroimidazole-Triphenylamine-Based Yellow Organic Emitter for Organic Light Emitting Diodes'', ChemistrySelect. 2 2611–2620.
39. Thurakkal, S. Sanju, K.S. Soman, A. Unni K.N. Joseph,J. Ramaiah, D. (2018) "Design and Synthesis of solution processable green fluorescent D-π-A dyads for OLED applications". *New J Chem*.;42(7):5456-5464.
40. Thomas, K.R.J. Lin, J.T. Velusamy, M, Tao, Y.T. Chuen, C.H. (2004) "Color tuning in Benzo[1,2,5]thiadiazole-based small molecules by amino conjugation/deconjugation: Bright red-light-emitting diodes". *Adv Funct Mater*.;14(1):83-90.
41. Tagare, J. Ulla, H. Kajjam, A.B. Satyanarayan, M.N. Vaidyanathan, S. (2017) "Star-Shaped Phenanthroimidazole-Triphenylamine-Based Yellow Organic Emitter for Organic Light Emitting Diodes". *ChemistrySelect*.;2(8):2611-2620.
42. Tagare, J. Ulla, H. Satyanarayan, M.N. Vaidyanathan, S. (2018) "Synthesis, photophysical and electroluminescence studies of new triphenylamine-phenanthroimidazole based materials for organic light emitting diodes". *J Lumin*. 194:600-609.
43. Tagare, J. Ulla, H. Satyanarayan, M.N. Vaidyanathan, S. (2018) "Efficient non-doped bluish-green organic light emitting devices based on N1

functionalized star-shaped phenanthroimidazole fluorophores". *J Photochem Photobiol A Chem*. 353:53-64.

44. Thirion, D. Rault-Berthelot, Vignau, J, Poriel, L, "Synthesis and properties of a blue bipolar indenofluorene emitter based on a D-π-A design". *Org Lett*. 13(16):4418-4421.
45. Ulla, H. Garudachari, B. Satyanarayan, M.N. Umesh, G. Isloor, A.M. (2014) "Blue organic light emitting materials: Synthesis and characterization of novel 1,8-naphthalimide derivatives'', Opt. Mater. 36 704–711.
46. Ulla, H. Kiran, M.R. Garudachari, B. Ahipa, T.N. Tarafder, K. Adhikari, A.V. Umesh, G. Satyanarayan, M.N. (2017) "Blue emitting 1,8-naphthalimides with electron transport properties for organic light emitting diode applications'', J. Mol. Struct. 1143 344–354.
47. Ulla, H. Raveendra Kiran, M. Garudachari, B. Satyanarayan, M.N. Umesh, G. Isloor, A.M. (2014) ''Blue emitting halogen–phenoxy substituted 1,8-naphthalimides for potential organic light emitting diode applications'', Opt. Mater. 37 311–321.
48. Umasankar, G. Ulla, H. Madhu, C. Reddy, G.R. Shanigaram, B. Nanubolu, J.B. Kotamarthi, B.. Karunakar, G.V Satyanarayan, M.N. Rao, V.J. (2021) '' Imidazole-Pyrene Hybrid Luminescent Materials for Organic Light-Emitting Diodes: Synthesis, Characterization & Electroluminescent Properties, J. Mol. Struct. 1236 130306.
49. Ulla, H. Kiran, M.R. Garudachari, B. et al. (2017) "Blue emitting 1,8-naphthalimides with electron transport properties for organic light emitting diode applications". *J Mol Struct*.;1143:344-354.
50. Ulla,H. Kiran, M.R. Garudachari, B. Satyanarayan, M.N. Umesh, G. Isloor, A.M. (2014) "Blue emitting halogen-phenoxy substituted 1,8-naphthalimides for potential organic light emitting diode applications". *Opt Mater (Amst)*.;37(C):311-321.
51. Umasankar, G. Ulla, H. Madhu, C. et al.(2021) "Imidazole-Pyrene Hybrid Luminescent Materials for Organic Light-Emitting Diodes: Synthesis, Characterization & Electroluminescent Properties". *J Mol Struct*. 1236.
52. Vinayakumara, D.R. Ulla, H. Kumar, S. Satyanarayan, M.N. Adhikari, A.V. (2018) "New fluorescent columnar mesogens derived from phenanthrene-cyanopyridone hybrids for OLED applications". *Mater Chem Front*.;2(12):2297-2306.
53. Vinayakumara, D.R. Kesavan, R. Kumar, S. Adhikari, A.V. (2019) "New cyanopyridone-based unsymmetrical dyads: the effect of donor strength on their optoelectronic properties'', Photochem. Photobiol. Sci. 18 2052–2060.
54. Vishnumurthy, K.A. Sunitha, M.S. Philip, R. Adhikari, A.V. (2011) "New diphenylamine-based donor-acceptor-type conjugated polymers as potential photonic materials". *React Funct Polym*.;71(12):1119-1128.
55. Vijaykumar, B.V.D. Nalluri S, Uppada, M.K. et al. (2022) "Ligand-Free Suzuki Coupling for the Practical Synthesis of 4-(Triphenylen-2-yl) dibenzothiophene for Solution-Processed OLEDs". *ChemistrySelect*.;7(25).
56. Wu, Q. Braveenth, R. Zhang, H.Q. Bae, I.J. Kim, M. Chai, K.Y. (2018) "Oxadiazole-based highly efficient bipolar fluorescent emitters for organic light-emitting diodes". *Molecules*.;23(4).

57. Woo, S.J. Kim, Y. Kim, M.J. et al. (2018) “Strategies for the Molecular Design of Donor-Acceptor-type Fluorescent Emitters for Efficient Deep Blue Organic Light Emitting Diodes”. *Chem Mater*.;30(3):857-863.
58. Wen, Z. Yang, T. Zhang, D. Wang, Z. Dong, S. Xu, H. Miao, Y. Zhao, B. Wang, H. (2022) “A multifunctional luminescent material based on quinoxaline and triphenylamine groups: polymorphism, mechanochromic luminescence, and applications in high-efficiency fluorescent OLEDs’’, J. Mater. Chem. C. 10 3396–3403.
59. Wang, C. Dong, H. Hu, W. Liu, Y. Zhu, D. (2012) “Semiconducting π-conjugated systems in field-effect transistors: a material odyssey of organic electronics’’, Chem. Rev. 112 2208–2267.
60. Zhu, M.C. and Yang, (2013).“Blue fluorescent emitters: design tactics and applications in organic light-emitting diodes’’, Chem. Soc. Rev. 42 4963–4976
61. Zou, S.J Y. Shen, F.-M. Xie, J.-D. Chen, Y.-Q. Li, J.-X. Tang, Recent advances in organic light-emitting diodes: toward smart lighting and displays, Mater. Chem. Front. 4 (2020) 788–820.
62. Zhu, W. Hu, M. Yao, R. Tian, H. (2003) “A novel family of twisted molecular luminescent materials containing carbazole unit for single-layer organic electroluminescent devices’’, J. Photochem. Photobiol. Chem. 154 169–177.
63. Zhu, M. Yang, C. (2013) “Blue fluorescent emitters: Design tactics and applications in organic light-emitting diodes’’. *Chem Soc Rev*.;42(12):4963-4976.
64. Zhang, G. Auer-Berger, M. Gehrig, D.W. et al. (2016) “Blue light emitting polyphenylene dendrimers with bipolar charge transport moieties’’. *Molecules*.;21(10):1-15.
65. Zhu, Y. Kulkarni ,A.P. Jenekhe , S.A. (2005) “Phenoxazine-based emissive donor-acceptor materials for efficient organic light-emitting diodes’’. *Chem Mater*.;17(21):5225-5227.
66. Zhu,W. Hu,M. Yao, R. Tian, H. (2003) “A novel family of twisted molecular luminescent materials containing carbazole unit for single-layer organic electroluminscent devices”. *J Photochem Photobiol A Chem*.;154(2-3):169-177.
67. Zhan, Y. Peng, J. Ye, K. Xue, P. Lu, R. (2013) “Pyrene functionalized triphenylamine-based dyes: Synthesis, photophysical properties and applications in OLEDs”. *Org Biomol Chem*.;11(39):6814-6823.

LIST OF PUBLICATIONS

Paper published in international journals

K. S. Vishrutha, Hidayath Ulla, Badekai Ramachandra Bhat, Airody Vasudeva Adhikari, (2023) "Cyanopyridone-cored fluorophores with triphenylamine Peripheries From Molecular design to OLED Fabrication Studies." Journal of Photochemistry and Photobiology A. 435 (2023) 114344, DOI: https://doi.org/10.1016/j.jphotochem.2022.114344.

K. S. Vishrutha, Hidayath Ulla, Badekai Ramachandra Bhat, Airody Vasudeva Adhikari, (2023) "New Green Emitters Based on Push-Pull Type Pyrene Substituted Cyanopyridones: Design Strategies and Utilization in Organic Light-Emitting Diodes." Dyes and Pigments, 219(2023)11560, DOI: https://doi.org/10.1016/j.dyepig.2023.111560.

K. S. Vishrutha, Hidayath Ulla, Badekai Ramachandra Bhat, Airody Vasudeva Adhikari, "Utilization of Newly Configured Carbazole-Cyanopyridone Structural Hybrids towards Achieving High-Performance Cyan Fluorescent Organic Light-Emitting Diodes." Materials Advances (RSC) on November 03, 2023, DOI: 10.1039/D3MA00922J

Manuscript to be communicated

K. S. Vishrutha, Hidayath Ulla, Badekai Ramachandra Bhat, Airody Vasudeva Adhikari, "New Fluorescent Emitters Based on Donor-Acceptor Type Cyanopyridone Containing Phenothiazine Moiety: Design, Synthesis and Characterization and device studies", (Manuscript ready for communication to JMCC, *RSC*).

K. S. Vishrutha, Hidayath Ulla, Badekai Ramachandra Bhat, and Airody Vasudeva Adhikari "New Fluorescent Emitters Based on Donor-Acceptor Type Cyanopyridones Containing Diphenylamine Moiety: Design, Synthesis and Characterization and Device studies" (Manuscript ready for communication to ACS Applied Energy Materials).

Manuscript under preparations

K. S. Vishrutha, Hidayath Ulla, Badekai Ramachandra Bhat, Airody Vasudeva Adhikari, "New Fluorescent Emitters Based on Donor-Acceptor Type Cyanopyridone small molecules: Design, Synthesis, Characterization and Device Studies".

K.S Vishrutha, Hidayath Ulla, Badekai Ramachandra Bhat, Airody Vasudeva Adhikari, "New Fluorescent Emitters Based on Donor-Acceptor Type Cyanopyridone Containing small molecules for OLED application".

Conferences attended:

K. S. Vishrutha, and Airody Vasudeva Adhikari, "Simple Triphenylamine-Based High-Performance Electroluminescent Materials: From Molecular Design to Device Fabrication Studies", International conference on Advancements in Materials Science and Technology iCAM 2022, Organized by Satyabhama University, Chennai, **during November 3-6, 2022.**

K. S. Vishrutha, and Airody Vasudeva Adhikari, "Simple pyrene-based new molecules for optoelectronic applications", International Conference on Recent Trends in Material Science and Technology, Organized by the Department of Chemistry, Indian Institute of Space Science and Technology, **during December 28-30**,2022.

CURRICULUM VITAE

VISHRUTHA K S

PRESENT ADDRESS

Department of Chemistry
National Institute of Technology Karnataka
Surathkal,Mangalore-575025
Karnataka, India

PERMANENT ADDRESS

Masthambika Road, Kaalidasa nagar
Kadur (t), Chikkamagalure(d)
Karnataka, India-577548

CONTACT DETAILS

Email: vishruthaks92@gmail.com
Mobile: +919611784158

EDUCATION

Doctor of Philosophy (Ph.D.) Chemistry, National Institute of Technology-Karnataka,(NITK) Surathkal,India	December 2023 - present
Masters of Science (M.Sc.) General Chemistry, Kuvempu University, Shankaragatta,Shivamogga Karnataka, India	2015 First Class with Distinction
Bachelor of Science (B.Sc) Physics, Chemistry, Mathematics (PCM) Kuvempu University Shankaragatta, Shivamogga Karnataka, India	2013 First Class
National Eligibility Test (NET)	**December-2016**

RESEARCH EXPERIENCE

11-07-2018-on going (Supervisor: Prof.A.V.Adhikari)	National Institute of Technology-Karnataka (NITK)-Surathkal	Doctoral Student	Organic materials for optoelectronic applications

TEACHING EXPERIENCE

10-07-2015 to 30-08-2016	IDSG College, Chikkamangalure	Guest Lecturer
15-07-2017 to 05-07-2018	Kuvempu University Shankaragatta	Guest Lecturer

RESERCH PUBLICATIONS

Paper published in international journals 03

Paper Presented in international conference 02

PERSONAL INFORMATION

Date of Birth: 25/05/1993

Sex: Female

Nationality: Indian

Language: Kannada, English,Hindi